Ultrafast Nonlinear Nano-Optics via Collinear Characterization of Few-Cycle Pulses

Dissertation

zur Erlangung des akademischen Grades

DOCTOR RERUM NATURALIUM
(Dr. rer. nat.)
im Fach Physik

eingereicht an der
Mathematisch-Naturwissenschaftlichen Fakultät
der Humboldt-Universität zu Berlin

von
M. Sc. (Tech.) Janne Juhani Hyyti

Präsidentin der Humboldt-Universität zu Berlin
Prof. Dr.-Ing. Dr. Sabine Kunst

Dekan der Mathematisch-Naturwissenschaftlichen Fakultät
Prof. Dr. Elmar Kulke

Gutachter:	1. Prof. Dr. Günter Steinmeyer
	2. Prof. Dr. Kurt Busch
	3. Prof. Dr. Christoph Lienau
Eingereicht am:	26.04.2018
Tag der Disputation:	09.07.2018

Abstract

The ultrashort laser pulse characterization method *interferometric frequency-resolved optical gating* (iFROG), introduced in the 2000s, is extended. Both second- and third harmonic generation (SHG and THG) are separately employed as the optical nonlinearity. An iFROG measurement represents an inverse problem, where the electric field amplitude and phase of the underlying laser pulse can only be reconstructed by an iterative algorithm. In this work, a mathematical formalism generalizing both the SHG and THG variants of iFROG is developed and combined with *differential evolution*, an evolutionary optimization algorithm, to create a novel pulse retrieval algorithm for iFROG.

While iFROG was originally conceived solely for the characterization of laser pulses, the technique can equally well be applied for spectroscopic purposes. By replacing the nonlinear medium in iFROG with an object of study — say a nanostructure — and characterizing a known pulse again such that the sample affects the harmonic generation process, the complex response function of the object can be deciphered with subfemtosecond precision. As no previous solution for the THG variant exists, the presented retrieval algorithm allows iFROG to be exploited in the study of ultrafast third-order nonlinear effects for the first time.

During the process of extending iFROG, various pulse retrieval algorithms are discussed. One of these originates from ptychography, a lensless imaging technique. Paired with a modified iFROG device where nonidentical pulse replicas break the symmetry of time, the ptychographic retrieval algorithm identifies trailing and leading satellite structures in the pulse unambiguously. The performance of this new pulse characterization modality named πFROG is verified experimentally via a comparison with a commercial measurement device, and by artificially adding and correctly reconstructing additional spectral phase. Similarly, the presented iFROG method is evaluated both numerically and in real life experiments, and pitted against rival algorithms employing SHG, where — in contrast to THG — competition does exists.

The spectroscopic capability of iFROG is put to test by studying three differing physical systems, each consisting of nanostructures resting on dielectric substrates. Subjecting these specimen to few-cycle near-infrared pulses, a rich variety of nonlinear optical phenomena is observed. In ZnO nanorods, the power dependence of multiphoton-absorption induced photoluminescence is measured, and found to be connected to a

morphology-induced localization of the optical near-field. A three-photon resonance in a thin film of TiO_2 and a localized surface plasmon resonance in Au nanoantennas both lead to a finite lifetime of the induced material polarization. The THG-iFROG method is harnessed to measure the ultrafast temporal dynamics of these systems at the nanometer and few-femtosecond scales.

Zusammenfassung

Die Methode *interferometric frequency-resolved optical gating* (iFROG) zur Charakterisierung ultrakurzer Laserimpulse, eingeführt in den 2000er Jahren, wurde erweitert. Sowohl die Erzeugung der zweiten als auch der dritten Harmonischen (SHG und THG) werden separat als die optische Nichtlinearität verwendet. Eine iFROG-Messung stellt ein inverses Problem dar, bei dem die Amplitude und Phase des elektrischen Feldes des zugrundeliegenden Laserimpulses nur durch einen iterativen Algorithmus rekonstruiert werden kann. In dieser Arbeit wird ein mathematischer Formalismus, der sowohl die SHG- als auch die THG-Variante von iFROG nutzen kann, entwickelt und mit einem evolutionären Optimierungsalgorithmus (*differential evolution*) kombiniert, um einen neuartigen Impuls-Rekonstruktions-Algorithmus für iFROG zu erschaffen.

Während iFROG ursprünglich ausschließlich zur Charakterisierung von Laserimpulsen konzipiert wurde, kann die Technik gleichermaßen für spektroskopische Zwecke eingesetzt werden. Wird das nichtlineare Medium in iFROG durch ein Untersuchungsobjekt — etwa eine Nanostruktur — ersetzt und ein bekannter Laserimpuls erneut charakterisiert, so kann der Einfluss der Probe auf den Prozess der Erzeugung der Harmonischen dazu genutzt werden, die komplexe Antwortfunktion des Untersuchungsobjekts mit einer sub-Femtosekunden-Auflösung zu entschlüsseln. Da für die THG-Variante bisher keine Lösung bekannt ist, ermöglicht der vorgestellte Retrieval-Algorithmus die erstmalige Nutzung von iFROG zur Untersuchung ultraschneller nichtlinearer Effekte dritter Ordnung.

Während des Prozesses der Weiterentwicklung von iFROG werden verschiedene Algorithmen zur Impuls-Rekonstruktion diskutiert. Eine davon stammt aus der Ptychographie, einer linsenlosen Bildgebungstechnik. In Kombination mit einem modifizierten iFROG-Gerät, in dem nicht-identische Impuls-Replikate genutzt werden, kann der ptychographische Retrieval-Algorithmus dazu verwendet werden eindeutig zwischen vorangehend und nachfolgenden Satellitenimpulsen zu unterscheiden. Die Performance dieser neuen Impuls-Charakterisierungs-Modalität mit dem Namen πFROG wird über einen Vergleich mit einem kommerziellen Messgerät experimentell bestätigt und darüber hinaus mit Hilfe einer artifiziell hinzugefügten und korrekt rekonstruierten spektraler Phasen verifiziert. In ähnlicher Weise wird die vorgestellte iFROG-Methode sowohl numerisch als auch in realen Experimenten evaluiert und gegen konkurrierende Algorithmen,

welche auf der SHG basieren und im Gegensatz zur THG einer Konkurrenz unterliegen, eingesetzt.

Die spektroskopische Fähigkeit iFROG wird durch das Studium von drei unterschiedlichen physikalischen Systemen geprüft, die jeweils aus Nanostrukturen bestehen, die auf dielektrischen Substraten aufgetragen sind. Werden diese Proben mit few-cycle Lichtimpulses im nahen Infrarotbereich angeregt, ist eine große Vielzahl von nichtlinearer optischer Phänomene zu beobachten. In ZnO-Nanostäben wird die Leistungsabhängigkeit der durch Multiphotonenabsorption induzierten Photolumineszenz gemessen, wobei nachgewiesen werden konnte, dass diese mit einer Morphologie induzierten Lokalisierung des optischen Nahfelds verknüpft ist. Eine Dreiphotonenresonanz in einem dünnen TiO_2-Film und eine lokalisierte Oberflächenplasmonenresonanz in Au-Nanoantennen führen beide zu einer endlichen Lebensdauer der induzierten Materialpolarisation. Die THG-iFROG-Methode wird verwendet, um die ultraschnelle zeitliche Dynamik dieser Systeme auf der Nanometer- und wenige Femtosekunden-Skala zu messen.

Preface

The research I have described in this dissertation was mainly conducted in the Max Born Institute of Berlin, funded partly by Tekniikan edistämissäätiö, and aided by many a people to whom I am indebted.

First and foremost I wish to thank my supervisor Prof. Günter Steinmeyer for giving me an opportunity to become a doctor. Along the way, he was always helpful and supportive, patiently responding to my sometimes incessant stream of questions and showing trust in my abilities.

All the coauthors and colleagues at collaborating universities and institutes are thanked for their efforts. I especially wish to mention those with whom I had the pleasure to work extensively with in person: Prof. Daniele Brida and Dr. Vanessa Knittel of University of Konstanz, and Prof. Enda McGlynn of Dublin City University. In particular, I am grateful for the endless faith and patience Prof. McGlynn showed in our ultimately successful, long running collaboration even when it seemed destined to fail, and for going out of his way to help me better understand the physics in a territory previously unfamiliar to me.

Colleagues and coworkers at the Max Born Institute should of course not be forgotten. I had many long, often entertaining and mostly fruitful discussions with Dr. Rüdiger Grunwald and Dr. Jens Tomm among others. Fellow students were great company, help and support, both in and out of office. Lorenz, Nils, Simon, Felix, Esmerando, Marko, Marcel, Tony, Christoph, Jannick... the list goes on.

Friends and family back home in Finland and around the globe, you know who you are and you're awesome. Kiitos ja kumarrus!

Contents

List of Publications

Listed below are all the publications related to this dissertation, in descending chronological order.

Peer-Reviewed Journal Articles

Authors marked with a dagger (†) contributed equally to the corresponding publication.

[I] J. Hyyti, M. Perestjuk, R. Grunwald, F. Güell, C. Gray, E. McGlynn, G. Steinmeyer. *Field Enhancement of Multiphoton Induced Luminescence Processes in ZnO Nanorods*. J. Phys. D, **51**, 105306 (2018).

[II] J. Hyyti, E. Escoto, and G. Steinmeyer, *Third-harmonic interferometric frequency-resolved optical gating*. J. Opt. Soc. Am. B, 34(11), 2367–2375 (2017).

[III] J. Hyyti, E. Escoto, and G. Steinmeyer *Pulse retrieval algorithm for interferometric frequency-resolved optical gating based on differential evolution*. Rev. Sci. Instrum. 88, 103102 (2017).

[IV] J. Hyyti, E. Escoto, G. Steinmeyer, and T. Witting, *Interferometric time-domain ptychography for ultrafast pulse characterization*. Opt. Lett. 42, 2185–2188 (2017).

[V] M. Hofmann†, J. Hyyti†, S. Birkholz, M. Bock, S. K. Das, R. Grundwald, M. Hoffmann, T. Nagy, A. Demircan, M. Jupé, D. Ristau, U. Morgner, C. Breé, M. Woerner, T. Elsässer, and G. Steinmeyer. *Noninstantaneous polarization dynamics in dielectric media.* Optica **2**, 151–157 (2015).

[VI] L. Orsila, A. Härkonen, J. Hyyti, M. Guina, and G. Steinmeyer. *Ultrahigh precision nonlinear reflectivity measurement system for saturable absorber mirrors with self-referenced fluence characterization.* Opt. Lett. **39** 4384–4387 (2014).

Conference Contributions

Presentations given by the thesis author are indicated with an asterisk (⋆).

1. J. Hyyti, M. Perestjuk, R. Grunwald, F. Güell, C. Gray, E. McGlynn, G. Steinmeyer. *Field Enhancement of Multiphoton Induced Luminescence Processes in ZnO Nanorods*. at *Laserlab Europe User Meeting*, Vilnus, Lithuania (2017).

2. E. Escoto, A. Tajalli, J. Hyyti, T. Nagy, and G. Steinmeyer, *Improved phase retrieval for dispersion scan*. in CD-15.5. at *CLEO/Europe-EQEC 2017*, Munich, Germany (2017).

3. J. Hyyti*, E. Escoto, G. Steinmeyer, and T. Witting, *Interferometric time-domain ptychography for ultrafast pulse characterization*. in CF-11.4. at *CLEO/Europe-EQEC 2017*, Munich, Germany (2017).

4. J. Hyyti*, R. Grunwald, M. Perestjuk, F. Güell, C. Gray, E. McGlynn, G. Steinmeyer. *Short Wavelength Tail Effects in Multiphoton Induced Luminescence from ZnO Using sub-10 fs Ti:Sa Pulses*. in Conference on Lasers and Electro-Optics, OSA Technical Digest, paper STu4I.5 (2016). at *CLEO: Science and Innovations 2016*, San Jose, USA (2016).

5. J. Hyyti, N. Raabe, and G. Steinmeyer. *Characterization of Ultrashort Laser Pulses and Carrier-Envelope Phase Stabilization.* Proceedings of the International School of Physics "Enrico Fermi," Course 190 "Frontiers in Modern Optics," edited by D. Faccio, J. Dudley, and M. Clerici, pp. 207–231 (2016).

6. J. Hyyti* and G. Steinmeyer, *Noninstantaneous polarization dynamics in dielectric media*. at *International Summer School "New Frontiers in Optical Technologies"*, Tampere, Finland (2015).

7. J. Hyyti, M. Hofmann, S. Birkholz, M. Bock, S. K. Das, R. Grundwald, M. Hoffmann, T. Nagy, A. Demircan, M. Jupé, D. Ristau, U. Morgner, C. Breé, M. Woerner, T. Elsässer, and G. Steinmeyer, *Non-instantaneous Polarization Decay in Resonant Dielectrics*. at *PIERS 2015*, Prague, Czech Republic (2015).

8. L. Orsila, J. Hyyti, G. Steinmeyer, and M. Guina, *Self-referenced fluence characterization method for nonlinear reflectivity measurements of semiconductor components*. at *Northern Optics and Photonics*, Lappeenranta, Finland (2015).

9. J. Hyyti*, M. Hofmann, S. Birkholz, M. Bock, S. K. Das, R. Grundwald, M. Hoffmann, T. Nagy, A. Demircan, M. Jupé, D. Ristau, U. Morgner, C. Breé, M. Woerner, T. Elsässer, and G. Steinmeyer, *Non-instantaneous polarization dynamics in resonant dielectrics*. in 2015 European Conference on Lasers and Electro-Optics - European Quantum Electronics Conference, paper EE_5b_2 (2015). at *CLEO/Europe-EQEC 2015*, Munich, Germany (2015).

10. M. Hofmann, C. Breé, M. Hoffmann, A. Demircan, T. Nagy, D. Ristau, U. Morgner, S. Birkholz, S. K. Das, M. Bock, R. Grundwald, J. Hyyti, T. Elsässer, and G. Steinmeyer, *Non-instantaneous polarization decay in dielectric media*. in CLEO: 2014, OSA Technical Digest (online), paper STh3E.5 (2014). at *CLEO: Science and Innovations 2014*, San Jose, USA (2014).

11. M. Hofmann, C. Breé, M. Hoffmann, A. Demircan, T. Nagy, D. Ristau, U. Morgner, S. Birkholz, S. K. Das, M. Bock, R. Grundwald, J. Hyyti, T. Elsässer, and G. Steinmeyer, *Non-instantaneous polarization decay in dielectric media*. in 19th International Conference on Ultrafast Phenomena, OSA Technical Digest (online), paper 10.Thu.C.5 (2014). at *International Conference on Ultrafast Phenomena*, Okinawa, Japan (2014).

12. J. Hyyti* and G. Steinmeyer, *Non-instantaneous polarization dynamics in dielectric media*. at *International School of Physics "Enrico Fermi"*, Varenna, Italy (2014).

13. L. Orsila, J. Hyyti, A. Härkonen, G. Steinmeyer, and M. Guina, *High-accuracy method for sample positioning in tightly focused nonlinear reflectivity measurement systems for semiconductor saturable absorber mirrors*. in Optics and Photonics Days 2014, OPD2014 Proceedings, 20-22 May, 2014, Turku, Finland, page 51 (2014). at *Optics and Photonics Days 2014*, Turku, Finland (2014).

14. L. Orsila, J. Hyyti, A. Härkonen, M. Guina, and G. Steinmeyer, *Ultrahigh precision nonlinear reflectivity measurement system for semiconductor mirrors with in situ fluence characterization*. in Physics Days 2014, Tampere, The 48th annual meeting of the Finnish Physical Society, P:I.74 (2014). at *Physics Days 2014*, Tampere, Finland (2014).

15. S. K. Das, M. Bock, R. Grundwald, B. Borchers, J. Hyyti, G. Steinmeyer, D. Ristau, A. Harth, T. Vockerodt, T. Nagy, and U. Morgner, *First measurement of the non-instantaneous response time of a $\chi^{(3)}$ nonlinear optical effect*. in EPJ Web of Conferences **41**, 12005 (2013). at *XVIIIth International Conference on Ultrafast Phenomena*, Lausanne, Switzerland (2012).

16. S. K. Das, M. Bock, R. Grundwald, B. Borchers, J. Hyyti, G. Steinmeyer, D. Ristau, T. Vockerodt, and U. Morgner, *Non-instantaneity of $\chi^{(3)}$ nonlinear optical effects*. in Conference on Lasers and Electro-Optics 2012, OSA Technical Digest (online), paper CM1J.4 (2012). at *CLEO: Science and Innovations 2012*, San Jose, USA (2012).

17. J. Hyyti*, L. Orsila, and G. Steinmeyer, *Analysis of non-instantaneous lifetime of Kerr-effect in interferometric FROG measurements*. in Physics Days 2012, Joensuu, The 46th annual meeting of the Finnish Physical Society, Proceedings, P1.36 (2012). at *Physics Days 2012*, Joensuu, Finland (2012).

Awards

1. *Best presentation* at *International School of Physics "Enrico Fermi"*, Varenna, Italy (2014).

CHAPTER 1

Introduction

Modern light sources allow the routine generation of near-infrared (NIR) laser pulses whose electric field amplitude rises and falls within the course of only a few optical cycles, corresponding to pulse widths of but a few femtoseconds (10^{-15} s) [1]. Confining even a moderate amount of energy into such a short window of time allows extremely high peak powers to be reached. Focusing these bursts of energy close to the diffraction limit, the electric field intensity can exceed the Coulombic binding forces in atoms, tearing electrons from their nuclei. Once ionized, an electron can be accelerated by the light up to relativistic speeds [2], made to recollide with the ion and create even shorter extreme-ultraviolet (XUV) pulses down to tens of attoseconds (10^{-18} s) in duration [3, 4], or, should the free electron scatter from bound electrons in a dielectric, start a chain of new ionization events leading to a catastrophic breakdown of the material [5]. Operating slightly below the threshold for material damage, a range of phenomena whose efficiency depends nonlinearly on the incident field intensity can occur for successive laser pulses over extended periods of time. Nonlinear optical effects such as the generation of light at harmonic frequencies, multiphoton absorption (MPA), or the transient modification of the refractive index are widely exploited in both scientific and commercial applications.

At these ultrafast timescales, the temporal dynamics of the employed optical medium must be taken into consideration. The time it takes for an electron to respond to an incident electric field can be extremely fast, from femtoseconds down to tens of attoseconds, close to the atomic unit of time (24 as) [3, 6]. Outside of the realm of attosecond physics, the material response time is often much shorter than the optical cycle of visible light and can therefore be considered instantaneous for most practical purposes. Considerably slower electronic response is expected, however, if the optical medium is resonantly excited [7, 8]. As the induced material polarization no longer follows the incident electric field of the laser pulse instantaneously, temporal resolution is diminished. This can

be detrimental for both the generation and the characterization [9] of ultrashort pulses, where nonlinear optical effects are commonly perused and frequently assumed instantaneous [10]. On the other hand, resonant excitation can have the often desired effect of enhancing the nonlinear interaction [7]. Striking a balance between the various consequences of resonant excitation requires a precise knowledge of the associated temporal dynamics, necessitating an experimental verification of systemic behavior as predicted by models.

During the course of this work, three differing physical systems with nanometer scale structures are studied at unprecedented timescales. Subjecting the highly nonlinear media to few-cycle NIR pulses, their ultrafast optical response is analyzed via the state-of-the-art pulse characterization technique interferometric FROG (iFROG) [11, 12]. Owing to its collinear beam geometry, iFROG allows tighter focusing than its noncollinear rivals — most notably the many variants of frequency-resolved optical gating (FROG) [13] and spectral-shearing methods such as spectral-interferometry for direct electric-field reconstruction (SPIDER) [14] — allowing high field intensities to be reached with unamplified pulses, in turn leading to a high sensitivity at a sub-femtosecond time resolution.

The first and in many ways the simplest system is an Au nanoantenna [15, 16], where the incident NIR pulses are coupled into localized surface plasmon polaritons (SPPs) — oscillations of the electron cloud engulfing the nanostructure. This resonant light-plasmon interaction is purely linear, and can be described analytically with a simple harmonic oscillator model yielding a Lorentzian line shape. The SPPs can, however, confine the electric field into tiny volumes of space beyond the diffraction limit, leading to a high nonlinearity. The second system to be studied is a thin film of titanium dioxide [17], a dielectric that is in three-photon resonance with the employed NIR pulses. Contrary to the plasmonic resonance, this resonant third-harmonic generation (THG) can only be described with a full quantum-mechanical model. The third and final system is a thin film of ZnO nanorods, where MPA leads to photoluminescence (PL) in the blue to UV wavelengths, close to the second harmonic of the NIR pulses. Previous studies on the SHG in similar structures suggest that the electric near-field in the nanorod arrays can become localized, leading to a manyfold intensity enhancement of the local field in comparison to the incident field [18, 19].

The simplest way to quantify the noninstantaneous, resonant response of a nonlinear optical medium is via intensity autocorrelation methods. Many examples of femtosecond-scale measurements of the plasmonic dephasing time via the collinear interferometric autocorrelation (iAC) can be found in the literature [20–26]. In essence, autocorrelation methods are crude pulse characterization techniques which are in many ways outdated. They have been largely replaced by techniques such as the above mentioned FROG, iFROG and SPIDER that are much more accurate and far less ambiguous, capable of measuring both the electric field amplitude and phase. As iFROG is essentially a spectrally-resolved iAC measurement, it appears straightforward to improve the quality of the previous plasmonic measurements by replacing iAC with iFROG. Indeed, this has been demonstrated with SHG-based iFROG, allowing the full complex-valued spectral response of Au nanotips surrounded by air to be reconstructed [27, 28]. For sub-

wavelength scale nanoantennas resting on a substrate with a nonlinear response of its own, a far greater and consistent sensitivity is achieved by employing THG instead [16, 23, 29], as evinced by previous studies [21–25]. Unfortunately, the iFROG retrieval algorithms are far less developed than their classical FROG counterparts. In fact, prior to this work, no solution for the THG-iFROG inverse problem existed, limiting the precision of THG-based measurements of noninstantaneous effects.

For the plasmonic nanoantennas with a few-femtosecond dephasing time — let alone for the resonant THG in a dielectric — competing characterization techniques offer no immediate solution to the measurement problem. High field intensities close to the damage threshold of the medium must be reached in order for efficient harmonic generation to take place. In order to reach the same incident field intensities accessible by iFROG with unamplified pulses, noncollinear methods such as FROG or SPIDER must rely on pulse amplification. In addition to making a given measurement system more complicated, amplifiers typically reduce the repetition rate of a titanium-sapphire oscillator from $\approx 100\,\mathrm{MHz}$ to $\approx 1\,\mathrm{kHz}$, corresponding to a reduction in the achievable signal-to-noise ratio (SNR) by orders of magnitude. Considering that THG is in general a relatively weak process, the inevitable drop in SNR renders noncollinear approaches an arduous endeavor. This is especially true for single nanostructures such as our nanoantennas which have a very limited luminosity. Moreover, currently no SPIDER-like methods based on $\chi^{(3)}$ nonlinearities exist, making spectral shearing techniques useless for our applications. Even if $\chi^{(2)}$ effects were an option, and all SNR constraints were overcome, it is unclear how — and even if — spectral-shearing methods could be applied to measure noninstantaneous effects. Noncollinear multi-shot FROG variants suffer from the geometrical time-smearing effect, overestimating the measured pulse duration by a few percent [30]. For a typical example with NIR pulses this amounts to $\approx 0.4\,\mathrm{fs}$ [31], which constitutes a significant error margin for the measurement of few-femtosecond effects. Temporal dynamics of propagating SPPs have been studied with various techniques from ultrafast near-field imaging [32] to linear spectral interferometry [33], but these approaches either do not offer an improvement in temporal resolution over iAC (the former), or are limited in size of the studied nanostructures (the latter). While techniques employing attosecond bursts of XUV radiation can offer a superior time resolution for experiments performed with gaseous media or even jets of nanoparticles [34], solid samples, such as our dielectric thin films and nanostructures resting on a substrate, remain a largely unconquered territory [35] save for a few recent examples not directly applicable here [36, 37]. Attosecond streaking experiments could in principle be used to temporally characterize the localized fields at plasmonic nanostructures, but in practice the comparatively large area probed via XUV-induced photoemission can distort the streaking field, and lead to prohibitively low signal-to-noise ratios [35]. For the resonant THG experiments, attosecond streaking offers no clear solution.

All things considered, it is clear that the lack of a retrieval algorithm for THG-iFROG presents a barrier for progress in the study of ultrafast, nearly instantaneous optical effects. The primary objective of this dissertation is therefore to find such a solution. For this purpose, several algorithms are studied. A viable solution for THG-iFROG should be

applicable to SHG-iFROG as well. As the latter can also be inverted with standard FROG algorithms by exploiting a FROG trace contained within the iFROG trace, we may test the performance of any new solution we come up with against the old. Aside from employing the embedded SHG-FROG trace, another previous solution for the SHG-iFROG problem does exist. Making use of the higher-order modulation bands found in the interferometric trace, Stibenz *et al.* performed an iterative pulse retrieval via line minimization [12, 38]. It should be possible to modify this approach to suit THG-iFROG as well. As the minimization routine can in principle be realized with any given general optimization algorithm, we also aim to find a more robust, consistent, and faster alternative for the line minimization. Among the tested candidates, the evolutionary algorithm called differential evolution (DE) [39, 40] seems most promising, offering a predictable speed of convergence towards the global minimum, that is, the pulse to be retrieved. As a second objective — once a reliable solution for THG-iFROG has been established — we wish to employ the technique to measure the few-femtosecond dynamics of the resonant THG in a dielectric and plasmonic resonance in nanoantennas.

In the past few years, several existing ultrashort pulse characterization methods have been adapted [41–43] for a novel algorithm [44] based on ptychography [45, 46], in turn a lensless imaging technique [47]. Entirely new methods have also been introduced [48]. The third objective of this work is to explore the possibility to adopt a ptychographic algorithm for iFROG, or a similar method.

Another interesting property of an iFROG measurement is that the inherent temporal resolution allows one to identify coherent and incoherent spectra, for example the concomitant SHG and PL emission in the ZnO nanorods [49]. Capturing these two processes simultaneously in a single iFROG trace, their power dependence can be quantified individually by analyzing the variations in measured spectral intensities. Combining these capabilities of iFROG, as a fourth objective for this dissertation, we wish to study the PL process whose underlying mechanism has been attributed to various processes such as two- [50–55] three- [56, 57] and even four-photon [58] absorption (#PA) of NIR photons. In particular, we wish to operate as close as possible yet still below the 2PA threshold of ZnO. This way we can evaluate whether proposed mechanisms such as bandgap renormalization [52] can make 2PA efficient, leading to a quadratic power dependence. Simulations based on Keldysh-theory of photoionization [5, 59] should prove useful in determining the role of different multiphoton processes as well as localized electric fields in the experimental findings.

Prior to applying iFROG for the three physical systems described above — the plasmonic nanoantennas, the three-photon resonant dielectric thin film, and the field-enhancing nanorods — we start from the basics, gradually proceeding towards the pulse characterization techniques paramount for our ultimate goal: pushing the frontiers of fundamental research on nonlinear optical phenomena at the femtosecond and nanometer scales.

CHAPTER II

Ultrafast Light-Matter Interaction

In this chapter we discuss the theoretical foundations [7, 8, 16, 60–65] for the experiments we design, simulate and finally perform with few-cycle near-infrared laser pulses and a selection of optical media differing both in their linear and nonlinear properties. After this initial treatment, the relevant concepts for each individual experiment will be refined as needed in the chapters that follow.

II.1. Laser Pulses

Experimenting with ultrashort laser pulses, the temporal evolution of the electric field is naturally of utmost interest. Neglecting any spatial dependence for now, we loosely follow Refs. [7, 60] and define the time-dependent electric field $\bar{\mathcal{E}}(t)$ of such a pulse as

$$\bar{\mathcal{E}}(t) = \frac{1}{2}\sqrt{I(t)}e^{i[\omega_0 t - \phi'(t) + \phi_0]} + \text{c.c.}\,. \tag{II.1}$$

Here c.c. denotes the complex conjugate of the first term on the rhs, the inclusion of which assures that $\bar{\mathcal{E}}$ is real, as is expected for the physical quantity. The slowly-varying envelope function $\sqrt{I(t)}$, where $I(t)$ is the intensity, describes the evolution of the field amplitude. We define the pulse duration τ_p as the FWHM of the intensity envelope $I(t)$. The rapidly oscillating carrier wave $e^{i\omega_0 t}$ is separated for convenience. Deviations from the linear phase evolution of the carrier are accounted for by the phase $\phi'(t)$. The absolute phase ϕ_0 essentially describes the phase difference between the carrier wave and the maximum of the intensity envelope. For pulses close to a single optical cycle in duration, the absolute phase can significantly affect the peak electric field amplitude. In our experiments, the effect ϕ_0 has is not measurable, so we mostly ignore it in our treatment. We do this by assimilating the absolute phase into the time-dependent phase,

$\phi(t) = \phi'(t) + \phi_0$.

The electric field can equally well be described in the frequency domain by taking the Fourier transform of the time-domain field,

$$\bar{\mathcal{E}}(\omega) = \frac{1}{\sqrt{2\pi}} \int_{-\infty}^{+\infty} \bar{\mathcal{E}}(t) e^{-i\omega t} \, \mathrm{d}t \,. \tag{II.2}$$

As $\bar{\mathcal{E}}(t)$ is real, its Fourier transform will be complex. The negative frequencies hold exactly the same information as the positive frequencies, adhering to the simple connection $\bar{\mathcal{E}}(\omega) = \bar{\mathcal{E}}^*(-\omega)$. Neglecting the negative frequencies, we define the carrier frequency ω_0 as the center of gravity of the spectral intensity $\left|\bar{\mathcal{E}}(\omega)\right|^2$ for $\omega > 0$,

$$\omega_0 = \frac{\int_0^{+\infty} \omega \left|\bar{\mathcal{E}}(\omega)\right|^2 \mathrm{d}\omega}{\int_0^{+\infty} \left|\bar{\mathcal{E}}(\omega)\right|^2 \mathrm{d}\omega} \,. \tag{II.3}$$

An inverse Fourier transform of $\bar{\mathcal{E}}(\omega)$ yields once again the temporal description

$$\bar{\mathcal{E}}(t) = \frac{1}{\sqrt{2\pi}} \int_{-\infty}^{+\infty} \bar{\mathcal{E}}(\omega) e^{i\omega t} \, \mathrm{d}t \,. \tag{II.4}$$

In the mathematical analysis of light-matter interaction, one finds that it is often more convenient to deal with a complex electric field instead a real-valued one. The complex field $\mathcal{E}(t)$ is obtained from Eq. (II.1) by discarding the complex conjugate and the prefactor $\frac{1}{2}$,

$$\mathcal{E}(t) = \sqrt{I(t)} e^{i[\omega_0 t - \phi(t)]} = E(t) e^{i\omega_0 t} \,. \tag{II.5}$$

Here, the complex amplitude $E(t)$ is defined via

$$E(t) \equiv \sqrt{I(t)} e^{-i\phi(t)} \,. \tag{II.6}$$

Note that now the intensity envelope is simply $I(t) = |E(t)|^2$, while the slowly-varying phase is given by the argument $\phi(t) = -\mathrm{Arg}\{E(t)\}$. Similar definitions can also be given for the spectral domain. Taking the Fourier transform of Eq. (II.5), we gain the single-sided spectrum $E(\omega)$,

$$E(\omega) = \frac{1}{\sqrt{2\pi}} \int_{-\infty}^{+\infty} \mathcal{E}(t) e^{-i\omega t} \, \mathrm{d}t \,, \tag{II.7}$$

for which we give a definition analogous to the time domain field in Eq. (II.6),

$$E(\omega) \equiv \sqrt{I(\omega)} e^{-i\varphi(\omega)} \,. \tag{II.8}$$

As above, the spectral intensity is given by $I(\omega) = |E(\omega)|^2$, and the spectral phase $\varphi(\omega) = -\mathrm{Arg}\{E(\omega)\}$. Note that $I(\omega) = 2\left|\bar{\mathcal{E}}(\omega)\right|^2$ for $\omega > 0$.

II.1.1. Relation of $E(t)$ to Measurable Quantities

The definitions introduced above will be used extensively during the course of this work, especially in the context of pulse retrieval where the quantity of interest is $E(t)$. In most cases however, the intensity envelope $I(t) = |E(t)|^2$ reconstructed by the pulse retrieval algorithm does not actually represent the physical magnitude of the corresponding field (i.e., the optical power $\mathcal{P}$) but rather its temporal evolution $I(t) = \frac{\mathcal{P}(t)}{\mathcal{P}_{\max}}$, where $\mathcal{P}_{\max}$ is the peak power. For many practical purposes, the physical field strength is nevertheless of great interest. If such information is needed, the optical power can be deduced by distributing the energy of a single pulse to the retrieved intensity envelope $I(t)$. We do this by first normalizing the retrieved intensity distribution to unit area, and then multiplying the result with the pulse energy E_p,

$$\mathcal{P}(t) = \frac{I(t)}{\int_{-\infty}^{+\infty} I(t)\,\mathrm{d}t} E_p\,. \tag{II.9}$$

The pulse energy E_p is the quotient of the average power $\mathcal{P}_{\mathrm{ave}}$, easily measured by placing a power meter on the beam path, and the repetition rate of the laser f_{rep},

$$E_p = \frac{\mathcal{P}_{\mathrm{ave}}}{f_{\mathrm{rep}}}\,. \tag{II.10}$$

For many experiments, the irradiance $\mathcal{I}$ is a more relevant quantity than optical power. Provided that the effective beam area A_{eff} is known, the irradiance can be easily obtained from the optical power:

$$\mathcal{I}(t) = \frac{\mathcal{P}(t)}{A_{\mathrm{eff}}}\,. \tag{II.11}$$

In the remainder of this chapter, we use E to describe electric fields in general with no reference to the terminology above. Next, we shall explore what consequences the inclusion of a spatial coordinate to the pulse description brings.

II.2. Propagation of Light in Optical Media

The propagation of light in general is governed by Maxwell's equations [66]. Following Ref. [7], we find that for a nonmagnetic, homogeneous isotropic medium where no free charges or electric currents are present, one obtains the wave equation

$$\left[\nabla^2 - \frac{1}{c^2}\frac{\partial^2}{\partial t^2}\right]\mathbf{E}(t,\mathbf{r}) = \mu_0 \frac{\partial^2 \mathbf{P}(t,\mathbf{r})}{\partial t^2}\,, \tag{II.12}$$

where c is the speed of light in vacuum, and ϵ_0, μ_0 are the vacuum permittivity and permeability, respectively. As we are mostly dealing with collinearly propagating, linearly-polarized electric fields, it suffices to reduce the above vectorial equation into a scalar form with a single spatial dimension along the direction of propagation $+z$,

$$\left[\frac{\partial^2}{\partial z^2} - \frac{1}{c^2}\frac{\partial^2}{\partial t^2}\right] E(t,z) = \mu_0 \frac{\partial^2}{\partial t^2}\left[P^{(1)}(t,z) + P^{\mathrm{NL}}(t,z)\right]. \tag{II.13}$$

Here the polarization has been separated into linear $P^{(1)}$ and nonlinear P^{NL} parts. What Eq. (II.13) essentially shows is that the electric field can induce both a linear and a nonlinear polarization in the optical medium. *Vice versa*, material polarization can act as a source for new electric field components.

Let us focus our attention on the linear polarization for now. The interaction between $P^{(1)}$ and E is mediated by the linear susceptibility $\chi^{(1)}$, defined in the frequency domain via

$$P^{(1)}(\omega, z) = \epsilon_0 \chi^{(1)}(\omega) E(\omega, z). \tag{II.14}$$

As a product in one domain corresponds to a convolution in the corresponding Fourier domain, the time-domain equivalent of Eq. (II.14) reads

$$P^{(1)}(t,z) = \epsilon_0 \int_{-\infty}^{t} \chi^{(1)}(t') E(t-t', z)\, \mathrm{d}t'. \tag{II.15}$$

Here the integration is carried over the interval $[-\infty, t]$ instead of $[-\infty, +\infty]$ to ensure causality. Eq. (II.15) clearly shows that the polarization at time t is affected by the light-matter interaction at previous times, that is, the system has a memory. Together Eqs. (II.14) and (II.15) show that an optical medium with dispersion (frequency-dependent $\chi^{(1)}$) will have a noninstantaneous response to an incident electric field. If the susceptibility is constant instead, the response will be instantaneous. In practice, dispersion cannot be avoided for broadband pulses so that the medium response is never truly instantaneous. For an approximately flat frequency dependence, however, the response can be extremely fast and thus effectively instantaneous for most practical purposes. Similar results can be derived for higher order polarization terms as well [7, 61, 62].

Returning our attention to the reduced wave equation above, we take the Fourier transform of Eq. (II.13) and ignore the nonlinear polarization by setting $P^{\mathrm{NL}} = 0$. This yields a wave equation in frequency domain,

$$\left\{\frac{\partial^2}{\partial z^2} + \frac{\omega^2}{c^2}\left[1 + \chi^{(1)}(\omega)\right]\right\} E(\omega, z) = 0, \tag{II.16}$$

whose general solution is

$$E(\omega, z) = E(\omega, 0) e^{-ikz}. \tag{II.17}$$

The definition for the wave number k is found by substituting Eq. (II.17) into Eq. (II.16).

This gives

$$k(\omega) = \frac{\omega}{c}\sqrt{1+\chi^{(1)}(\omega)} = \frac{\omega}{c}n(\omega), \tag{II.18}$$

where $n(\omega) = \sqrt{1+\chi^{(1)}(\omega)}$ is the refractive index. Solving Eq. (II.18) for c/n, we obtain the phase velocity v_{phase} describing the speed of propagation of a monochromatic wave in a dispersive medium,

$$v_{\text{phase}} = \frac{\omega}{k} = \frac{c}{n(\omega)}. \tag{II.19}$$

In addition to the forms discussed in the previous section, a laser pulse can also be described as a sum of monochromatic waves. Such a wave packet propagates at the group velocity,

$$v_{\text{group}} = \left(\left.\frac{\mathrm{d}k}{\mathrm{d}\omega}\right|_{\omega_0}\right)^{-1}. \tag{II.20}$$

As the pulse travels, a phase $\varphi(\omega) = -k(\omega)z$ is acquired according to Eq. (II.17). Taking the Taylor expansion of the spectral phase at the carrier frequency ω_0, one obtains

$$\varphi(\omega) = \varphi_0 + \underbrace{\left.\frac{\mathrm{d}\varphi}{\mathrm{d}\omega}\right|_{\omega_0}}_{\text{GD}}(\omega-\omega_0) + \frac{1}{2!}\underbrace{\left.\frac{\mathrm{d}^2\varphi}{\mathrm{d}\omega^2}\right|_{\omega_0}}_{\text{GDD}}(\omega-\omega_0)^2 + \frac{1}{3!}\underbrace{\left.\frac{\mathrm{d}^2\varphi}{\mathrm{d}\omega^2}\right|_{\omega_0}}_{\text{TOD}}(\omega-\omega_0)^3 + \dots . \tag{II.21}$$

Each of the terms in the above expansion have their own physical significance, the relevant quantity indicated by the abbreviations below. The absolute spectral phase φ_0 is exactly equal to its time-domain counterpart ϕ_0. The linear phase is known as the group delay (GD), also given by $\tau_{\text{group}} = \frac{z}{v_{\text{group}}}$. This is the time it takes for a pulse to travel the distance z, or equally well the time of arrival onto a detector. As our experiments are not sensitive to these two lowest-order phase terms, we can treat them as being equal to zero for all practical purposes. The higher-order terms cannot be ignored, however. The second-order phase or the group-delay dispersion (GDD) can lead to the broadening or compression of ultrashort pulses. A closely related quantity is the group-velocity dispersion (GVD), which is simply GDD per unit length. In our experiments, we employ dispersion compensation in order to minimize GDD. The reason for this is that the shortest pulse duration supported by a given spectrum is achieved when GDD and all the higher-order terms in Eq. (II.21) are exactly zero. Such a pulse is said to be Fourier-transform limited (FTL), referring to the fact that for a flat spectral phase, the time-domain electric field is obtained simply via the Fourier transform of the spectral intensity. The transform-limited pulse also has a constant temporal phase $\phi(t)$. Compensation of the cubic phase, also known as third-order dispersion (TOD), and of higher-order phase can be difficult, and in practice the spectral phase is never entirely flat.

For a given optical element of length L, say a fused silica window, the phase introduced to a traversing pulse can be estimated with the help of a Sellmeier equation. Typically of

the form

$$n^2(\lambda) = 1 + \frac{B_1\lambda^2}{\lambda^2 - C_1} + \frac{B_2\lambda^2}{\lambda^2 - C_2} + \frac{B_3\lambda^2}{\lambda^2 - C_3}, \tag{II.22}$$

where the coefficients B_i, C_i depend on the material, the Sellmeier equation estimates the dispersion of the refractive index. The knowledge of the added phase,

$$\phi(\omega) = -k(\omega)L = -\frac{\omega L}{c} n\left(\frac{2\pi c}{\omega}\right),$$

facilitates the design of dispersion compensation. On the other hand, adding a known amount of dispersion can be used as a test for a given pulse characterization method, i.e., by comparing the measured spectral phases before and after a dispersive element was introduced to the beam path. Later on, we will use this technique to test our novel characterization modalities.

II.3. Nonlinear Optics

In the previous section, the nonlinear polarization P^{NL} in Eq. (II.13) was ignored in order to obtain key results from linear optics. The reduced wave equation can equally well be solved analytically for the nonlinear polarization, provided that some concessions are made. Perhaps the most important of these is the slowly-varying envelope approximation (SVEA), which essentially allows some higher-order derivatives of the electric field and polarization with respect to t and z to be ignored. If the material is in addition assumed to be only weakly dispersive such that GVD and higher-order phase can be neglected, one arrives in the following simple result,

$$\frac{\partial E(t,z)}{\partial z} = -i\frac{\omega_0\mu_0 c}{2n} P^{\mathrm{NL}}(t,z). \tag{II.23}$$

Using Eq. (II.23) (or more elaborate equations if necessary), nonlinear effects such as harmonic generation can then be described. Here we merely present the relevant results.

II.3.1. Phase matching

Let us briefly consider second-harmonic generation (SHG) with a β-barium borate (BBO) crystal. Unless special care is taken, the phase velocities of the second-harmonic and fundamental fields will differ in the crystal, leading to the two fields being periodically in-phase and out-of-phase. Energy will oscillate between the two fields, never leading to efficient SHG. Constructive interference and a flow of energy from the fundamental to the harmonic field can therefore only occur if the phase mismatch Δk, given by

$$\Delta k = k(2\omega) - 2k(\omega) = 2\frac{\omega}{c}\left[n(2\omega) - n(\omega)\right], \tag{II.24}$$

is approximately zero. In the so-called type I phase-matching scheme (which we will employ) the incident fundamental field and the generated second-harmonic field travel along different optical axes of the birefringent BBO crystal. These are the ordinary and the extraordinary axes which have their own refractive indices n_o, n_e, respectively. By cutting the crystal at a specific angle, one can assure that $n_e(\omega_0) = n_o(2\omega_0)$ so that perfect phase matching ($\Delta k = 0$) is achieved at the carrier frequency.

As a further complication, even when the phase-matching condition is approximately fulfilled, the difference between the group velocities of the fundamental and second-harmonic fields limits the range of frequencies across which harmonic generation can occur efficiently. The *phase-matching bandwidth* can however be increased by reducing the length of the nonlinear interaction, namely by using a very thin crystal. In order to characterize few-cycle pulses with very broad spectra, BBO crystals with thicknesses in the order of 10 µm are routinely employed. Another option is to focus the incident beam very tightly so that the field intensity remains high only for a very short distance along the direction of propagation. Phase matching of focused beams leads to further complications, however, which will be addressed in the context of surface third-harmonic generation in later chapters.

II.3.2. Nonresonant Processes

In the perturbative limit where the field intensities involved are not exceedingly high, the various nonlinear effects of different orders can be described by forming a power series of the polarization P [8],

$$P = \epsilon_0 \left[\chi^{(1)} E + \chi^{(2)} E^2 + \chi^{(3)} E^3 + \dots \right]. \tag{II.25}$$

Due to the vectorial nature of the fields **E** and **P**, the susceptibilities $\chi^{(n)}$ are properly described as tensors of order $n+1$, not scalars as implied by Eqs. (II.14) and (II.25). For example, the second-order polarization at the frequency $\omega_3 = \omega_1 + \omega_2$ reads [62]

$$P_i(\omega_3) = \frac{1}{2} \sum_p \sum_{jk} \chi_{ijk}(\omega_3; \omega_1, \omega_2) E_j(\omega_1) E_k(\omega_2), \tag{II.26}$$

where the relevant component of the second-order susceptibility tensor $\chi_{ijk}(\omega_3; \omega_1, \omega_2)$ depends on the frequencies ω_1, ω_2 of the incident electric field components E_j, E_k along j, k, respectively. Each of the indices i, j, k represent any of the three Cartesian coordinates x, y, z. χ_{ijk} is a third-order tensor with 27 components. Only some of these components are independent, however, depending on the symmetry properties of the nonlinear medium. The sign and magnitude of the frequencies ω_1, ω_2 define which nonlinear process is being considered, and $\sum_p$ takes the permutations of the terms with ω_1, ω_2 into account. For example, setting $\omega_2 = \omega_1$, Eq. (II.26) describes SHG with $\omega_3 = 2\omega_1$, while $\omega_2 = -\omega_1$ gives $\omega_3 = 0$ and thus describes optical rectification, where a DC polarization is induced across the nonlinear medium.

If the nonlinear medium has an inversion symmetry, as is the case for amorphous

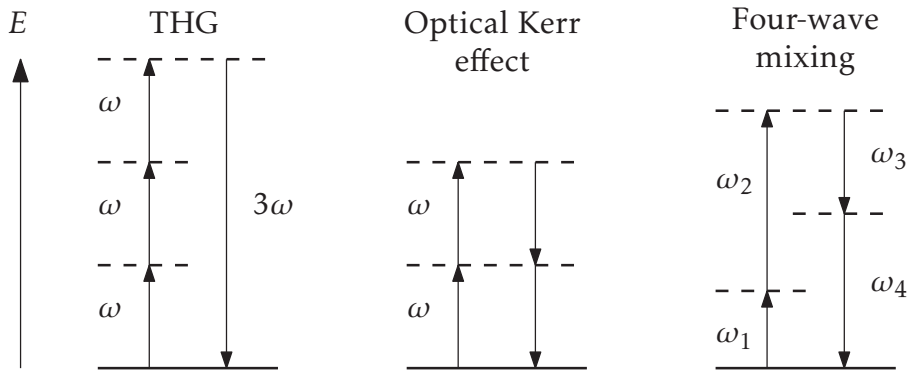

Figure II.1 – *Photon diagrams for selected nonresonant third-order nonlinear effects. The upward arrows correspond to the annihilation of a photon, while the downward arrows indicate that a photon is created. The length of an arrow corresponds to the energy $E = \hbar\omega$. Energy conservation is ensured by choosing the frequencies such that the vector sum of the arrows is zero for each interaction. Dashed lines represent virtual states, while solid lines correspond to real eletronic states. Adapted from Ref. [8].*

materials and gases, the second-order susceptibility tensor vanishes ($\chi_{ijk} = 0$) and no second-order polarization can occur. The same is true for all even-order polarizations, leaving only odd-order terms in Eq. (II.25). As the susceptibilities for increasing polarization orders get weaker and weaker, typically only the lowest-order nonlinearities must be considered. Thus, for amorphous media such as the fused silica windows we employ, only $\chi^{(3)}$ is relevant.

The third-order polarization can be described analogously to Eq. (II.26), with the third-order susceptibility tensor written as $\chi_{ijk}(\omega_4;\omega_1,\omega_2,\omega_3)$. Various third-order nonlinear effects obtained for different sets of frequencies ω_n are illustrated in Fig. II.1. For our purposes the most important ones are third-harmonic generation (THG), and the optical Kerr effect. The latter is also known as the intensity-dependent refractive index, described via [8]

$$n = n_0 + n_2 I\,, \tag{II.27}$$

where n_0 is the refractive index in the absence of a strong electric field, and n_2 is given by

$$n_2 = \frac{3}{4n_0^2\epsilon_0 c}\chi^{(3)}. \tag{II.28}$$

Here we have ignored the tensorial nature of the susceptibility, and continue to do so henceforth. By modifying the refractive index, an intense pulse will alter its own phase as it passes through a nonlinear medium. This effect is known as self-phase modulation (SPM). For laser beams with, for example, a Gaussian transverse intensity profile, the center of the pulse will experience a higher n than the periphery. Thus, an effective lens is formed, leading to the spatial effect of *self-focusing*.

Notice that all the interactions described in Fig. II.1 involve only so-called virtual states (intermediate states that cannot be observed) and the ground state. As such, these *nonresonant* processes are extremely fast. If real electronic states lie close to the virtual

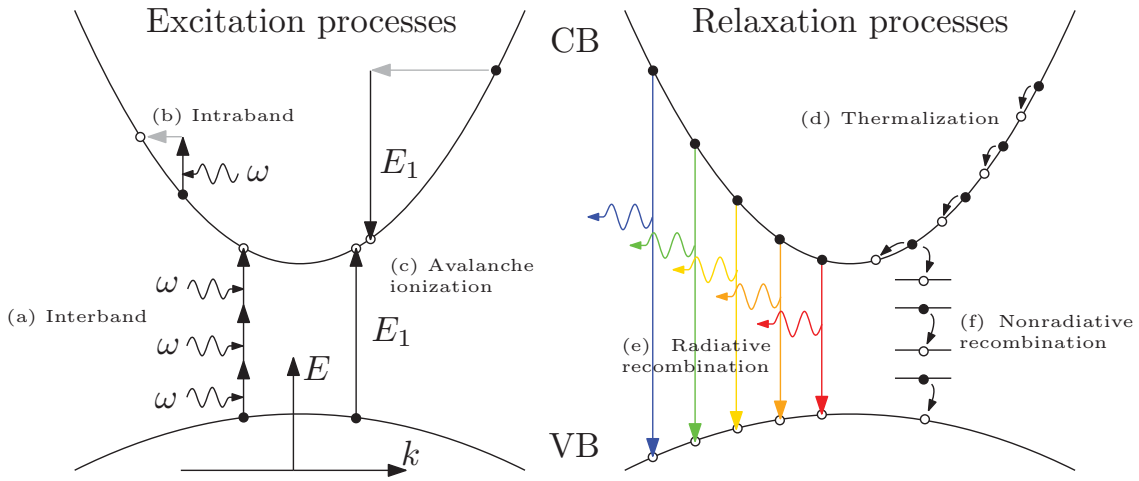

Figure II.2 – *Excitation and relaxation processes for a direct-bandgap semiconductor. Electrons are depicted as black dots, holes as circles. Photons are represented by curly arrows.*

states, however, the interaction is modified and the processes become resonant. We will now briefly discuss two types of media relevant for our experiments, semiconductors and metallic nanoantennas, where resonant behavior is expected. After explaining the specifics of these media, we will elaborate on resonant processes in general.

II.4. Nonlinear Optics with Semiconductors

At room temperature, solids can be classified as insulators, semiconductors or metals based on their electrical conductivity [64]. In this work we employ all three types. Note that the case of insulators is described by the nonresonant processes above and in Fig. II.1. Conductivity is largely determined by the electronic band structure of a given material, especially by the bandgap energy E_g which is the difference between the lowest conduction band (CB) and highest valence band (VB) points. If the bandgap is narrow enough, electrons can be thermally excited into the CB, leaving a positively charged *hole* in the VB. Both of these can act as charge carriers. In addition, electrons and holes can form bound pairs called excitons. We will encounter these quasi-particles in our study of ZnO nanorods in Chapter VII. Metals such as gold have a partially filled CB so that there is an abundance of carriers, making metals excellent conductors, while insulators like fused silica have such large bandgaps that virtually no carriers are found at room temperature. Between these two extremes lie semiconductors, whose bandgaps are small enough to allow a degree of control over the conductivity, for example by creating electron-hole pairs via absorption of light.

The excitation and relaxation processes relevant for our experiments are illustrated for a direct-bandgap semiconductor in Fig. II.2. The semiconductors we are dealing with, ZnO and TiO_2, have direct bandgaps of 3.4 and 3.2 eV, respectively. The employed near-infrared photons with energies of ≈ 1.5 eV are therefore too weak to allow a single-photon

interband excitation over the bandgap for either of our semiconductors, but multiphoton absorption (MPA) can still occur, see Fig. II.2 (a). Once electrons are found in the conduction band, single photons may be absorbed to promote an electron to a higher-energy state within the CB in an *intraband* excitation, cf. Fig. II.2 (b). Strictly speaking, intraband dipole transitions are forbidden by selection rules. However, for tightly confined fields such as those found in the nanostructures we study, higher-order transition moments can be substantially increased. This allows intraband excitation for example via quadrupole transitions [67]. After many intraband transitions, these *hot electrons* high up the conduction band distort the energy distribution of carriers from an ideal Fermi-Dirac distribution. Given time, the system will move towards the ideal distribution via relaxation processes such as thermalization, where energy is lost nonradiatively, see Fig. II.2 (d). Hot electrons can also scatter from a VB electron, and if the hot electron is energetic enough, the VB electron can be promoted to the CB in this impact- or avalanche ionization (AI) event, cf. Fig. II.2 (c). To ensure the conservation of momentum in a given transition, the lattice must provide the missing momentum (represented by the gray arrows) by creating phonons, quanta of lattice vibrations. Phonons can also account for energy conservation, for example in thermalization, but their energies are typically small compared to the bandgap so that energetic photons or hot electrons are always required for interband excitations. Electrons and holes (as well as excitons) can also recombine radiatively, see Fig. II.2 (e), emitting photons with the frequency $\omega = E/\hbar$, where E is the energy difference between the two annihilated carriers. For a well populated CB, radiative recombination can lead to a broad photoluminescence (PL) emission spectrum, illustrated by the range of colors. The radiative recombination process can also be coupled to phonons, further broadening the spectrum. If the lattice is imperfect due to defects or impurities, a small amount of defect states might be found even in the bandgap, allowing CB electrons to gradually relax into the VB in a nonradiative fashion via phonons as shown in Fig. II.2 (f).

Note that aside from these transitions to real states, the previously described nonlinearities may still take place in semiconductors, and, depending on the employed photon energies, the interaction can either be resonant or nonresonant. In Chapter VIII, we study resonant THG in a TiO_2 thin film.

II.5. Nonlinear Optics with Plasmonic Nanoantennas

In metals, a plasmon is a quantum of longitudinal oscillation of the conduction electron cloud [64]. As with previous examples, the interaction between a metallic particle and an electric field is described by the susceptibility χ, or equally well by the dielectric function

$$\epsilon = \epsilon_0(1 + \chi). \tag{II.29}$$

A simple way to derive ϵ for a metal is via the Drude–Sommerfeld model of a free electron gas. Following Ref. [16], the equation of motion for an electron moving between heavy

(stationary) ions is a damped harmonic oscillator,

$$\frac{\partial^2 r}{\partial t^2} + \gamma_d \frac{\partial r}{\partial t} = -\frac{e}{m_e} E\,. \tag{II.30}$$

Here e is the elementary charge, and γ_d is a damping constant. Using a plane-wave ansatz $r = r_0 e^{-i\omega t}$, the solution for Eq. (II.30) is

$$r = \frac{e/m_e}{\omega^2 + i\gamma_d \omega} E\,. \tag{II.31}$$

Taking the macroscopic polarization P as the sum of N electrons with dipole moments $p = -er$, and using Eqs. (II.14), (II.29) and (II.31), one obtains the dielectric function,

$$\frac{\epsilon(\omega)}{\epsilon_0} = \epsilon_\infty - \frac{\omega_p^2}{\omega^2 + i\gamma_d \omega}\,. \tag{II.32}$$

Here the screening effects from bound electrons are taken into account by ϵ_∞. The plasma frequency ω_p, given by

$$\omega_p = \sqrt{\frac{Ne^2}{\epsilon_0 m_e}}\,, \tag{II.33}$$

divides the response of the metal particle into two frequency regions. Ignoring the damping and screening effects ($\gamma_d = 0, \epsilon_\infty = 1$), the refractive index $n = \sqrt{\epsilon/\epsilon_0}$ becomes imaginary for $\omega < \omega_p$, implying that electric fields cannot propagate far inside the metal. The penetration depth is known as the skin depth. Thus, light with $\omega < \omega_p$ will be reflected, while for frequencies $\omega > \omega_p$ the metal becomes transparent because the electron cloud is not fast enough to respond to the incident electric field. More realistically, the higher frequencies can be absorbed by the electrons, much like with semiconductors in Fig. II.2.

While electromagnetic waves cannot propagate inside metals, they can exist along an interface between the metal and a dielectric such as air. Coupling of light into such a surface plasmon polariton (SPP) is, however, typically possible only if a prism or a grating is used to essentially match the wave vector components k_x along the interface for the SPP and the incident light. On the other hand, if a metallic particle is much smaller than the wavelength along one or more dimensions, the entire charge cloud covering the surface of the particle can start to oscillate collectively in response to the incident electric field. These localized SPPs, sometimes referred to as particle plasmon polaritons [16], can be readily excited in our experiments simply by focusing NIR pulses onto Au nanoparticles. Regardless of whether coupling of light is possible, surface plasmons can be excited by bombarding a metal structure with high-velocity electrons. Moreover, depending on the dimensions of the structure, localized or propagating surface plasmons may emerge and in some cases even coexist [68]. As we are exclusively using light to excite localized surface plasmons, the term *polariton* is appropriate here. For brevity, however, we often speak of particle plasmons, or simply plasmons. Unless otherwise noted, we use all these

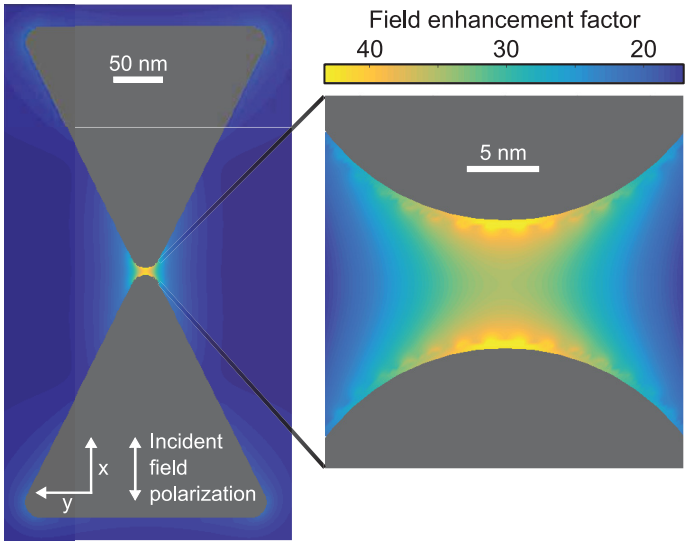

Figure II.3 – *Enhancement of near field around a bowtie nanoantenna similar to ours, as estimated via a boundary element method simulation [70–72]. Shape of the bowtie shown in gray. Courtesy of Vanessa Knittel, University of Konstanz.*

terms to refer to localized SPPs.

As the existence of localized SPPs essentially makes the nanoparticles resonators, their characteristics influence the optical response of the nanostructures greatly. The plasmonic resonance frequency and damping rate can be tuned by altering the size and shape of the nanoparticle. The dielectric environment of the nanostructure can also be perturbed, for example by a binding molecule, such that the plasmonic resonance frequency is shifted, which is why nanoparticles can also be employed for sensing applications even down to the single-molecule level [69]. Gold is a common choice of material for plasmonic nanostructures as it is chemically inert and has the desired Drude-like behavior (i.e., is described by Eq. (II.32)) for red to near NIR wavelengths [15], such as those employed in our experiments. Moreover, the available fabrication methods have matured to the point that gold nanostructures can be produced at the relevant, sub-wavelength scale with sufficient precision so that the resonances can be tuned to optical frequencies. The ability to absorb and emit light efficiently, and in general the enhancement of light-matter interaction in a limited band around the resonance frequency allows the nanoparticles to act as optical antennas [15].

The laser-induced charge oscillations along these *nanoantennas* can focus the electric field far beyond the diffraction limit of light such that the near field is greatly enhanced, in some cases by many orders of magnitude [73]. This enhancement is especially pronounced at sharp tips, such as the gap between the bowtie-shaped Au nanoantennas we employ, cf. Fig. II.3. With intense fields, nonlinear optical effects such as harmonic generation are expected, as usual. Moreover, the bowtie antennas have (in comparison to other common geometries) a broad plasmon resonance bandwidth which allows ultrafast interaction with broadband few-cycle pulses [15]. Owing to the strong field enhancement,

we can be sure that the harmonic radiation is generated primarily at the bowtie apexes and not at the surrounding substrate, simplifying further analysis. THG can in fact occur both in the gold interfaces and in the dielectric substrate found in the gap between the antennas. The relevant strengths of the two emitters depend on the geometry of the nanoantennas and the gap between them, as well as of the substrate $\chi^{(3)}$ [74]. What matters to us is that efficient THG *does* occur, and that it is mediated by the particle plasmon polaritons whose dynamics we are investigating. As we will show later on, the harmonic radiation can be harnessed to measure the plasmonic dephasing time.

II.6. Resonant Processes

As stated above, nonlinear processes become resonant if the virtual states involved lie close to real states. Similarly, when a part of the fundamental pulse spectrum overlaps with the energy of a transition to a real state, the system can be considered resonant in the linear sense [7]. A resonant system can typically interact with its surroundings, for example by releasing stored energy over time via scattering events. More generally, this interaction corresponds to the coupling of the resonant system with a dissipative system [7, 75]. Thus, physical properties such as the carrier population of the resonant system become time dependent, implying that the strength of light-matter interaction is also time dependent. That is, the optical response of the system can depend on events at previous times, or be delayed.

The dissipative behavior can be taken into account by introducing relaxation time constants. Two such constants are obtained via a semiclassical treatment of a resonant two-level system. T_1 is related to the decay of excited states (relaxation of energy), while T_2 describes how long the system remembers its phase after an excitation (relaxation of phase). Moreover, a system with a finite T_1 is said to have a memory, while a finite T_2 corresponds to a noninstantaneous response [7]. Various conventions exist for what exactly the time constants signify, depending on the nature of the studied system [65]. For plasmonic nanoparticles, the dephasing time T_2 is often thought to be connected [76] to the energetic decay T_1 and relaxation due to purely elastic scattering processes T^* via

$$\frac{1}{T_2} = \frac{1}{2T_1} + \frac{1}{T^*}. \tag{II.34}$$

On the other hand, for macroscopic solids, one typically finds that $T_1 \gg T_2$, implying that the decay rate $1/T^*$ is dominant [7, 65]. For our purposes it is sufficient to consider T_2 as a phenomenological relaxation time constant for the decay of the polarization amplitude — which we are measuring — irrespective of the quantum-mechanical origins.

Let us first consider a single-photon resonance using a classical approach to obtain the dephasing time T_2. Much like above, we derive the complex linear susceptibility via a damped harmonic oscillator model. In a system with the resonance frequency ω_r, the

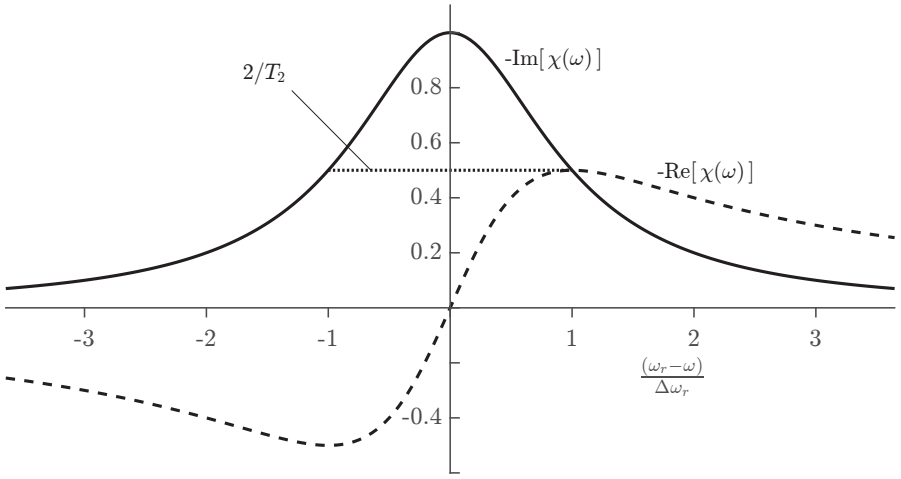

Figure II.4 – *Complex Lorentzian line shape. Adapted from Ref. [65].*

equation of motion for an electron is given by [7, 65]

$$\frac{\partial^2 z}{\partial t^2} + \gamma_d \frac{\partial z}{\partial t} + \omega_r^2 z = -\frac{e}{m_e} E\,, \tag{II.35}$$

where $\gamma_d = 1/T_1$ is a damping constant describing the decay of energy. In other words, the amplitude of the oscillation decreases with the rate $\gamma_d/2$. For a large number of dipoles, the damping rate is increased due to random collision events where the dipoles get out of phase. If the collisions occur at a mean rate of $1/T^*$, the amplitude decay rate becomes $1/2T_1 + 1/T^*$, which is equal to the decay rate $1/T_2$ as given by Eq. (II.34). The updated energy decay rate is then $\Delta\omega_r = 2/T_2$. Note that Eq. (II.35) is essentially just Eq. (II.30) with the additional resonance term $\omega_r^2 z$. Once again, we take a plane-wave ansatz $z = z_0 e^{i\omega t}$, sum over the dipoles, and use Eq. (II.14) to obtain the complex susceptibility

$$\chi(\omega) = \frac{Ne^2}{\epsilon_0 m_e} \frac{1}{\omega_r^2 - \omega^2 + i\omega\Delta\omega_r}\,. \tag{II.36}$$

Eq. (II.36) corresponds (approximately) to a complex Lorentzian line shape with the FWHM of $\Delta\omega_r = 2/T_2$, where the imaginary part defines the absorption (or amplification) spectrum, and the real part gives the phase response, see Fig. II.4. In the time domain, the Lorentzian line shape is equivalent to an exponential decay of the induced polarization amplitude with the time constant T_2.

To see why the complex χ results in absorption, we substitute Eq. (II.36) into Eq. (II.18), leading to a complex wave vector k. Substituting the complex k into Eq. (II.17), we find that a positive (negative) imaginary part of k leads to exponential absorption (gain) upon propagation by introducing the term $e^{\mp \mathrm{Im}\{k\} z}$. Absorption is expected over gain, unless a population inversion is somehow induced, i.e., if the upper-level population of the two-level system implied here exceeds the ground state population. This analysis underlines

the fact that a complex χ, absorption, resonance and a finite dephasing time are very much intertwined. The real and imaginary parts of the linear susceptibility are in fact bound to one another by the Kramers–Kronig relation, essentially linking absorption and the phase response described by the real part of the refractive index. In general, one finds that the noninstantaneous material response is synonymous with a complex, frequency-dependent susceptibility.

For nonlinear resonant processes, behavior similar to the linear case is expected, including the emergence of an absorption linewidth, phase contribution and a finite dephasing time. The analytical description of resonant nonlinear processes can however be exquisitely complicated, especially when pulse durations are comparable to the dephasing time [7]. The interplay of transient absorption and dispersion, propagation, as well as coherent and nonlinear phenomena renders the prediction of a dephasing time difficult. Fortunately, we may access T_2 experimentally via pulse characterization, the topic of our next chapter.

CHAPTER III

Ultrafast Laser Pulse Characterization

In an ideal world, one could measure all the desired properties of ultrashort laser pulses with a single technique. This perfect measurement would yield the complex-valued spatio-temporal electric field $E(t, \mathbf{r})$ for an individual pulse. As the shortest pulses today are typically not isolated events, but produced instead at megahertz repetition rates with solid-state mode-locked lasers, a full characterization would also be able to tell how stable the pulse train is, and by how much and in which way the pulses differ from one another. The measurement should also be applicable to pulses of arbitrarily short or long temporal extent, and work in any given wavelength range from the extreme ultraviolet (XUV) to the mid infrared. Ideally, the measurement data could be obtained and processed in real time, yielding the electric field in an unambiguous, deterministic manner. The measurement should also be self-referenced, so that no *a priori* knowledge of the employed or investigated pulses is required.

In reality, compromises must of course be made. Isolating and characterizing a single pulse can be challenging, due to e.g. a high repetition rate or a low pulse energy, so that averaging over countless pulses is required, yielding at best a representative answer of how a typical pulse looks like. Because of the employed nonlinearities and the spectral sensitivity of available photon detectors, any given characterization technique is limited in bandwidth and the applicable range of the optical spectrum. The absolute phase, also known as the carrier-envelope phase (CEP), is impossible to be measured with commonly used techniques, simply because the measured traces are independent of the absolute phase [9]. Although examples exist where one [77, 78] or two [79] spatial dimensions are measured simultaneously (or via repeated measurements while scanning through space [80]) with the complex temporal envelope of the electric field, most techniques are limited to the temporal or spectral domains. Without a spatial resolution, unwanted spatio-temporal couplings cannot be identified, possibly leading to a myriad of detri-

mental effects [81]. For many techniques such as the popular frequency-resolved optical gating (FROG) [13, 60, 82, 83], obtaining the pulse electric field from measurement data is an inverse problem, often riddled with nontrivial ambiguities. Such a problem can only be solved or *inverted* with an iterative algorithm which is not only time consuming but can also fail to reach the correct answer. If an algebraic, deterministic solution exists, the inversion of measurement data can be very fast, as is the case with another common technique, spectral-interferometry for direct electric-field reconstruction (SPIDER) [14, 84]. At the same time, the lack of redundancy in data can make such a technique less reliable, e.g. in the presence of pulse train instability [85].

Considering most applications, however, these obstacles can be overcome. The unmeasured and unstable CEP can be stabilized and measured externally if needed [86]. Moreover, the CEP only becomes important for few-cycle pulses and highly nonlinear processes, most prominently so in high-harmonic generation, where the harmonics yield can be severely affected [87]. While the capability to spatially resolve the pulse electric field can be crucial for some applications, for example obtaining the highest possible focal intensity for an ultra-high intensity laser [79], having only a temporal resolution is more than sufficient in most situations. Pulse train instabilities can in principle be detected with FROG-like techniques [85]. Nevertheless, many pulsed laser sources such as the passively mode-locked titanium-sapphire lasers employed in this work are highly stable, and the produced pulses very much alike. Thus, the electric field of a single, averaged pulse can safely be used to represent the entire pulse train. Recent developments [41] in inversion algorithms and novel measurement techniques, including those presented in Publications [II–IV], have shown that FROG and related methods are highly robust. A suitable characterization technique can often be chosen based on the approximate pulse duration and the employed region of the optical spectrum, and by defining the parameters of interest to be measured. For example, XUV pulses with attosecond time scales can be measured with FROG for complete reconstruction of attosecond bursts (FROG-CRAB) [88], and over octave-spanning pulses from the visible range up to mid IR with SEA-F-SPIDER [89] or time-domain ptychography [48], for example.

In the context of this thesis, we are mainly interested in the self-referenced measurement of the complex temporal profile $E(t)$, as given by Eq. (II.6), for unamplified ultrashort pulses in the near infrared (NIR), ranging from few optical cycles to over a hundred femtoseconds in duration. While many characterization modalities suitable for such pulses exist, our use-case is somewhat more involved: we wish to study the response of the nonlinear medium employed in the pulse measurements, not only the pulse *per se*. The chosen nonlinear media present some restrictions and requirements for the applicable pulse characterization techniques. First and foremost, we mainly employ third-order nonlinearities in solid media. The fact is that currently no SPIDER-like techniques based on $\chi^{(3)}$ nonlinearities exist. Even if such techniques were available, it is unclear how and *if* they could be applied here. Attosecond streaking might in principle be applied in some cases, but the technique remains of limited used in solids [35]. Thus, out of the characterization techniques suitable for few-cycle pulses, FROG-like methods based on THG present the most promising choice. For reasons that will be discussed in more de-

tail later on, collinear techniques are strongly preferred over the traditional noncollinear FROG variants. This chain of reasoning leads us to interferometric FROG (iFROG) [11, 12] employing THG as the nonlinearity. As no previous solution to invert THG-iFROG measurements exists, we must develop one ourselves. A large portion of this work, including the rest of the present chapter, is therefore devoted to introducing and demonstrating the aptitude of our novel solution to THG-iFROG. We begin by giving a general view of ultrafast pulse characterization techniques.

III.1. Complete Characterization

The simultaneous measurement of both the amplitude and the phase of a pulse electric field, in either temporal or spectral domain is generally referred to as *complete characterization*. The two domains, as stated above, are connected by a simple Fourier transform, so that either representation of the pulse can be easily obtained from the other. There are many ways to classify complete characterization modalities. Walmsley [9] divided the numerous techniques into three principal categories: spectrography, interferometry, and tomography. Loosely speaking, spectrography encompasses techniques such as FROG, while SPIDER falls under interferometry. Considering that we are investigating interferometric FROG — a method that has little to do with SPIDER yet its very name contains the word *interferometric* — it is clear that using the terms *spectrography* and *interferometry* in this context can be quite confusing. For our purposes it suffices to speak of *FROG-like* and *spectral shearing* techniques instead, with no direct reference to Walmsley's definitions of spectrography or interferometry. Here we call a characterization technique FROG-like if an iterative algorithm is employed to reconstruct a 1D electric field from a 2D dataset where one of the dimensions is the frequency ω. Spectral shearing modalities, on the other hand, have a direct algebraic solution, and may employ 1D or 2D data to obtain the 1D electric field [90], and in some cases a 2D electric field (one spatial coordinate) from a 2D dataset.

The most important example of spectral shearing within the context of this work is SPIDER [14]. In SPIDER, two relatively delayed test pulse replicas are mixed via sum-frequency generation with a third, heavily chirped copy of the test pulse. Because of the temporal delay between them, the unchirped pulses are mixed with a different spectral component of the chirped pulse, resulting in two upconverted pulses with a known frequency shift between them. This frequency shift is one way of introducing a *spectral shear* [90], hence the name to our category. Thus, the upconverted pulses interfere to create a fringe pattern in the spectral domain, subsequently recorded by a spectrometer. When the spectral phase of the test pulse — algebraically obtained from the fringe pattern — is combined with an independently measured fundamental spectrum, the electric field is fully characterized in the spectral domain.

Pulse characterization modalities falling into Walmsley's third category, tomography, are markedly different from FROG-like methods or spectral shearing, making the definition useful here as well. Tomographic techniques are based on the idea that if the Wigner

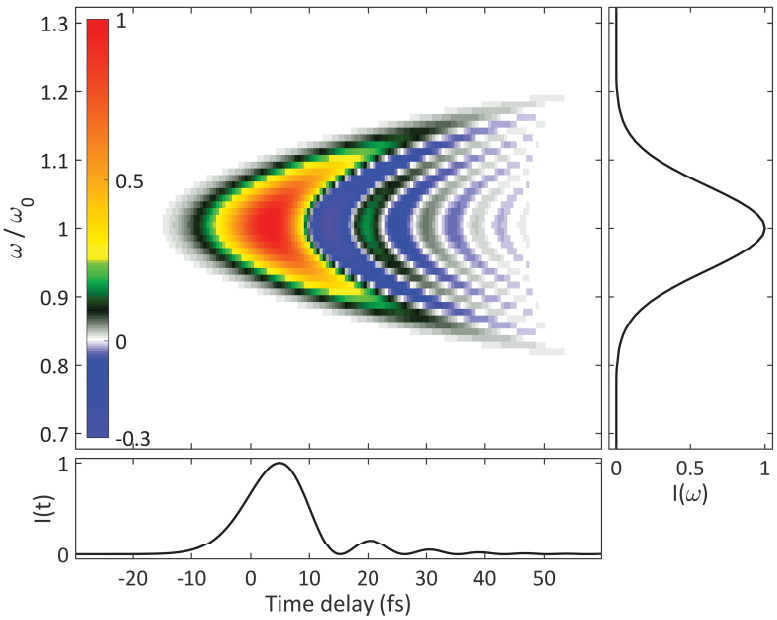

Figure III.1 – *Simulated Wigner trace (top left) for a three-cycle pulse with a carrier wavelength of 800 nm after introducing some third-order dispersion. Integrating (i.e. taking a projection) over either coordinate yields the intensity envelopes of the test pulse in time- (bottom) or frequency domain (right).*

function for the test pulse, defined as

$$W(t,\omega) = \frac{1}{\sqrt{2}} \int_{-\infty}^{+\infty} E\left(t + \frac{t'}{2}\right) E^*\left(t - \frac{t'}{2}\right) e^{i\omega t'} \, \mathrm{d}t', \tag{III.1}$$

can be rotated or sheared in the chronocyclic (time-versus-frequency) space in a controlled fashion, a set of measured projections of the Wigner function (spectral or temporal intensity) can then be used to deterministically reconstruct the underlying function, and subsequently the test pulse [91]. See Fig. III.1 for an illustration of the Wigner function and the two projections. The rotation of the Wigner function can be realized via successive quadratic phase modulations performed in frequency and time domains, having spatial analogues to free-space propagation and a spatial lens, respectively. Temporal imaging [92] uses these phase modulations in alternate domains to produce a magnified pulse in the time domain, which can then be measured with a comparatively slow detector. Recently, temporal imaging was used to completely characterize each and every individual pulse in a train of picosecond pulses with a 50 MHz repetition rate over a time span of ≈ 100 ms [93]. Producing a precise quadratic temporal phase modulation has proved difficult, however, limiting the temporal resolution of tomography to hundreds of femtoseconds at best [9, 94, 95]. Moreover, tomographic modalities for ultrashort pulses characterization have been demonstrated mainly for fiber-optic systems, while in the focus of the present work are pulses propagating in free space.

In contrast to tomography, a myriad of FROG-like and spectral shearing techniques have been developed for the characterization of ultrashort pulses, along with a few stellar demonstrations close to the single-cycle regime [48, 96–98]. Further examples of equally capable techniques include multiphoton intrapulse interference phase scan (MIIPS) [99] and dispersion scan (d-scan) [100] which are based on a combination of a fundamental spectrum measurement and a set of spectra measured after introducing a controlled amount of dispersion to the test pulse. Recently, a 1.4-cycle pulse was characterized with d-scan [101]. Neither MIIPS or d-scan fall into any of the three categories described by Walmsley, but clearly fit our definition of FROG-like techniques. In Chapters IV to VI two novel FROG-like pulse characterization modalities, THG-iFROG and ptychographic-interferometric FROG (πFROG), are introduced, along with a new solution for the SHG variant of iFROG. Next, we will discuss the concepts relevant to these techniques, and their predecessors, while spectral shearing methods and tomography are left to less attention.

III.2. Autocorrelation

One of the earliest ways to measure the duration of a laser pulse is intensity autocorrelation, which, owing to its simplicity, is still widely used. In intensity autocorrelation, the test pulse is split into two replicas which are then subjected to a nonlinear mixing process, typically SHG [102, 103] or two-photon absorption [104], serving as a time-nonstationary gate. By varying the time delay τ between the pulse replicas, the nonlinear signal is modulated such that the pulse effectively samples itself in time domain. The two possible beam geometries are illustrated in Fig. III.2 employing SHG. With the

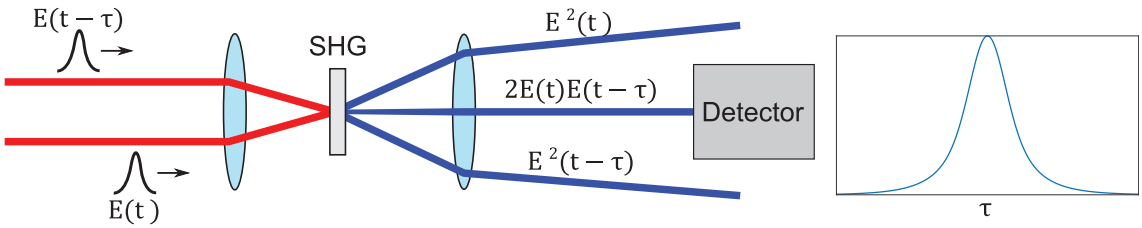

(a) *Noncollinear (background-free)*

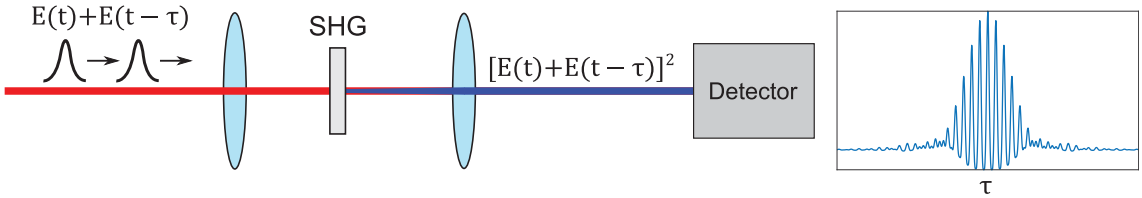

(b) *Collinear*

Figure III.2 – *Autocorrelation geometries. Simulated signals for a few-cycle pulse as measured by either system shown on the right. Figure adapted from Ref. [11].*

noncollinear geometry in Fig. III.2(a), the mixing term $|E(t)E(t-\tau)|^2$ of the two pulses can be measured without the influence of either of the individual correlations $|E(t)|^2$ and $|E(t-\tau)|^2$, which is why this measurement scheme is also referred to as the *background-free intensity autocorrelator*. The resulting one-dimensional autocorrelation signal [60]

$$I_{\mathrm{AC}}(\tau) = \int_{-\infty}^{+\infty} |E(t)E(t-\tau)|^2 \,\mathrm{d}t = \int_{-\infty}^{+\infty} I(t)I(t-\tau)\,\mathrm{d}t \tag{III.2}$$

can subsequently be used to estimate the temporal intensity envelope of the test pulse. As is clear from the right hand side of Eq. (III.2), the autocorrelation measurement is independent of the temporal phase of the test pulse. Complete characterization of the complex electric field $E(t)$ is therefore impossible.

Attempts have been made to allow at least some degree of phase sensitivity to autocorrelation measurements. Interferometric autocorrelation [105] or *fringe-resolved autocorrelation* employs the collinear beam geometry of Fig. III.2(b), where the above rejected background terms are now interfering with the mixing term,

$$I_{\mathrm{iAC}}(\tau) = \int_{-\infty}^{+\infty} |E(t) + E(t-\tau)|^2 \,\mathrm{d}t\,, \tag{III.3}$$

producing a phase-sensitive fringe structure, modulated at ω_0 and $2\omega_0$. The temporal phase can then be estimated, to an extent. Independently measured fundamental spectrum can help narrow the solution space [106], but *a priori* knowledge such as the pulse shape is always required, and even then the solution is not unique. For both beam geometries, the measured signal is always symmetric with respect to τ, making intensity and interferometric autocorrelations blind to the direction of time, i.e. it is impossible to tell which side of the measured intensity envelope arrived first. All these hindrances make simple autocorrelation measurements insufficient for complete pulse characterization. Nevertheless, their simplicity has also made autocorrelators a very popular measurement tool when a mere estimate of the pulse duration will suffice.

III.3. Collinear and Noncollinear Frequency-Resolved Optical Gating

In many ways a successor of the autocorrelation methods, FROG is one of the first and most widely spread of all complete characterization methods for ultrashort laser pulses [60]. Considering the measurement device, FROG is a simple extension of the noncollinear intensity autocorrelator as the only necessary modification is to replace the simple power meter with a spectrometer. Thus, a FROG measurement produces a spectrogram, also known as a *FROG trace*. A simulated example of a FROG trace is shown in Fig. III.3(a).

Similarly, an iFROG trace is a spectrally-resolved collinear interferometric autocorre-

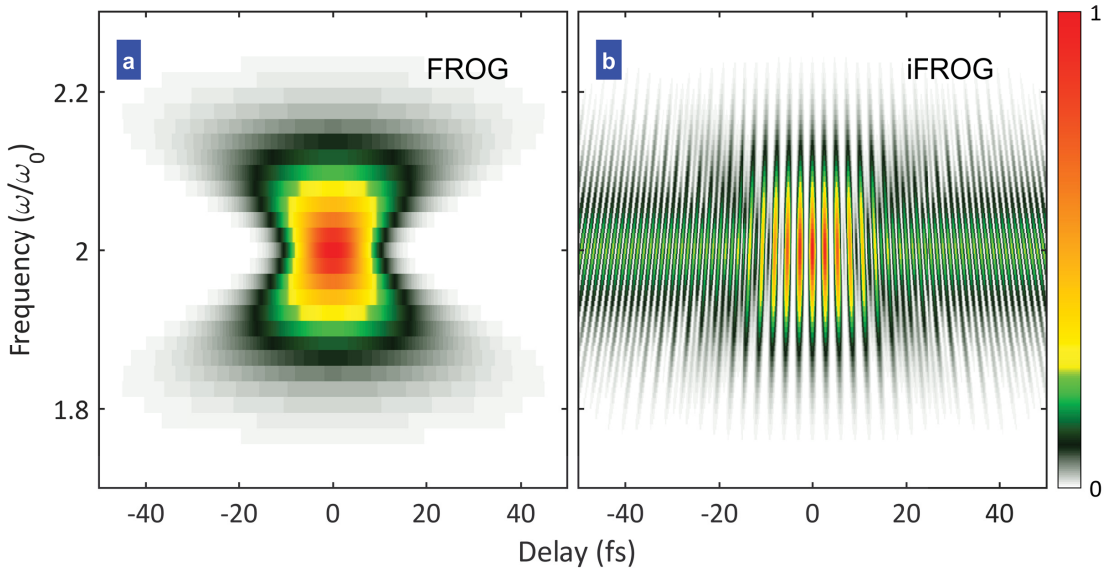

Figure III.3 – *Simulated SHG-based (a) FROG and (b) iFROG traces for a three-cycle pulse with a carrier wavelength of 800 nm and some third-order dispersion.*

lation [11, 12]. A simulated iFROG trace corresponding to the FROG trace on its left hand side can be seen in Fig. III.3(b). As with interferometric autocorrelation, the use of a collinear beam geometry in iFROG leads to the appearance of an interferometric fringe structure, a characteristic feature of every iFROG measurement. The interferometric spectrogram contains more redundant data than the corresponding FROG trace, giving iFROG additional sensitivity to the spectral phase, an increased robustness against noise and measurement errors, and the possibility to use several independent but simultaneously recorded data sets for pulse retrieval [12, 38]. Moreover, collinearity enables the use of high numerical aperture objectives and other focusing optics, vastly increasing the sensitivity of the technique over noncollinear FROG. Pulse characterization in the focus of such objectives is important for example in the context of biological measurements, where careful optimization of the incident electric field can prolong the lifetime of fragile, microscopic biological samples [11]. On the other hand, the tight focusing can also be used to produce very high incident field intensities for less-sensitive samples, such as dielectrics, allowing efficient nonlinear light-matter interaction to occur. We will demonstrate that this facilitates the measurement of nanojoule pulses directly from an oscillator (Chapters IV and V), and fundamental research of nonlinear effects (Chapters VII and VIII, see Refs. [27, 28, 107] for more examples). Further still, the so-called geometrical time-smearing effect [60] is avoided entirely. This distortion results in an increased error margin for the retrieved pulse, limiting the usability of noncollinear FROG variants for few-cycle pulses [108]. Yet another advantage is that the tighter focusing allowed by collinearity also decreases the interaction length within a nonlinear medium during harmonic generation, thus increasing the phase-matching bandwidth and finally facilitating the characterization of few-cycle pulses with concomitantly wide spectra.

While FROG and its decade younger sibling, iFROG, are in many ways alike they differ in how the electric field of the pulse is reconstructed from the measured spectrogram, namely the retrieval algorithm. Specifically, FROG algorithms are either limited in capability or not applicable at all for iFROG variants. Difficulties in solving the more complex iFROG pulse retrieval problem is perhaps the main reason for the 10-year gap between first demonstrations of FROG and iFROG, and why iFROG is not nearly as well known as the classic SHG-based FROG [83], along with its many variants such as polarization-gating [82] and self-diffraction [13] FROGs. The retrieval algorithms and their differences will be discussed thoroughly below.

Collinear variants of FROG where special care has been taken to remove the interferometric fringes either computationally [11] or experimentally [109–111] have also been demonstrated. The advantage of these techniques is that standard FROG algorithms maybe used directly on the measurement data without extensive post-processing. Unfortunately, this simplification of the measurement data comes with the cost of losing the additional information carried by the fringes, reduction of obtainable dynamic range or signal strength, and, for the experimental cases, a more complicated measurement setup is required.

In addition to being capable measuring the complex electric field of a pulse, iFROG and most FROG variants are also self-referenced. A notable exception to this rule is the cross-correlation FROG (XFROG) [112], which uses a completely characterized reference pulse to measure an unknown pulse. XFROG is especially well suited for weak or highly structured pulses. The accuracy of XFROG, however, relies on accurately measured reference pulse, highlighting the importance of self-referenced techniques.

III.4. Iterative Solutions to Inverse Problems

Unlike in spectral shearing where the test pulse can be obtained algebraically, only an iterative deconvolution strategy can yield the solution for FROG-like methods [9]. Measured nonlinear spectrograms may correspond to many solutions, underlining the need for a robust algorithm capable of finding the correct pulse shape. Here we introduce a selection of iterative algorithms that are suitable for pulse retrieval using FROG traces, or similar measurements, such as iFROG traces or the newly introduced πFROG traces. In the following discussion, the focus will be on the applicability of the algorithms to our methods of choice, iFROG and πFROG.

III.4.1. Generalized Projections

Most of the commonly used FROG algorithms are based on the concept of generalized projections (GP). The aim of a GP algorithm is to find a *signal field* $E_{\mathrm{sig}}(t,\tau)$ that satisfies two conditions: a mathematical-form constraint, and a data constraint. The former states that the signal field must conform to a mathematical form as defined by the employed nonlinearity, e.g., $E_{\mathrm{sig}}(t,\tau) \propto E(t)E(t-\tau)$ for SHG-FROG. The latter condition requires that the signal field, after a Fourier transform into the frequency domain, matches the

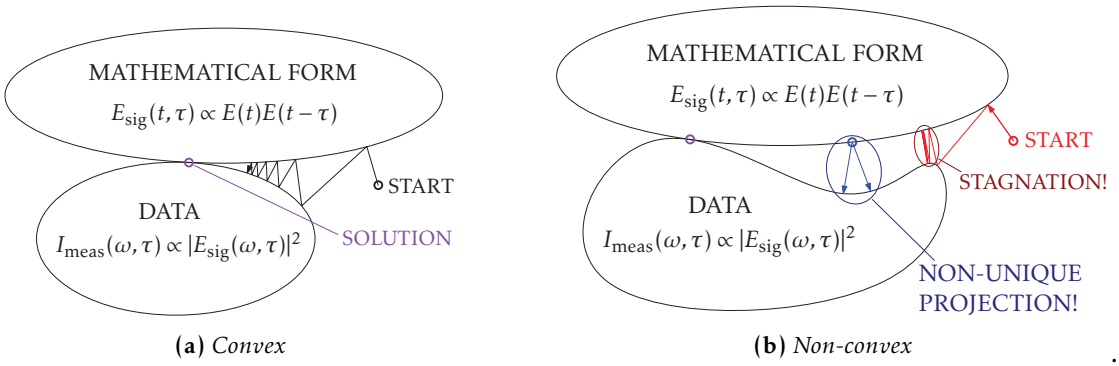

(a) *Convex* **(b)** *Non-convex*

Figure III.4 – *Effect of constraint set topology on the act of making projections in the case of SHG-FROG. Here, the page represents the space of all possible signal fields $E_{sig}(t,\tau)$, and the two constraint sets are subsets of this space. A projection is made by moving from a randomly selected point (start) to the nearest point in either constraint set along a straight line. Subsequent projections are made between the two constraint sets. When both sets are convex (a), convergence is guaranteed. If either set is non-convex (b), GP can stagnate on a local minimum, preventing the algorithm from reaching the solution (red path). Non-convexity can also lead to a situation where a projection is not uniquely defined (blue paths), which is why a generalized projection must be defined. Figure (a) adapted from Ref. [60].*

measured FROG trace.

Both of these constraints define a (possibly) non-convex set within the complex space of all the possible $E_{\text{sig}}(t,\tau)$. For a geometrical illustration see Fig. III.4. A FROG algorithm based on GP makes a series of projections between the two sets, hopefully converging to a point that is a member of both sets, i.e. the solution, cf. Fig. III.4(a). In practice an exact solution is difficult to achieve, especially in the presence of measurement noise, and as a compromise it is considered sufficient that the two constraints are only approximately fulfilled [60]. The need for such a compromise is related to the fact that the two constraint sets are not necessarily convex. This observation leads to two important consequences. First, convergence is not guaranteed, that is, a solution (let alone the correct one) may not be reached. Instead, the algorithm can stagnate or get stuck to a local minimum, cf. red path in Fig. III.4(b). While this problem can be mitigated, for example by switching algorithms during pulse retrieval, the fundamental nature of the problem means that it cannot be completely removed, which is why GP algorithms are known to struggle especially with noisy data [113]. A second consequence of non-convexity is that a projection is not necessarily unique. A projection onto either of the two sets corresponds to moving a minimal distance within the space of signal fields in order to reach the destination set. At times, the non-convexity of the sets results in a situation where several points of the destination set are found equally close to the starting point, cf. blue paths in Fig. III.4(b). Thus, a projection to the nearest point is not unique, and a *generalized projection* must be defined.

A GP onto the data constraint set is easily made. As a FROG trace is an intensity measurement, the data constraint is fulfilled simply by replacing the amplitude of the Fourier-transformed signal field $\mathcal{F}\left\{E_{\text{sig}}(t,\tau)\right\} = E_{\text{sig}}(\omega,\tau)$ with the square root of the mea-

sured FROG trace while leaving the phase intact. Although this newly acquired signal field $E'_{\mathrm{sig}}(t,\tau)$ is by definition a member of the data constraint set, it most likely does not belong to the mathematical-form constraint set. A GP to the latter set is therefore required next and, as it turns out, it is a much more complicated task than fulfilling the data constraint.

In the classical realization of a GP-based FROG algorithm [114], the generalized projection onto the mathematical-form constraint set is executed by minimizing the functional distance Z between the current iteration of the signal field, $E^{(k)}_{\mathrm{sig}}(t,\tau)$, and a new signal field generated from the next iteration of the electric field $E^{(k+1)}(t)$. For an SHG-FROG trace sampled on an $N \cdot N$ grid this reads

$$Z \equiv \sum_{i,j=1}^{N} \left| E^{(k)}_{\mathrm{sig}}(t_i,\tau_j) - E^{(k+1)}(t_i) E^{(k+1)}(t_i-\tau_j) \right|^2 . \tag{III.4}$$

Z is minimized by computing the gradient $\partial Z/\partial E^{(k+1)}(t)$ at the current iteration $E^{(k)}(t)$, and then moving from $E^{(k)}(t)$ in the direction of steepest descent until an approximate minimum is found [60]. Because the distance between the data-constrained $E^{(k)}_{\mathrm{sig}}(t,\tau)$ and the mathematical-form abiding new signal field is minimized, this procedure is a generalized projection. Having acquired a new $E(t)$, the next iteration of the algorithm begins, and the cycle is continued until the signal field is deemed a sufficiently close match to the measured trace. How well the two agree is measured by the FROG error G,

$$G \equiv \sqrt{\frac{1}{N^2} \sum_{i,j=1}^{N} \left[I^{(\mathrm{meas})}_{\mathrm{FROG}}(\omega_i,\tau_j) - \mu \left| E_{\mathrm{sig}}(\omega_i,\tau_j) \right|^2 \right]^2} , \tag{III.5}$$

where $I^{(\mathrm{meas})}_{\mathrm{FROG}}$ is the measured trace and μ is a constant which minimizes G.

Alternatives to the classical GP algorithm do exist. A clever way of making a generalized projection onto the mathematical-form constraint set without the need for gradients or a minimization procedure can be found using matrix algebra. The principal component generalized projections (PCGP) [115] employs a so-called outer product form (analogous to the signal field in classic GP) that can be easily computed for a probe and a gate pulse, and subsequently transformed to a FROG field. After applying the measurement constraint as above, the outer product form is obtained from the FROG field. Instead of minimization, the probe and gate pulses can be efficiently and directly obtained through a singular-value decomposition of the outer product matrix (a generalized projection onto mathematical-constraint space).

For an iFROG trace, defining a signal field or an outer product form is difficult or even impossible, and thus a GP-based pulse retrieval algorithm is generally not feasible [12]. A notable exception is the SHG-iFROG, which allows the extraction of an SHG-FROG trace, for which any standard FROG algorithm is applicable [11]. Analogously to SHG-iFROG, a subtrace pertaining to the outer product form can be extracted from a πFROG measurement. This effectively reduces the πFROG to a blind FROG measurement, where

two unknown pulses are retrieved instead of just one, and for which PCGP can be used. While this possibility of using PCGP for πFROG measurements is not pursued in this work, comparing the performance of the two algorithms could present an interesting case study.

III.4.2. Differential Evolution

The difficulties in implementing GP for iFROG necessitate an alternative strategy for pulse retrieval. Casting the concept of projections aside, the iFROG subtraces can nevertheless be extracted from measurement data and computed numerically for a given $E(t)$. Using a cost function for difference between synthetic and measured data (e.g. analogous to Eq. (III.4) or Eq. (III.5)) then allows, in principle, to use an arbitrary minimization algorithm to alter the simulated electric field in a way that minimizes the chosen measure, thus yielding the correct pulse. A previously discovered solution for SHG-iFROG [38] uses a line minimization strategy employing analytically defined gradients of the Z-error akin to the classic GP (Eq. (III.4)), but therein Z is defined in the frequency domain and for a subtrace of iFROG (acquired through Fourier filtering), not the entire trace. Moreover, no projections corresponding to the data constraint are employed. Essentially a local gradient fitting strategy like the classic GP, this solution of the iFROG problem is unfortunately inflicted with some of the same problems associated with GP, most importantly the tendency to stagnate in local minima, especially for noisy data [116]. For THG-iFROG, analytical solutions for the corresponding gradients have not been found, so that the strategy in [38] cannot be applied. In publication [V], an iFROG solution based on the Nelder–Mead direct search method [117] was implemented, but as a local minimization strategy this algorithm is also easily caught in local minima, and is relatively slow to converge.

In Chapter IV we implement differential evolution (DE) to minimize a cost function analogous to the G-error in Eq. (III.5). Through a multitude of tests both numerical and physical, this novel solution of the iFROG problem is shown to be highly robust, containing several intrinsic error correction mechanisms, being resistant against detection noise and to stagnation in local minima, all the while converging approximately as fast as standard FROG algorithms, but with a more predictable behavior. The algorithm is suitable for both second- and third-harmonic generation variants, utilizing all the information contained within an iFROG trace. We call the method, or the combination of the adapted algorithm and the measurement technique, DE-iFROG. To emphasize, our implementation of DE is conceptually different from the GP in the sense that no projections between two sets of constraints are made. Instead, all the iterations satisfy the mathematical-form constraint, i.e., that a pulse and the corresponding trace are in perfect agreement, and the pulse is simply altered such that the corresponding trace converges towards the measurement data. We will now describe DE from a general perspective, while the implementation for iFROG is discussed in Section IV.3.2 in greater detail.

Differential evolution is an evolutionary algorithm suitable for global minimization of complicated cost functions [39]. This direct search method has many beneficial qualities, such as consistent convergence to the global minimum and the ability to escape

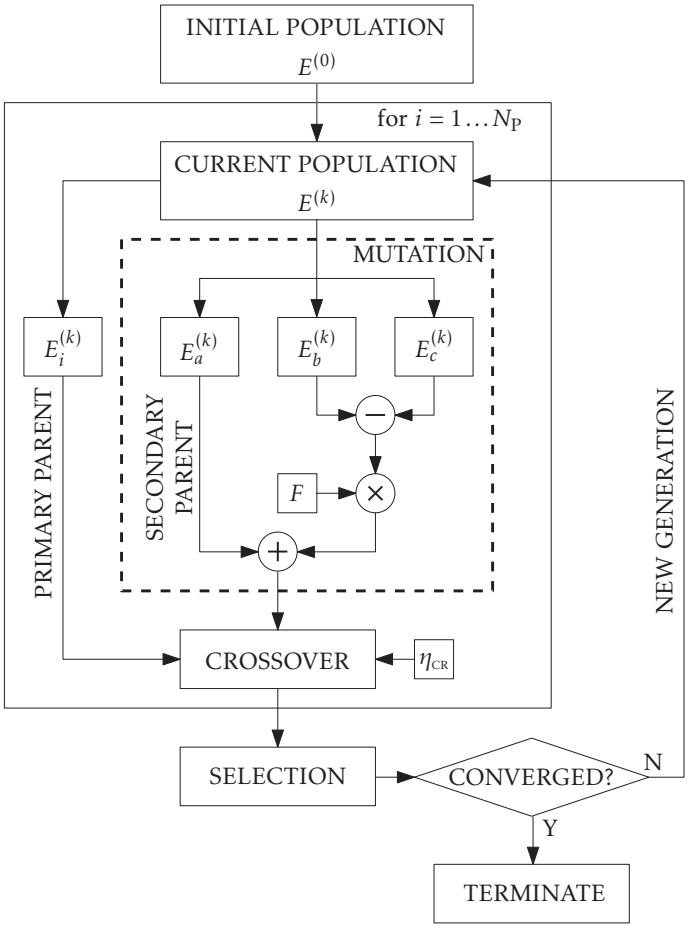

Figure III.5 – *Flowchart describing the chosen variant of the differential evolution algorithm. The best-of-random mutation operation is highlighted with the dashed rectangle. Adapted from Ref. [40] and Publication [III].*

local minima, suitability for parallel computation for increased speed, and a relatively few control variables for ease of use. DE employs the evolutionary operations of *mutation*, *crossover*, and *selection* to breed a population of real-valued parameter vectors or *individuals* toward the global minimum.

There are many ways to implement DE, but we selected the best-of-random approach [40, 118], illustrated in Fig. III.5. Starting with a random population $E^{(0)}$ that ideally covers the entire parameter space, the *fitness* of each of the N_P number of individuals is first measured with the cost function Ψ. Each vector $E_i^{(k)}$ of the current generation k then acts as a primary parent for the offspring, while a secondary parent $E_a^{(k)}$ undergoes a mutation process. The mutation vector is produced from a randomly selected set of three vectors a, b and c ($a, b, c \neq i$), of which the fittest (i.e. lowest associated value of the cost function) is selected as the secondary parent. The difference of the two remaining

vectors $E_b^{(k)}$ and $E_c^{(k)}$ is computed, multiplied with a random number F, and added to the secondary parent. The offspring are then generated by combining the primary parent and the mutant vector in the crossover step such that each element of the mutant vector has a crossover probability η_{CR} to replace the corresponding element of the primary parent. Once all the offspring have been generated, their fitness is measured, and the offspring are combined with the current population and ordered according to their fitness. The fittest N_{P} individuals are selected to form the next generation, while the equally many weaker specimens are discarded. If the fittest individual has a sufficiently low cost-function value the algorithm terminates, otherwise the next iteration begins.

To implement DE for the iFROG problem, the parameter vectors are defined as complex electric field vectors in the time domain $\mathbf{E}(t)$, while the cost function $\Psi(\mathbf{E})$ compares the rms difference between subtraces extracted from the iFROG measurement and their synthetic counterparts produced using $\mathbf{E}$. This makes $\Psi(\mathbf{E})$ analogous to the FROG error G of Eq. (III.5), as was already mentioned. The subtraces will be introduced and thoroughly discussed in Section IV.2.

III.4.3. Time-Domain Ptychography

While GP and our implementation of DE are fundamentally different approaches to the pulse retrieval problem from spectrograms, the common denominator is that the entire spectrogram is used in each evaluation of a cost function. The recently discovered pulse retrieval technique of time-domain ptychography (TDP) differs from the previous examples in this respect, as each spectral slice of the spectrogram (i.e., one delay sample at a time) are independently employed by a cost function in a successive manner. TDP is a temporal domain analogue of the real space imaging technique *ptychography*, which we will briefly discuss next.

Much like GP, ptychography is a phase-retrieval algorithm, but for far-field diffraction patterns instead of a spectrogram. In a generalized diffraction experiment, an illuminating beam is diffracted from a real space object, creating a diffraction pattern that is most conveniently described in the reciprocal space with the amplitude $|F(\mathbf{q})|$. The complex field $F(\mathbf{q})$ is connected to the real space object $f(\mathbf{r})$ through a simple Fourier transform. In order to access spatial information of the diffracting object, the phase of $F(\mathbf{q})$ must be obtained so that an inverse Fourier transform can be carried out. The concept of ptychography was first proposed by Hoppe in 1969 [47] to solve this phase problem for diffraction experiments. In essence, Hoppe proposed that the phase can be measured if adjacent points in the reciprocal space (reflexes) are “folded" such that they partly overlap, e.g. by introducing a narrow-slit aperture before the object. The term ptychography coined in Ref. [119] refers to this folding of the reflexes (“ptycho" is Greek for “to fold").

In 2015, decades after Hoppe’s first publication on the subject, it was shown that ptychography could be adapted for time domain phase retrieval, essentially by replacing the far-field diffraction pattern with a spectrum, and the real space object with one in the time domain, such as an ultrashort laser pulse [44, 120]. The most advanced ptychographic algorithms, ptychographic iterative engine (PIE) [45] and extended ptycho-

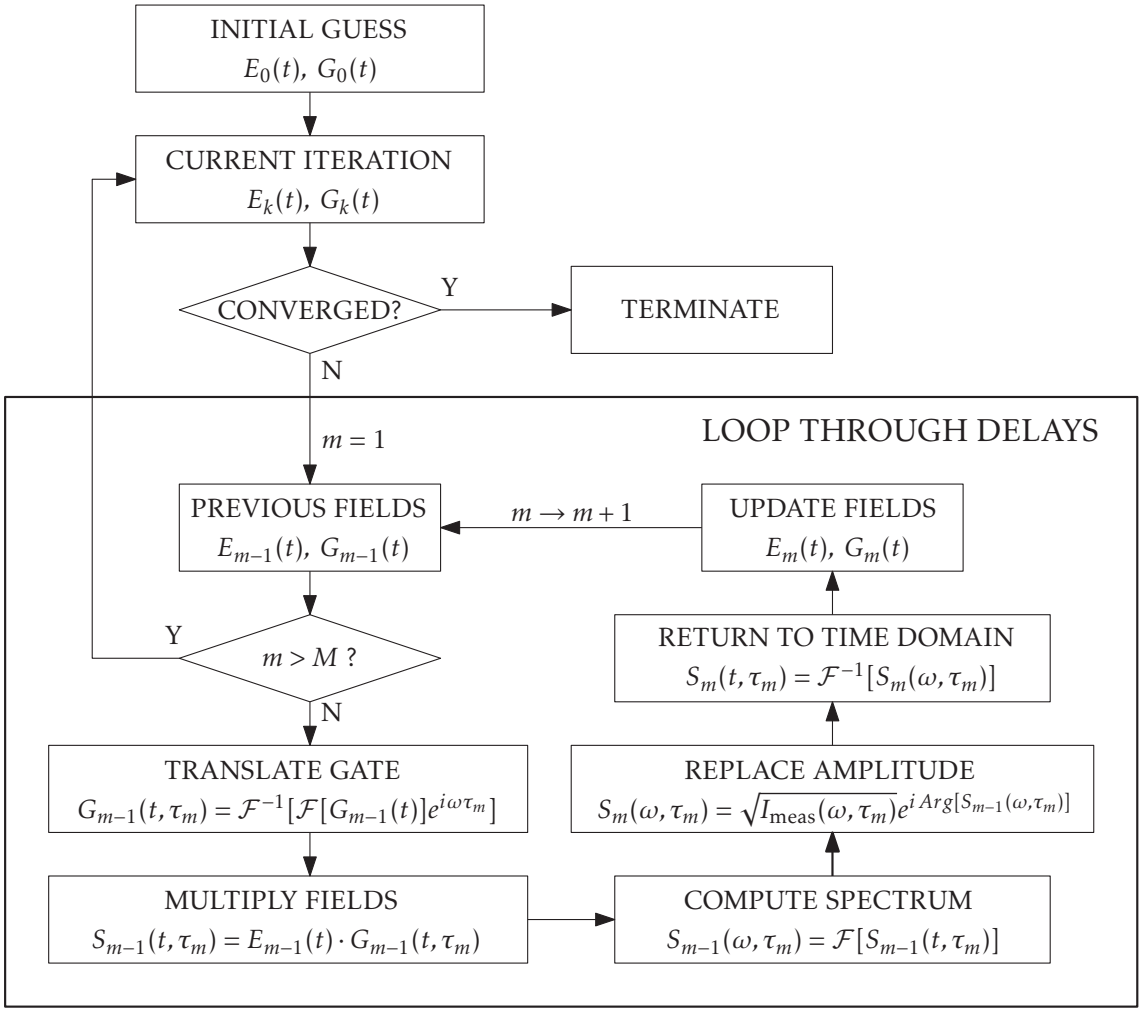

Figure III.6 – *Flowchart for a time-domain ptychography algorithm. Adapted from Refs. [46, 48].*

graphic iterative engine (ePIE) [46], can be applied with relatively small adjustments to pulse measurement schemes both old and new, ushering the way for TDP techniques. For example, SHG-FROG and blind FROG measurements can be robustly solved with TDP [41]. All TDP modalities involve a probe pulse and a gate pulse, which can also be one and the same thing. The main difference between PIE and ePIE from the perspective of TDP is, roughly speaking, that PIE can only retrieve a probe pulse if the gate pulse is known, while ePIE is capable of retrieving both. Thus, for self-referenced pulse characterization methods, ePIE is the obvious choice.

The ePIE algorithm, as applied to TDP by Witting *et al.* [48], and also later in this work, is illustrated in Fig. III.6. Starting with random complex vectors with N_t elements for the test pulse $E(t)$ and the gate pulse $G(t)$, the TDP algorithm loops through the M number of delay points τ_m, each corresponding to a spectrum in the measured data set $I_{\mathrm{meas}}(\omega,\tau_m)$,

and updates the two pulse fields at the end of each loop iteration. Unlike with a GP-based FROG, the spectrogram in TDP does not have to be sampled on a square grid, so that $M \neq N_t$ and any number of spectra at delays τ_m can be recorded, even with arbitrary step sizes. Similar flexibility of the delay coordinates is offered by our DE-based iFROG pulse retrieval. The cycle m begins with the translation of the gate pulse by the current delay τ_m. The delayed gate pulse $G_{m-1}(t, \tau_m)$ is multiplied with the previous iteration of the test pulse, $E_{m-1}(t)$, and subsequently Fourier transformed ($\mathcal{F}$) to obtain the spectrum $S_{m-1}(\omega, \tau_m)$. After replacing the amplitude of this spectrum with the measurement data, i.e. a slice of the spectrogram $I_{\text{meas}}(\omega, \tau_m)$, we return to the time domain by taking an inverse Fourier transform ($\mathcal{F}^{-1}$), arriving at the field $S_m(t, \tau_m)$. The following formulas are then applied to update the test and the gate pulses:

$$E_m(t) = E_{m-1}(t) + \beta_E \cdot \frac{G^*_{m-1}(t, \tau_m)}{\max|G_{m-1}(t, \tau_m)|^2} \cdot \Delta S \tag{III.6}$$

$$G_m(t) = G_{m-1}(t) + \beta_G \cdot \frac{E^*_{m-1}(t, \tau_m)}{\max|E_{m-1}(t, \tau_m)|^2} \cdot \Delta S\,. \tag{III.7}$$

Here $\Delta S = S_m(t, \tau_m) - S_{m-1}(t, \tau_m)$ is the difference between the multiplied fields from previous iteration, and a similar quantity after the data constraint has been applied. For time coordinates where this difference is comparatively large, the next iteration of the pulse fields experiences the largest change. Thus, ΔS serves as a measure for close a given coordinate of the current iteration of the fields is to convergence. The rate of change between iterations can be scaled with the constants β_E and β_G. After the algorithm has cycled through all the delay coordinates, the rms difference (analogous to the FROG error G in Eq. (III.5)) between the thus obtained spectrogram and the measured trace is computed. If the difference is small enough, the algorithm has converged and terminates, otherwise a new cycle through the delays begins.

As we will show in Chapter VI, the above described TDP algorithm can be readily adapted for inverting πFROG traces. Prior to this, we will now move on to an in-depth discussion on iFROG.

CHAPTER IV

Interferometric Frequency-Resolved Optical Gating

As discussed previously, the complete characterization method iFROG [11, 12, 38] is a collinear adaptation of the typically noncollinear FROG [13, 60, 83], offering many advantages over its better known predecessor. The present Chapter builds on Publications [II] and [III] describing two variants of DE-iFROG, and to some extent on Publication [V] which employed a more primitive version of iFROG, as well as Publication [IV] about πFROG. Some of the mathematical analysis and the data processing related to Publication [V] were already discussed in the Master's Thesis of the author [121], but the analysis has been considerably refined since. In fact, much of the formalism presented here is previously unpublished, while details of the experiments and related design issues are discussed more thoroughly than in the cited works of the author.

The structure goes as follows. We begin by presenting our experimentally measured iFROG traces in Section IV.1. The structure of the traces is treated analytically in Section IV.2, separately for the two variants based on either SHG or THG. We also explain how the subtraces are extracted from an iFROG trace. Discussion on how these subtraces can be employed for pulse retrieval is given in Section IV.3, while the presentation of retrieval results for both experimental and synthetic data is deferred until Chapter V. For those interested, Appendix A holds more technical information on the measurement of iFROG traces, along with features and design issues of a general iFROG apparatus.

IV.1. Experiments

A detailed illustration of our iFROG setup, suitable for both SHG-iFROG and THG-iFROG measurements, is presented in Fig. IV.1. The choice of filters and the particular BBO crystal (cut at 29.6°) for type I SHG make this apparatus optimized for a fundamental wavelength of approximately 800 nm. This is of course no coincidence, as the

carrier wavelength of our sub-10-fs test pulses provided by a passively mode-locked titanium-sapphire oscillator (*Pulse One*, Venteon) is roughly 800 nm, see an example of a typical fundamental spectrum produced in Fig. IV.2. This particular spectrum has been measured with a fiber spectrometer (AvaSpec, Avantes), which was calibrated with a deuterium-halogen calibration light source (AvaLight-DH-BAL-CAL, Avantes).

Before entering the iFROG setup, the pulse is compressed by first introducing negative group-delay dispersion (GDD) with a pair of double-chirped mirrors (DCMs) and subsequently fine-tuning the result with a pair of fused-silica prisms. The amount of glass was tuned with the help of a real-time SPIDER measurement (*FC-SPIDER*, APE Angewandte Physik & Elektronik), such that the resulting spectral phase was as flat as possible for the estimated amount of air traversed by the pulse upon reaching the nonlinear medium in the iFROG setup—the path to the SPIDER measurement was approximately 100 cm longer, and the corresponding amount of GDD was subtracted from the phase measured by SPIDER. This pulse with a relatively flat spectral phase is henceforth referred to with the adjective *unchirped*, not with *Fourier-transform limited*, simply because the phase is not absolutely flat, as will be seen from the retrieved pulses to be presented later on in Chapter V. A further reason to call the pulse unchirped is that we will also place various dispersive elements (transparent windows of fused silica or calcium fluoride) to the beam path before the iFROG apparatus, consequently introducing differing amounts of additional dispersion to the pulse, making it *chirped*. The reason for this is that the additional dispersion can be precisely estimated using the relevant Sellmeier equations, Eq. (II.22), for a given window with a measured thickness. The eventual pulse retrieval for all the test pulses will yield certain spectral phases, and by subtracting the retrieved phase of the unchirped pulse from the phases of the chirped pulses, the differences in the phases should be equal to the nominal phases calculated with the Sellmeier equations. As we will learn in Chapter V, the results help to ascertain that the iFROG measurements are indeed accurate.

The measured SHG-iFROG traces for the unchirped and three chirped pulses are shown in Figs. IV.3(a)–(d). The chirped pulses were obtained by inserting 1.1 or 6.4 mm of fused silica, or 3.0 mm of CaF_2 to the beam path, corresponding to 39, 232, or 84 fs^2 of GDD, respectively. Notice the characteristic fringe-pattern found in all standard iFROG measurements. What is also immediately visible even to the naked eye is that the higher the dispersion, the flatter the trace: the sharpest peak around $\tau = 0$ is found for the unchirped pulse, decreasing to ambient level within just a few fringes, while this decrease takes tens of fringes for the chirped pulses. Another observation can be made by looking at the spectra at the edges of the delay axis, most clearly in Fig. IV.3(a). The fairly delay-independent envelope of the fringe structure continues throughout the trace (albeit obscured by other features near $\tau = 0$) and would in fact continue until the next pair of pulses overlaps at a delay corresponding to the inverse of the repetition rate of the titanium-sapphire oscillator. This corresponds to the harmonic spectrum of the individual pulses. The interference fringes would eventually disappear, however, once the inverse spectral resolution of the spectrograph exceeds τ [49]. For our spectrograph's manufacturer given specification and the wavelength ranges employed, this would cor-

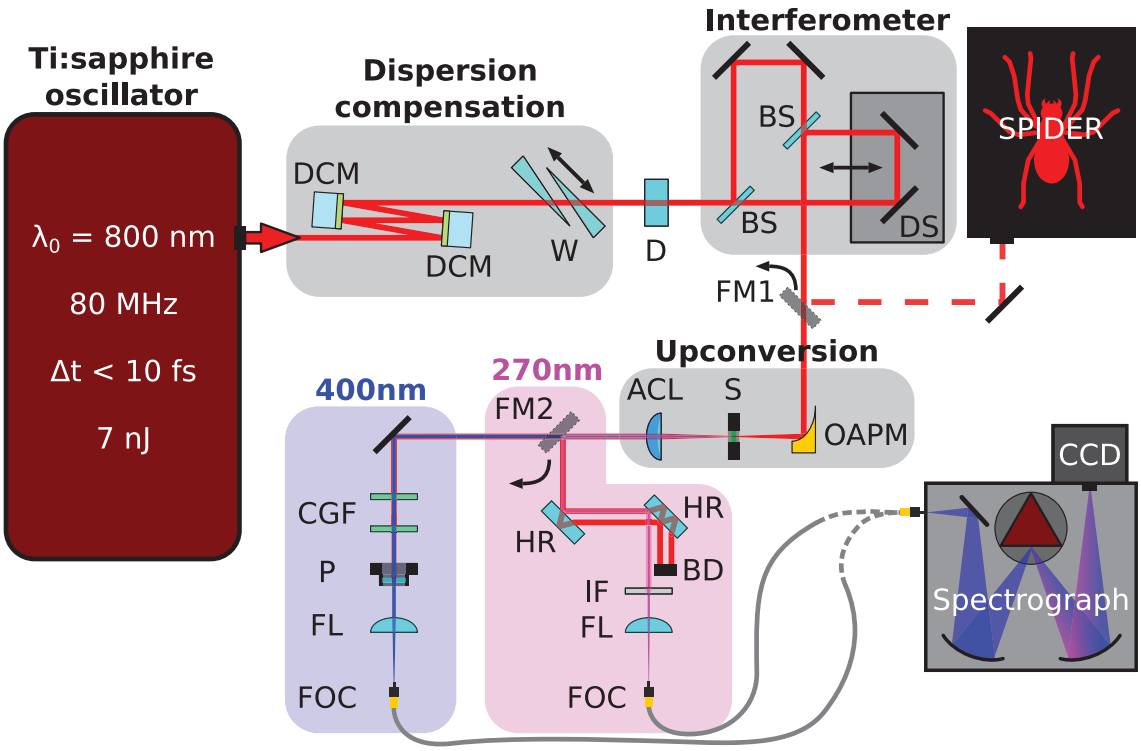

Figure IV.1 – *A detailed schematic of the iFROG measurement system employed in the experiments presented in this work. List of abbreviations, categorized according to the logical parts of the setup, follows.* ***Dispersion compensation:*** *DCM double-chirped mirror, W glass wedges.* ***Interferometer:*** *BS beamsplitter, DS delay stage.* ***Upconversion:*** *OAPM off-axis parabolic mirror, S sample (e.g. BBO), ACL aspherical collimating lens.* ***Detection for THG (270 nm):*** *HR highly-reflecting mirror, BD beam dump, IF interference filter.* ***Detection for SHG (400 nm):*** *CGF color glass filter, P polarizer.* ***Additional components:*** *D dispersive element, FM flip mirror, FL focusing lens, FOC fiber optic cable.*

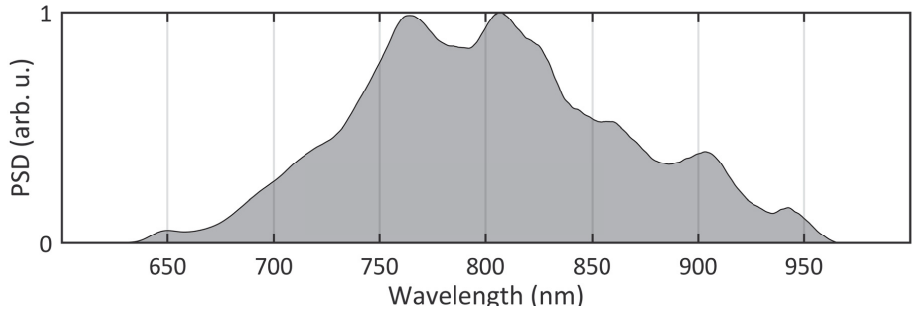

Figure IV.2 – *A typical example for the power spectral density (PSD) of pulses produced by the mode-locked titanium-sapphire oscillator and used in the iFROG experiments presented in this chapter. The spectrum was measured with a calibrated fiber spectrometer.*

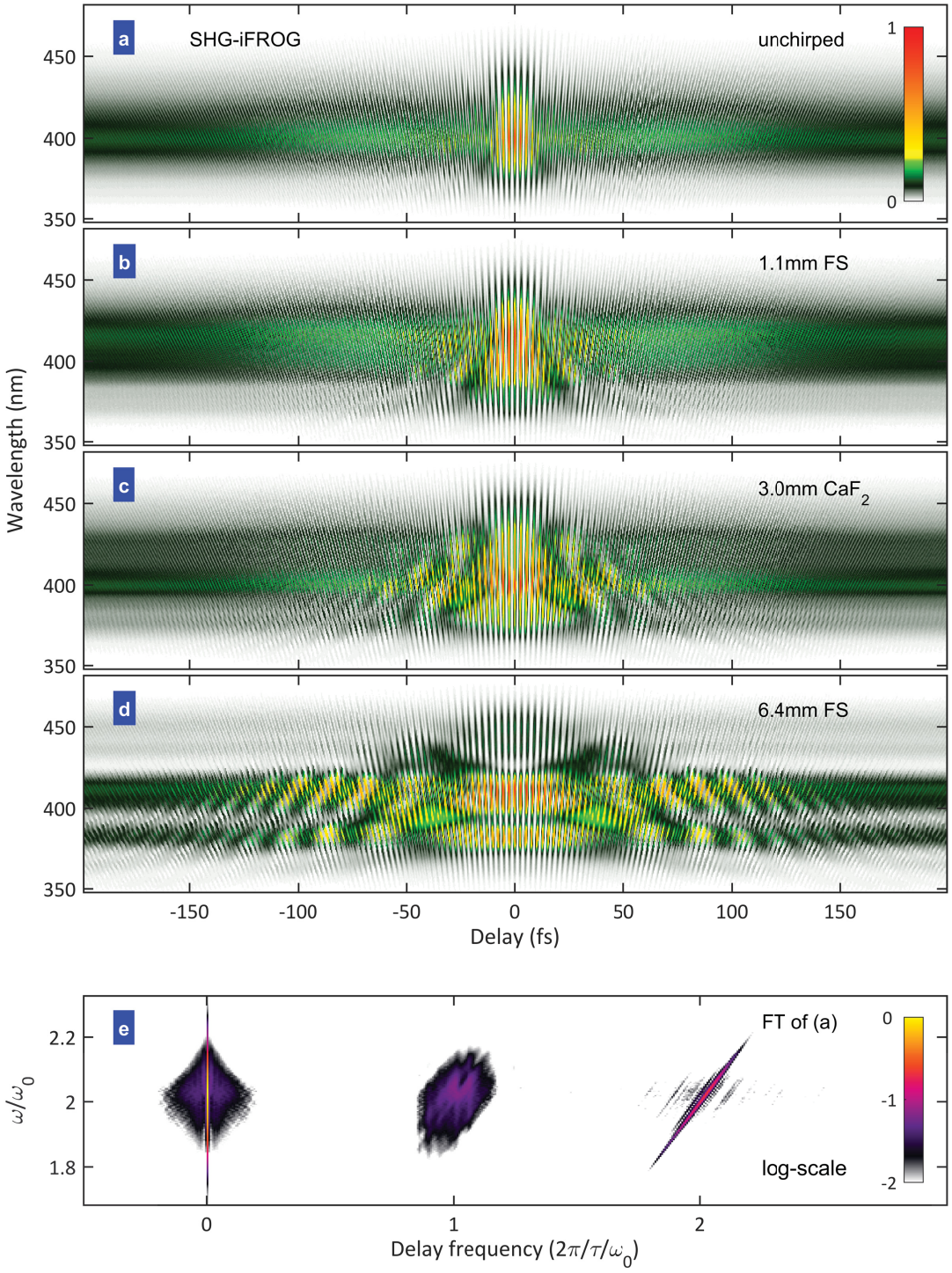

Figure IV.3 – *Experimentally measured SHG-iFROG traces for various test pulses.* ***a*** *Unchirped pulse.* ***b–d*** *Chirped pulses, obtained from the unchirped pulse after traversing (b) 1.1 mm of fused silica (FS), (c) 3.0 mm of CaF_2, or (d) 6.4 mm of FS.* ***e*** *Fourier transform of (a) along the delay axis reveals three distinct modulation bands. Adapted from Publication [III].*

respond to $\tau > 10\,\mathrm{ps}$ for the second-harmonic experiments, and $\tau > 4\,\mathrm{ps}$ for the THG ones, i.e., far beyond the temporal extent of a few hundred femtoseconds covered in our measurements.

The Fourier-transform of the unchirped trace Fig. IV.3(a) is plotted in in Fig. IV.3(e), revealing several distinct modulation bands that can be found at (angular) delay-frequencies ξ corresponding to multiples $0, \pm 1, \pm 2$ of the carrier frequency ω_0. The negative delay-frequencies $\xi < 0$ contain precisely the same information as the positive delay-frequencies $\xi > 0$, hence there are only three distinct modulation bands, not five. These will be discussed in greater detail in Section IV.2. Note that the term *delay-frequency* is used here to refer to the Fourier-domain variable ξ corresponding to delay τ in the time domain: $\mathcal{F}\{f(\tau)\} = \hat{f}(\xi)$.

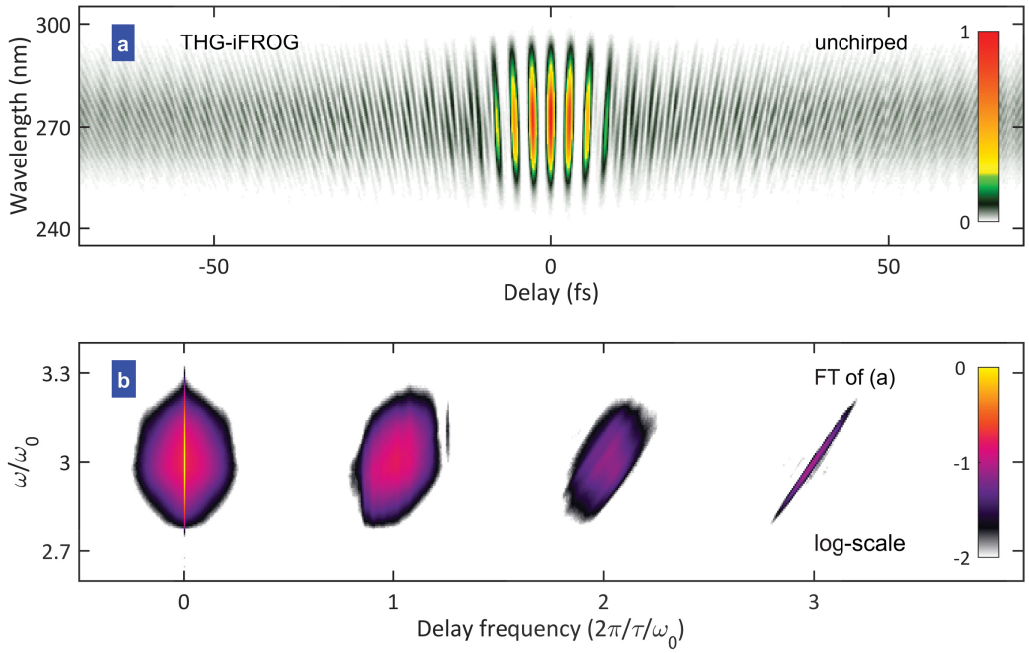

Figure IV.4 – ***a*** *Experimentally measured THG-iFROG trace for an unchirped pulse, after background removal.* ***b*** *Fourier-transform of (a). Contrary to SHG-iFROG, 4 modulation bands are found in the Fourier domain, cf. Fig. IV.3(e). Adapted from Publication [II].*

While four traces were given above for SHG-iFROG, only an unchirped pulse measurement is presented here for THG-iFROG. During the THG-iFROG measurements, a weak but noticeable fringe pattern was observed, even when the nonlinear medium was removed and no THG should occur. Measuring the background and integrating over wavelength, we took the Fourier transform of this autocorrelation signal and found it to match the fundamental spectrum of our oscillator, i.e. corresponding to a Fourier-transform spectroscopy measurement [122]. This background signal was most likely caused by a minor fraction of the fundamental light leaking onto the CCD camera, despite all filtering efforts, and the grating of the spectrograph. Fortunately, a simple subtraction from

the iFROG data was sufficient to remove this contamination. The measured trace, after the background removal, is shown in Fig. IV.4(a). As before, the trace is Fourier transformed in Fig. IV.4(b), this time revealing four distinct modulation bands at $0, \pm 1, \pm 2$, and $\pm 3\omega_0$. While test measurements with chirped pulses were also conducted, these iFROG traces were ultimately deemed to contain too high an amount of measurement noise. The increased dispersion caused the peak intensities of the test pulses to drop by a factor of $\lessapprox 10$, leading to a massive decrease of harmonic field strength due to the cubic intensity dependence, and finally to very low SNRs in the measured spectra. While pulse retrieval was still possible, the initial results indicated a high error margin in the retrieved electric field, leading to the decision to limit further measurements to the unchirped case where sufficient SNR for reliable pulse retrieval could be obtained. Nevertheless, the retrieved unchirped pulse was in excellent agreement with an accompanying SPIDER measurement, as we will learn in Section V.2.2, and as such serves well as a proof of concept for the novel THG-iFROG method.

This concludes the initial treatment of the iFROG measurements. In the next section, the structure of iFROG traces will be thoroughly discussed from an analytical point of view, paving the way for simulations and the ultimate objective of pulse retrieval from both experimental and synthetic data. The experimental data presented here will be revisited for error correction and other procedures in Section IV.3.1. These steps are made in preparation for pulse retrieval, the results of which are presented in Chapter V.

IV.2. Structure of iFROG Traces

As we have seen in the previous section, a physical iFROG measurement produces a 2D trace, or intensity data with respect to the detection wavelength λ and the time delay τ. For reasons of computational convenience, the measured trace is converted from wavelengths to (angular) frequencies ω in order to facilitate comparison to simulated data in the context of pulse retrieval. The analytical computation of an iFROG trace from an electric field in time domain necessitates the use of Fourier transforms, producing spectral data as a function of frequency, not wavelength. Neglecting constant factors and spectral dependence—e.g., due to imperfect phase matching in the harmonic generation process or varying detection efficiency—and assuming an instantaneous upconversion process, the trace of an iFROG variant based on h^{th} order harmonic generation can be described as [11]

$$I^{(h)}_{\text{iFROG}}(\omega, \tau) \equiv \left| \int_{-\infty}^{+\infty} \left[\mathcal{E}(t) + \mathcal{E}(t-\tau)\right]^h e^{-i\omega t} \, \mathrm{d}t \right|^2 . \tag{IV.1}$$

The rhs of Eq. (IV.1) is simply the power spectral density of the harmonic field generated by the two replicas of the test pulse $\mathcal{E}(t)$, as a function of the delay between the pulses. Here the complex electric field $\mathcal{E}(t)$ contains the carrier wave at the frequency ω_0 and the complex envelope $E(t)$, as defined by Eqs. (II.5) and (II.6). The eventual pulse retrieval aims to obtain exactly this, the complex electric field envelope $E(t)$ of the test pulse. In Fig. IV.5(b) we give an example of a simulated SHG-iFROG trace computed

with Eq. (IV.1) by setting $h = 2$ and using an arbitrary electric field shown in Fig. IV.5(a).

IV.2.1. On the Modulation Bands and Subtraces

Besides via Eq. (IV.1), another way of describing an iFROG trace is through the *modulation bands* which are a consequence of the interfering harmonic fields. An iFROG trace comprises $h+1$ distinct modulation bands M

$$I^{(h)}_{\mathrm{iFROG}}(\omega,\tau) = \sum_{m=0}^{h} M^{(h)}_m(\omega,\tau), \tag{IV.2}$$

where h is the order of employed nonlinearity. The index $m = 0\ldots h$ signifies the modulation frequency as multiple of the carrier frequency ω_0, such that in the Fourier domain a given band $M^{(h)}_m(\omega,\xi)$ is found at the delay-frequencies $\xi = \pm m\omega_0$. See Fig. IV.5(d) for the Fourier transform of our example trace with respect to the delay coordinate τ. The analytical source for this separation of the bands is due to a cosine factor present in each band, being of the form

$$M^{(h)}_m(\omega,\tau) \propto \cos[m\,\omega_0\tau + \phi(\omega,\tau)]\,, \tag{IV.3}$$

where $\phi(\omega,\tau)$ is an arbitrary phase function. For convenience, we also define the modulation band $\widehat{M} \in \mathbb{R}^2$ from which the cosine (and therefore the fringes) have been removed such that the previous proportionality of Eq. (IV.3) no longer holds:

$$\begin{aligned} &\cos[m\,\omega_0\tau]\,\widehat{M}^{(h)}_m(\omega,\tau) \equiv M^{(h)}_m(\omega,\tau) \\ &\widehat{M}^{(h)}_m(\omega,\tau) \not\propto \cos[m\,\omega_0\tau + \phi(\omega,\tau)]\,. \end{aligned} \tag{IV.4}$$

Because an iFROG trace is an intensity measurement, the data is real-valued. Properties of the Fourier transform then dictate that the two portions of the modulation bands at either positive or negative delay-frequencies contain exactly the same information. As these modulation bands are well separated in the Fourier domain, they can be extracted by Fourier filtering [12]. In Fig. IV.5(d) we apply a 4^{th} order super-Gaussian filter to isolate the band at $\xi = \omega_0$. Taking an inverse Fourier transform back into the time domain, followed by the modulus, results in the isolated modulation band $\widehat{M}^{(2)}_1(\omega,\tau)$ without the fringes. The result is shown in Fig. IV.5(c). By using only one of the two Fourier domain bands, the originally cosine-modulated, real-valued band of the form $\cos[m\,\omega_0\tau + \phi(\omega,\tau)]\,\widehat{M}^{(h)}_m(\omega,\tau)$ becomes complex: $\frac{1}{2}e^{i(m\,\omega_0\tau+\phi(\omega,\tau))}\widehat{M}^{(h)}_m(\omega,\tau)$. Because we will need this procedure of picking only one of the two band replicas later on, we define an operator $\mathscr{C} : \mathbb{R}^2 \to \mathbb{C}^2$ to describe the procedure:

$$\begin{aligned} \mathscr{C}\left\{M^{(h)}_m(\omega,\tau)\right\} &= \mathscr{C}\left\{\cos[\phi_1(\omega,\tau)]\,\widehat{M}^{(h)}_{m,1}(\omega,\tau) + \cos[\phi_2(\omega,\tau)]\,\widehat{M}^{(h)}_{m,2}(\omega,\tau) + \ldots\right\} \\ &= \tfrac{1}{2}e^{i\phi_1(\omega,\tau)}\widehat{M}^{(h)}_{m,1}(\omega,\tau) + \tfrac{1}{2}e^{i\phi_2(\omega,\tau)}\widehat{M}^{(h)}_{m,2}(\omega,\tau) + \ldots\,. \end{aligned} \tag{IV.5}$$

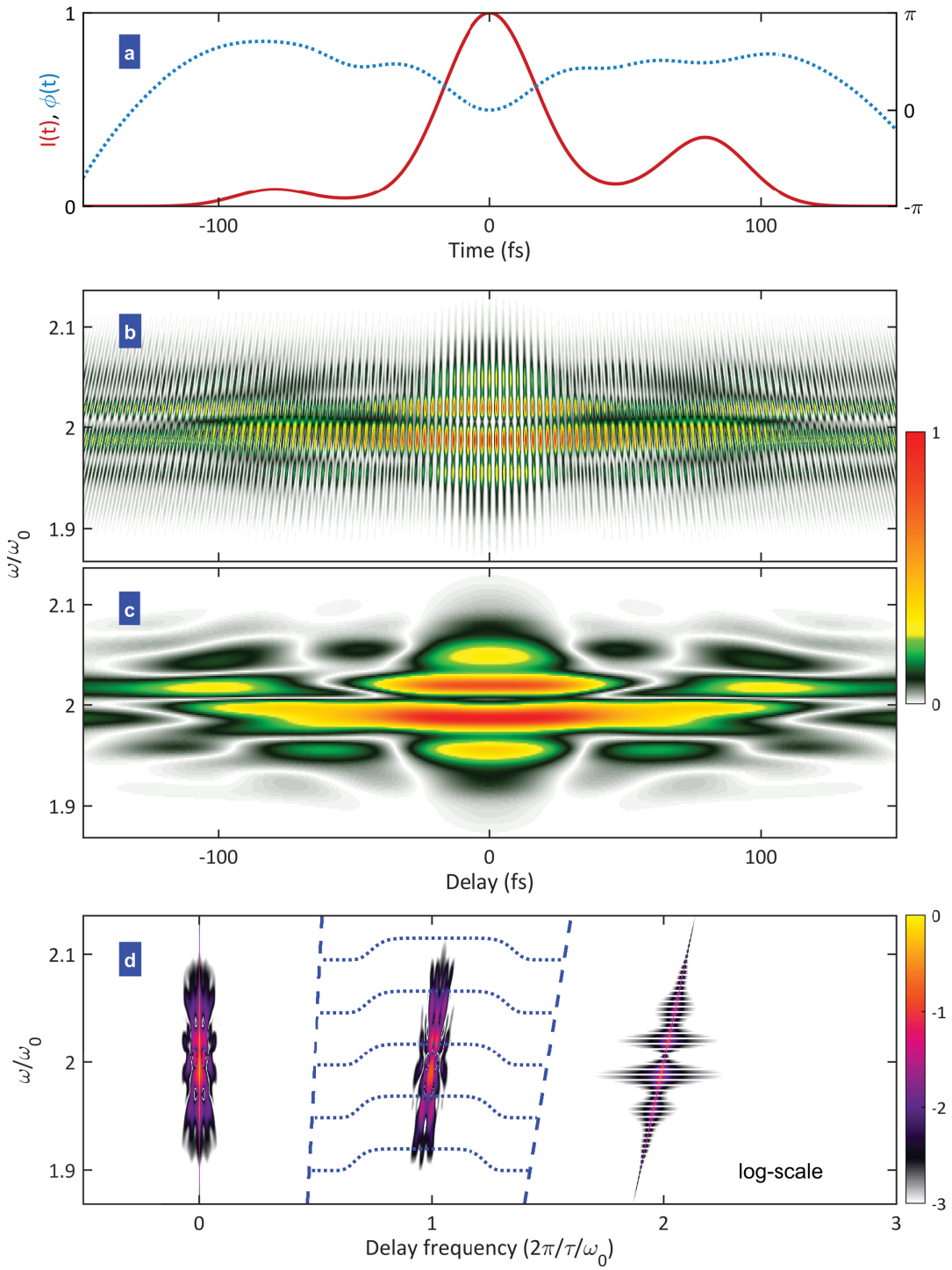

Figure IV.5 – *Employing the temporal intensity (red line) and phase (blue line) for an ultrashort pulse **a**, an SHG-iFROG trace is computed **b**. For **d**, the trace in (b) is Fourier transformed along the delay axis. **c** Using a super-Gaussian filter illustrated with the blue dotted curves in (d), a single modulation band is isolated in the Fourier domain, and transformed back into the time domain. Taking the modulus of the result gives the fundamental modulation band. Figure adapted from Publication [III].*

Here we have allowed a single modulation band $M_m^{(h)}$ to be composed of a number of terms, each containing a cosine factor. This property is needed further below for the band $M_1^{(3)}$, which contains two terms. Once the operator $\mathscr{C}$ has been applied, taking the modulus of the Fourier filtered band removes the fringes, revealing the underlying envelope of the band, i.e. $\widehat{M}_m^{(h)}(\omega,\tau)$. Unfortunately, taking the modulus destroys part of the information contained in the modulation band, namely the phase $\phi(\omega,\tau)$. Thus, the modulus is used here only for illustrative purposes, and is not part of the eventual pulse retrieval. To access the phase, the argument is taken instead of the modulus. Because the thus acquired phase is indeterminate to a factor of 2π, an unwrapping procedure is used to make the phase continuous. The fast oscillation due $m\omega_0\tau$ can be removed by shifting the isolated band to zero frequency in the Fourier domain, prior to taking the argument. This phase extraction procedure corresponds to the Takeda algorithm [123].

A more detailed analysis below shows that each of the modulation bands $m < h$ contain information about the nonlinear mixing of the two relatively delayed pulses, and as such can be individually used for pulse retrieval. On the other hand, the band $m = h$ contains only the sum of the harmonic field intensities of each pulse, and therefore no information on the phase of the test pulse remains. While this fact prohibits direct retrieval of the complex electric field of the test pulse, it turns out that the phase of the $m = h$ band can still be extracted with the above described Takeda algorithm, and used to measure the movement of the translation stage responsible for introducing the relative delay τ between the two pulse replicas [12, 38]. With this knowledge, it is possible to correct for measurement errors caused by the inevitable irregularities in the measurement points τ, and subsequently remove the fringes of the modulation bands $0 < m < h$. Unlike the above described procedure, where the modulus of a band was taken, this latter approach preserves all the information of the band. Once the fringes have been removed from the bands, what remains are the *subtraces* $S_n^{(h)}(\omega,\tau)$, where $n = 0 \ldots h-1$ corresponds roughly to m. There are a total of h number of subtraces that can be obtained, i.e., two for SHG-iFROG, three for THG-iFROG. The direct current (DC) modulation band $m = 0$ does not require the removal of a modulation, however, and the corresponding subtrace is exactly equal to the modulation band, i.e. $S_0^{(h)}(\omega,\tau) \equiv M_0^{(h)}(\omega,\tau)$. Once these subtraces are obtained from the measurement data, they can be fed into the iterative pulse retrieval algorithm which aims to reproduce the measured subtraces. Using predefined formulas, the algorithm produces synthetic subtraces for a given electric field, and, through gradual adjustments of the electric field, minimizes the difference between the measured and simulated subtraces, thus retrieving the correct pulse.

IV.2.2. Summary of the iFROG Subtraces

As the derivation of the subtraces is somewhat tedious, we only show the results here. The full derivations are presented in Appendices B and C for SHG-iFROG and THG-iFROG, respectively. These results are an integral part of the pulse retrieval algorithm for iFROG, the subject of Section IV.3.2. For the definitions of the various fields and variables, the reader is encouraged to find the information in the relevant Appendices.

Noting that the square modulus of a complex electric field $E(\omega)$ is equal to its spectral intensity, i.e. $|E(\omega)|^2 = I(\omega)$, the two SHG-iFROG subtraces are:

$$S_0^{(2)}(\Delta\omega,\tau) \equiv 2I^{(2)}(\Delta\omega) + 4I_{\mathrm{FROG}}^{(2)}(\Delta\omega,\tau) \tag{IV.6a}$$

$$S_1^{(2)}(\Delta\omega,\tau) \equiv \left|E_{\mathrm{FROG}}^{(2)}(\Delta\omega,\tau)E^{(2)*}(\Delta\omega)\right| \cdot \cos\left[\phi_{\mathrm{FROG}}^{(2)}(\omega,\tau) - \phi^{(2)}(\omega,\tau) + \tfrac{1}{2}\Delta\omega\tau\right]. \tag{IV.6b}$$

The relevant definitions are found in Appendix B.

Following the above presentation style, the three THG-iFROG subtraces are:

$$S_0^{(3)}(\Delta\omega,\tau) \equiv 2I^{(3)}(\Delta\omega) \;+\; 9I_{\mathrm{FROG}}^{(3)}(\Delta\omega,\tau) \;+\; 9I_{\mathrm{FROG}}^{(3)}(\Delta\omega,-\tau) \tag{IV.7a}$$

$$S_1^{(3)}(\Delta\omega,\tau) \equiv 3|K(\Delta\omega,\tau)| \cdot \cos\left[\phi_K(\Delta\omega,\tau) - \tfrac{1}{3}\Delta\omega\tau\right] + 9|L(\Delta\omega,\tau)| \cdot \cos\left[\phi_L(\Delta\omega,\tau) - \tfrac{2}{3}\Delta\omega\tau\right] \tag{IV.7b}$$

$$S_2^{(3)}(\Delta\omega,\tau) \equiv |K(\Delta\omega,\tau)| \cdot \cos\left[\phi_K(\Delta\omega,\tau) - \tfrac{1}{3}\Delta\omega\tau\right], \tag{IV.7c}$$

with the relevant definitions found in Appendix C.

A subtrace can be derived from experimental or synthetic numerical data via

$$S_n^{(h)}(\Delta\omega,\tau) = e^{-i\frac{n}{h}\phi_{\mathrm{mod}}(\Delta\omega,\tau)} \cdot \mathscr{C}\left\{M_{m=n}^{(h)}(\Delta\omega,\tau)\right\}, \tag{IV.8}$$

where the operator $\mathscr{C}$ as defined by Eq. (IV.5) refers to Fourier filtering of the operand $M_{m=n}^{(h)}$, such that only the positive (or the negative) delay-frequencies are considered, while the negative (positive) delay-frequencies are zeroed.

The phase ϕ_{mod} is extracted from the highest order modulation band $M_{m=h}^{(h)}$ according to Eq. (B.7), that is, by Fourier filtering the band on either positive or negative delay-frequencies and taking the argument of the complex field, followed by an unwrapping which makes the phase continuous along τ. This unwrapping is absolutely necessary, otherwise the multiplication $\frac{n}{h}\phi_{\mathrm{mod}}$ in Eq. (IV.8) produces nonsensical results. After the annealed phase has been obtained, the timing jitter τ_{jitter} of the measured tau can be estimated by taking a weighted average of the 2D phase matrix $\mathrm{Arg}\left\{\mathscr{C}\left\{M_{m=h}^{(h)}(\Delta\omega,\tau)\right\}\right\}$ with respect to the frequencies, weighted by the power spectral density. The power spectral density is given by integrating the modulation band along the delay τ. The linear phase, i.e. the ideal delay τ, must also be removed. Once obtained, the timing jitter τ_{jitter} can then be used as a correction term that essentially conforms the ideal τ to better fit the measured data:

$$\tau' = \tau + \tau_{\mathrm{jitter}}. \tag{IV.9}$$

The phase ϕ_{mod} can then be computed using the corrected τ', and the known frequencies ω, e.g. for SHG-iFROG $\phi_{\text{mod}} = (\Delta\omega + 2\omega_0)\tau'$, and subsequently employed to obtain the subtraces $S^{(h)}_{n>0}$ via Eqs. (IV.6) to (IV.8).

Once the subtraces have been extracted from the iFROG measurement as described here, and the formulas to compute their synthetic counterparts for a given electric field are established, all that is missing for a complete pulse retrieval method is an iterative retrieval algorithm. This, along with some practical issues and their solutions, is discussed in the next Chapter.

IV.2.3. Examples of iFROG Subtraces

In order to give a more tangible idea on the appearance of the iFROG subtraces, and how the characteristic features therein might change when the test pulse is altered, we present a few examples here.

The two SHG-iFROG subtraces for the test pulse in Fig. IV.5 are depicted in Fig. IV.6. In contrast to the corresponding $S^{(2)}_0$ subtrace in Fig. IV.6(a), and to the FM modulation band shown in Fig. IV.5(c), the FM subtrace $S^{(2)}_1$ in Fig. IV.6(b) also contains negative values, as indicated by the color blue. In other words, the higher-order subtraces are no longer simple intensity measurements. As we will explain below, the negative values in a subtrace can be beneficial in detecting a chirp of the test pulse.

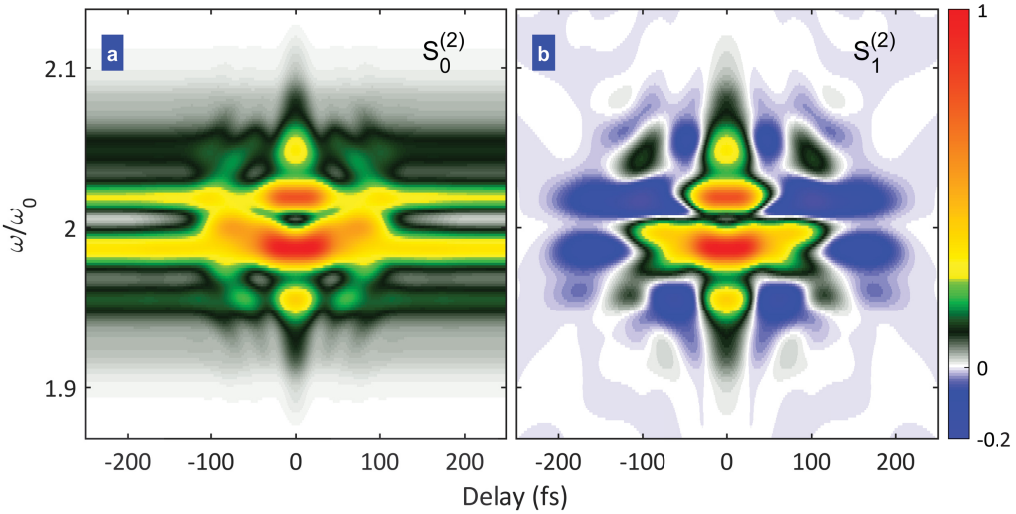

Figure IV.6 – *Simulated* ***a*** *DC ($S^{(2)}_0$) and* ***b*** *FM ($S^{(2)}_1$) subtraces for SHG-iFROG, corresponding to the test pulse in Fig. IV.5.*

For THG-iFROG, Fig. IV.7 displays a set subtraces computed for few simple test cases. These examples are discussed in Publication [II], while a similar account can be found for SHG-iFROG in Ref. [38]. The time-domain intensities and phases of the test pulses are shown on the top row, while the spectral presentation is given one row below. Going

further towards the bottom of the figure, the three bottom rows respectively depict the three subtraces, $S_0^{(3)}$, $S_1^{(3)}$, and $S_2^{(3)}$, or the DC, FM, and SHM subtraces for THG-iFROG.

The simplest pulse, in Figs. IV.7(a) and (b), is Fourier-transform limited (FTL), and has a Gaussian spectrum. The three subtraces, Figs. IV.7(i), (m), and (q), are rather similar in appearance, consisting of a single Gaussian peak, excluding the constant harmonic background found in the DC subtrace. Taking a closer look at the DC subtraces for the rest of the examples in Figs. IV.7(j)–(l), it is evident that such a background is a ubiquitous feature. Another noteworthy feature is that all of the three subtraces for the FTL pulse contain solely nonnegative values.

In Fig. IV.7(b), we have a similar pulse but this time with added group-delay dispersion. This dispersion not only causes the time-domain intensity envelope to stretch, but also changes the appearance of the FM and SHM subtraces dramatically, as there are now regions with negative values, cf. Figs. IV.7(n) and (r). Indeed, for subtraces other than the lowest order, $S_0^{(h)}$, such negative regions appear whenever the spectral phase is not completely flat. This is also true for the FM subtrace $S_1^{(2)}$ in SHG-iFROG [38]. Negative values are therefore a clear and intuitive means to identify the presence of chirp in a test pulse, even prior to any pulse retrieval. This property could possibly be exploited in dispersion tuning, for example to obtain an FTL pulse. Moreover, the negative portions are also easily identified by a retrieval algorithm based on the subtraces, making the pulse retrieval more sensitive for the spectral phase.

Because of the employed nonlinearity, THG-iFROG is ambiguous to phase jumps for multiples of $\frac{2\pi}{3}$. This is in fact an advantage over SHG-iFROG, which has an ambiguity for multiples of $\frac{\pi}{2}$, and is therefore unable to detect phase jumps of π, which commonly occur at interfaces when approaching an optically more dense medium. This property is demonstrated in the two rightmost columns of Fig. IV.7. The double pulse in Fig. IV.7(c) is otherwise identical (in time domain) to the pulse in Fig. IV.7(d), but the train of two pulses are in-phase in the former example, yet out-of-phase in the latter. This is reflected in the spectra Figs. IV.7(g) and (h), and also in all of the corresponding subtraces, where the in-phase pulse leads to a single maximum, while the out-of-phase yields two equal maxima. The difference is again easily noticed by any retrieval algorithm exploiting the subtraces.

IV.3. Pulse retrieval

Now that the analytical framework for processing iFROG traces has been established, we may move on to discuss the actual pulse retrieval. First, in Section IV.3.1, the preparation of experimental data into a form suitable for a retrieval algorithm is discussed and subsequently applied to the measured iFROG traces, presented above in Section IV.1. Next, the previously covered differential evolution algorithm is adapted for iFROG in Section IV.3.2. Once the full iFROG method has been thoroughly explained, we will demonstrate pulse retrieval with iFROG in Chapter V for the prepared experimental data, as well as for synthetic test data. A comparison to rivaling characterization tech-

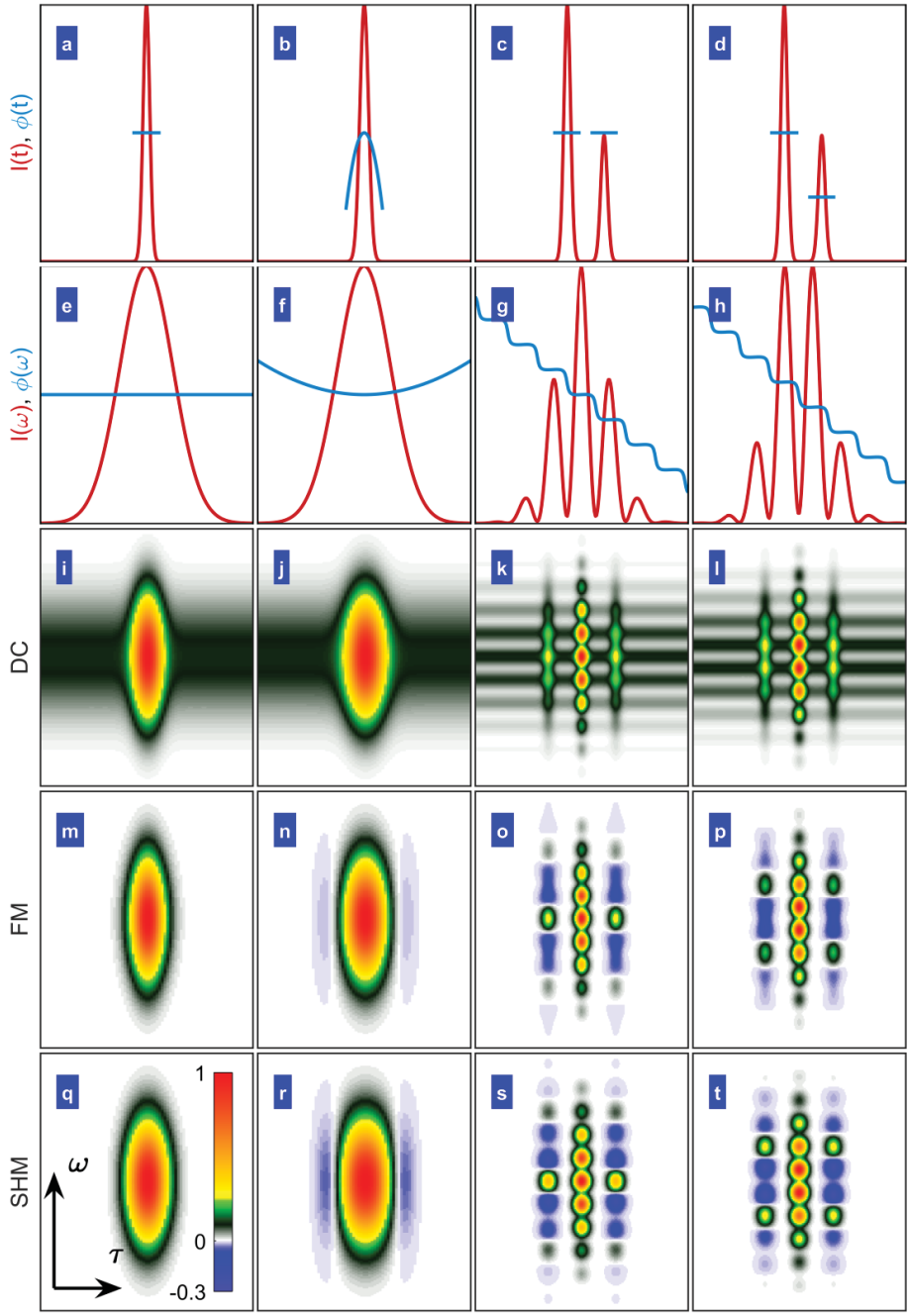

Figure IV.7 – *Simulated subtraces for THG-iFROG, each column representing a different test pulse. From left to right, these are: Fourier-transform limited pulse, linearly chirped pulse, and double pulses in-phase, and out-of-phase.* ***a–d*** *pulse intensity and phase in time domain.* ***e–h*** *pulse intensity and phase in frequency domain.* ***i–l*** *DC subtraces* $S_0^{(3)}$. ***m–p*** *FM subtraces* $S_1^{(3)}$. ***q–t*** *SHM subtraces* $S_2^{(3)}$. *Figure adapted from Publication [II].*

niques is also given.

IV.3.1. Preparations

As briefly mentioned in Section IV.2, the measured iFROG trace is converted from wavelengths to frequencies prior to any further processing for reasons of computational convenience. To ensure that the spectra $S_\omega(\omega)$ and $S_\lambda(\lambda)$ measured in frequencies or wavelengths, respectively, contain an equal amount of energy we integrate over each domain and set the two quantities equal:

$$\int_{-\infty}^{+\infty} S_\omega(\omega)\,\mathrm{d}\omega = \int_{-\infty}^{+\infty} S_\lambda(\lambda)\,\mathrm{d}\lambda\,. \tag{IV.10}$$

As $\lambda = 2\pi c/\omega$, we have $\mathrm{d}\lambda = (-2\pi c/\omega^2)\,\mathrm{d}\omega$. After a replacement of variables in Eq. (IV.10), one obtains the conversion formula [60]

$$S_\omega(\omega) = \frac{2\pi c}{\omega^2} S_\lambda\left(\tfrac{2\pi c}{\omega}\right) = \frac{\lambda^2}{2\pi c} S_\lambda(\lambda)\,, \tag{IV.11}$$

This procedure produces a set of frequency coordinates with varying spacing. Therefore, in order to accommodate the upcoming and necessary discrete Fourier transforms, the spectra have to be interpolated to equidistant frequency sampling.

Next, the delay axis is calibrated, and possible experimental flaws maybe taken into account with the steps described below. This discussion loosely follows Publications [II] and [III].

Marginals

As previously discussed, the ideal iFROG intensity $I^{(h)}_{\mathrm{iFROG}}(\omega,\tau)$ given by Eq. (B.1) neglects any spectral dependence in the generation, transmission, or detection of the harmonic spectrum to be measured. A more accurate description for the *measured* iFROG intensity, taking these effects into account by including a spectral transfer function $R(\omega)$, can also be given:

$$I^{(h)}_{\mathrm{iFROG,\,meas}}(\omega,\tau) \propto R(\omega)\, I^{(h)}_{\mathrm{iFROG}}(\omega,\tau) = R(\omega) \left| \int_{-\infty}^{+\infty} \left[\mathcal{E}(t) + \mathcal{E}(t-\tau)\right]^h e^{-i\omega t}\,\mathrm{d}t \right|^2 . \tag{IV.12}$$

For a nonconstant $R(\omega)$, the measured trace differs from the trace produced by Eq. (IV.1), the latter of which is assumed correct by the pulse retrieval algorithm described in Section IV.3.2. Unless corrected for, this difference can lead to a systematic error, and an increased uncertainty in pulse retrieval. It turns out that the function $R(\omega)$ can in fact be measured using the so-called *marginals*, and subsequently used to correct the measured trace for experimental flaws.

Two distinct marginals can be computed for a given iFROG trace, obtained via integration along either coordinate: the frequency, giving the delay marginal

$$\mathcal{M}_\tau^{(h)}(\tau) \equiv \int_{-\infty}^{+\infty} I_{\mathrm{iFROG}}^{(h)}(\omega,\tau)\,\mathrm{d}\omega\,, \tag{IV.13}$$

or the delay, giving the spectral marginal

$$\mathcal{M}_\omega^{(h)}(\omega) \equiv \int_{-\infty}^{+\infty} I_{\mathrm{iFROG}}^{(h)}(\omega,\tau)\,\mathrm{d}\tau\,. \tag{IV.14}$$

These can then be compared to independently measured interferometric autocorrelation (iAC) or harmonic spectrum, respectively, as a consistency check, similar to standard noncollinear FROG variants [60, 124, 125]. Besides these simple tests, the marginals have much more useful purposes as well. The delay marginal $\mathcal{M}_\tau^{(h)}(\tau)$ can be used the accurately pinpoint the zero point for the delay τ, e.g. by isolating the strongest fringe, fitting a polynomial on top, and finally picking the maximum of the fitting function. Finding the zero delay is extremely important for the pulse retrieval, otherwise the simulated subtraces will never fit to the poorly centered measurement data.

Rather than using the spectral margin for an entire iFROG trace as given by Eq. (IV.14), a more practical use is found for the background-free spectral marginals of the DC-modulation bands $M_0^{(h)}$. After extraction of the DC-modulation bands (Eqs. (B.6a) and (C.16a) for SHG-iFROG and THG-iFROG, respectively) through Fourier filtering, the delay-independent harmonic signals can be easily removed from the time-domain modulation bands $M_0^{(h)}(\omega,\tau)$ by subtracting the spectrum at the edges of the delay range from the entire band. For SHG-iFROG, this procedure leaves the standard SHG-FROG trace $\left|E_{\mathrm{FROG}}^{(2)}(\omega,\tau)\right|^2$, so that integration over delays yields the spectral marginal for SHG-FROG [125]

$$\mathcal{M}_\omega^{\mathrm{SHG}}(\omega) \equiv \int_{-\infty}^{+\infty} \left|E_{\mathrm{FROG}}^{(2)}(\omega,\tau)\right|^2 \mathrm{d}\tau\,. \tag{IV.15}$$

For THG-iFROG, the same procedure gives the sum $\left|E_{\mathrm{FROG}}^{(3)}(\omega,\tau)\right|^2 + \left|E_{\mathrm{FROG}}^{(3)}(\omega,-\tau)\right|^2$, which does not cause any complications here because the integration can be carried out for each term separately, yielding simply twice the THG-FROG spectral marginal

$$\mathcal{M}_\omega^{\mathrm{THG}}(\omega) \equiv \int_{-\infty}^{+\infty} \left|E_{\mathrm{FROG}}^{(3)}(\omega,\tau)\right|^2 \mathrm{d}\tau\,. \tag{IV.16}$$

The usefulness of these spectral marginals $\mathcal{M}_\omega$, derived from an iFROG trace, is based on the fact that an analytically equivalent marginal $\mathfrak{M}_\omega$ can also be computed from sep-

arately measured spectra [125]. For SHG-FROG, the spectral margin is equal to the autoconvolution of the fundamental spectrum [125],

$$\mathfrak{M}_{\omega}^{\mathrm{SHG}}(\omega - 2\omega_0) \equiv S_{\mathrm{fund}}(\omega - \omega_0) * S_{\mathrm{fund}}(\omega - \omega_0). \tag{IV.17}$$

And for THG-FROG, both the fundamental S_{fund} and the second-harmonic S_{SHG} spectra are required,

$$\mathfrak{M}_{\omega}^{\mathrm{THG}}(\omega - 3\omega_0) \equiv S_{\mathrm{fund}}(\omega - \omega_0) * S_{\mathrm{SHG}}(\omega - 2\omega_0). \tag{IV.18}$$

If there is a discrepancy between the two differently obtained marginals, this indicates that the measured iFROG trace deviates from an ideal measurement by some frequency-dependent transfer function, which we equate to transfer function $R(\omega)$ as defined in Eq. (IV.12). Using the two marginals, the transfer function can be measured

$$\mathcal{M}_{\omega}(\omega) = R(\omega)\, \mathfrak{M}_{\omega}(\omega) \quad \Rightarrow \quad R(\omega) \equiv \frac{\mathcal{M}_{\omega}(\omega)}{\mathfrak{M}_{\omega}(\omega)}. \tag{IV.19}$$

The iFROG trace can then be at least partially corrected for any such wavelength-dependent deficiencies, due to e.g. absorption, imperfect detection, or limited phase-matching bandwidth:

$$I_{\mathrm{iFROG}}^{(h)}(\omega, \tau) \approx \frac{I_{\mathrm{iFROG,\,meas}}^{(h)}(\omega, \tau)}{R(\omega)}. \tag{IV.20}$$

Zero signal is of course impossible to recover, for example when there is a zero in the phase-matching efficiency curve, cf. Fig. IV.8(c). Likewise, for wavelength ranges with very low values of the transfer function $R(\omega)$, detection noise can be greatly amplified. For this reason, the transfer function should be given a lower limit. Note that all of the above definitions are for (angular) frequencies, while the physical measurements are invariably in wavelengths. Several conversions between the two domains are therefore required in order to execute the marginal correction as defined by Eq. (IV.20).

In Fig. IV.8 we illustrate the spectral marginal-correction for a synthetic SHG-iFROG trace. The trace in Fig. IV.8(a) is obtained by spectrally weighting our example trace in Fig. IV.5(b) by a typical, sinc^2 shaped phase-matching curve, plotted as a black dotted line in Fig. IV.8(c), along with the spectral marginals of the traces. Both the corrected and uncorrected traces are later on, in Section V.1.1, subjected to pulse characterization, illustrating the beneficial effect of the procedure.

In practice, one might not always have access to the independently measured spectra, especially the SHG spectrum in the case of THG-iFROG. Fortunately, performing a marginal correction is not absolutely necessary, and was found to have only a *marginal* effect on the results of pulse retrievals performed on our experimentally measured traces. Instead, a simple background removal was often enough to prepare the measurement data for use by the retrieval algorithm. This is likely a consequence of the spectral weighting function being relatively flat and featuring no zeros of the phase-matching efficiency within the wavelength range employed, i.e. the effect is not as dramatic as with our numerical example in Fig. IV.8.

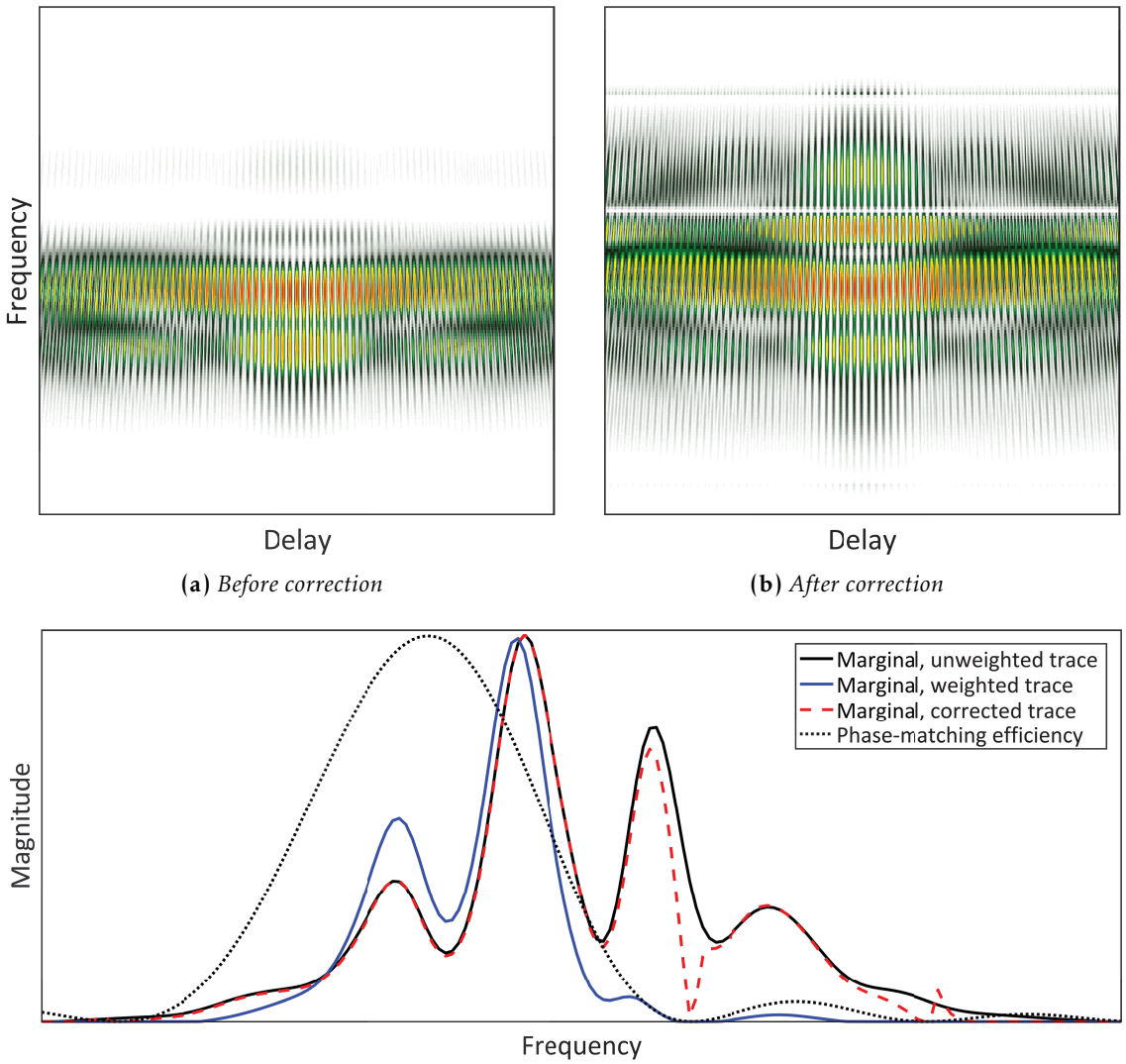

(a) *Before correction*

(b) *After correction*

(c) *Measured margins*

Figure IV.8 – *Spectral marginal-correction for a simulated iFROG trace which has been subjected to a frequency-dependent weighting function. Traces shown before (a) and after (b) the marginal correction. The procedure is based on the comparison of frequency marginals (c) measured for the weighted trace before (blue solid line) and after (red dashed line) the marginal correction. For most of the frequency range, the marginal of the corrected trace matches the marginal of the iFROG trace before the spectral weighting (black solid line) perfectly. For spectral regions where the weighted trace has negligible signal content due to a low phase-matching efficiency (black dotted line), the signal cannot be reliably recovered, causing the corrected margin to miss its target. Figure adapted from Publication [III].*

Removal of Timing Jitter

In addition to the above described marginal correction—essentially adjusting the measured trace via frequency-dependent weighting—the iFROG traces can be corrected for errors in the delay sampling, due to e.g. nonuniform movement of the translation stage, or mechanical instability of the interferometer. These imperfections can be described by the timing jitter τ_{jitter}, which, as explained in Section IV.2.2, can be measured from the phase of the highest order modulation band $M^{(h)}_{m=h}$. Once measured, the delay axis can be corrected according to Eq. (IV.9). In Fig. IV.9 we demonstrate the jitter measurement with synthetic data. A nonuniform delay sampling was simulated by iteratively constructing a delay axis where a normally distributed random number was added after each delay step, i.e. the k^{th} delay coordinate is given by

$$\tau_k = \tau_{k-1} + \Delta\tau + \delta(\sigma_{\text{jitter}}),$$

where $\Delta\tau$ is the step size, $\delta(\sigma_{\text{jitter}})$ is a normally distributed random number with a mean of zero and a standard deviation σ_{jitter}. One particular result of this procedure was chosen, the deviation of which from an equidistant delay sampling (i.e. setting $\sigma_{\text{jitter}} = 0$) is plotted in Fig. IV.9(b) with a blue line, corresponding to a timing jitter τ_{jitter}. This noisy set of delay coordinates was then used to construct an iFROG trace $I^{(h)}_{\text{jitter}}$ with a timing jitter. In Fig. IV.9(a) the difference between $I^{(h)}_{\text{jitter}}$ and the trace $I^{(h)}_{\text{ideal}}$ with noise-free delay sampling is shown. The timing jitter measured from $I^{(h)}_{\text{jitter}}$ is shown in Fig. IV.9(b), green line, matching the input jitter τ_{jitter} very well. Numerical tests indicate that an RMS timing-jitter of 2π, corresponding to an entire optical cycle, can still be recovered. In Section V.1.2 we perform two sets of pulse retrievals for the trace with jitter, $I^{(h)}_{\text{jitter}}$, one with and a second without the jitter correction described by Eq. (IV.9) to demonstrate the effect.

The timing jitter can also be measured from the experimental data sets. In Fig. IV.10(a), the timing jitter extracted from each of the four SHG-iFROG measurements presented earlier in Figs. IV.3(a)–(d), and the single THG-iFROG measurement shown in Fig. IV.4(a), are presented in a single plot for easy comparison. Curiously, the measured timing jitters are very similar for all of the five experiments, indicative of a systematic error. Most likely culprit is the piezoelectric actuator, i.e. the delay stage, which upon closer inspection revealed a small but significant positioning error, akin to hysteresis. In order to make the similarity between the measured timing jitters more obvious, we compute cross-correlations with the measurement employing 1 mm fused silica window, and the rest of the measurements, see Fig. IV.10(b). Linear trends were removed at 50 fs intervals from the curves in Fig. IV.10(a) to mitigate the influence of slow changes in the jitter (possibly due to interferometer drift), and the signal was limited to the 200 fs range shown. The cross-correlations are scaled such that the value 1 corresponds to two identical signals, −1 to anti-correlation, while ≈ 0 indicates no correlation. The high values of ≈ 1 near zero displacement prove that the timing jitter repeats similar patterns in every measurement, in other words there is definitely a systematic error in the delay τ for our iFROG measurements. While the chirped-pulse SHG-iFROG measurements, and the

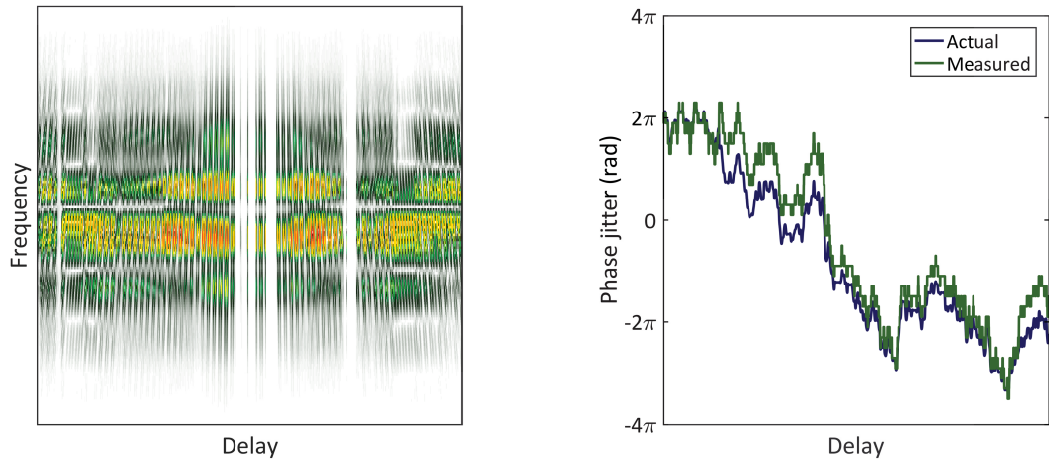

(a) *Deviation from a perfect trace* **(b)** *Jitter measurement*

Figure IV.9 – *Measurement of timing jitter from synthetic data.* ***a*** *The difference between a simulated SHG-iFROG trace with irregular delay sampling—corresponding to an imperfect movement of the translation stage in an interferometer creating the pulse replicas—and a perfectly sampled trace.* ***b*** *Inserted (blue line) and measured (green line) timing jitter, with an rms value of* ≈ 1.8 *radians. Figure adapted from Publication [III].*

unchirped measurement for THG-iFROG, all have an rms timing-jitter of 70 ± 5 attoseconds, the unchirped measurement for SHG-iFROG has a slightly larger value of $\approx$110 as. This is mostly likely due to some mechanical disturbance in the laboratory during measurement, e.g. increased airflow from an open door, vibration of the optical table, etc. The fact that iFROG can measure such small discrepancies is already remarkable, but that these measurement errors can also be compensated for (see Section V.2) is even more impressive.

Extraction of Subtraces from iFROG Measurements

Once the marginal correction has been made, and the timing jitter measured, the subtraces $S_n^{(h)}(\Delta\omega, \tau)$ may be extracted from a given iFROG trace using Eq. (IV.8), as described in Section IV.2.2. Most of the extracted subtraces for our four SHG-iFROG, and a single THG-iFROG measurement are shown together with the pulse retrieval results in Section V.2.

IV.3.2. Differential Evolution for iFROG

With the extracted subtraces at hand, we may finally move on to pulse retrieval. For this purpose, we employ differential evolution (DE), an evolutionary algorithm (EA) previously discussed in Section III.4.2 from a more general perspective. We will now describe the modifications required to adopt DE for the global optimization problem of pulse retrieval with iFROG.

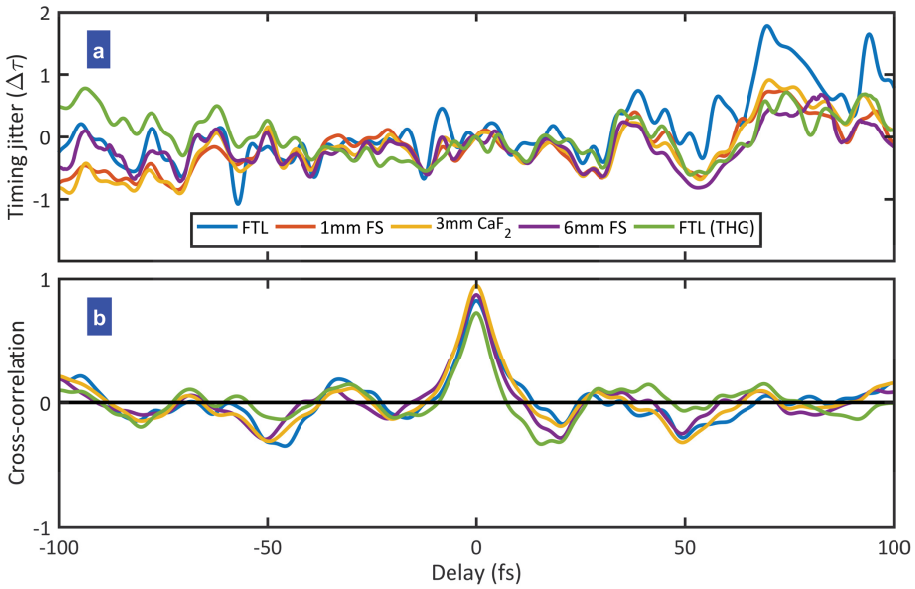

Figure IV.10 – ***a*** *Measured timing jitters, as multiples of the delay step* $\Delta\tau = 200\,\text{as}$*, for the experimental SHG-iFROG and THG-iFROG traces presented in Section IV.1.* ***b*** *Cross-correlations between the timing jitter for 1 mm fused silica sample and the rest of the curves in (a), after detrending.*

Although DE is designed for real-valued parameter vectors [39], nothing in the original formulation prevents an extension of the optimization algorithm for complex-valued problems. For our purposes of retrieving a complex-valued electric field, this is of course most convenient. As a starting point for the evolutionary optimization process, we can therefore define an initial population (the first generation) to be a set of complex vectors $\mathbf{E}$ distributed randomly across the parameter space. Each of these *individuals* then represents an electric field with a finite temporal extent. More precisely, each generation is composed of N_P number of N_E-dimensional complex vectors,

$$\mathbf{E}_s^{(k)} \in \mathbb{C}^{N_\text{E}}, \tag{IV.21}$$

where $s = 1, 2, \ldots N_\text{P}$ identifies the individual within the k^th generation, or iteration of the algorithm. A delay step $\Delta\tau$ must also be defined, such that the electric field is composed of N_E points encompassing a time span of $(N_\text{E} - 1) \cdot \Delta\tau$. Special care needs to be taken when choosing N_E and $\Delta\tau$ so that all the main features of the underlying electric field $E(t)$ can be described within the time window. Moreover, if no electric-field amplitude is expected beyond a certain time window, it is fruitless to select a larger scope and sacrifice precious computational resources in retrieving a large number of data points that will, if successfully retrieved, consist only of noise with close to zero values. The choice of a time window may seem arbitrary at first glance, but an educated guess for the approximate pulse duration can already be made from the interferometric autocorrelation signal, easily derived from an iFROG trace through integration over frequencies, as previously

described in Section IV.3.1. For example, choosing $N_\mathrm{E} = 64$ and $\Delta\tau = \frac{1}{2}T_\mathrm{cycle}$, where T_cycle is the duration of a single cycle of the carrier wave, $\mathbf{E}$ then covers 31.5 oscillations of the carrier, which is enough for describing few-cycle pulses, but does not leave an excessive number of points with no signal content. Choosing $\Delta\tau \ll T_\mathrm{cycle}$ will pose no problems for the algorithm, but retrieval of sub-cycle features of the electric-field envelope is of questionable physical significance, considering that the slowly-varying envelope approximation is implicitly employed. One should also bear in mind that the higher the value for N_E, the higher the computational effort, and (in most cases) the slower the algorithm will converge.

An alternative representation for the electric field $\mathbf{E}$ would be to use twice as many real numbers instead of complex ones, and dedicate half of these to the amplitude, while the remaining half would describe the phase. This, however, brings about an additional complication, as the amplitudes must be confined to nonnegative real numbers, simply because a negative amplitude is physically meaningless. Such a problem is conveniently avoided via the use of complex numbers, because in this case the amplitude is given trivially by the norm $|\mathbf{E}|$, which is by definition nonnegative.

To evaluate the fitness Ψ of an individual $\mathbf{E}_s^{(k)}$, we must define a criterion on how well the iFROG trace produced by the simulated electric field represents the measurement data. This is where the subtraces come into the picture. First, using a given individual $\mathbf{E}_s^{(k)}$, a selection of subtraces $S_n^{(\mathrm{sim})}(\Delta\omega, \tau, \mathbf{E}_s^{(k)})$ are computed via Eqs. (IV.6a), (IV.6b) and (IV.7a) to (IV.7c), for SHG-iFROG or THG-iFROG, respectively. These analytically computed subtraces are then compared to the corresponding subtraces $S_n^{(\mathrm{meas})}(\Delta\omega, \tau)$—extracted from the measured iFROG trace via Eq. (IV.8)—by computing the RMS differences between each pair of the 2D datasets. For this purpose we define the FROG error G_n for a single subtrace S_n,

$$G_n(\mathbf{E}) \equiv \frac{1}{\sqrt{N_\omega N_\tau}} \sqrt{\sum_{i=1}^{N_\omega} \sum_{j=1}^{N_\tau} \left[S_n^{(\mathrm{meas})}(\Delta\omega_i, \tau_j) - \mu S_n^{(\mathrm{sim})}(\Delta\omega_i, \tau_j, \mathbf{E}) \right]^2}. \tag{IV.22}$$

This is otherwise identical in form to the classical FROG error as defined in Ref. [60], but here the trace is not required to be square, i.e. the number of frequency and delay coordinates are not connected, $N_\omega \neq N_\tau$. Any combination of the available subtraces S_n can be selected to serve as a component for the iFROG *cost function* Ψ (fitness), which is defined simply as a weighted sum of individual subtrace FROG errors, with the weights w_n,

$$\Psi(\mathbf{E}) \equiv \sum_n w_n G_n(\mathbf{E}). \tag{IV.23}$$

That is, one or two subtraces can be chosen for SHG-iFROG, while up to three subtraces can be used with THG-iFROG. Now that the fitness $\Psi(\mathbf{E}_s^{(k)})$ of a given individual $\mathbf{E}_s^{(k)}$ can be measured, the rest of the DE algorithm functions without alterations exactly as described in Section III.4.2, using the steps of mutation, crossover, and selection to refine the population of electric fields towards the optimal solution, i.e. the test pulse that

created the measured iFROG trace. Thus, we have essentially defined all the necessary changes to make DE suitable for pulse retrieval with iFROG.

Some elaboration should nevertheless be made. There are a number of control parameters that must be chosen for our implementation of DE for iFROG. These are summarized in Table IV.1, along with a range of values that were found to be suitable during testing of the pulse retrieval algorithm, using the examples given in Ref. [40] as a starting point. The functions of each DE specific parameter are explained in Section III.4.2. The scaling factor F is chosen randomly from the interval $(0,1]$ for each mutation step. Some references [126–128] suggest to use $F = (0.4,1]$, and in our case limiting the interval from which F is selected to these values, instead of what is quoted in Table IV.1, was found to work as well.

Table IV.1 – *Control parameters for DE employed in the iFROG implementation*

Description	Symbol	Range of values
	Standard DE parameters	
Crossover probability	η_{CR}	0.7
Scaling factor	F	$(0,1]$
Population size	N_{P}	$[50,100]$
	iFROG specific	
Electric field length	N_{E}	$2^a, a = \{5,6,7,8\}$; i.e. $N_{\mathrm{E}} \in [32,256]$
Delay step	$\Delta\tau$	$[0.5,2] \cdot T_{\mathrm{cycle}}$

CHAPTER V

iFROG in Action

All the necessary parts to perform pulse characterization for iFROG traces, both experimental and synthetic in origin, are now in place. We have shown in Section IV.1 and Appendix A how experimental measurements of iFROG are conducted in practice, and presented a set of experimental traces for both SHG and THG based variants of iFROG. Mathematical formalism for an analytical description of iFROG traces and the newly introduced subtraces was given in Section IV.2. Finally, intrinsic error correction mechanisms and the retrieval algorithm based on differential evolution were discussed in Section IV.3.

In Section V.2 below, we perform a series of pulse retrievals for all the already revealed experimental iFROG traces, as well as one new test case to evaluate the performance of the method for very low signal-to-noise ratio (SNR) measurement conditions. Before moving on to experiments, we conduct a battery of numerical tests in Section V.1 to evaluate the accuracy, error correction capability, and resilience to measurement noise for the DE-iFROG method. Finally, in Section V.3, we end the treatment of iFROG with a short discussion on the presented results and our DE-based implementation of this promising pulse characterization method.

V.1. Simulations

The simulations here are based on the SHG variant of iFROG using synthetic traces, some of which were already introduced above. The results below have been reported in Publication [III], and we will closely follow said reference in our presentation. The test cases shown are based on a single, arbitrarily chosen pulse, with a relatively complicated temporal phase, and a two satellite structures on either side of the main intensity lobe. The test pulse, along with the corresponding SHG-iFROG trace and its Fourier transform

was illustrated above in Fig. IV.5, while the subtraces are shown in Fig. IV.6. During our investigation, a myriad of iFROG traces generated with differing test pulses (trains of pulses, pulses with different orders of spectral dispersion, and so on) were also fed to the retrieval algorithm, with the pulses successfully reconstructed. Because no significant difference in algorithm performance was observed, a single pulse was deemed adequate for the more rigorous numerical trials. For each test case, a set of 10 retrieval runs was conducted. The resulting statistics are subsequently used to judge the success of the retrievals. In the various figures below, depicting the ensemble of retrieved pulses in time domain, we plot a shaded area around the statistical mean of the intensity and phase, extending one standard deviation below the mean, and one above. Thus, the thicker the curve for intensity or phase is at any given time coordinate t, the more uncertain the retrieved value $I(t)$ or $\phi(t)$ is. In some cases the standard deviations were so small that the mean had to be plotted as well, otherwise the lines would not have been visible.

V.1.1. Spectral Marginal Correction

As discussed above in Section IV.3.1, an iFROG trace that has been spectrally weighted with the function $R(\omega)$ can lead to a systematic error and an increased uncertainty in retrieved pulses. Here we demonstrate this adverse effect by performing a set of retrievals for the iFROG trace shown in Fig. IV.8(a), e.g., the test pulse trace after weighting with a phase-matching efficiency curve as depicted in Fig. IV.8(c). Both the $S_0^{(2)}$ (DC) and $S_1^{(2)}$ (FM) subtraces are employed, i.e. their individual FROG errors as described by Eq. (IV.22) are included in the cost function with equal weights Eq. (IV.23). The statistics for these retrievals are summarized in Fig. V.1(a). Although the main features of the test pulse are adequately reproduced, there is clearly some ambiguity in the retrievals. This uncertainty manifests in the relatively large standard deviations for both the retrieved intensities and the phases, as indicated by the broadened curves.

Next, the retrievals are repeated for the iFROG trace in Fig. IV.8(b), i.e. the same trace as above, but after the marginal correction (as depicted in Fig. IV.8) has been made. This time, the statistics shown in Fig. V.1(b) reveal a significantly improved outcome for the retrieval. The test pulse is accurately reconstructed in each and every retrieval run, as can be seen from the thin plotted lines. This numerical test for the marginal correction not only indicates that the correction procedure works very well, but also that the DE algorithm can readily handle imperfect measurement data, and still give highly accurate and consistent results, time after time.

V.1.2. Timing Jitter

Repeating what was done above for the marginal correction, the retrievals for the timing-jitter test case yield a comparatively similar outcome. Taking our trusted SHG-iFROG trace and inflicting it with a timing jitter (see Fig. IV.9), we obtain the retrieval statistics shown in Fig. V.2(a). Both the $S_0^{(2)}$ (DC) and $S_1^{(2)}$ (FM) subtraces were employed, with equal weights. Again, there is some uncertainty in the reconstructed intensity and

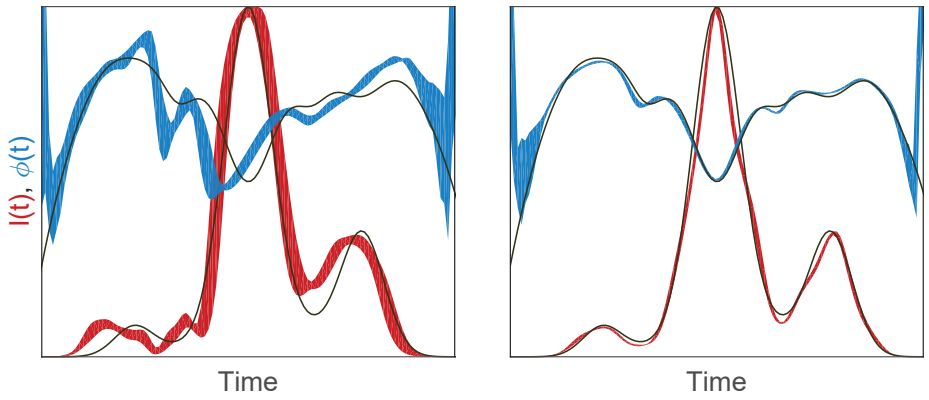

(a) *Before correction* **(b)** *After correction*

Figure V.1 – *Pulse retrieval for an iFROG trace, for which a spectral weighting function was used. Statistics of 10 retrievals shown for two cases: before (a) and after (b) a marginal correction was applied. Standard deviation of the reconstructed temporal intensities are plotted in red, and phases in blue, while the test pulse intensity and phase are plotted as black solid lines. The corresponding traces are shown in Figs. IV.8(a) and IV.8(b), respectively. Figure adapted from Publication [III].*

phase, as evinced by the broadened curves. Interestingly, a narrower main peak of the intensity envelope is seen to be systematically retrieved. This is most likely due to an unfortunate slip of the delay close to the intensity peak at zero delay. Correcting for the measured timing jitter (Fig. V.2(b)) removes this systematic error entirely, allowing DE to once again produce very accurate and precise results. This is an encouraging result, because it somewhat relaxes the stringent requirement for an accurate delay sampling, which, in the absence of such a correction procedure, would have to be made with attosecond precision to ensure reliable pulse measurement. These simulations indicate that an RMS timing-jitter of 2π, corresponding to an entire optical cycle, can still be adequately rectified. For our experimental conditions, this would correspond to a very high timing-jitter of 2800 as rms. As commercial piezoelectric actuators can offer positioning precision in the few-nanometer range, corresponding to a time delay of <100 as, the timing jitter correction capability of iFROG should be more than adequate in mending most experimental traces.

V.1.3. Noise

Another source of error is the ubiquitous and unavoidable noise, manifesting in both the measurement process, and in the optical field itself. Considering detection noise, there are a myriad of contributing factors in the measurement of iFROG spectra via a charge-coupled device (CCD). To name a few, readout noise arises in the electronic circuitry between photoreceptors and the analog-to-digital conversion (ADC), including thermal noise, or dark current, due thermally excited carriers within the CCD device, and $1/f$ noise [129]. Quantization noise occurs when the accumulated voltage is digitized. For the noise in the optical field, a fundamental lower limit is given by quantum noise (shot

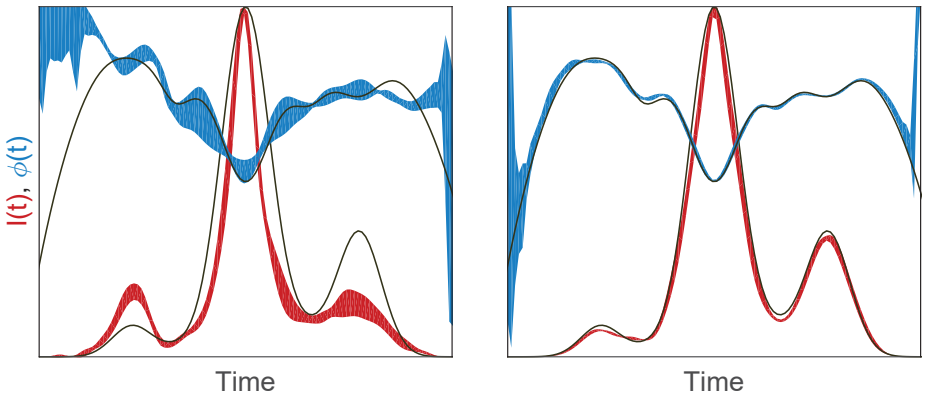

(a) *No compensation* **(b)** *Jitter compensation*

Figure V.2 – *Pulse retrieval using a simulated iFROG trace corrupted with a severe timing jitter. Retrieval results before (a) and after (b) compensating for the measured timing jitter, cf. Fig. IV.9(b). Construction of the corrupted iFROG trace and the jitter measurement is described in detail in Section IV.3.1. Figure adapted from Publication [III].*

noise) associated with the particle nature of light [130]. As a side note, this limit can actually be exceeded with the so-called squeezed states of light [131], but this is hardly relevant for our purposes. Yet another noise contribution comes from the laser itself, with intensity noise (fluctuation in the output power), phase noise, and even coupling of the two, affecting the emitted pulse train [132]. All these noise sources play a role, but their influence can be somewhat mitigated by the averaging occurring in most iFROG measurements. For a titanium-sapphire oscillator with tens-of-megahertz repetition rate and a CCD camera with a minimum exposure time of a millisecond, tens of thousands of pulses are recorded for each spectrum in an iFROG trace. On the other hand, a single pulse may in principle be used for a spectral measurement if a pulse amplifier with a kilohertz repetition rate is used. These fields are typically so strong that the generated harmonics simply dwarf any noise in the detection, but nothing guarantees that the amplified pulses are identical. For measurement of weaker fields, exposure time can be adjusted to allow sufficient statistics to form such that the background noise from a CCD can be reliably identified and accounted for. Regardless of efforts made, some amount of noise will always be present in an iFROG measurement, sometimes to an extent where pulse retrieval becomes difficult or even impossible. In order to asses the noise resilience of iFROG, extensive numerical trials were carried out.

For reasons of simplicity, we modeled the noise numerically by adding normally distributed noise to our synthetic SHG-iFROG trace, and varied the standard deviation in order to produce a set of traces with differing signal-to-noise ratios (SNR). Technically, a more accurate noise model could be made using a Poisson distribution, but for a large mean number of photons arriving to our simulated detector the normal distribution is approximately equal to the Poisson distribution and will thus suffice for our purposes. Two noisy datasets were generated, with standard deviations corresponding to 5 % and

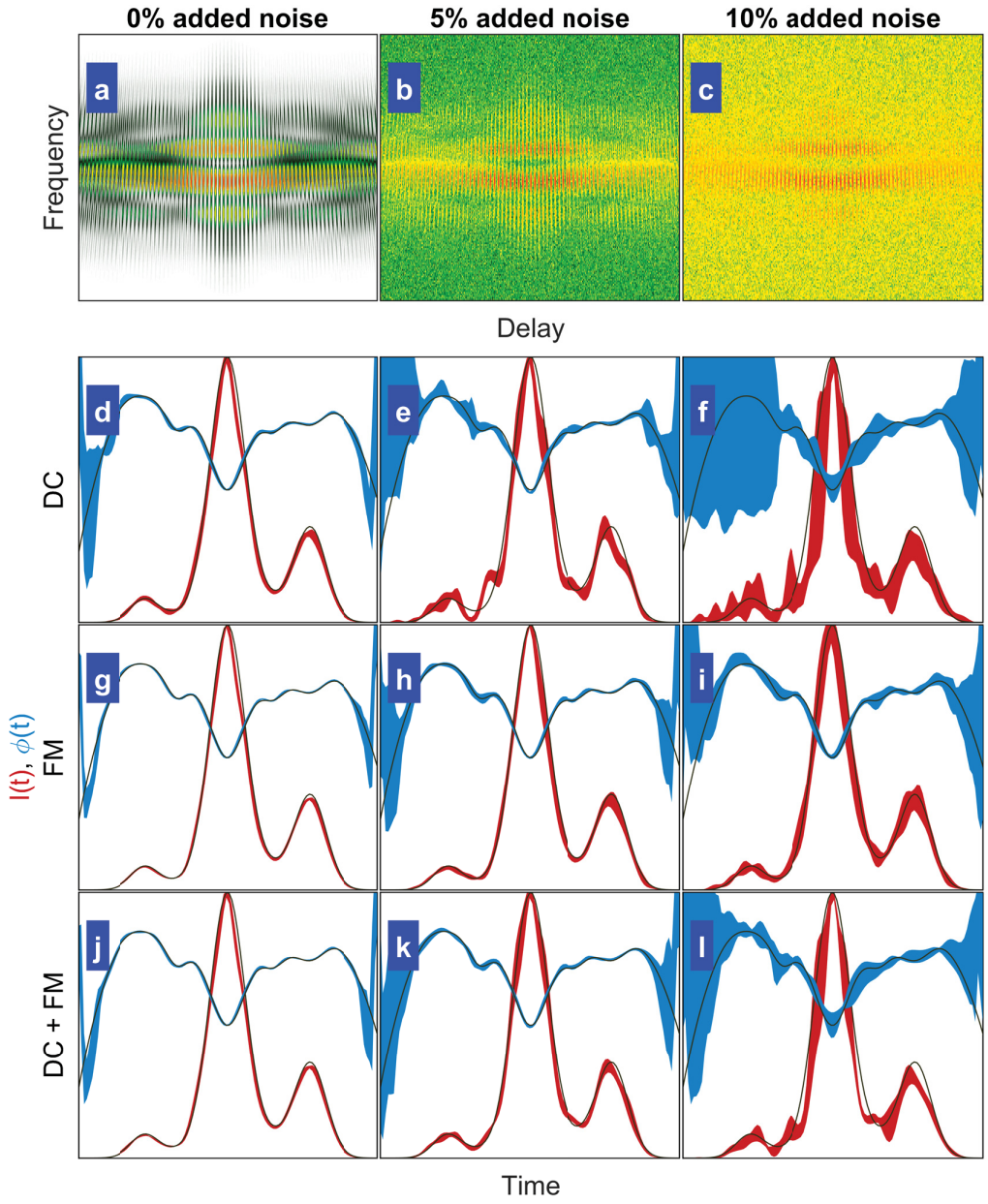

Figure V.3 – *The effect of additive noise on DE pulse retrieval is tested by* $3 \cdot 3$ *sets of ten retrieval runs, using the three possible combinations of the two available subtraces (DC and FM) for each of the three SHG-iFROG traces* ***a–c****, requiring a total of 90 DE retrievals. Each column illustrates the retrievals for the trace on the top. The noise is increased towards right in steps of 5 %, starting with no noise in the leftmost column. Second to fourth row: retrieval statistics for intensity (red) and phase (blue) using* ***d–f*** *only DC,* ***g–i*** *only FM, or* ***j–l*** *both DC and FM subtraces. The test pulse phase and intensity are plotted in black. Reproduced from Publication [III], with the permission of AIP Publishing.*

10 % of the intensity maximum, shown respectively in Fig. V.3(b) and (c), along with the noise-free trace in Fig. V.3(a). Prior to pulse retrieval, no effort was made to mitigate the noise present in the traces. As above, we made 10 retrieval runs for each test case, but this time we used all of the three possible combinations for the two available subtraces, $S_0^{(2)}$ (DC) and $S_1^{(2)}$ (FM), in order to test if the choice of employed subtraces makes a difference for the results.

Taking a look at the leftmost column, retrievals with all three of the subtrace combinations reproduce the test pulse well for the noise-free trace in Fig. V.3(a). Using only the FM subtrace (Fig. V.3(d)) seems to yield slightly more reliable results than the DC subtrace (Fig. V.3(g)), while the combination of the two (Fig. V.3(j)) is on equal footing with the FM retrieval. Introduction of 5 % noise to the trace (Fig. V.3(b)) increases the standard deviations of all the retrievals, but while the FM (Fig. V.3(h)) and DC + FM (Fig. V.3(k)) reconstructions are still very accurate, employing only the DC subtrace (Fig. V.3(e)) introduces some intensity fluctuations, especially for the weaker satellite structure. Increasing the noise to a fairly large 10 %, we see the same trend continue. The DC case (Fig. V.3(f)) gives only adequate results, losing the phase of the weaker satellite almost completely, while the intensity envelope suffers from increasing fluctuations. The FM subtrace, on the contrary, still recreates the test pulse very accurately, and even if the standard deviations have increased slightly, they are still much lower than for the DC case. Unsurprisingly, perhaps, the DC + FM reconstruction produces a mixture of the two above examples employing only a single subtrace: the reconstruction is fairly accurate, and the difference between retrieval runs is not very large, but the fluctuations seen in the DC results are also present here, albeit much more constrained.

These results indicate that using higher-order subtraces $S_{n>0}^{(h)}$ for pulse retrieval, instead of just the DC subtrace $S_0^{(h)}$, improves the reliability of pulse reconstruction significantly. A possible explanation for this behavior is that because the higher-order subtraces are much more detailed than their DC counterpart (cf. Fig. IV.6), the features that DE tries to recreate can still be recognizable in the FM subtrace when they are already obscured by noise in the DC subtrace.

Comparison to Generalized Projections As previously discussed in Section IV.3.1, generalized projections (GP) can also be readily employed for pulse retrieval with SHG-iFROG (but not for THG-iFROG) traces, by first extracting the SHG-FROG trace. In order to compare the two algorithms, DE and GP, we again used the traces in Fig. V.3(a)–(c), corrupted with varying degrees of additive noise, and performed GP retrievals in sets of ten for the extracted SHG-FROG traces. This test scenario is especially intriguing, as GP is known to struggle with noise-ridden data [116]. We chose to use a freely-available implementation of the GP [133], maintained by one of the fathers of FROG, Rick Trebino, and his group at Georgia Institute of Technology.

The extracted SHG-FROG traces depicted in Figs. V.4(a)–(c) clearly show that the additive noise prevails even in the DC modulation band $M_0^{(2)}$, from which these SHG-FROG traces are extracted. The respective GP retrieval statistics are illustrated in Figs. V.4(d)–

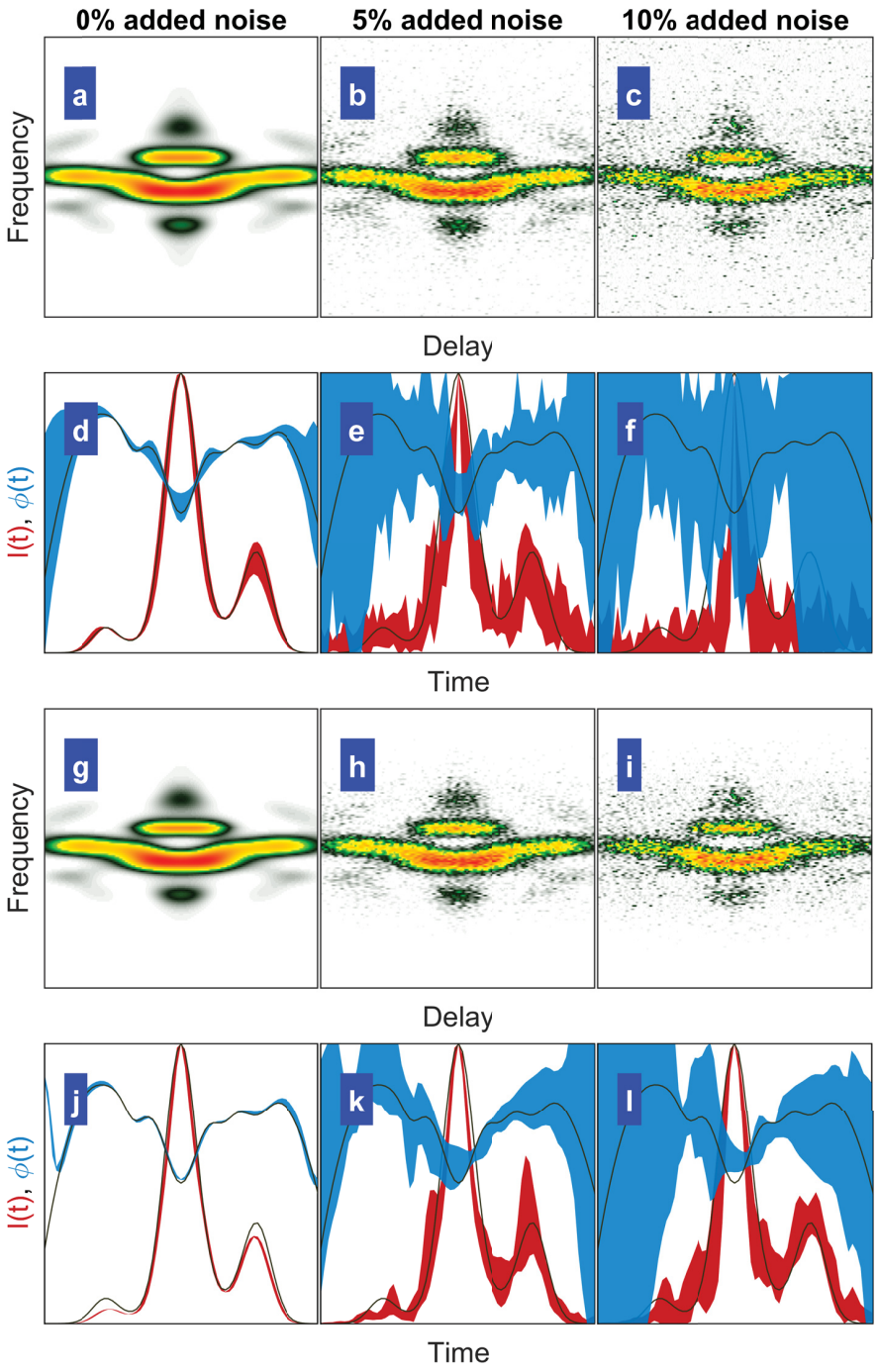

Figure V.4 – *Generalized projections based pulse retrieval with SHG-FROG traces extracted from simulated SHG-iFROG traces with varying degrees of additive noise.* ***a–c*** *Extracted SHG-FROG traces.* ***d–f*** *Standard deviations for retrieved pulse intensities (red) and phases (blue) in time domain for the traces (a)–(c).* ***g–i*** *Same as (a)–(c), but with manual isolation of the harmonic signal from the surrounding noise floor.* ***j–l*** *Retrieval results for the isolated traces (g)–(i). Reproduced from Publication [III], with the permission of AIP Publishing.*

(f). The noise-free reconstruction in Fig. V.4(d) proves fairly accurate, but a comparison to the DE results in Figs. V.3(d), (g), and (j) leaves DE as a clear winner with better accuracy and much lower standard deviations for any given subtrace selection. While the increase of noise did not severely affect the outcomes of DE retrievals, the situation is much worse for GP. The uncertainty in retrieved pulse envelopes for 5% noise, in Fig. V.4(e), is already quite large and by far exceeds the uncertainty in the corresponding DE reconstructions, even for the higher noise content of 10% and the worst-performing subtrace selection of using only the DC subtrace, cf. Fig. V.3(f). Increasing the noise to 10% makes successful pulse retrieval a hopeless task for GP, see Fig. V.4(f).

One major problem for the GP is that the measurement is supposed to be background-free, but the normally distributed additive noise is found in every region of the trace, cf. Fig. V.4(c). One way to mitigate this problem is to manually isolate a region of the SHG-FROG trace where the harmonic signal is thought to reside, and set every outlying value to zero. This isolation step is also routinely made for standard SHG-FROG measurements, and is a built-in feature for the Georgia Tech implementation of GP. Isolating the FROG signal best as we could gives the SHG-FROG traces in Figs. V.4(g)–(i), while the respective GP retrieval results are shown in Figs. V.4(j)–(l). The improvement is obvious for all three of the test cases, as the standard deviations are considerably smaller than above in Figs. V.4(d)–(f), where no zeroing of data was carried out. Considering the standard deviations, the noise-free retrieval is comparable to the DE test case using only the DC subtrace (Fig. V.3(d)). While the GP retrievals for 5% and 10% noise cases have improved, there is still a severe uncertainty in the results, especially for the phase, see Fig. V.4(l). Furthermore, GP is still nowhere near the accuracy and reliability of DE, especially when the FM subtrace is employed, cf. Fig. V.3(i).

Even though the standard deviations are quite low in the noise-free case (Fig. V.4(j)), curiously, the GP retrieval consistently fails to reconstruct the correct intensities for the two satellite structures. This is an indication that although the isolation of the SHG-FROG signal can improve the consistency of the retrieval results, the arbitrary selection of the preserved region can lead to a rejection of weak but physically significant features that are simply buried in noise. As such decisions are not necessary in our DE implementation, this problem of accidentally rejecting important data is avoided altogether.

To summarize the results of pulse retrieval with simulated noise in the iFROG traces, the introduced method, DE-iFROG, proved itself highly robust against noise, and, with the help of higher-order subtraces, was relatively unaffected even by a high level of noise. The competing method, generalized projections, on the other hand was severely hindered, producing unreliable results even for the lower of the two tested noise levels, and even when the measurement data was manually improved.

V.2. Experiments

Using the subtraces extracted from the experimentally measured iFROG traces, we will now perform a set of pulse retrievals using DE. We start with SHG-iFROG, and the unchirped pulse measurement, followed by the chirped pulse measurements. In addition,

two new SHG-iFROG traces are introduced. The experimental conditions are otherwise identical for the two traces, but one of the traces is much noisier than the other. Following the numerical example above, we conduct pulse retrievals using both DE and GP, and compare the accuracy and precision of the two techniques for low and high noise conditions. Finally, a single THG-iFROG reconstruction for an unchirped pulse is made. All the results are compared to independent pulse characterizations made with a commercial SPIDER apparatus optimized for < 60 fs pulses (*FC-SPIDER*, APE Angewandte Physik & Elektronik), the experimental arrangement following the schematic in Fig. IV.1. This helps us to evaluate the results in an objective manner. Additionally, the spectral phases of the chirped pulses are compared to the nominal dispersions of the dispersive elements that caused the chirp in the first place, so that the consistency of the results between the different pulses can be confirmed. These results have been previously reported in Publications [II] and [III].

V.2.1. SHG-iFROG

Unchirped pulse The DE pulse retrieval results for the unchirped SHG-iFROG measurement are shown in Fig. V.5. Both the $S_0^{(2)}$ (DC) and $S_1^{(2)}$ (FM) subtraces were used with an equal weight for the retrieval. Comparing the DC and FM subtraces extracted from the measurement, Fig. V.5(b) and (c), and the retrieved subtraces, Fig. V.5(d) and (e), we see that all the major features of the subtraces are reproduced by the retrieval algorithm. While the measured data is not perfectly symmetric with respect to the delay, the retrieved subtraces are. This is simply because the formalism cannot produce asymmetric traces, see Section IV.2.2. The asymmetries in experimental data are indicative of measurement errors, such as the timing jitter discussed in Section IV.3.1, detection noise, and possibly a slight misalignment of the interferometer. These small shortcomings are not a problem for the algorithm, which will, for two differing values at given coordinates $(\pm\tau, \omega)$, aim to produce a value between the two extrema. Deviation from the mean value will result in an increased error for the two points with a parabolic dependence, as can be deduced from the error function Eq. (IV.22). Thus, small discrepancies are simply averaged out and do not have a major effect in the final result of the reconstruction.

In Fig. V.5(f), the temporal representation of the pulse measured with SHG-iFROG is shown in red. The retrieved intensity (solid line) and phase (dotted line) closely follow the values measured by the SPIDER apparatus, strongly suggesting that the SHG-iFROG measurement is accurate. Switching into the spectral domain by Fourier transforming the time-domain pulse, the results are further corroborated, see Fig. V.5. It is particularly impressive that the SHG-iFROG could reproduce (red solid line) the independently measured fundamental spectrum (blue solid line) impeccably. The spectral phases (dotted lines) are also in excellent agreement. Such a level of accuracy in the reconstructed spectrum is something not typically seen in standard FROG measurements, which is perhaps the reason why some authors choose to simply omit retrieved spectra from publications.

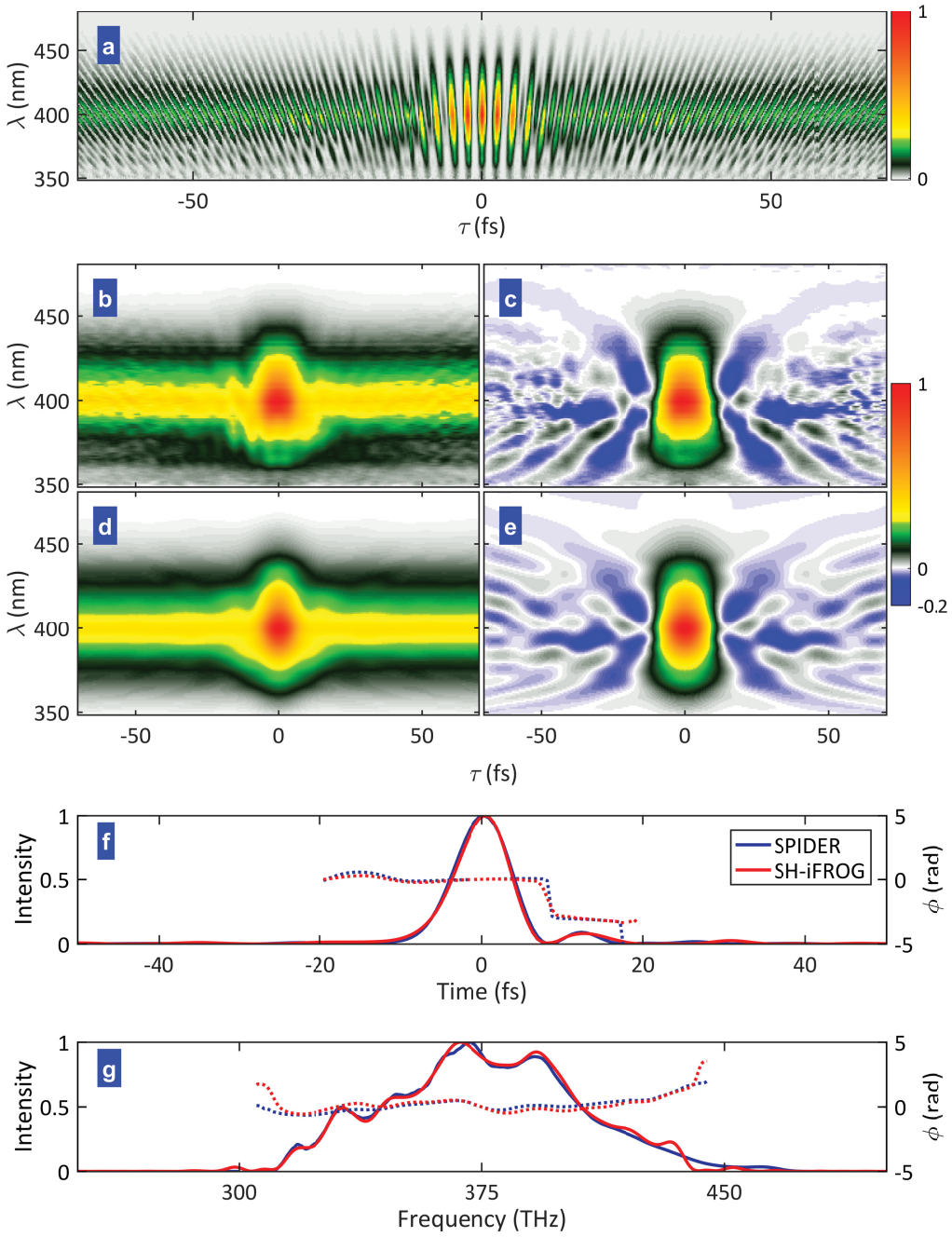

Figure V.5 – *DE pulse retrieval results for the unchirped pulse SHG-iFROG experiment.* ***a*** *Measured SHG-iFROG trace.* ***b, c*** *Extracted and* ***d, e*** *retrieved DC* $S_0^{(2)}$ *(left) and FM* $S_1^{(2)}$ *(right) subtraces for SHG-iFROG.* ***f*** *Retrieved pulse intensities (solid lines) and phases (dashed lines) in time domain for DE (red) and SPIDER(blue).* ***g*** *Same as above but in spectral domain. Adapted from Publication [III].*

Chirped pulses The results for the chirped pulse measurements with SHG-iFROG are summarized in Fig. V.6. Here we only show the DC subtraces to keep the figure compact. What was seen above for the unchirped pulse is again witnessed in the present results, with all the major subtrace features of extracted subtraces, Figs. V.6(d)–(f), clearly reproduced in the reconstructed subtraces, Figs. V.6(g)–(i). The retrieved pulses (red) in time domain for the two lower dispersions, Figs. V.6(j) and (k), are again in excellent agreement with the SPIDER measurements (blue). However, the two measured intensities (solid lines) for the pulse with the highest dispersion of $\approx 230\,\mathrm{fs}^2$, Fig. V.6(l), do not fully agree. A possible explanation for this is that the SPIDER apparatus is not specified to measure pulses beyond a width of 60 fs, while the measured pulses extended well beyond a hundred femtoseconds. The small oscillations in intensity recovered by SHG-iFROG for the range $\tau > 50\,\mathrm{fs}$ are likely an artifact of the reconstruction, which could be avoided by optimizing the parameters of the retrieval. We chose not to do so, however, but instead kept the algorithm parameters constant for these measurements. This way the reliability of DE can better be assessed, independent of the test pulse. Consequently, we can say that a single set of parameters worked well for a wide range of pulses, and an adjustment could be in order only for the very longest pulse.

Instead of showing the measured spectral phases, in Figs. V.6(m)–(o) we plot the values from which the unchirped pulse phase (Fig. V.5(g), dotted line) has been subtracted (red solid lines). These are then compared to the nominal dispersions (solid green lines) calculated using the Sellmeier equations and the measured thicknesses for the three dispersive elements of fused silica and calcium fluoride with varying thicknesses. It is immediately obvious that all three of the measurements accurately reproduce the nominal spectral phases of the dispersive elements. This is true even for the highest dispersion case, regardless of the fact that the temporal intensity did not perfectly agree with the SPIDER measurement. This additional check further corroborates the conclusion that the iFROG measurements are accurate, and are suitable for measuring these unamplified pulses with varying pulse durations and chirps.

Noisy data As a final test for SHG-iFROG, we repeated one of the chirped pulse measurements, using a calcium fluoride window with a thickness of 3.0 cm, but this time the measurement was made twice: once with the normal experimental setup Fig. V.7(a) (high signal-to-noise ratio (SNR)), and a second time with a heavily attenuated signal beam Fig. V.7(b) (low SNR). These two measurements have a noise component with a standard deviation corresponding to a meager 0.1 % of the maximum intensity for the high SNR trace, and a fairly high 8 % for the low SNR case. Thus, these two test cases roughly correspond to the simulated noise-free Fig. V.3(a) and 10 % Fig. V.3(c) SHG-iFROG traces. We then made two sets of ten retrievals using either DE for the subtraces, or GP for the SHG-FROG trace extracted from the SHG-iFROG trace. As before, the retrieval statistics are then plotted for both the time and frequency domains. Both algorithms were allowed to run approximately one minute for each run.

Taking a look at the DE retrievals in the time domain, Fig. V.3(c) and (d), we see that the increase of noise in the measurement data has barely a noticeable effect on the recon-

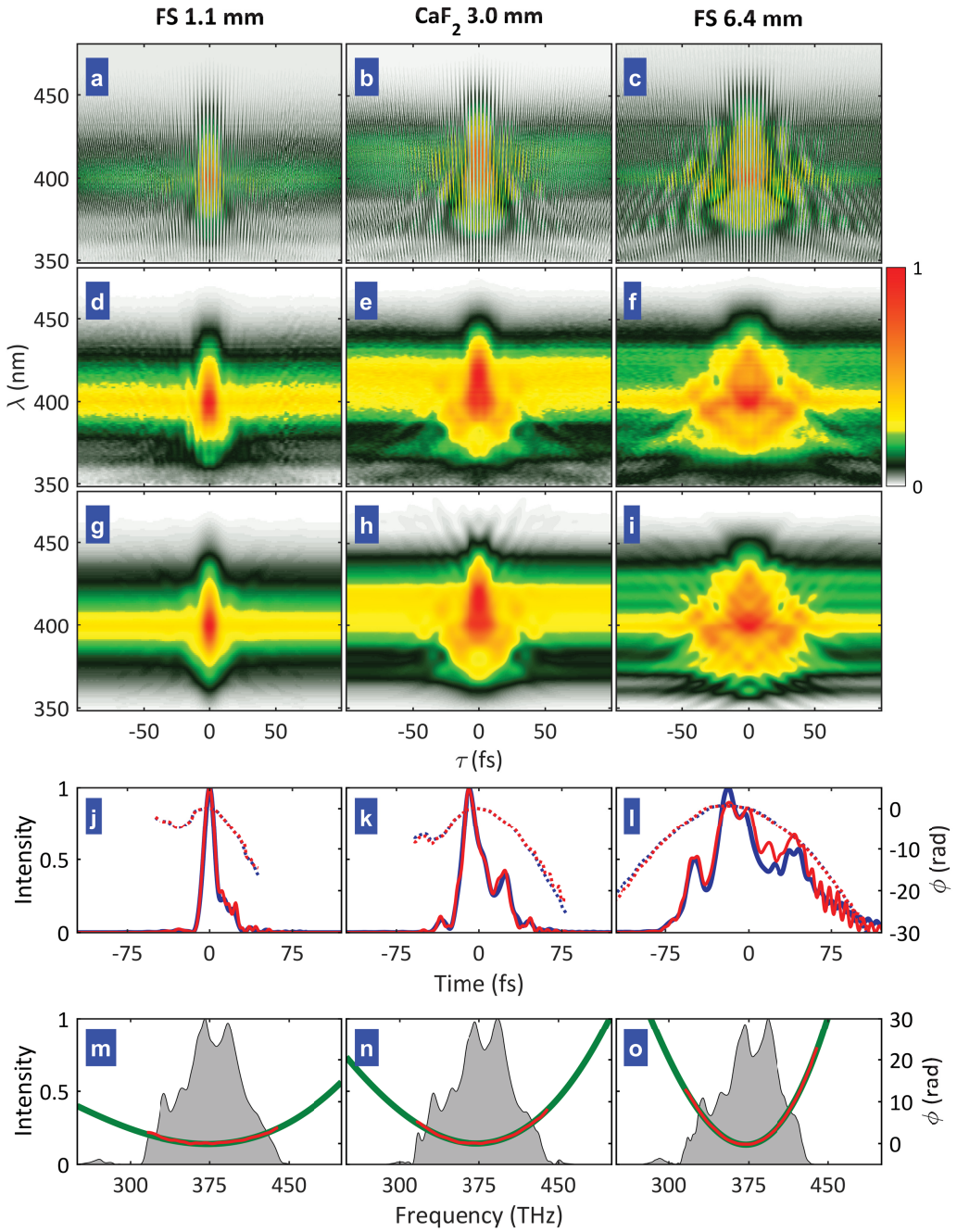

Figure V.6 – *DE pulse retrieval results for the three chirped-pulse SHG-iFROG experiments.* ***a–c*** *Measured SHG-iFROG traces.* ***d–f*** *Extracted and* ***g–i*** *retrieved DC subtraces* $S_0^{(2)}$ *for SHG-iFROG.* ***j–l*** *Retrieved pulse intensities (solid lines) and phases (dotted lines) in time domain for DE (red) and SPIDER(blue).* ***m–o*** *DE-retrieved spectral phases (red solid lines), after subtraction of the unchirped pulse phase, compared to the nominal phases for the dispersive elements (green solid lines). Reproduced from Publication [III], with the permission of AIP Publishing.*

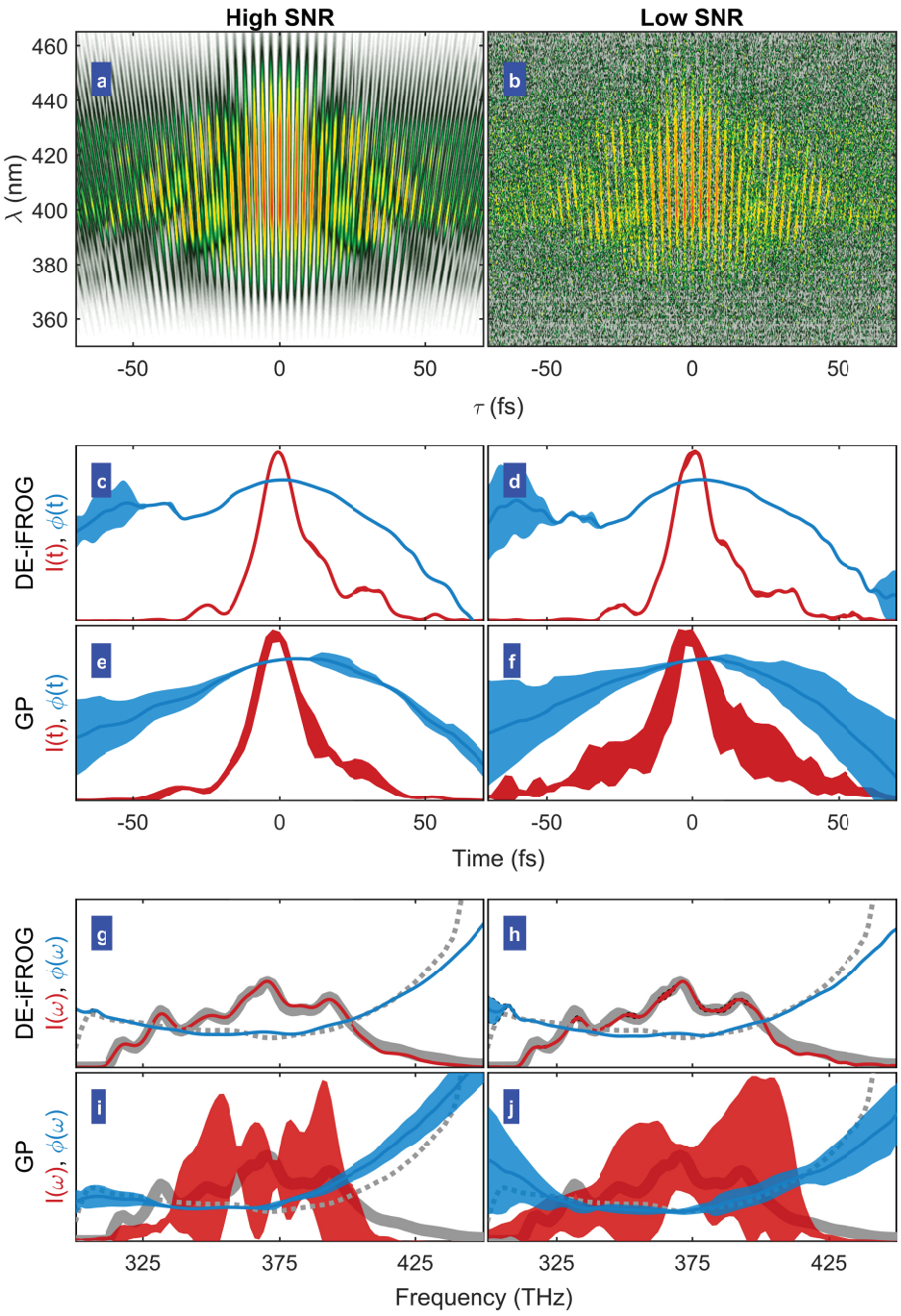

Figure V.7 – *Comparison of pulse retrieval with DE and GP using experimental data with high (left column) or low (right column) signal-to-noise ratio (SNR).* ***a, b*** *Measured SHG-iFROG traces. Statistics in time domain for pulses retrieved with* ***c, d*** *DE, and* ***e, f*** *GP.* ***g–j*** *Frequency-domain statistics. Reproduced from Publication [III], with the permission of AIP Publishing.*

structed pulses, with both measurements producing almost identical results. Moving to the low SNR case, the standard deviations are slightly elevated for the intensity envelope (red), but the phase remains precise. Only the regions where no significant intensity is found, has the phase uncertainty increased, but this is inconsequential, because defining a phase for complex value with zero amplitude (i.e. zero intensity) is meaningless. GP, on the contrary, is already more uncertain of the pulse shape for the high SNR case Fig. V.7(e) than DE is for the low SNR case. Increasing the noise level has a great detrimental effect on GP, apparent from the greatly increased standard deviations for both the intensity and phase in the low SNR measurement Fig. V.7(f).

In the spectral domain, the DE continues to impress. In comparison the SPIDER measurement for the unattenuated beam (gray), the DE yet again impressively reconstructs the independently measured fundamental spectrum for both the high and low SNR cases, Fig. V.7(g) and (h), respectively. Note that it was not possible to make a SPIDER measurement for the low SNR case, and the high SNR data is simply repeated in Fig. V.7(h). This indicates that SPIDER is less sensitive, and less tolerant to experimental noise compared to iFROG. The phases for DE (blue area) and SPIDER (dotted gray line) agree well, only starting to deviate for the high-frequency tail of spectrum. For GP, the attempt to reconstruct the fundamental spectrum is quite hopeless already in the high SNR case Fig. V.7(i), with the intensity being highly uncertain throughout the spectral range (red area). The spectral phase appears to be a little better under control, with a much lower standard deviation than the intensity. Nevertheless, the phase misses the goal given by the SPIDER measurement, and the standard deviation is not comparable to what is delivered by DE, even in the low SNR case. Increasing the noise level makes, again, the situation worse for GP, with increasing uncertainty for both the retrieved spectral intensity and phase, cf. Fig. V.7(j).

V.2.2. THG-iFROG

Now that the SHG-iFROG measurements have been covered, we can move on to the THG-iFROG experiment, employing a fused silica window for surface third-harmonic generation and an unchirped pulse. Applying the DE-iFROG method, a pulse retrieval was performed using all three available subtraces with equal weights, the results illustrated in Fig. V.8. The three measured subtraces, $S_0^{(3)}$ (DC), $S_1^{(3)}$ (FM), and $S_2^{(3)}$ (SHM) are extracted from the THG-iFROG trace Fig. V.8(a) as explained in Section IV.2.2, these are shown in Figs. V.8(b)–(d). The retrieved subtraces are presented below in Figs. V.8(e)–(g). As with SHG-iFROG, the characteristics of the subtraces are well reproduced by DE. It is worth noting that aside from the central peak, the SHM subtrace, Fig. V.8(d), has the strongest features of the three subtraces, and will likely have a larger influence on the outcome than the remaining, lower-order subtraces. Again, a SPIDER measurement was made to serve as an objective benchmark. A marginal correction was applied here according to Eq. (IV.16), with the fundamental and second harmonic spectra obtained from the SPIDER apparatus, which features two dedicated spectrometers for measuring these very spectra.

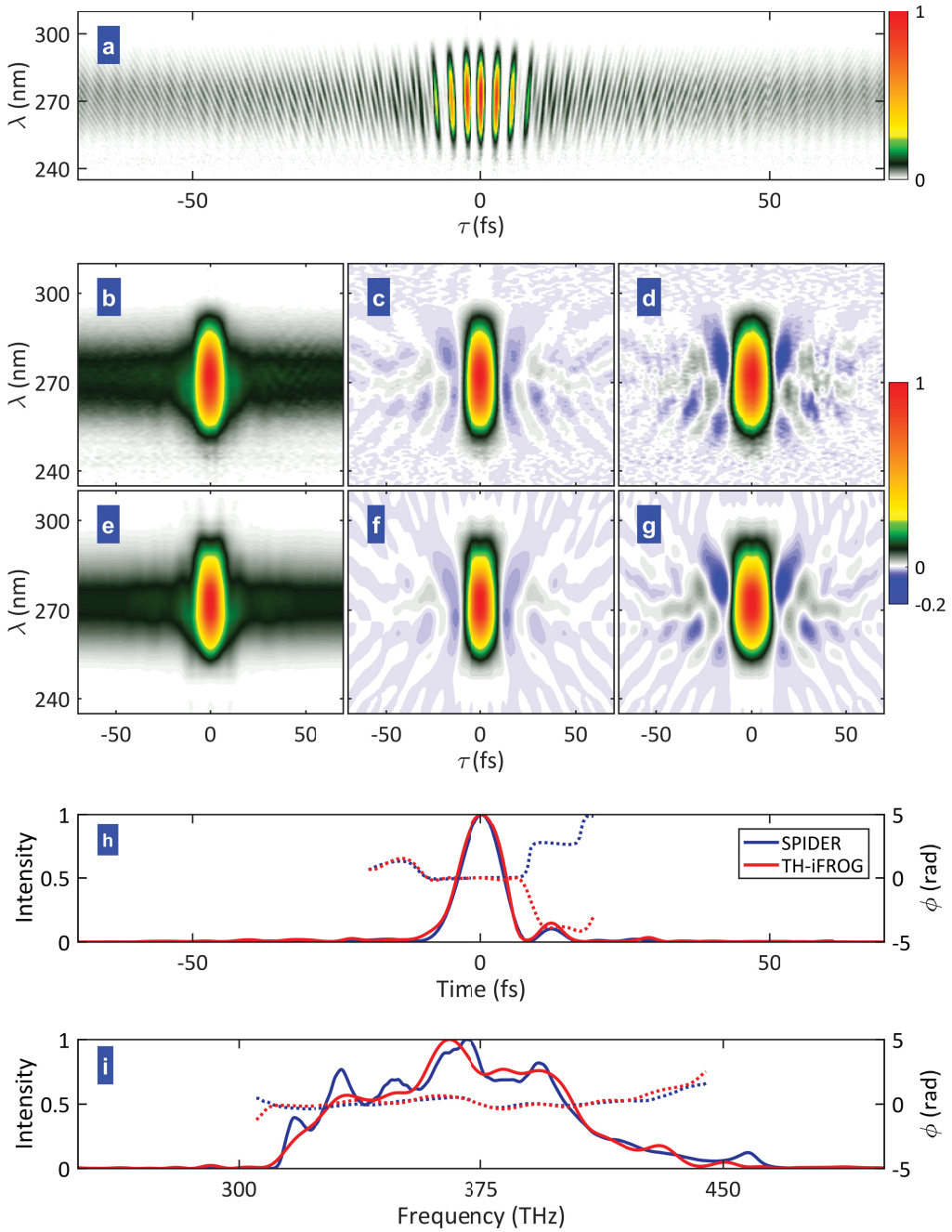

Figure V.8 – *DE pulse retrieval results for the unchirped-pulse THG-iFROG experiment.* ***a*** *Measured THG-iFROG trace after marginal correction.* ***b–d*** *Extracted and* ***e–g*** *retrieved DC $S_0^{(3)}$ (left), FM $S_1^{(3)}$ (middle), SHM $S_2^{(3)}$ (right) subtraces.* ***h*** *Retrieved pulse intensities (solid lines) and phases (dashed lines) in time domain for DE (red) and SPIDER(blue).* ***g*** *Same as above but in spectral domain. Adapted from Publication [II].*

The retrieved pulse for THG-iFROG (red) in time domain plotted in Fig. V.8(h) is yet again in excellent agreement with the SPIDER measurement (blue). The only discrepancy between the two measurements is the absolute phase of the trailing satellite pulse at $\tau \approx 15\,\mathrm{fs}$. A closer inspection reveals that the difference between the two measurements is approximately 2π. As the phase retrieved by THG-iFROG is ambiguous to multiples of $\frac{2}{3}\pi$, and because the intensity reaches zero between the main pulse and the trailing satellite, this phase difference has no physical significance, and thus the two methods agree even for the temporal phase.

The spectral domain presentation for THG-iFROG is again obtained via a Fourier transform of the retrieved $E(t)$, and is depicted in Fig. V.8(i). The spectral intensities for THG-iFROG and SPIDER agree well, but some of the finer peaks seen in the SPIDER measurement (blue solid line) are somewhat smoothened in the iFROG reconstruction (red solid line). The spectral phases, on the other hand, are a near perfect match.

V.3. Discussion

A clear conclusion from the DE-based iFROG retrievals for experimental data, and the achieved excellent agreement with accompanying SPIDER measurements, is that the DE-iFROG method works extremely well in real life. Moreover, it is well suited for the complete characterization of unamplified few-cycle pulses—a challenging regime. The numerical studies simulating various error sources, and the experiment with a varying signal-to-noise ratio, indicate that DE-iFROG is highly robust. The possibility to correct for spectral imperfections through a marginal correction, the built-in measurement and mending of a timing jitter, together with the superior noise resilience make DE-iFROG a very reliable technique. The evolutionary algorithm, differential evolution, produces consistent results, always arriving at approximately the same pulse shape in a predictable time. This is in stark comparison to generalized projections, an algorithm that is prone to stagnation in local minima. This tendency to get stuck in a suboptimal solution, together with the decreased dynamic range of the measurement due to the extraction of SHG-FROG traces, are the most probable explanations for the weaker performance of GP in both the experimental and numerical tests for SHG-iFROG traces. For THG-iFROG traces, DE is shown to work equally well, and remains unrivaled as GP has not been applied for such measurements.

Evolutionary algorithms have a reputation of being slow, and to some extent this applies to DE-iFROG as well, because for each generation, many an evaluation, from tens to a few hundred, must be made to ensure that the gene pool covers enough of the N-dimensional phase space to contain the global solution. This computational effort is, however, greatly mitigated by the use of subtraces, which can be sampled with arbitrarily few delay and frequency coordinates if necessary. Initial tests indicate that a successful DE-iFROG reconstruction can be made in only a few seconds of computation time on a desktop PC, with a suitable selection of parameters. The above retrievals with DE and GP for the noisy experimental data were made with no such optimizations, and within the same computational time of approximately one minute, DE always converged, while

GP did not. Although the possibility was not thoroughly tested, it is highly likely that DE could be made considerably faster by limiting the amount of delay points (i.e. the number of spectra from a subtrace) selected, thus surpassing GP in performance, at the very least for noisy experimental data. For the unrealistic numerical experiments with no noise or flaws in the SHG-iFROG traces, GP was much faster than with experimental data, but, with proper adjustments, DE could always be tuned to perform on par with GP. Furthermore, a significant, so far not utilized, computational advantage could be achieved for DE by parallelizing the algorithm, i.e. by computing subtraces for the tens of individuals in the population simultaneously. Computing multiple traces at once is not feasible for GP, thus parallelization could tip the scales in favor of DE. As a further point, the SHG-FROG traces had to be manually adjusted by removing peripheral noise for GP, while no manual tinkering with the iFROG traces or subtraces was necessary for DE-iFROG, another feather to the cap of DE-iFROG.

To summarize, our results indicate that for pulse retrieval with SHG-iFROG data, DE-iFROG is a far superior option to applying GP for the extracted SHG-FROG traces. For THG-iFROG, the numerical results apply equally well for DE-iFROG, and GP simply cannot be applied. Coupled with the advantages of a collinear geometry, DE-iFROG is a formidable choice for a complete characterization of a variety of ultrashort laser pulses.

As we will see later on in Chapters VII and VIII, iFROG can be also useful beyond simple pulse characterization. By essentially replacing the nonlinear medium with an object of study, the iFROG method can bring a femtosecond temporal resolution to experiments where such a capability would be otherwise difficult to achieve. In our chosen examples, we will use iFROG to study the nonlinear response of nanoscale objects, and to measure the ultrashort lifetimes of excited states of matter. Before exploring these applications, we will introduce in the following chapter the previously mentioned, novel pulse characterization technique πFROG, a close cousin of SHG-iFROG based on a ptychographic algorithm.

CHAPTER VI

Ptychographic Adaptation of iFROG

The first description of time-domain ptychography (TDP), previously discussed in Section III.4.3, was given by Spangenberg *et al.* as recently as 2015 [120]. This was quickly followed by a full-blooded pulse characterization via TDP [44], conducted by the same research group as above. Since then, many new complete characterization techniques based on TDP have been reported. These techniques can be divided into two categories: those that retrieve only a single pulse (the probe), and those that also retrieve a second, unknown pulse (the gate), akin to the blind FROG [134]. All the modalities falling into the former group share identical measurement setups with already established techniques and simply apply a TDP-based pulse retrieval for the measured spectrograms. Examples include the FROG variants SHG-FROG [41, 135] and XFROG [42], as well as a technique suitable for the characterization of attosecond pulses in the XUV, known as attosecond streaking [43]. In Refs. [41–43], the TDP algorithm was shown to exceed the performance and robustness of the predominant retrieval algorithms based on generalized projections. In Ref. [135], it was shown that TDP could be used to characterize several pulses in a train from a single spectrogram. For the second group of blind-FROG-like techniques, the unknown gate pulse is produced by splitting the test pulse and modifying one of the two replica pulses by varying means, such as a glass window [41], a spatial light modulator [44], spectral filtering via a grating [136], or a bandpass filter [48]. All these modalities used an additional measurement of the fundamental spectrum to aid the pulse retrieval, except for last mentioned Ref. [48]. This is the very paper by Witting and coworkers, wherein the specific version of the TDP algorithm discussed in Section III.4.3 was first reported. Aside from our results presented below, Ref. [48] is, at time of writing, also the only example of TDP modalities successfully employed for self-referenced characterization of few-cycle pulses.

Here we expand the selection of TDP-based pulse characterization modalities with

a novel spectrographic variant called ptychographic-interferometric FROG (πFROG), featuring a collinear beam geometry much like iFROG. The results, given in Publication [IV], serve as a basis for this chapter. Due to the many similarities to SHG-iFROG, we seek to avoid excessive repetition by not explaining every minute detail of πFROG from the ground up, but making frequent references to the previously discussed topics in Chapters IV and V and Appendix A and merely stating the differences instead. We will also follow the order presentation used in the iFROG chapter, starting with the measurements in Section VI.1, continuing with an analytical study of the πFROG trace in Section VI.2, and finally presenting experimental results for the TDP pulse retrievals in Section VI.3. Our discussion on TDP is concluded in Section VI.4.

VI.1. πFROG Measurements

Taking the iFROG experimental setup as a starting point, the πFROG setup is trivially obtained by simply inserting a bandpass filter (BPF) in one of the interferometer arms, see Fig. VI.1. The pass band of the filter is centered at 800 nm and has a full width at half maximum (FWHM) of 50 nm, i.e. the pass band is approximately aligned with the carrier wavelength λ_0 of the test pulse created with the same titanium-sapphire oscillator as before, cf. Fig. IV.2. By cutting a small part of the fundamental spectrum for one of the test pulse replicas, the gated spectrum no longer supports pulses close to the original Fourier-transform limited (FTL) pulse width. The BPF therefore creates (in the case of an approximately FTL pulse) a gate pulse with a much broader temporal extent than the unaltered replica, the latter referred to as the probe pulse. Thus, analogously to the original spatial domain modality of ptychography where a large illuminating beam is used to sample small spatial features, the short probe pulse can be sampled in the time domain with the longer gate pulse, or vice versa. Furthermore, introduction of the BPF breaks the symmetry of the delay τ, so that asymmetric traces will be produced. This ensures that the direction-of-time ambiguity inflicting both SHG-FROG and SHG-iFROG is lifted, allowing possible leading and trailing satellites to be distinguished in the subsequent retrieval. A selection of different BPFs was tested with similar results, but the one with the widest bandpass was ultimately chosen because this also yielded the highest intensity for the gate pulse, and thus the strongest signal in the resulting πFROG trace. A previous study suggests that choosing a wider passband comes at the expense of slower algorithm convergence [44], but this was not an issue for our purposes. The center wavelength of the pass band could be tuned by changing the test pulse angle of incidence for the dielectric BPFs. The effect of such tuning on TDP pulse retrieval was also tested, and found to have only a minor effect on the retrieval. Thus, normal incidence was chosen for the subsequent experiments.

As with SHG-iFROG in Chapter IV, four different test pulses with varying amounts of added dispersion were employed for the measurements, using windows of fused silica and calcium fluoride as dispersive elements providing up to 232 fs^2 of group-delay dispersion (GDD), or no window at all in case of the unchirped test pulse. The recorded πFROG traces are shown in Figs. VI.2(a)–(d). A delay range of 500 fs was used for each

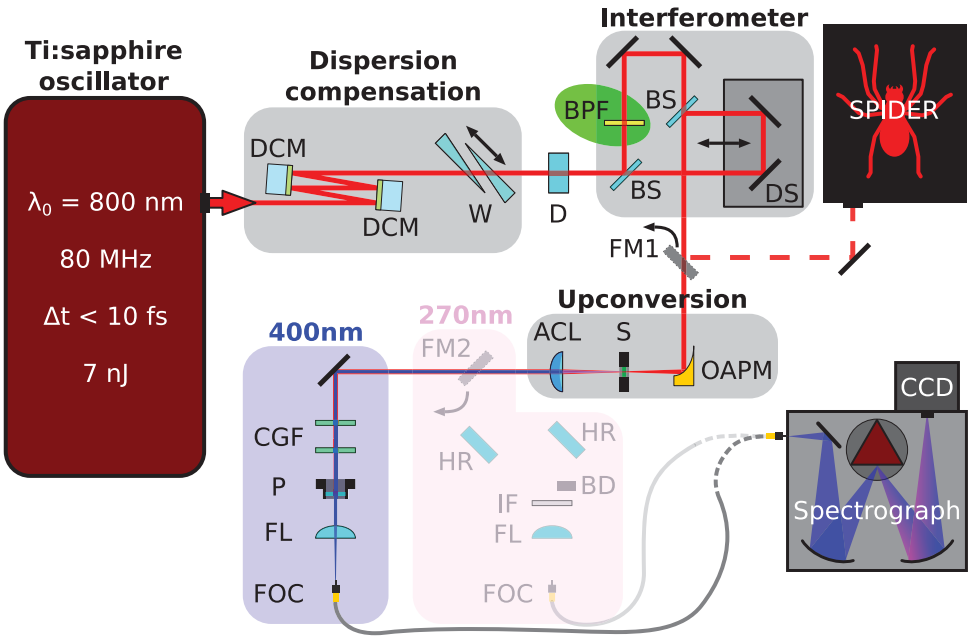

Figure VI.1 – *A detailed schematic of the πFROG measurement system employed in the experiments presented in this work. This is otherwise identical to the iFROG setup depicted in Fig. IV.1, but the THG detection arm (faded components) is not used, and a bandpass filter (BPF) has been inserted into one of the two interferometer arms, highlighted in green. For a list of abbreviations see the iFROG setup.*

measurement, but only a 300-fs window is shown here so that the fringes are more easily discerned. Comparing these measurements to the SHG-iFROG traces in Fig. IV.3, one sees that the features of πFROG traces are much less pronounced, and that the temporal broadening of the test pulse has a less dramatic visual effect. The unchirped pulse produces a πFROG trace (Fig. VI.2(a)) where the high-intensity feature at zero delay extends to $\tau = \pm 50\,\mathrm{fs}$, while a much narrower lobe with much higher intensity contrast is formed in the corresponding SHG-iFROG trace (Fig. IV.3(a)) within $\tau = \pm 20\,\mathrm{fs}$. This is of course expected, because one of the two pulse replicas is now considerably weakened: the BPF rejects most of the $\approx 300\,\mathrm{nm}$ wide fundamental spectrum, leaving only a fraction of the optical power to the gate pulse which then only serves as a weak modulation for the stronger probe pulse. Moreover, the short probe pulse has a much higher peak intensity than the temporally broadened gate, further contributing to the contrast between the two. When more and more dispersion is introduced to the test pulse, the difference between probe and gate pulse intensities is lessened as their temporal widths are converging. This is because cutting the spectrum of a pulse with a high amount of GDD does not affect the pulse duration as much as it would for an FTL pulse. Thus, for the highest amount of dispersion in Fig. VI.2(d), the πFROG trace already has much more easily recognizable features than what the unchirped pulse produced in Fig. VI.2(a).

A Fourier transform of the πFROG trace for the unchirped pulse reveals three modulation bands, see Fig. VI.2(e). Unsurprisingly, perhaps, the modulation bands are very

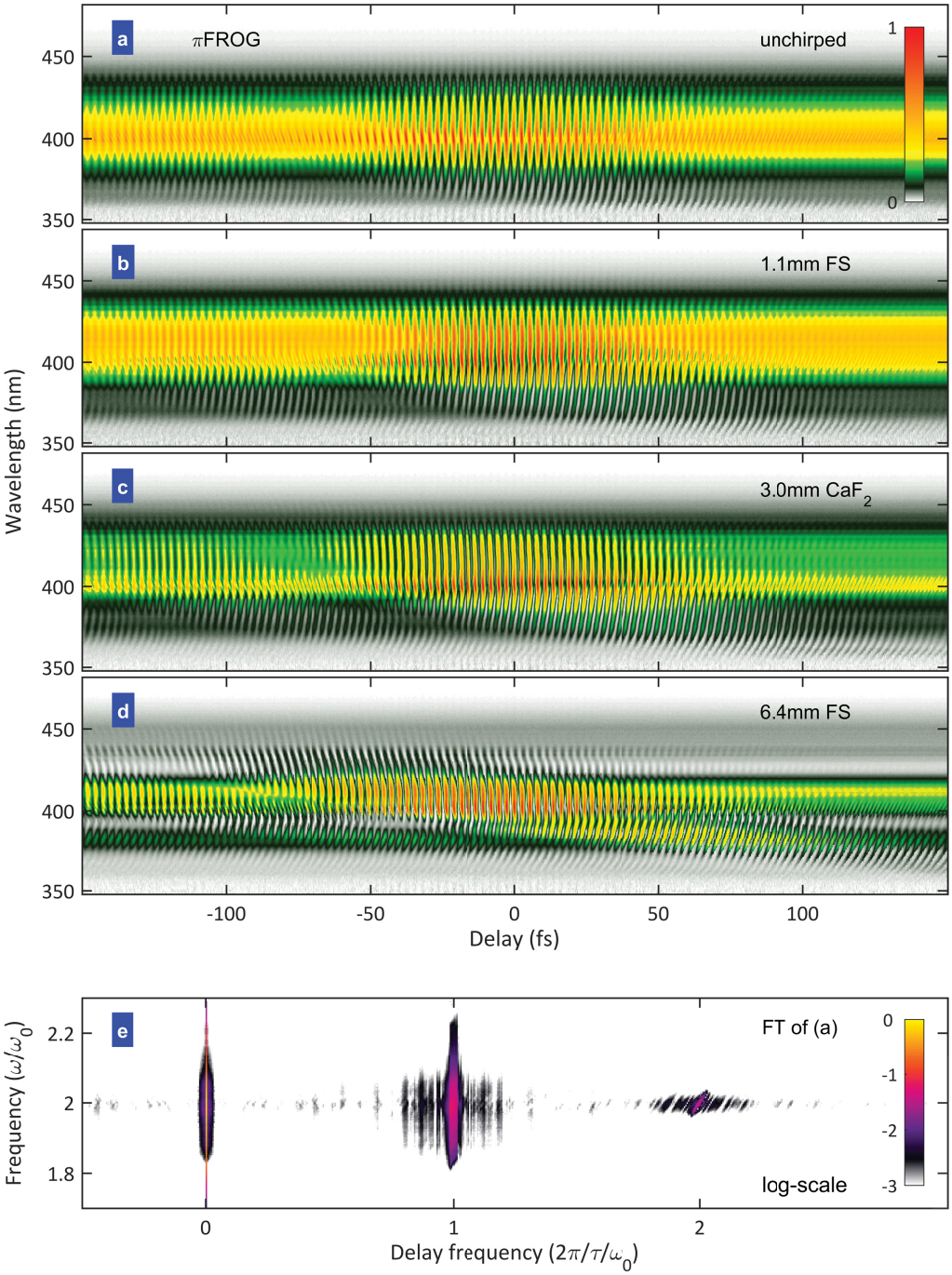

Figure VI.2 – *Experimentally measured πFROG traces for various test pulses.* ***a*** *Unchirped pulse.* ***b–d*** *Chirped pulses, obtained from the unchirped pulse after traversing (b) 1.1 mm of fused silica (FS), (c) 3.0 mm of CaF_2, or (d) 6.4 mm of FS.* ***e*** *Fourier transform of (a) along the delay axis reveals three distinct modulation bands. Adapted from Publication [IV].*

similar to the corresponding bands for SHG-iFROG, cf. Figs. IV.3(e) and IV.5(d). Possibly the most striking difference between the two techniques is that the modulation bands in the πFROG trace are much narrower along the horizontal delay frequency axis. Why this is the case will be easier to understand once the mathematical structure of the πFROG trace has been uncovered.

VI.2. Structure of a πFROG Trace

For given probe $\mathcal{E}(t)$ and gate $\mathcal{G}(t)$ pulses, the πFROG trace can be written as

$$I_{\pi\mathrm{FROG}}(\omega,\tau) \equiv \left| \int_{-\infty}^{+\infty} [\mathcal{E}(t-\tau) + \mathcal{G}(t)]^2 \, e^{-i\omega t} \, \mathrm{d}t \right|^2 . \tag{VI.1}$$

The probe pulse $\mathcal{E}(t)$ is defined through Eq. (II.5), and the gate is given by

$$\mathcal{G}(t) \equiv G(t) e^{i\omega_0 t} , \tag{VI.2}$$

where $G(t)$ is the complex temporal envelope of the gate pulse. The gate pulse is derived from the probe via a spectral filter T:

$$\mathcal{G}(t) \equiv \mathcal{E}(t) * T(t) = \mathcal{F}^{-1}\{\mathcal{E}(\omega) T(\omega)\} . \tag{VI.3}$$

In our experiments, $T(\omega)$ corresponds to the spectral response of the bandpass filter, ideally an amplitude-only filter. In reality, a dielectric filter such as ours will certainly affect the spectral phase as well, but this does not pose a problem for the TDP algorithm. Technically any filter could be used, even with a unity value $T(\omega) = 1$ so that $\mathcal{G}(t) = \mathcal{E}(t)$. In this case the trace would correspond to an SHG-iFROG measurement, from which a standard SHG-FROG trace can be extracted, and further employed for pulse retrieval not only with standard FROG algorithms (as discussed in Chapter V), but also with ptychographic algorithms [41]. This would however needlessly reintroduce the direction-of-time ambiguity which the BPF conveniently removes. Thus we will limit the discussion to a simple amplitude-only filter from here on.

Comparing Eq. (VI.1) to the SHG-iFROG trace in Eq. (B.1), we see that the two are otherwise identical but one of the fields $\mathcal{E}$ has been exchanged to the gate pulse in the πFROG equation. Here we have chosen the undelayed field to be replaced, $\mathcal{E}(t) \to \mathcal{G}(t)$, but could equally well have picked the delayed field $\mathcal{E}(t-\tau)$. The effect of choosing the latter option instead of the former would be the mirroring of the trace along the delay axis. As with iFROG, this simplified equation does not take a possible spectral weighting function into account, but can be readily included similar to Eq. (IV.12). The discussion in Section II.1.1 regarding the (subsequently retrieved) electric field, the measured trace, and physical quantities related to the two applies to πFROG as well.

Following the strategy in Appendix B, we can study the structure of the πFROG trace by expanding Eq. (VI.1). To aid us in our derivation, a few shorthand notations are

introduced. The frequency $\Delta\omega$ is the same as with SHG-iFROG, i.e. $\Delta\omega = \omega - 2\omega_0$. The second-harmonic fields of the probe and gate are respectively given by

$$E_{\mathrm{SH}}(\Delta\omega) \equiv \int_{-\infty}^{+\infty} E^2(t) e^{-i\Delta\omega t}\,\mathrm{d}t \tag{VI.4}$$

$$G_{\mathrm{SH}}(\Delta\omega) \equiv \int_{-\infty}^{+\infty} G^2(t) e^{-i\Delta\omega t}\,\mathrm{d}t\,. \tag{VI.5}$$

The SHG-FROG field in Eq. (B.4) is modified to include the gate pulse, and thus becomes a cross term describing interaction between the probe and gate pulses:

$$E_{\mathrm{X}}(\Delta\omega,\tau) \equiv \int_{-\infty}^{+\infty} G(t)E(t-\tau) e^{-i\Delta\omega t}\,\mathrm{d}t\,. \tag{VI.6}$$

With these definitions, the expansion and rearrangement of Eq. (VI.1) yields

$$\begin{aligned}
I_{\pi\mathrm{FROG}}(\omega,\tau) &= |E_{\mathrm{SH}}(\Delta\omega)|^2 + |G_{\mathrm{SH}}(\Delta\omega)|^2 + 4|E_{\mathrm{X}}(\Delta\omega,\tau)|^2 && \text{(VI.7a)}\\
&+ |E^*_{\mathrm{SH}}(\Delta\omega)\cdot E_{\mathrm{X}}(\Delta\omega,\tau)|\cdot\cos[\phi_{\mathrm{X}}(\Delta\omega,\tau) - \phi_{\mathrm{ESH}}(\Delta\omega) + (\omega_0+\Delta\omega)\,\tau] && \text{(VI.7b)}\\
&+ |G^*_{\mathrm{SH}}(\Delta\omega)\cdot E_{\mathrm{X}}(\Delta\omega,\tau)|\cdot\cos[\phi_{\mathrm{X}}(\Delta\omega,\tau) - \phi_{\mathrm{GSH}}(\Delta\omega) - \omega_0\tau] && \text{(VI.7c)}\\
&+ |E^*_{\mathrm{SH}}(\Delta\omega)\cdot G_{\mathrm{SH}}(\Delta\omega)|\cdot\cos[(\omega_0+2\Delta\omega)\,\tau]\,. && \text{(VI.7d)}
\end{aligned}$$

Here ϕ_{ESH}, ϕ_{GSH}, and ϕ_{X} are the phases of the complex fields E_{SH}, G_{SH}, and E_{X}, respectively. Via the cosine factors, we may assign the four terms of Eq. (VI.7) to three modulation bands (cf. Fig. VI.2(e)), as with SHG-iFROG in Eq. (B.5). After omitting the coordinates of the fields from notation, the three modulation bands $M_m^{(\pi)}(\Delta\omega,\tau)$ for πFROG read

$$M_0^{(\pi)} \equiv |E_{\mathrm{SH}}|^2 + |G_{\mathrm{SH}}|^2 + 4|E_{\mathrm{X}}|^2 \tag{VI.8}$$

$$M_1^{(\pi)} \equiv |E^*_{\mathrm{SH}}E_{\mathrm{X}}|\cdot\cos[\phi_{\mathrm{X}} - \phi_{\mathrm{ESH}} + (\omega_0+\Delta\omega)\,\tau] + |G^*_{\mathrm{SH}}E_{\mathrm{X}}|\cdot\cos[\phi_{\mathrm{X}} - \phi_{\mathrm{GSH}} - \omega_0\tau] \tag{VI.9}$$

$$M_2^{(\pi)} \equiv |E^*_{\mathrm{SH}}G_{\mathrm{SH}}|\cdot\cos[(\omega_0+2\Delta\omega)\,\tau]\,. \tag{VI.10}$$

Going back to the phenomenon we came across in the previous section upon inspecting the Fourier transform of a πFROG trace (Fig. VI.2(e)), we can now explain why the modulation bands are confined to a smaller range of delay-frequencies ξ than in SHG-iFROG. The second-harmonic modulation (SHM) band $M_2^{(\pi)}(\Delta\omega,\xi)$ is actually confined to a smaller range of frequencies ω (vertical axis), and is narrower with respect to ξ because the band is tilted. The frequency range is limited because the intensity of the SHM band is proportional to the product of the pulse spectral amplitudes, $|E^*_{\mathrm{SH}}(\Delta\omega)|\cdot|G_{\mathrm{SH}}(\Delta\omega)|$, which is zero for $|G_{\mathrm{SH}}(\Delta\omega)| = 0$, i.e., the SHM band bandwidth is limited by the bandwidth of the gate pulse, which in turn is limited by the BPF. For the two remaining modulation

bands, $M_0^{(\pi)}$ (DC) and $M_1^{(\pi)}$ (FM), the issue is a bit more involved. For simplicity, let us assume that the test pulse is Fourier-transform limited (a fair approximation for our unchirped pulse) so that the phase in both temporal and spectral domains is flat and can be ignored. The range of delays τ spanned by either the DC or the FM band is now determined by the cross term $|E_{\mathrm{X}}(\Delta\omega,\tau)|$. The product $G(t)E(t-\tau)$ in Eq. (VI.6) is non-zero for a wider range of delays the longer the gate pulse is. With a flat phase, a wider envelope with respect to the delays corresponds to a narrower envelope in the Fourier domain, i.e., the delay frequency domain (ω vs. ξ). Thus, for a temporally broadened gate pulse, $E_x(\Delta\omega,\xi)$ is non-zero for a narrower range of delay frequencies, therefore making the DC and FM bands narrower in comparison to SHG-iFROG, where the gate pulse is as short as the test pulse. Note that although the FM band in Fig. VI.2(e) appears parallel to the ω axis, it in fact contains a tilted component as well. Specifically this is due to the $\Delta\omega\tau$ term in Eq. (VI.7b). The tilt is more visible in the corresponding iFROG examples, for example in Fig. IV.5(d), where the narrowing of the FM band does not occur.

The TDP algorithm, as described in Section III.4.3, can only function if each spectrum of the trace to be reconstructed can be computed using a simple product of the probe and gate pulses. This condition is fulfilled by the cross term $|E_{\mathrm{X}}(\Delta\omega,\tau)|^2$ (cf. Eq. (VI.6)) which, fortunately, can be easily extracted from the DC band $M_0^{(\pi)}$ in Eq. (VI.8). The extraction can be made exactly in the same manner as the SHG-FROG trace is separated from the SHG-iFROG trace, i.e., Fourier filtering the DC band, then subtracting an average of the spectra at the edges of the DC spectrogram, thus removing the delay-independent harmonic fields $|E_{\mathrm{SH}}(\Delta\omega)|^2$ and $|G_{\mathrm{SH}}(\Delta\omega)|^2$. We use a fourth-order super-Gaussian for the Fourier filtering, similar to what was shown for the fundamental modulation (FM) band of SHG-iFROG in Fig. IV.5(d), but this time the filter is centered at the delay-frequency $\xi = 0$.

The complicated analytical form of the FM band $M_1^{(\pi)}$ in Eq. (VI.9) makes the extraction of the cross term E_{X} difficult, if not impossible, so that the retrieval algorithm cannot make use of this modulation band. The SHM band in Eq. (VI.10) is not usable for pulse reconstruction either, because it does not contain E_{X}. Thus, only a single usable subtrace can be derived for πFROG, in contrast to SHG-iFROG for which two subtraces could be obtained and independently employed in the differential evolution based pulse retrieval, see Appendix B. In accordance with the terminology established for iFROG in Chapter IV we refer to field the $|E_{\mathrm{X}}(\Delta\omega,\tau)|^2$ extracted from the modulation band $M_0^{(\pi)}$ as a *subtrace*, even if it is not obtained strictly in the same manner as the iFROG subtraces $S_n^{(h)}$ are. We therefore define the single πFROG subtrace as

$$S_0^{(\pi)}(\Delta\omega,\tau) \equiv |E_{\mathrm{X}}(\Delta\omega,\tau)|^2 \,. \tag{VI.11}$$

Examples of the extracted subtraces $S_0^{(\pi)}$ are given in context of the pulse retrieval, e.g. in Figs. VI.3(a) and (b). While the FM band serves no purpose in our implementation of the ptychographic algorithm, the SHM band can still be used for measurement of the timing jitter, exactly as with iFROG, see Section IV.3.1. For the data presented in Fig. VI.3, we

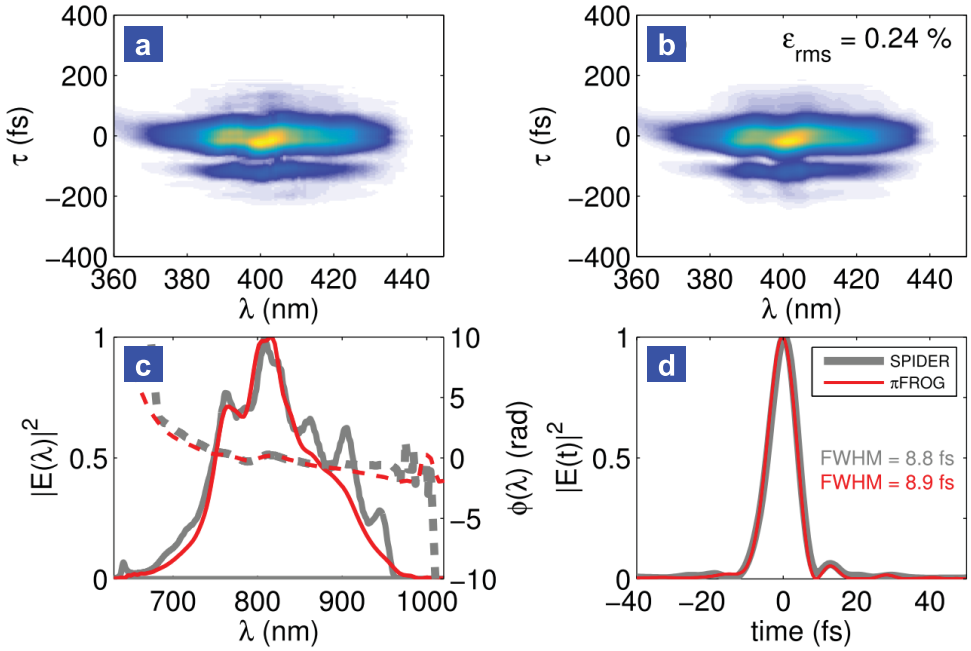

Figure VI.3 – *Pulse retrieval with TDP for the unchirped πFROG measurement. Measured* ***a*** *and retrieved* ***b*** *πFROG subtraces* $S_0^{(\pi)}$. ***c*** *Measured pulse intensity (solid lines) and phases (dashed lines) in frequency domain for πFROG (red) and SPIDER gray.* ***d*** *The same as (c) but in time domain. Reproduced from Publication [IV].*

obtained rms timing-jitter values of ≈ 70 attoseconds, in excellent agreement with those measured for our iFROG measurements.

VI.3. Pulse Retrieval with πFROG

The ptychographic pulse retrieval algorithm described in Section III.4.3 can now be applied for the inversion of πFROG traces. In fact, the mathematical form of the subtrace $S_0^{(\pi)}$ is identical to the spectrogram obtained experimentally by Witting *et al.* in Ref. [48], wherein the very same algorithm was already shown to work. No modifications to the TDP algorithm are therefore required, and we can simply replace the measured spectrogram $I_{\text{meas}}(\Delta\omega, \tau)$ with the Fourier-filtered subtrace $S_0^{(\pi)}(\Delta\omega, \tau)$ as an input for the algorithm. Note that while interferometric precision and a regular step size is required for the delays in order to record the raw πFROG trace as described by Eqs. (VI.1) and (VI.7), the extracted subtrace $S_0^{(\pi)}$ can be resampled to an arbitrary grid size. By reducing the resolution of the spectrogram, the computational effort of the pulse retrieval can be significantly reduced, allowing an increased speed of convergence.

We first apply the TDP algorithm to the unchirped pulse measurement, shown above in Fig. VI.2(a). The extracted subtrace in Fig. VI.3(a) is fed to the algorithm, which after

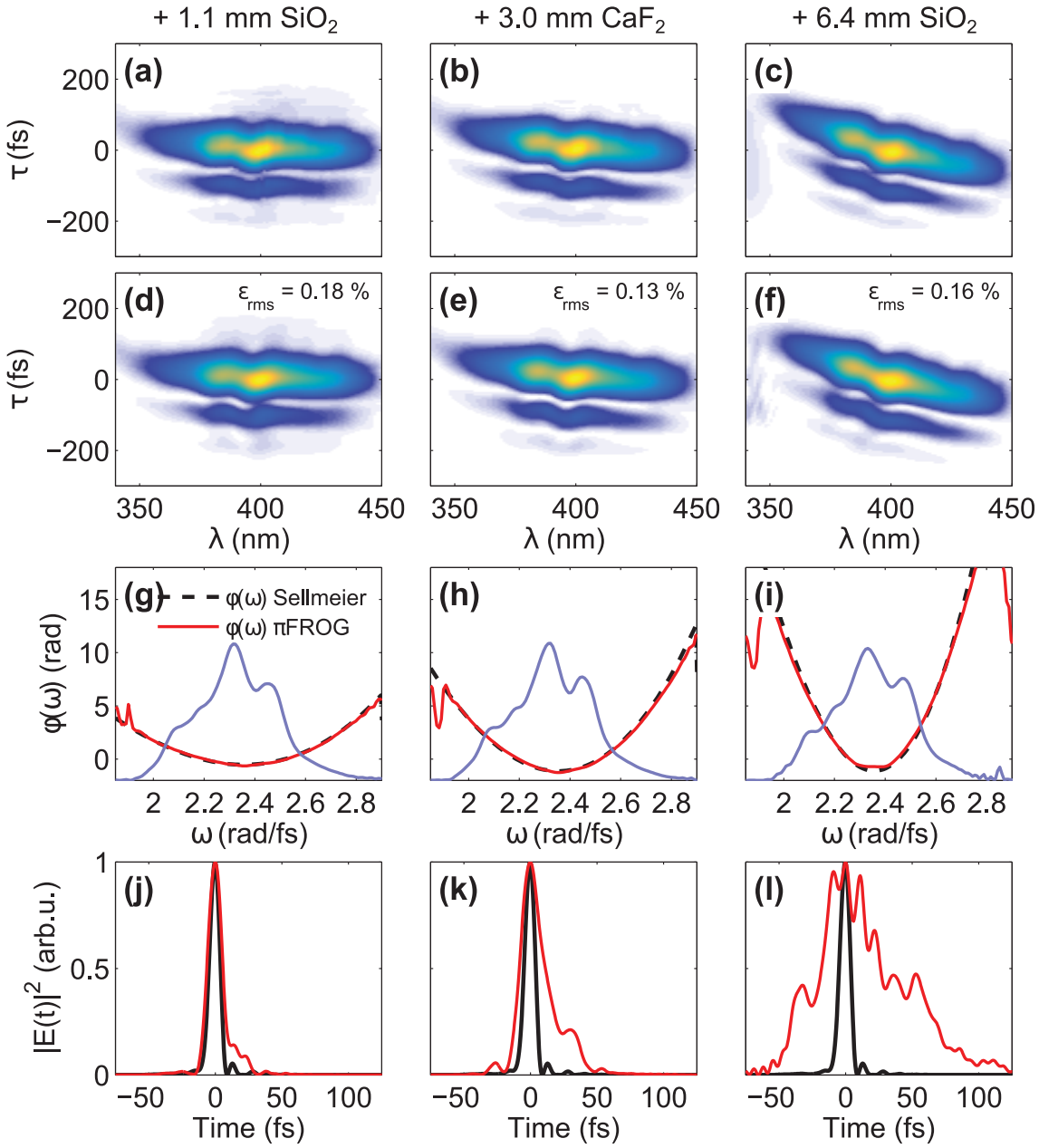

Figure VI.4 – *Pulse retrieval with TDP for the chirped πFROG measurements with different amounts of added dispersion, as indicated with the dispersive element thickness and material on top of each column. Measured **a**–**c** and retrieved **d**–**f** πFROG subtraces $S_0^{(\pi)}$. **g**–**i** Retrieved spectral intensities (blue solid lines) and phases (red solid lines). The phase as measured for the unchirped pulse, cf. Fig. VI.3(c), has been subtraced from the phases here, so that only the additional phase brought by the dispersive elements is left. These are compared to the nominal dispersion of the elements (black dashed lines). **j**–**l** Retrieved intensity envelopes in time domain for the chirped pulses (red solid lines) and the unchirped pulse (black solid lines). Reproduced from Publication [IV].*

50 iterations yields the reconstructed subtrace in Fig. VI.3(b). As can be clearly seen, the measured and simulated subtraces match each other very closely, the rms error being only 0.24 %. The 8.9 fs wide temporal intensity envelope of the retrieved test pulse (red thin line) shown in Fig. VI.3(d) is a near-perfect match to the pulse measured by SPIDER (gray thick line), with pulse durations differing only by 0.1 fs. The reconstructed spectral intensity (red solid line) in Fig. VI.3(c) is a very good match to the fundamental spectrum physically measured by SPIDER (gray solid line), although some of finer details at 850 to 950 nm have been washed away. Likewise, the spectral phases (dashed lines) retrieved by either technique are in excellent agreement.

The measured and extracted πFROG subtraces for the three chirped pulses are shown in Figs. VI.4(a)–(c), and the retrieved subtraces below them in Figs. VI.4(d)–(f). As with the unchirped pulse, the excellent agreement between the experimental and simulated spectrograms is clearly seen with a naked eye. The rms errors are even lower than before, simply due to the fact that the TDP algorithm was allowed to run more iterations. The retrieved spectral intensities (blue solid lines) and the added phase with respect to the unchirped pulse spectral phase (red solid line) are presented in Figs. VI.4(g)–(i). The added phases are a very close match to the nominal phases of the employed silica and calcium fluoride windows computed via Sellmeier equations (black dashed lines), corroborating the good performance of the measurement system. Taking a look at the time domain in Figs. VI.4(j)–(l), the retrieved intensity envelopes (red solid lines) are seen to experience varying amounts of temporal broadening in comparison to the unchirped pulse (black solid lines). For the largest added group delay dispersion in Fig. VI.4(l), the chirped pulse is more than ten times longer than its unchirped seed.

VI.4. Discussion

The above results clearly demonstrate that πFROG is very much suited for the measurement of near infrared pulses ranging from few to tens of cycles in duration. The spectral phase is accurately retrieved by the TDP algorithm in all test cases, with the spectra closely matching the fundamental spectrum measured independently with a commercial SPIDER apparatus. The high quality of the unchirped pulse measurement is confirmed by the accompanying SPIDER measurement.

The method shares some of the advantages of iFROG brought by the collinear beam geometry, such as a high sensitivity due to tight focusing, and immunity to geometrical time-smearing. There are a few notable differences between πFROG and iFROG as well. The use of two differing pulses, namely the temporally broadened gate pulse and the unmodified probe pulse, breaks the symmetry of the πFROG spectrogram with respect to delay, allowing the correct assignment for the direction of time and thus the distinction of trailing and leading satellites. The ptychographic algorithm is known to be robust, even surpassing generalized projections in performance [41–43], but no real comparison between TDP and differential evolution, our weapon of choice for iFROG, has been made as of yet, prompting further studies. One clear disadvantage of πFROG is that the dynamical range is unavoidably reduced in the extraction of the subtrace from

measurement data, somewhat limiting the sensitivity of the technique. This is analogous to the extraction of the SHG-FROG trace from a SHG-iFROG trace, which put GP in disadvantageous position in comparison to DE as discussed in Chapter V. Nevertheless, the fairly weak, unamplified few-nanojoule pulses provided by our titanium-sapphire oscillator were characterized with aplomb. It is feasible to extend πFROG to employ third-harmonic generation instead, although changes to the retrieval algorithm might be necessary—another possible direction for further research.

CHAPTER VII

Multiphoton Absorption Induced Luminescence in ZnO Nanorods

In this chapter, the UV photoluminescence (PL) process in zinc oxide nanorod thin films, as induced by femtosecond NIR pulses, is investigated with iFROG. This application of the iFROG method differs from the previous discussion and the examples that will be given in Chapter VIII in the sense that here were are not primarily concerned in pulse characterization, or measuring what influence the nonlinear medium has on the laser pulses. Instead, we seek to obtain the power dependence of the nonlinear luminescence process by analyzing the contrast ratios of emission spectra found within the iFROG trace. While there are certainly simpler ways to measure a power dependence, the temporal resolution of iFROG offers a few advantages over the competition which will be discussed in due course. With the help of additional time-resolved PL, knife edge, and scanning electron microscope measurements, as well as numerical simulations based on Keldysh-theory of photoionization, the obtained power dependence will provide an insight into the processes leading to the UV-PL emission.

Based on Publication [I], this chapter is structured as follows. We start by giving a short motivation for the present study in Section VII.1. The ZnO nanorod samples are introduced in Section VII.2. The iFROG measurements are explained next in Section VII.3, followed by the time-resolved PL experiments in Section VII.4. The experimental measurements are combined and summarized in Section VII.5. The supporting numerical simulations are the topic of Section VII.6. We conclude with a discussion of the results in Section VII.7.

VII.1. Introduction to ZnO Nanorods

Zinc oxide is a wide-bandgap semiconductor which has been researched extensively since the 1930's [137]. After peaking in the 70's and early 80's, the activity around ZnO

was fading, partly because of a shift of focus to GaAs quantum wells and other low-dimensionality structures, and partly because of the difficulties encountered in the doping of ZnO, limiting the applicability of the material for optoelectronics applications. A renewed interest in ZnO sparked towards the end of the 90's with the maturing of fabrication techniques, allowing the growth of ZnO nanostructures such as thin films, quantum dots and, most importantly for our own study, nanorods. This multitude of morphologies greatly extended the capabilities of ZnO and made it once more attractive for a wide variety of applications. Examples include sensors [138], light emitting diodes [139] and even lasers [140, 141] in the spectral range from blue to UV. ZnO could also be used as a cheap, durable and transparent conductor for electronics, optoelectronics and photovoltaics [142], and for photodynamic therapy [143, 144].

Two distinct luminescence bands can be found for ZnO at room temperature, a narrow one in the UV (UV-PL) and a second, wider one in the visible part of the spectrum (VIS-PL) [145]. The latter originates from defect emission [146], although the exact mechanism is still debated [147]. By controlling the properties and quantity of defects, the VIS-PL band can shift color and strength [147], and for high quality nanorod samples the band can be eliminated entirely [54]. The UV-PL band is due to the recombination of free excitons and their longitudinal-optical (LO) phonon replicas across the bandgap of $E_g = 3.37\,\mathrm{eV}$, emitting light at energies slightly below the bandgap with the peak wavelength depending on nanorod morphology [54, 145]. The high exciton binding energy of $E_x = 60\,\mathrm{meV}$ assures that excitons can exist at relatively high temperatures [148]. Thus, the excitonic UV-PL emission is possible even at room temperature, a fact which underlines the potential of ZnO as a UV light source [145]. Aside from deep-UV pumping, the UV-PL process in ZnO nanostructures can also be induced via multiphoton absorption (MPA) of NIR laser pulses [54]. This is especially interesting for photodynamic therapy because UV emission from ZnO devices implanted deep within the skin could be triggered noninvasively by passing NIR pulses through the skin via the tissue optical window at 700–1100 nm [143].

How exactly the MPA induced luminescence works in nanorods is, however, still an open question. Previous accounts have attributed the UV-PL process to two- [50–55] three- [56, 57] and even four-photon [58] absorption (#PA) of NIR photons. Fractional exponential dependences on input intensity are often reported, which suggests that multiple nonlinear processes are at play, making the attribution to a single MPA process problematic. Adding to the confusion, 2PA is sometimes claimed even when the photon energies of incident pulses are below half the bandgap. To justify these claims, various explanations as to why 2PA might still occur have been given, based on Rabi oscillations [50, 52], or changes in the band structure via bandgap renormalization [52] or bandgap narrowing due to heat accumulation [51, 52].

We tackled these questions by conducting power dependence measurements with three differing ZnO nanorod samples. Photon energies below, yet as close as possible to the 2PA threshold energy were employed, corresponding to wavelengths above 750 nm. If a square dependence of UV-PL emission strength versus input intensity were to be observed, this would indicate that a 2PA enhancing mechanism is at play. Instead, frac-

tional exponents from 3 to above 4 were measured with iFROG, suggesting that 3PA, 4PA or other processes besides MPA are dominating over 2PA. To explain these results, a model based on Keldysh-theory of photoionization [5, 59] was built. Computing the Keldysh parameter [149] for our experimental conditions

$$\gamma_K = \frac{U_p}{\hbar\omega_0} \approx 0.04 \ll 1\,, \tag{VII.1}$$

where U_p is the ponderomotive energy, one finds that we are clearly in the MPA regime, so that an MPA approximation excluding tunneling effects may be employed. While the simulations correctly yielded fractional exponents above 3, they also indicated that the higher values measured could not possibly be reached with the incident intensities employed. If the *local* intensity was stronger, however, the measurements could be explained. Thus, additional experiments were made in order to establish whether field enhancement [18] was taking place in the nanorod samples. Time-resolved photoluminescence (TRPL) measurements gave the relative emission strengths of each sample, while scanning electron microscope (SEM) and knife edge measurements were used to estimate the amount of ZnO in the focal volume in the iFROG experiments. Combining the results of the four measurement techniques, the local field enhancement could be reconstructed. Correcting the local field intensities in each sample with the thus obtained enhancement factors, the measured fractional exponents are shown to be in agreement with the simulations without the need to result in any of the previously suggested 2PA enhancing mechanisms.

VII.2. Sample Preparation and Characterization

There is a wealth of methods to produce ZnO nanorods, leading to optically and geometrically varying results [151]. Here we chose three techniques that are known to produce high quality nanorods with very little defects. Using samples produced in differing ways and even in different laboratories ensures that our conclusions are widely applicable. First two of the samples, (i) and (ii), were synthesized at the University of Barcelona by F. Güell and coworkers using the vapor-liquid-solid (VLS) technique [152, 153]. The nanorods were grown on fused quartz substrates with (i) Au nanoparticles and (ii) an Au thin film as the catalysts. The third sample (iii) was produced at Dublin City University by E. McGlynn and C. Gray via vapor phase transport (VPT) [154, 155] without using a catalyst, the nanorods grown on a fused silica substrate coated with a buffer layer of ZnO. SEM images of the three samples are shown in Fig. VII.1. Apart from size differences and possible Au deposits in the vicinity of the VLS-grown nanorods, the samples share the same intrinsic material properties as shown by previous studies [153, 155]. We verified this with x-ray diffraction measurements, conducted by G. Mangalgiri and B. Heidmann at the Helmholtz-Zentrum Berlin, indicating that all samples boast high quality ZnO wurtzite lattices, see Fig. VII.2. No traces of Au was found in these measurements, which is not a surprise considering that the amount of gold catalyst is tiny compared to the de-

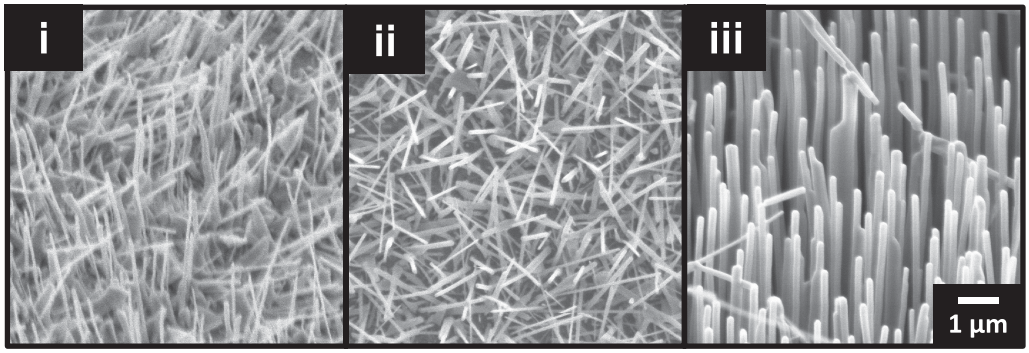

Figure VII.1 – *SEM images of the nanorods samples taken at ∡45°. (i) VLS with Au nanoparticle catalyst. (ii) VLS with Au thin film catalyst. (i) VPT with no catalyst. Reproduced from Publication [I].*

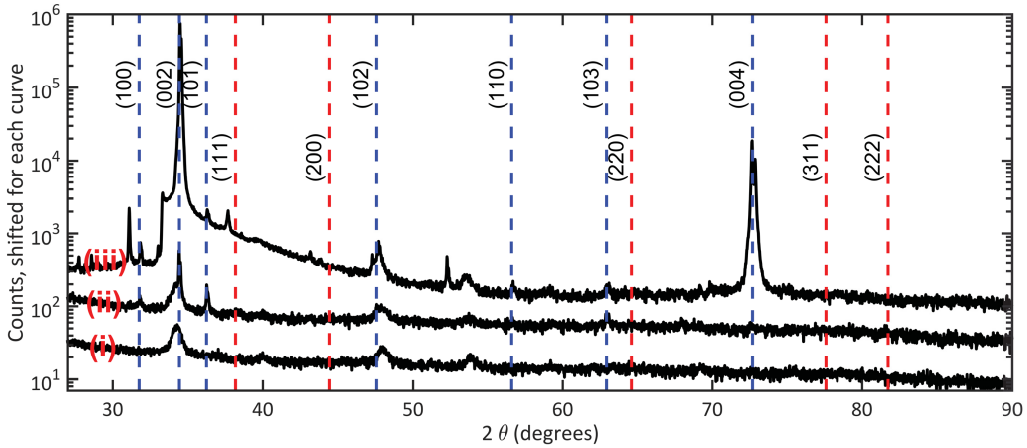

Figure VII.2 – *X-ray diffraction measurements for the three nanorods samples (black solid lines), the bottom curve is for sample (i), middle for (ii), and top for (iii). Calculated reflexes for ZnO (blue) and Au (red) are marked by the dashed lines and labeled with the corresponding Miller indices. The (004) peak found in sample (iii) indicates consistent orientation of nanorods perpendicular to the subtrate plane [150], a fact that can be easily verified from the SEM measurements, cf. Fig. VII.1.*

Table VII.1 – *Quantities derived from SEM and knife edge measurements, compared to the single crystal sample*

Sample	(i)	(ii)	(iii)	single crystal
SEM				
Film thickness (μm)	1.5	0.9	40	1000
Nanorod diameter (nm)	88	96	175	-
2D fill factor (%)	3.5	4.2	9.0	100
SEM + KNIFE EDGE				
3D fill factor ρ (%)	0.1	0.07	7	100

posited ZnO. Nevertheless, residual Au should still be found in between, on top, and on the surfaces of the nanorods in the VLS samples. The thin film catalyst sample (ii) contains more Au than the nanoparticle sample (i). This notion is supported by the visibly pink hue of sample (ii), indicating absorption due to a plasmon resonance. Samples (i) and (iii) are both white.

The geometry of the nanorods in each sample was estimated via the SEM measurements, as reported in Table VII.1. A 3D fill factor was derived from the 2D fill factor and the focal volume in the iFROG system, i.e. where the sample is placed for the power dependence measurements. The focal volume, in turn, was obtained through a knife edge measurement, giving a beam waist parameter $w_0 = 2.6\,\mu\text{m}$. By assuming Gaussian beam propagation, the Rayleigh length $z_R = \pi w_0^2/\lambda_0$ then establishes the focal volume $V = 2z_R\pi w_0^2$, yielding the 3D fill factors also given in Table VII.1.

VII.3. iFROG Measurements

Owing to the temporal resolution and the exploitation of interference in an iFROG measurement, nonlinear processes with differing coherence properties can be identified [49]. Specifically, coherent processes lead to a wavelength dependent fringe spacing, while incoherent processes are modulated at the carrier frequency, regardless of the emission wavelength. This effect can be clearly seen in Fig. VII.3(b) where an example iFROG trace measured with sample (i) is shown, featuring concomitant UV-PL and SHG spectra. The incoherent UV-PL band at around 380 nm has a constant fringe spacing so that all the fringes are parallel to the wavelength axis, as indicated by the green dotted lines. On the contrary, the fringes of the coherent SHG emission at 410 nm are tilted due to the irregular modulation period, highlighted by the green dash-dotted lines. This allows us to reliably distinguish the two closely-lying spectra. Notice that the SHG emission is severely weakened at wavelengths close to the UV-PL band. This is intended, and accomplished via a longpass filter which limits the photon energies to below the 2PA threshold, cf. Fig. VII.4.

The iFROG trace in Fig. VII.3(b) has been divided into two parts, the UV-PL spectrum residing at wavelengths shorter than 391 nm, and SHG at wavelengths longer than this. The cut is shown with the white dashed line. As an iFROG trace is a spectrally resolved interferometric autocorrelation (iAC), spectral integration performed separately for the SHG and PL parts yields two iAC signals, plotted in Figs. VII.3(a) and (c), respectively. The ratio r between the peak and minimum values for an iAC signal is related to power dependence exponent m of the nonlinear process through

$$m = \frac{\log_2 r + 1}{2}. \tag{VII.2}$$

Taking a closer look at Figs. VII.3(a) and (c), drastically different contrast ratios of 7.3 and 84 are observed for the SHG and UV-PL processes, respectively. Plugging these values into Eq. (VII.2), we obtain the exponents $m_{\text{SHG}} = 1.93$ and $m_{\text{PL}} = 3.70$. The exponent for SHG is very close to the ideal value of 2, as two photons are annihilated in the creation

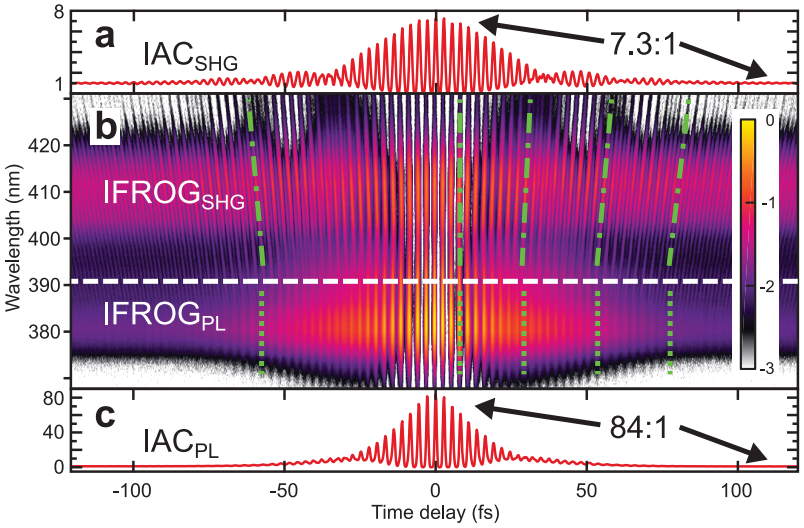

Figure VII.3 – *Power dependence measurement via iFROG, using sample (i). The concomitant PL and SHG emission bands are easily identified from the iFROG trace (b). Interferometric autocorrelation traces (a) & (c) are obtained by integrating over differing wavelengths ranges. Reproduced from Publication [I].*

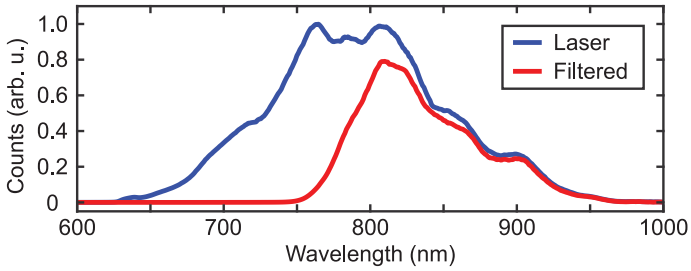

Figure VII.4 – *Spectra for the employed pulses before (blue) and after (red) longpass filtering. Reproduced from Publication [I].*

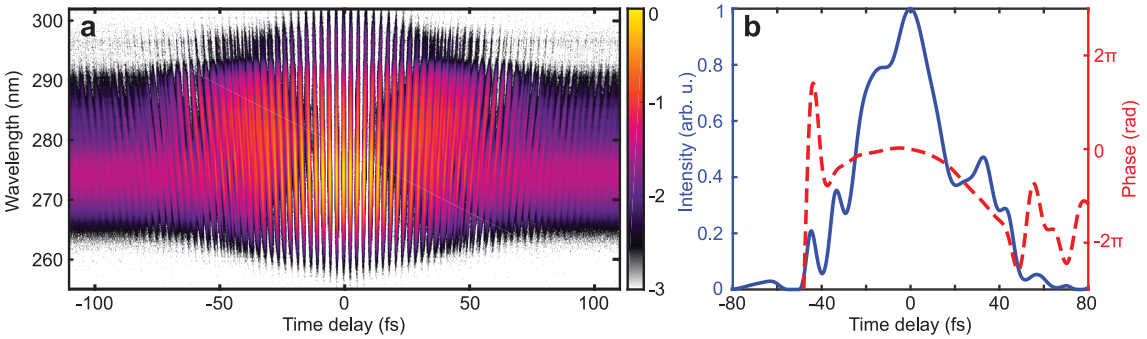

Figure VII.5 – ***a*** *THG-iFROG for sample (i).* ***b*** *Reconstructed intensity (blue solid line) and phase (red dashed line) in the time domain. The quadratic phase is caused by dispersion in the longpass filter. Reproduced from Publication [I].*

of a single frequency-doubled photon. The fractional exponent measured for UV-PL is more puzzling, indicating that on average a fractional number of photons is consumed to emit a single PL photon. These iFROG-based power dependence measurements were repeated many times for each sample at varying positions along the substrate plane so that a statistical sample of exponents was obtained. These values are reported further below in Table VII.3.

In addition to the power dependence measurements, we conducted THG-iFROG measurements to characterize the employed pulses *in situ* using the nanorods themselves. The reconstructed 39-fs pulse is shown in Fig. VII.5 along with the measured trace. Together with the knife edge and average power measurements, the temporal pulse profile yields a peak incident field intensity of $I_0 \approx 0.5\,\mathrm{TW\,cm^{-2}}$. The precise knowledge of I_0 will prove crucial in explaining the observed power dependences through our numerical simulations.

VII.4. Time-Resolved Photoluminescence Measurements

A total of three sets of TRPL measurements were conducted for different purposes. The primary interest was to establish relative emission strengths of each nanorods sample with respect to a commercial single crystal ZnO sample. This does not strictly require a temporal resolution, but the TRPL system available featured a tunable Ti:sapphire laser which allowed us to push the SHG peak farther away from the UV-PL peak ($\lambda_0 = 830\,\mathrm{nm}$ was selected). Moreover, a much broader spectrum than what was possible with our iFROG system could be recorded, which is necessary to capture the entire PL emission spectra. Thus, an intensity-calibrated set of measurements was made, which, after integrating over time, yield the emission spectra shown in Fig. VII.6(a). After removing the SHG contribution at $\approx 415\,\mathrm{nm}$ with an exponential fit (dotted lines), the luminous efficiencies η reported in Table VII.2 are obtained. Note that even though the amount of ZnO illuminated by the laser is tiny in the nanorods samples (in comparison to the single crystal case), the luminous efficiencies for all samples are within a factor 4 of each other, a clear proof that the nanostructures are highly nonlinear.

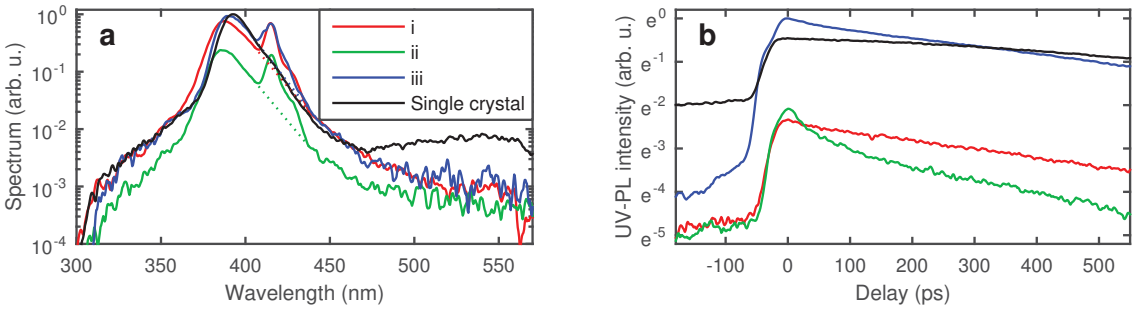

Figure VII.6 – *TRPL measurements with the aim of measuring (a) the luminous efficiencies η, and (b) the decay times T_{decay} for the UV-PL emission. Reproduced from Publication [I].*

A second set of TRPL measurements was made to measure the power dependence independently from iFROG, with slightly different experimental conditions. Namely, the pulses were longer, roughly 90 fs, and the SHG peak was far from the two-photon resonance wavelength. The incident intensity was adjusted with neutral density filters, and the emission spectra were integrated as above to give a single number for the emission strength. The resulting exponents m_{PL}, reported in Table VII.3, serve as a further test for the validity of our simulations and conclusions. It should be noted that the TRPL power dependence measurements could not have been made with the closely-lying UV-PL and SHG bands (required to study the involvement of 2PA) employed in the iFROG measurements, because TRPL cannot easily distinguish between the two contributions.

Finally, a third set of TRPL measurements was made, this time fully exploiting the high temporal resolution of the employed streak camera. The decay of the UV-PL emission was measured as shown in Fig. VII.6(b). Note that the employed incident field intensities differed, so that the emission strengths of different samples are not comparable. A fit of exponential functions yields the time constants given Table VII.2. All the samples have long decay times T_{decay} of few hundred picoseconds, indicating that the nanorods are of high quality with very few defects that could recombine the carriers nonradiatively. This conclusion is also supported by the lack of a VIS-PL band in the nanorods emission spectra, in contrast to the single crystal for which a green emission band is clearly seen, cf. the range > 470 nm in Fig. VII.6(a). Peculiarly, sample (ii) also features a second, fast decay process with $T_{\mathrm{decay}} = 30$ ps. A likely explanation is given in Ref. [156], where an equally fast decay dynamics were attributed to plasmonic effects via Au nanoparticles attached to walls of ZnO nanorods. Coincidentally, sample (ii) is precisely the one with the visibly pink hue, indicative of plasmonic effects.

Table VII.2 – *Quantities derived from TRPL measurements*

Sample	(i)	(ii)	(iii)	single crystal
Luminous efficiency η	0.92	0.28	1.03	1
Time constant T_{decay} (ps)	490	330 (30)	530	970

VII.5. Experimental Results

The measured exponents for iFROG and TRPL measurements are given with error bounds in Table VII.3. The SHG exponents are close to the ideal value of 2 for all samples, indicating good performance of the iFROG system. The UV-PL exponents obtained with either method agree within error bounds, although the uncertainty in the TRPL values is rather high.

Combining all the above results from SEM, knife edge, iFROG, and TRPL measurements, we can now reconstruct the field enhancement γ [18] though this simple equation

$$\gamma = \sqrt[2m]{\eta/\rho}. \tag{VII.3}$$

Table VII.3 – *Measured exponents m_{PL} and m_{SHG} for UV-PL and SHG emission bands, respectively.*

Sample	(i)	(ii)	(iii)
		iFROG	
m_{PL}	3.73 ± 0.20	3.88 ± 0.13	3.45 ± 0.14
m_{SHG}	1.94 ± 0.07	1.99 ± 0.06	1.87 ± 0.02
		TRPL	
m_{PL}	3.9 ± 0.2	4.3 ± 0.8	3.0 ± 0.3
		UV-PL emission peak wavelength	
λ_{PL} (nm)	381	381	384

The relevant values are assembled in Table VII.4 for easy reference. The highest field enhancement is obtained for sample (i). The results are in good agreement with a previous studies [18, 19], where up to 6 fold intensity enhancements γ^2 were observed for ZnO nanorods. The 1.5 to 2.5 fold amplitude enhancement γ over the single crystal might not seem overly impressive at first glance but the small difference becomes important for nonlinear processes. For example, SHG in the nanorods is 5 to 39 times more efficient than in the single crystal, and sample (i) has an 8-fold increase over sample (iii). This result shows that morphology and choice of a growth method can have a significant effect in the nonlinear properties of nanorods thin films. To better understand the mechanisms that led to these results, we turn to numerical simulations of the MPA process.

Table VII.4 – *Combined results from SEM, TRPL, and iFROG measurements*

Sample	(i)	(ii)	(iii)	single crystal
		SEM + knife edge		
3D fill factor ρ (%)	0.1	0.07	7	100
		TRPL		
Luminous efficiency η	0.92	0.28	1.03	1
		iFROG		
m_{PL}	3.73	3.88	3.45	—
		SEM + knife edge + TRPL + iFROG		
Field enhancement γ	2.49	2.16	1.48	1
Intensity enhancement γ^2	6.2	4.7	2.2	1

VII.6. MPA Simulations

Our model for the MPA induced luminescence process is based on a rate equation for the carrier density N given in Ref. [5]. After slight modifications, we obtain

$$\frac{\mathrm{d}N(t)}{\mathrm{d}t} = \alpha N(t) I(t) + \sum_{m=2}^{6} \mu_m(N) \beta_m(N) I(t)^m - \frac{N(t)}{T_{\mathrm{decay}}}. \tag{VII.4}$$

Here we are making the implicit assumption that the number of excited carriers is proportional to the UV-PL emission. The first term from the left on RHS of Eq. (VII.4) corresponds to avalanche ionization (AI), the second to MPA, and the third to relaxation processes. The local field intensity $I(t)$ is taken to be a sech^2 pulse with a peak intensity I_0 and a FWHM width of 39 or 90 fs, corresponding to the iFROG and TRPL experiments, respectively. As many of the material parameters are unknown for ZnO nanorods, and might very well depend on the specific sample morphology, we take the values for bulk ZnO where available. The avalanche constant is set to $\alpha = 34\,\mathrm{J\,cm^{-2}}$ [5], and $T_{\mathrm{decay}} = 0.7\,\mathrm{ps}$ [157].

Let us take a closer look at the MPA term $\sum_{m=2}^{6} \mu_m \beta_m I(t)^m$ in Eq. (VII.4). The order of the MPA process is denoted by m. By taking the sum over $m = 2 \ldots 6$, we consider MPA processes from second to sixth order simultaneously, implicitly allowing the generation of hot carriers. The Keldysh absorption coefficients β_m [5, 59] are defined as

$$\beta_m(N) \approx \frac{\omega_0}{9\pi} \left(\frac{m_r \omega_0}{\hbar} \right)^{3/2} \left(\frac{e^2}{8\omega_0^2 m_r c \epsilon_0} \right)^m \frac{e^{2m}}{[n_0 E_g(N)]^m}. \tag{VII.5}$$

Here $m_r = 0.28 m_e$ is the carrier reduced mass [158], m_{e} the electron rest mast, e the elementary charge, and $n_0 = 1.96$ the refractive index of ZnO [159]. In order to assess whether bandgap renormalization (BGR) could allow 2PA to be a significant factor in our experiments, we have allowed the bandgap $E_g(N)$, and subsequently the absorption $\beta_m(N)$, to depend on the carrier density N. The behavior of $E_g(N)$ is based on reported values of BGR-induced bandgap narrowing in Refs. [157, 160].

In order to account for the experimentally measured pulse spectra (different for iFROG and TRPL) in such a manner that no appreciable 2PA can occur unless photon energies exceed half of the bandgap, we introduce a weighting factor $\mu_m(N)$,

$$\mu_m(N) = \frac{\int_0^\infty S_m(\omega) D(\hbar\omega, N) \mathrm{d}\omega}{\int_0^\infty S_3(\omega) D(\hbar\omega, N) \mathrm{d}\omega}. \tag{VII.6}$$

In short, $\mu_m(N)$ describes the overlap of the computed harmonic spectra $S_m(\omega)$ of the incident pulse with the density of states (DoS) $D(\hbar\omega, N)$ of the ZnO nanorods. The higher the overlap, the stronger the weighting. Notice that the DoS depends on the carrier density N. This allows BGR to be taken into account such that the DoS is shifted to lower energies when the bandgap is reduced due to high carrier densities, thus increasing the

Table VII.5 – *Weighting factors μ_m for MPA orders 2 through 6 for $N = 0$.*

MPA order m	2	3	4	5	6
μ_m	$1.3 \cdot 10^{-5}$	1.0	2.8	5.0	3.6

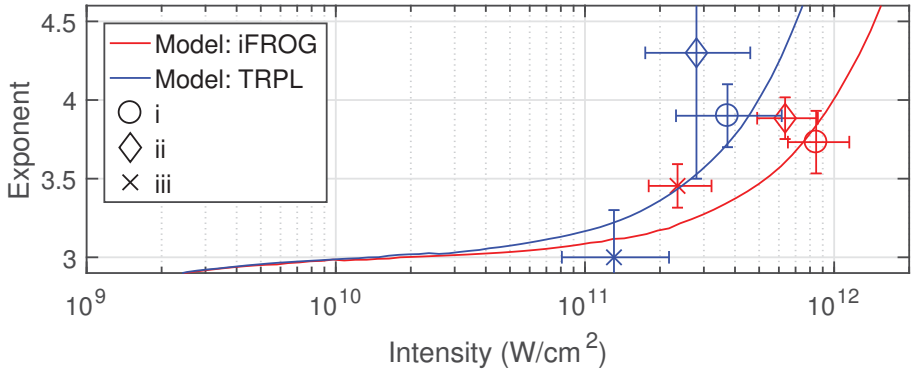

Figure VII.7 – *MPA exponents. Reproduced from Publication [I].*

overlap with harmonics. The weighting factors for the case of an unperturbed bandgap ($N = 0$, $E_g(0) = E_g$) are given in Table VII.5. The denominator in Eq. (VII.6) normalizes the weights such that 3PA is unaffected ($\mu_3(N) = 1$). Notice that $\mu_2(0)$ for 2PA is tiny in comparison. This is because only the weak short-wavelength tail of the SHG spectrum exceeds the bandgap, and because the DoS is low for states slightly above the bandgap. Plugging the weights $\mu_m(0)$ into equation Eq. (VII.4), we see that the SHG contribution to the carrier density is drastically reduced in favor of higher harmonics. The reasoning behind this DoS-based weighting is analogous to *Fermi's golden rule* [161], which, among other things, states that the transition probability from one quantum mechanical state (in our case a valence band electron) to a quasi-continuum (conduction band) is proportional to the density of the final states (conduction band DoS).

Solving the rate equation Eq. (VII.4) for a range of peak local field intensities I_0, we obtain the peak carrier densities $N_{\text{peak}}(I_0)$, i.e., a power dependence of the form

$$N_{\text{peak}}(I_0) = I_0^{m_{\text{PL}}(I_0)}. \tag{VII.7}$$

Solving for the exponent, we take the logarithm of Eq. (VII.7) and divide by $\log I_0$,

$$m_{\text{PL}}(I_0) = \frac{\log N_{\text{peak}}(I_0)}{\log I_0}. \tag{VII.8}$$

The results are plotted in Fig. VII.7. The two curves correspond to two separate runs of the simulations, conducted with parameters corresponding to the iFROG (red solid line) and TRPL (blue solid line) experiments. The experimentally measured exponents as given in Table VII.3 are shown as well. The vertical error bars are also taken from

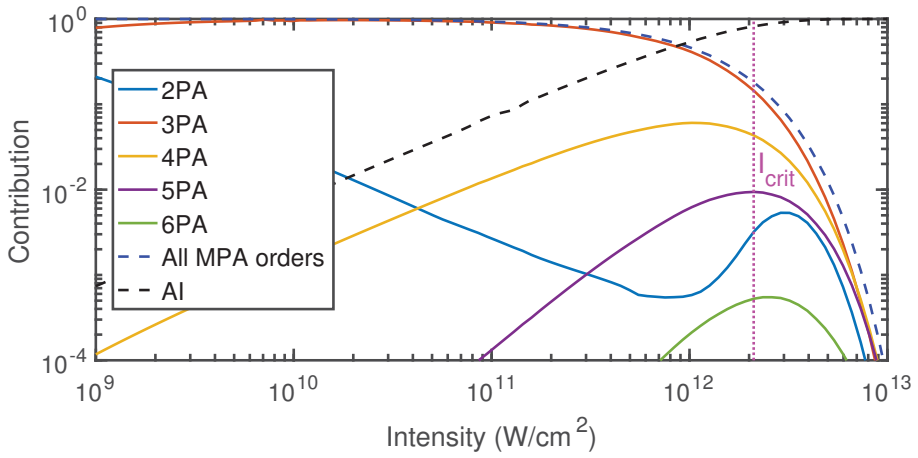

Figure VII.8 – *The simulated relative contributions of different MPA orders and avalanche ionization as the function of local field intensity. Reproduced from Publication [I].*

Table VII.3. The intensity coordinates of these points are derived by multiplying the incident field intensity (0.5 TW cm^{-2} for iFROG) with the squared field enhancement factors γ^2 given in Table VII.4, and adjusting for the neutral density filters employed in the experiments. The filters limited the incident intensity such that catastrophic material damage was avoided. The horizontal error bars are obtained by allowing an uncertainty of 30 % for the measured 3D fill factors in Table VII.1, and 10 % for the beam waist w_0.

Our model also makes it possible to quantify the number of carriers generated via each of the considered nonlinear processes. The relative contributions of each of the five MPA orders (solid lines), their sum total (blue dashed line), and avalanche ionization (black dashed line) in the iFROG simulation are shown in Fig. VII.8. Furthermore, the threshold intensity for material damage can be estimated. A commonly used criterion [5, 162] is to compute the critical carrier density N_{crit} for which the plasma frequency $\omega_p = \sqrt{Ne^2/(m_r\epsilon_0)}$ is equal to the carrier frequency ω_0 of the incident laser pulse. When this condition is met, linear absorption of the carrier quickly leads to damage. For the iFROG experimental conditions, we get $N_{\text{crit}} \approx 4.8 \cdot 10^{26}\,\text{m}^{-3}$ or $\approx 1\,\%$ of the total electron density, which can then be mapped via the simulation data to a local field intensity of $I_{\text{crit}} \approx 2.1\,\text{TW cm}^{-2}$.

VII.7. Discussion

Taking a look at Fig. VII.7, the first thing to notice is that the fractional exponent values from 3 to above 4, as measured via iFROG and TRPL, are readily reproduced by the numerical simulations for the experimentally accessible local field intensities in the order of $\approx 10^{11}\,\text{W cm}^{-2}$. We can also see the simulations and experiments agree within the margins of error. The curve for the TRPL model lies higher due to the longer pulse duration of 90 fs, which increases the influence of avalanche ionization at high intensities. Even

for the iFROG simulations with 39-fs pulses, AI is seen in Fig. VII.8 to reach parity with the MPA processes at $\approx 0.9\,\mathrm{TW\,cm^{-2}}$. These significant contributions from AI might seem surprising given that our pulses are fairly short, but previous reports employing wide-bandgap materials and similar pulses have shown that, at near breakdown intensities, most carriers are indeed generated by AI [5, 162, 163]. In contrast, the MPA processes only serve to seed AI with an initial population of hot conduction band electrons. We investigated the timescales of this phenomenon and found that, for the iFROG conditions, AI is most efficient 12 fs after the pulse maximum has passed. If a shorter 7-fs pulse is employed instead, AI never exceeds MPA in number of generated carriers.

Going back to the question of 2PA assisting processes posed in the introduction, let us look at the 2PA contribution (blue solid line) in Fig. VII.8. In the experimentally relevant range of $\approx 10^{11}\,\mathrm{W\,cm^{-2}}$, we see that $< 1\,\%$ of the carriers is generated by 2PA. Instead, 3PA dominates the MPA processes, with minor contributions of 4PA. At around $0.5\,\mathrm{TW\,cm^{-2}}$, once a high enough carrier density is reached, we see the bandgap renormalization included in our model kicking in. BGR increases the influence of 2PA for higher intensities, but even at the damage threshold I_{crit} we see that 3PA, 4PA, and even 5PA are more efficient. This shows that even though we made an effort to allow bandgap narrowing enhanced 2PA, the effect is still insignificant. The fact that 3PA and AI vastly exceed 2PA in their relative contributions to the carrier density strongly suggests that 2PA enhancing mechanism such as BGR are of little importance in the UV-PL process.

Let us compare the computed damage threshold $I_{\mathrm{crit}} \approx 2.1\,\mathrm{TW\,cm^{-2}}$ to our experimental observations. When no attenuating ND filters were used in the iFROG setup, catastrophic optical damage could be inflicted on all of the three nanorod samples while the single crystal was unaffected. Yet, the estimated incident intensity is only $0.5\,\mathrm{TW\,cm^{-2}}$ — four times smaller than the computed damage threshold. If field enhancement in the nanorods is included, however, I_{crit} can be reached for samples (i) and (ii). In the case of sample (iii), the observed damage is attributed to heat accumulation instead. This conclusion is supported by an observed redshift of the UV-PL emission peak in sample (iii) at intensities slightly below the empirical damage threshold. The redshift is associated with a narrowing of the bandgap, which can easily lead to more absorption, then to more heating and a still narrower bandgap, and so on until excessive heat or absorption (or both) breaks the nanorods.

On the other hand, such a redshift is also consistent with the onset of lasing [164]. We will now entertain the possibility of lasing, and explain why we find heat accumulation a more plausible explanation. Furthermore, we seek to rule out lasing as a possible factor in the measured exponents m_{PL} for all the samples. Room-temperature lasing in ZnO nanorods can be initiated with NIR pulses under certain conditions [141], but aside from the above mentioned redshift in sample (iii), we found no experimental evidence of lasing. Namely, we did not observe a step-like increase of the power dependence [165], sharp spectral features associated with Fabry–Pérot modes forming along the length of the nanorods [166], or quickly decaying strong peaks on top of the PL decay in the TRPL measurements [167]. Nevertheless, it is possible that we are operating very close to a lasing threshold where the above mentioned telltales are not very noticeable but could

still affect the m_{PL} measurements.

To settle this matter, we can take a closer look at the carrier densities reached in our experiments. Versteegh *et al.* reported [166] that, unless special measures are taken, carrier densities N well above the so called *Mott density* must be reached before lasing occurs. Once the Mott density of $N_{\mathrm{Mott}} = 1.5 \cdot 10^{23}\,\mathrm{m}^{-3}$ for ZnO is exceeded, excitons are destroyed via Coulomb screening, giving rise to an electron-hole plasma instead [157]. Onset of lasing can then be explained through many-body theory. Using our model, we can obtain the peak carrier density as a function of local field intensity, plotted in Fig. VII.9 (black solid line). The simulations indicate that we operate close to N_{Mott} or even exceed it locally when field enhancement is considered. Using the maximum local intensity I_{max} (blue solid line) as permitted by the error bounds shown in Fig. VII.7, we obtain an upper limit of $N_{\mathrm{max}} = 2 \cdot 10^{25}\,\mathrm{m}^{-3}$ for the carrier density reached in our experiments. Even in this extreme case, N_{max} is still below the lowest reported lasing threshold of $5.2 \cdot 10^{25}\,\mathrm{m}^{-3}$ in Ref. [166] for 100-fs NIR pulses. A more recent study employing pulses similar to our own [164] gave an even lower threshold value of $3 \cdot 10^{25}\,\mathrm{m}^{-3}$ (green dashed line), which is still slightly above N_{max}. Because the lasing thresholds found in the literature are unlikely to be exceeded in our power dependence measurements, we conclude against lasing having any effect to our results, or the observed redshift. Heat accumulation is therefore the only remaining candidate, and thus our explanation for the observer redshift in sample (iii). In any case, the m_{PL} were measured below the threshold intensity for the redshift, so neither heat or lasing can significantly affect our measurements.

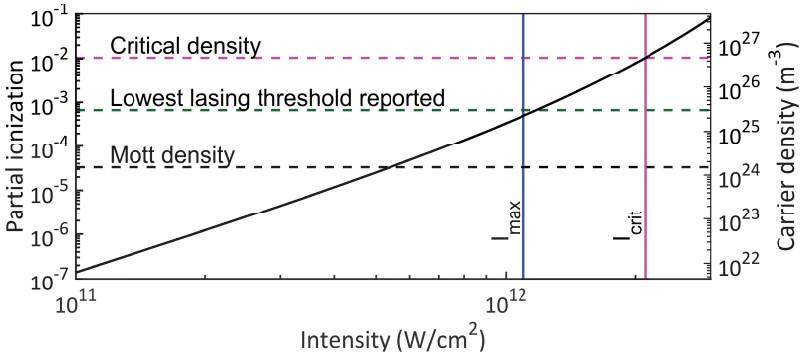

Figure VII.9 – *Simulated carrier density versus local field intensity (black solid line). While the Mott density (black dashed line) can be exceeded with the maximum local field intensity corresponding to our experiments (blue solid line), the resulting carrier density is still below the lowest reported [164] lasing threshold for NIR pulses.*

As for the differences between the three samples, we can only offer speculative answers. One clear trend is that the higher the amount of gold found in the samples, (iii) having none and (ii) more than (i), the higher the measured exponents in both iFROG and TRPL measurements are. It is possible that plasmonic effects in Au affect the field enhancement [168] in combination with nanorods morphology [18, 19], or result in an increased bandedge emission [156]. The seemingly contradicting fact that the highest

field enhancement was obtained for sample (i) while the highest exponents were measured for sample (ii) may be meaningless, as the exponent measurements for the two samples agree within error bounds. Definitive answers warrant further studies.

To summarize, we have studied the UV-PL process in ZnO nanorods, induced by multiphoton absorption of NIR pulses, via iFROG and other methods. It was shown that local field enhancement allows higher-than-expected local intensities to be reached, leading to large exponents for the power dependent emission process. Differing enhancement factors were found for the three employed nanorods samples, grown with different methods, corresponding to up to an 8-fold increase in SHG efficiency. The differences were ascribed to varying gold content and nanorods morphology, underlining that the choice of growth method can have a significant effect on the nonlinear properties of the nanorod thin films. Numerical simulations revealed that 3PA and avalanche ionization dominate over other MPA orders in carrier generation. Furthermore, the contribution of 2PA was found to be insignificant, even when bandgap renormalization was considered.

CHAPTER VIII

Investigation of Noninstantaneous Optical Processes

Now that the iFROG method has been established in Chapters IV and V, we may move on to the *primus motor* of this work — the investigation of noninstantaneous optical processes. Specifically, we employ THG-iFROG to measure the few-femtosecond dephasing times of (i) resonant third-order polarization in a dielectric thin film, and (ii) localized surface plasmon polaritons in metallic nanoantennas. We begin by explaining how iFROG can be exploited for this purpose in Section VIII.1. Based on Publication [V], the case of third-order polarization is studied in Section VIII.2. Lastly, in Section VIII.3, we discuss the plasmonic nanoantennas — a previously unpublished collaboration with the University of Konstanz.

VIII.1. Measurement of a Finite Dephasing Time with iFROG

After briefly considering noninstantaneous processes in Chapter II, we forwent the concept and instead presupposed, up to this point, that all the light-matter interaction we have described happens instantaneously. That is, the polarization $P(t)$ induced in a nonlinear medium was assumed to follow the incident electric field $E(t)$ immediately so that the two are in phase. Note that this true even for phase-matching: the phase difference between $E(t)$ and the nonlinear polarization $P^{(\mathrm{NL})}(t)$ arises from propagation effects, not from a finite response time.

In many situations, an instantaneous response of an optical medium is a reasonable assumption which can greatly simplify the analytical or numerical treatment of a given phenomenon. As discussed, optical processes where only virtual states are involved, such as harmonic generation under nonresonant conditions, are typically considered to be instantaneous. For resonant excitation, on the other hand, this assumption is likely to be unjustified. Strictly speaking, material response is truly instantaneous if and *only*

if the medium is lossless and there is no dispersion, i.e. the susceptibilities $\chi^{(n)}$ are real and independent of ω [7, 61]. For broadband pulses such as ours, these conditions are practically never even approximately fulfilled. Any light-matter interaction with ultrashort pulses is therefore noninstantaneous, but, depending on the application, the response can nevertheless be so fast that it bears no meaning for the outcome.

Considering pulse characterization, such a quasi-instantaneous material response is nearly always expected, especially with correlation methods such as FROG [10]. One can argue that this assumption is valid as long as the finest resolvable detail of the temporal envelope (e.g. the width of the main peak envelope) is much longer than the response time of the nonlinear medium. According to Boyd [8], the characteristic response time of a nonresonant electronic nonlinearity can be estimated by the time T it takes for an electron to orbit around its nucleus. Using the Bohr model, we have

$$T = \frac{2\pi a_0}{v},$$

where $a_0 = 0.5\,\text{Å}$ is the Bohr radius, and $v = c/137$ a typical velocity for an electron. This yields the response time $T \approx 0.15\,\text{fs}$, which is still a fraction of the shortest reported NIR pulse durations of $\approx 4\,\text{fs}$ [108, 169–171], or even the 2.5-fs pulse extending from NIR to near-UV demonstrated by Matsubara *et al.* [172]. Two-beam coupling experiments have confirmed that the electronic response time of fused silica is $< 1\,\text{fs}$ [173]. Recently, attosecond streaking measurements established an intensity-dependent delayed response in the range of 45–115 as for a gaseous medium under nonresonant conditions [174]. In practice, no self-referenced pulse characterization technique claims attosecond precision. Whatever detrimental effect a quasi-instantaneous ($< 1\,\text{fs}$) nonlinearity imposes is likely to be insignificant in comparison to other sources of error, especially if the pulses are much longer than a single cycle.

The story is quite different when a finite dephasing time T_2 is involved. Let us consider a medium with a response function $R^{(1)}(t)$ such that the linear polarization induced by an electric field $E(t)$ is

$$P^{(1)}(t) \propto R^{(1)}(t) * E(t). \tag{VIII.1}$$

Thus, for our collinearly-propagating variably-delayed twin pulses in iFROG, the linear polarization is

$$\begin{aligned} P^{(1)}_{\text{col}}(t,\tau) &\propto R^{(1)}(t) * [E(t) + E(t-\tau)] \\ &= R^{(1)}(t) * E(t) + R^{(1)}(t) * E(t-\tau) \\ &\propto P^{(1)}(t) + P^{(1)}(t-\tau). \end{aligned} \tag{VIII.2}$$

As explained in Chapter II, for metallic nanostructures with dimensions much smaller than the carrier wavelength, the coupling of the incident field into surface plasmon polaritons can lead to a greatly enhanced local electric field. The linear polarization can then act as a driving term for the nonlinear polarization, while the minuscule contribution of the incident field can be ignored [16, 25, 27]. If we also assume the nonlinear

polarization of order h to be an instantaneous process, we have [22, 25]

$$P^{(h)}(t) \propto \left[P^{(1)}(t)\right]^h = \left[R^{(1)}(t) * E(t)\right]^h, \tag{VIII.3}$$

so that the corresponding h^{th}-order polarization for the two collinear pulses is

$$P^{(h)}_{\text{col}}(t) \propto \left[P^{(1)}(t) + P^{(1)}(t-\tau)\right]^h. \tag{VIII.4}$$

The polarization $P^{(h)}_{\text{col}}(t)$ then acts as a source of harmonic radiation, which can be measured. Taking the Fourier transform of Eq. (VIII.4) with respect to t, and subsequently the absolute square, we have

$$I^{(h)}_{\text{iFROG}}(\omega,\tau) \propto \left| \int_{-\infty}^{+\infty} \left[\mathcal{P}^{(1)}(t) + \mathcal{P}^{(1)}(t-\tau)\right]^h e^{-i\omega t}\,\mathrm{d}t \right|^2, \tag{VIII.5}$$

which we define to be the iFROG trace for the case of an instantaneous harmonic generation via a noninstantaneous linear polarization. Here we have included the carrier wave via $\mathcal{P}^{(1)}(t) = P^{(1)}(t)e^{i\omega_0 t}$. Comparing Eq. (VIII.5) with the standard, instantaneous iFROG formula Eq. (IV.1), we see that that the electric field $\mathcal{E}(t)$ has been replaced by the linear polarization $\mathcal{P}^{(1)}(t)$, but otherwise the two equations are identical. Thus, if $R^{(1)}(t)$ describes the temporal linear-polarization response of the nonlinear medium (and leads to instantaneous harmonic generation), we effectively measure the temporal structure of the local electric field with iFROG, not the incident field itself [25].

Let us consider another scenario. Suppose that this time there is no appreciable field enhancement involved, so that a noninstantaneous linear polarization is *not* acting as the principal driving field for a higher-order polarization. Instead, let the third-order polarization itself be noninstantaneous, represented by the response function $R^{(3)}(t)$. The noninstantaneous third-order polarization is then given by [61]

$$\mathbf{P}^{(3)}_i(t) \propto \iiint_{-\infty}^{t} R^{(3)}_{ijkl}(t-\tau_1; t-\tau_2; t-\tau_3)\mathbf{E}_j(\tau_1)\mathbf{E}_k(\tau_2)\mathbf{E}_l(\tau_3)\,\mathrm{d}\tau_1\,\mathrm{d}\tau_2\,\mathrm{d}\tau_3\,. \tag{VIII.6}$$

Here the tensorial quality of the interaction has been included via the indices i, j, k, and l. We simplify Eq. (VIII.6) by (i) neglecting the tensor notation in favor of scalars, (ii) setting the incident fields to be identical, $E_j(t) = E_k(t) = E_l(t) = E(t)$, and (iii) assuming that the response function can be factorized, i.e., $R^{(3)}_{ijkl}(t-\tau_1; t-\tau_2; t-\tau_3) \to R^{(3)}(t-\tau_1)R^{(3)}(t-\tau_2)R^{(3)}(t-\tau_3)$. This leads to

$$P^{(3)}(t) \propto \left[R^{(3)}(t) * E(t)\right]^3. \tag{VIII.7}$$

Comparing this to Eq. (VIII.3), we can immediately see that a similar derivation as above yields another finite response time THG-iFROG equation akin to Eq. (VIII.5), but this

time we measure $R^{(3)}(t) * E(t)$ instead of $R^{(1)}(t) * E(t)$. That is, we probe the finite response time of the third-order nonlinearity associated with THG.

By measuring the same incident pulse $E(t)$ using a different nonlinear medium with an instantaneous response (i.e. $R(t)$ is a δ-function) we obtain $E(t)$ as usual. With both the noninstantaneous response,

$$E^{(\mathrm{NI})}(t) = R(t) * E(t), \tag{VIII.8}$$

and $E(t)$ at hand, a deconvolution analysis then yields the response function $R(t)$ of the noninstantaneous medium. To stress the importance of this result, we find that *iFROG allows us to measure the noninstantaneous response* of a given nonlinear optical medium via a comparison to a quasi-instantaneous medium.

While the above formulation permits $R(t)$ to be complex-valued, physical interpretation of such an entity can be problematic. As a first approximation, we therefore limit ourselves to real-valued $R(t)$. When performing the deconvolution of $E^{(\mathrm{NI})}(t) = R(t) * E(t)$ in the time domain, we found it sufficient to employ a right-sided exponential decay function

$$R(t, T_2) = u(t) e^{-t/T_2}, \quad u(t) = \begin{cases} 1 & t \geq 0 \\ 0 & t < 0 \end{cases}, \tag{VIII.9}$$

where T_2 is the dephasing time constant. The time constant T_2 is adjusted for best fit between $E^{(\mathrm{NI})}(t)$ and $R(t, T_2) * E(t)$. The Fourier transform of Eq. (VIII.9) yields a Lorentzian lineshape, which in turn corresponds to the ideal symmetric resonance as modeled via a damped harmonic oscillator, as discussed in Chapter II. Although an asymmetric Fano resonance (arising from the interference between a narrow-linewidth resonance and a continuum of states) might be more appropriate in certain situations [175], we do not expect to encounter narrow resonances in our experiments, which is why the Lorentzian and the corresponding exponential decay function of Eq. (VIII.9) will suffice.

Aside from the time-domain deconvolution described above, another possible approach is to perform the deconvolution in the spectral domain. Properties of the convolution function makes Eq. (VIII.8) a simple product in the Fourier domain,

$$\begin{aligned} & \mathcal{F}\left\{E^{(\mathrm{NI})}(t)\right\} = \mathcal{F}\{R(t) * E(t)\} = \mathcal{F}\{R(t)\} \cdot \mathcal{F}\{E(t)\} \\ \Leftrightarrow \quad & E^{(\mathrm{NI})}(\omega) = R(\omega) \cdot E(\omega). \end{aligned} \tag{VIII.10}$$

Typically, the deconvolution problem of Eq. (VIII.10) is used in a forward fashion with numerical minimization methods. Provided that one can ensure $|E(\omega)| \gg 0$ in the spectral interval under consideration, this process can be significantly simplified by simply dividing Eq. (VIII.10) with $E(\omega)$, yielding the complex-valued response function $R(\omega)$. This result can then be compared to the Lorentzian $\mathcal{F}\{R(t, T_2)\}$ obtained from the time-domain approach to deconvolution. To fully describe the nonlinear polarization, a nuclear (Raman, phonon) contribution should be included in addition to the stronger electronic response [176]. For simplicity, we limit ourselves to the electronic contribution in our models.

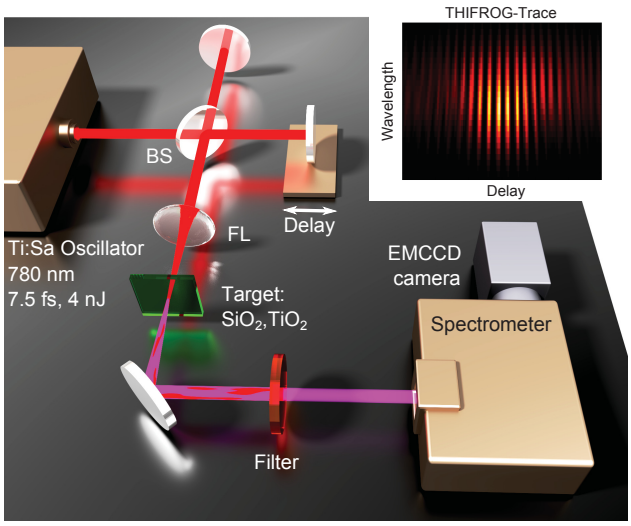

Figure VIII.1 – *Simplified illustration of the THG-iFROG setup employed. Reproduced with permission from Publication [V].*

VIII.2. Resonant Polarization Dynamics in a Dielectric Thin Film

Here we demonstrate the capability of THG-iFROG to measure a few-femtosecond dephasing time in dielectric media. Specifically, we employ two dielectrics, (i) a titania (TiO_2) thin film grown on a fused silica (FS, SiO_2) substrate, and (ii) a bare FS substrate. Titania is a broad bandgap semiconductor with $E_g = 3.2\,\mathrm{eV}$, while silica is an insulator with $E_g = 9.0\,\mathrm{eV}$. Employing NIR pulses with photon energies of $\approx 1.5\,\mathrm{eV}$, the third-harmonic of our laser exceeds the bandgap of titania, and is found to be in resonance with the second conduction band. Silica, on the other hand, is far from resonance, and thus serves as the quasi-instantaneous reference measurement. In terms of Eq. (VIII.8), the THG-iFROG measurement of titania yields $E^{(\mathrm{NI})}(t)$, and the silica measurement gives $E(t)$. A time-domain deconvolution analysis then yields the response function $R(t)$ of titania.

VIII.2.1. Experiments

Based on our previous description of the iFROG measurements in Chapter IV and Appendix A, the present experiments are easily explained. As a reminder, a simplified illustration of the THG-iFROG setup is shown in Fig. VIII.1. The only major difference to previous THG-iFROG experiments is that here the nonlinear medium is changed between the two measurements, employing (i) the titania thin film and (ii) the fused silica substrate. The titania thin film sample was produced at Laserzentrum Hannover by the group of Detlev Ristau.

In the normal dispersion regime (the case with our samples), THG from focused Gaussian beams vanishes if the focal plane is well within the bulk [8], but can still occur near

interfaces and in deposited thin films [177]. Specifically, constructive interference can only occur efficiently if the beam waist w_0 is located (along the direction of beam propagation) within one confocal parameter $b = kw_0$ of a discontinuity in the $\chi^{(3)}$ nonlinearity, i.e., an interface. In any other case THG is inefficient due to destructive interference, a consequence of the so-called *Gouy phase-shift* experienced by the beam as it passes through the focus. Consequently, we can be sure that the measured THG signal originates at (i) the titania thin film or (ii) the substrate surface. For the titania sample, a much stronger signal expected from the thin film than from the substrate [17].

The measured THG-iFROG traces, along with the retrieved electric field intensities and phases for both samples, are shown in Fig. VIII.2. Even with a naked eye one can see that the bright, high-intensity portion of the titania trace in Fig. VIII.2(b) is wider than the trace for silica in Fig. VIII.2(a), indicating a longer pulse for the titania case. This difference becomes clearer when the DC and FM modulation bands in Figs. VIII.2(c)–(f) are compared. The retrieved pulse intensities (solid lines) in Figs. VIII.2(g) and (h) confirm the difference in FWHM pulse durations, which are 10.1 fs for the bare fused silica substrate and a much longer 15.7 fs for the titania thin film. It should be stressed that both measurements were conducted with identical incident pulses, and that any difference between the measurements must be due to the employed nonlinear media. The retrieved parabolic phases (dashed green lines) indicate that the pulses were slightly chirped due to uncompensated group delay dispersion, which also explains why a pulse duration longer than the independently measured 7.5 fs output of the Ti:sapphire oscillator was obtained for the fused silica.

Note that these reconstructions were performed before the retrieval algorithm based on differential evolution and the subtraces $S_m^{(3)}$ as described in Chapter IV was developed. Here we used the Nelder–Mead algorithm [117] to minimize the RMS difference between measured and simulated modulation bands $M_m^{(3)}$, $m = 0, 1$. Although this approach is much cruder and slower than the later DE inversion algorithm, it still works for these relatively simple pulses. Several combinations (DC, FM, DC + FM) of the modulation bands were employed for different runs of the retrieval algorithm, producing similar results. The retrieved intensity envelopes were then used to establish the error bounds for different time coordinates t, shown with the purple bars in Figs. VIII.2(g) and (h).

We conduct a time-domain deconvolution analysis for the measured intensities $I_{\text{silica}}(t)$ and $I_{\text{titania}}(t)$ by minimizing the function

$$\epsilon(T_2) = \int_{t_1}^{t_2} \left| I_{\text{titania}}(t) - \int_{-\infty}^{+\infty} R(t', T_{\text{decay}}) \cdot I_{\text{silica}}(t - t')\, \mathrm{d}t' \right|^2 \mathrm{d}t\,, \tag{VIII.11}$$

where the response function $R(t, T_{\text{decay}})$ is described by Eq. (VIII.9). Here we are, however, measuring the decay time T_{decay} of the intensity, while the plasmonic study below employs the amplitude dephasing time T_2. This is a matter of taste, and the values obtained differ only slightly, T_2 being ≈ 0.7 fs longer than T_{decay}. The interval under inspection $[t_1, t_2] = [-15, 15]$ fs was chosen so that we may avoid the $I_{\text{titania}}(t)$ satellite

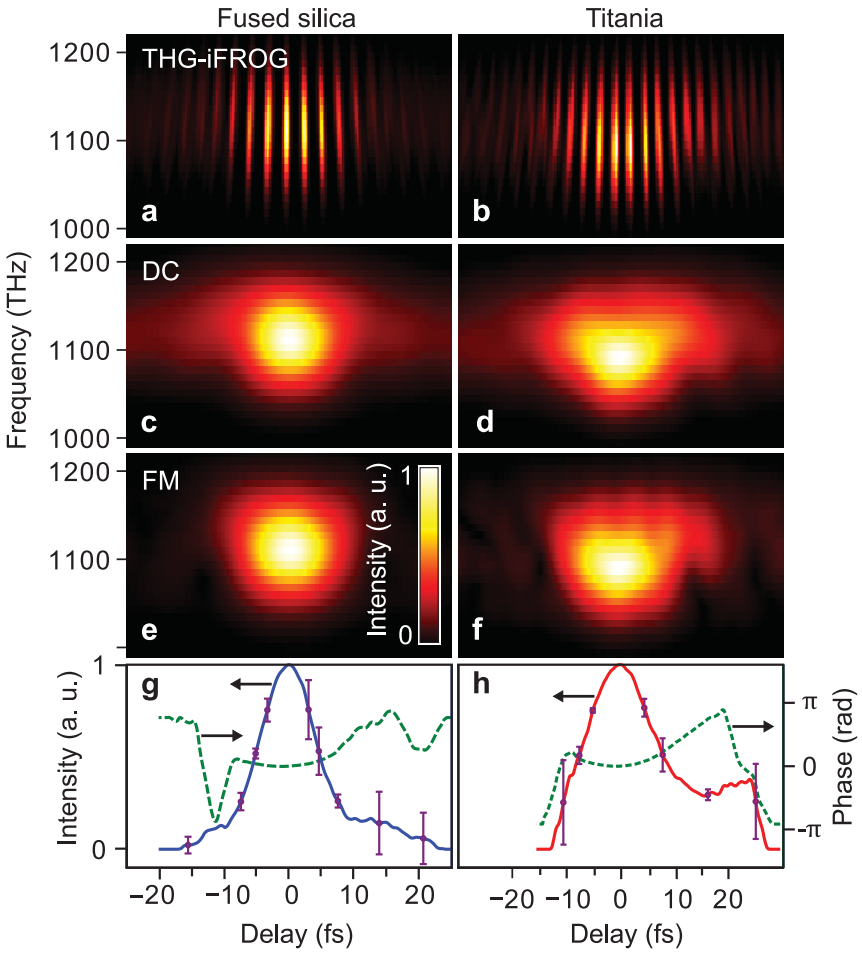

Figure VIII.2 – *THG-iFROG measurements for a fused silica substrate (left) and a titania thin film (right). Measured traces shown on top row, followed below by the DC and FM modulation bands. Retrieved electric field intensities (solid lines) and phases (green dashed lines) on bottom row. Error bars for the retrieved intensities in purple. Adapted from Publication [V].*

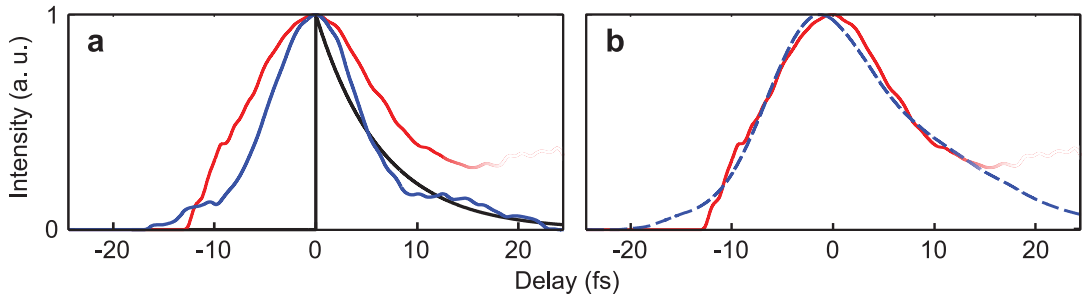

Figure VIII.3 – *Deconvolution analysis.* ***a*** *The reconstructed electric field intensities for fused silica (blue) and TiO_2 (red). Convolution of the fused silica intensity with an exponential decay function (black solid line) yields the blue dashed curve in* ***b****. TiO_2 intensities at $\tau > 15\,\mathrm{fs}$ are uncertain (cf. error bars in Fig. VIII.2(h)), and were excluded here. Adapted from Publication [V].*

structure at $t \approx 20\,\mathrm{fs}$ where the error bars are rather large. We have implicitly assumed that both the linear and nonlinear polarization are subject to the same response function, instead of limiting the noninstantaneous response to the linear polarization as with the nanoantennas. The results of this analysis are illustrated in Fig. VIII.3. A decay constant of $T_{\mathrm{decay}} \approx 6.5\,\mathrm{fs}$, or $T_2 \approx 7.2\,\mathrm{fs}$, for the third-order polarization is obtained, one of the fastest effects measured with NIR pulses to date.

VIII.2.2. Simulations

In order to better understand our measurement results, numerical simulations were carried out at the Weierstraß Institute of Berlin by M. Hofmann — whose dissertation [178] holds further details on the computational methods summarized here — and C. Brée. The response of a single atom to an incident field is simulated via the one-dimensional time-dependent Schrödinger equation (TDSE)

$$i\hbar\frac{\partial}{\partial t}\Psi_k(t) = \left(H_0 + \frac{e}{m_e}A(t)\right)\Psi_k(t), \tag{VIII.12}$$

Here e is the elementary charge, and m_e the electron mass. $A(t)$ is the vector potential of the incident pulse, represented by a 6.5-fs $\cos^4$ [179] pulse with the carrier wavelength $\lambda_0 = 780\,\mathrm{nm}$, corresponding to 1.55 eV. Note that propagation effects such as reabsorption of harmonics are ignored. $\Psi_k(t)$ is a superposition of the quasi-momentum k and single-electron Bloch waves. The lattice is described through the pseudopotential [180]

$$U(r) = \sum_{n=-\infty}^{\infty} c_1\left(\tanh^2(c_2(r+na)) - 1\right) + c_3\left(\tanh^4(c_2(r+na)) - 1\right), \tag{VIII.13}$$

with which the Hamiltonian of the stationary problem H_0 was solved. For silica, the material constants $c_1 = 54.86\,\mathrm{eV}$, $c_2 = 1.553\,\mathrm{Å}^{-1}$, and $a = 5.4\,\mathrm{Å}$ in Eq. (VIII.13) were taken from [180], while the $\tanh^4$ term was discarded by setting $c_3 = 0$. For titania, the values were tweaked until the electronic band structure was reproduced as closely as possible (evaluated via the material constants E_g and m^*) by a solution of H_0 [178]. This analysis produced the values $c_1 = c_3 = 31.31\,\mathrm{eV}$, $c_2 = 2.598\,\mathrm{Å}^{-1}$, $a = 9.51\,\mathrm{Å}$, and an effective mass $m^* = 0.61\,m_e$, slightly below reported experimental values. Similar analysis for silica yielded a bandgap of $E_g = 9.0\,\mathrm{eV}$ and an effective mass of $m^* = 0.4\,m_e$. With the stationary solutions H_0 at hand, the TDSE was solved for the single electron, conduction band at a time, for each value of k. A fully occupied valence band was assumed as an initial condition. The summation over these individual contributions yields the macroscopic probability-current density $J(t)$, which then gives the polarization via

$$P(t) = \int_{-\infty}^{t} J(t')\mathrm{d}t'. \tag{VIII.14}$$

The simulated polarizations for silica and titania are shown in Figs. VIII.4(a) and (b),

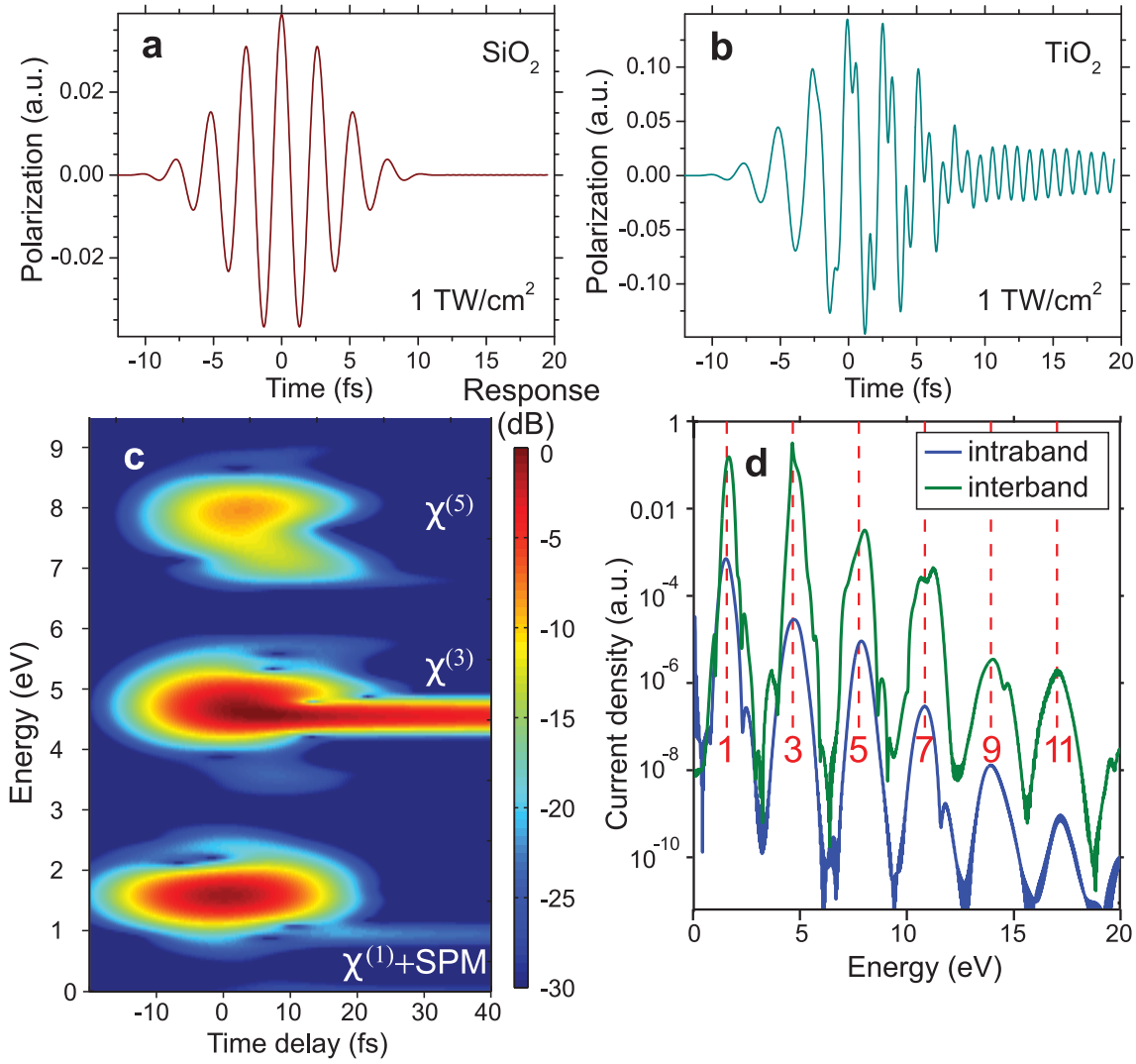

Figure VIII.4 – *TDSE simulations employing an incident intensity of 1 TW cm^{-2}. Simulated polarizations for* ***a*** *fused silica* ***b*** *titania.* ***c*** *Temporally gated spectrogram of (b).* ***d*** *Intra- and interband probability-current densities for titania. Odd harmonics are easily identified (red dashed lines). Adapted from Publication [V].*

respectively. A relatively high intensity of $I_0 = 1.0\,\mathrm{TW}$ was employed to accentuate the effects from resonant excitation. In the off-resonant silica case, the polarization closely follows the incident $\cos^4$ pulse, but a much more complicated interaction is seen to take place in titania. The resonant behavior in titania is clearly identified from the lasting, high-frequency oscillations at $\tau > 10\,\mathrm{fs}$, which are absent for silica. In Fig. VIII.4(c), a temporally gated spectrogram for the polarization in titania is shown. Odd harmonics are visible as separate bands which have been weighted here for visibility. The third harmonic at $\approx 4.7\,\mathrm{eV}$ displays the resonant behavior, which is missing or at least much

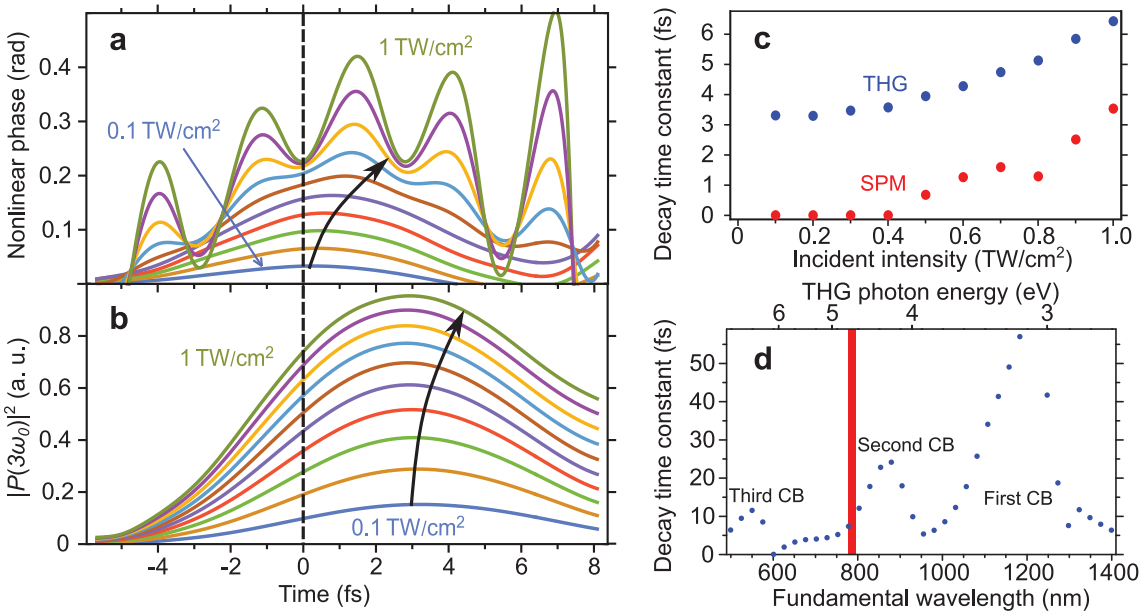

Figure VIII.5 – *TDSE simulations for titania. Incident intensities from* 0.1 *to* 1 TW cm^{-2} *in steps of* 0.1 TW cm^{-2} *are employed in (a)–(c), while only* 1 TW cm^{-2} *is used for (d).* ***a*** *Nonlinear phase.* ***b*** *Squared modulus of third-order polarization. The shift of the center of gravity for the curves in (a) and (b) to later delays is depicted via the black arrows. The black dashed line indicates the time at which the incident pulse maximum arrives to the medium.* ***c*** *Extracted decay time constants for THG (blue dots) and SPM (red dots) versus intensity.* ***d*** *Extracted THG decay time constants versus carrier wavelength. Adapted from Publication [V].*

less prominent for the fifth harmonic at ≈ 8 eV. Curiously, a lasting component is also observed at ≈ 1 eV, markedly below the linear polarization band maximum at 1.55 eV.

The origin of the ≈ 1 eV band becomes clearer when we take a look at the nonlinear contribution to the linear phase $\arg[P^{(\omega_0)}(t)]$. The nonlinear phase, plotted in Fig. VIII.5(a), is obtained by subtracting the linear phase of a weak incident field with $I_0 = 1 \cdot 10^4$ W cm^{-2} from the linear phase of a high intensity field (here 0.1–1.0 TW cm^{-2}). The driving pulse maximum arrives at $t = 0$. At the smallest intensity, the nonlinear phase is centered at zero delay, i.e., self-refraction immediately follows the incident field envelope. For higher intensities, the center of gravity for the induced nonlinear phase shifts to later delays (black arrow), indicating noninstantaneous self-phase modulation. Moreover, an oscillating behavior emerges for $I_0 \geq 0.6$ TW cm^{-2}. The period of this oscillation, ≈ 2.8 fs, corresponds to the energy separation of ≈ 1 eV between the first and second conduction bands of titania. This oscillation manifests as the lasting ≈ 1 eV component in the spectrogram of Fig. VIII.4(c), and evinces a fluctuating population between the first two conduction bands, i.e., a Rabi oscillation. It appears as though the decay time of SPM is related to conduction band populations via three photon absorption. This is not entirely surprising, considering that the Kramers-Kronig relations predict a change in the index of refraction in the presence of absorption and free electrons [181].

The extracted third-order polarization $|P^{(3\omega_0)}(t)|^2$ for varying incident field intensities I_0 is shown in Fig. VIII.5(b). In contrast to the nonlinear phase discussed above, the polarization is seen to lag the incident pulse by a few femtoseconds, even for the weakest intensity $I_0 = 0.1\,\mathrm{TW}$ corresponding to our experiments. Using a similar deconvolution analysis to our experiments, the time constants T_{decay} for the exponential decay are found, see the blue dots in Fig. VIII.5(c). The closest match to the experimentally measured $T_{\mathrm{decay}} = 6.5\,\mathrm{fs}$ is obtained with the highest simulated intensity of $I_0 = 1.0\,\mathrm{TW}$, which is already higher than the expected damage threshold for titania. This discrepancy may be attributed to the fact that the susceptibility of the titania thin film can be much higher than that of the bulk values simulated here [17]. A second possible explanation is connected to the wavelength dependence of the relaxation time constant, plotted for $I_0 = 1.0\,\mathrm{TW}$ in Fig. VIII.5(d). The experimental spectrum might have a larger overlap with the second conduction band than the corresponding simulated spectrum with $\lambda_0 = 780\,\mathrm{nm}$ (employed in the rest of the TDSE simulations), leading to a slower-than-expected relaxation in the experiments.

The sum total probability-current densities for interband (between valence and conduction bands) and intraband (within the conduction bands) excitations in titania, modeled up to the thirteenth conduction band, are shown in Fig. VIII.4(d). Odd harmonics of the carrier wave are clearly identified (red dashed lines). It is evident that the interband excitations (green curve) dominate the material response, intraband density (blue curve) being generally at least an order of magnitude weaker.

In addition to using pseudopotentials describing solids such as titania and silica, the TDSE simulations were also repeated for a hydrogen-like atomic potentials [182]. The ionization potential was matched to the titania band gap, resulting in a qualitatively similar outcome to above simulations. Regardless of the type of potential function employed, a finite lifetime of the nonlinear response was observed when the third harmonic spectrum overlaps with the conduction band for a solid, or a continuum of states for an atom. The exact value for the polarization decay was found to depend heavily on the effective mass employed, suggesting that the THG-iFROG method could also be used to measure the effective mass of valence electrons.

VIII.2.3. Discussion

The origin of the finite lifetime in our experiments can be qualitatively understood with a semi-classical picture of a damped harmonic oscillator [27], as was discussed in Chapter II. As long as the oscillator is driven at a frequency far from a resonance, the induced oscillations will disappear immediately after the driving field has passed. Close to a resonance, energy is stored into the system, and oscillations will continue even in the absence of a driver, gradually (exponentially) damping the motion to a halt. If the oscillator is anharmonic instead, the system can store energy when driven with a subharmonic of the resonance frequency, again leading to a persistent response. For a quantitative analysis, a quantum mechanical approach, such as our TDSE simulation, is required.

The experimentally measured 6.5 fs time constant for the ultrafast exponential decay of THG emission in titania is in excellent agreement with the TDSE simulations, which pro-

duce similar values for slightly higher intensities or slightly longer carrier wavelengths. In the simulations, a similar few-femtosecond lifetime is also observed for SPM. Note that SPM, let alone its rate of decay, cannot be directly measured with THG-iFROG. Although the time constants obtained computationally for SPM and THG are similar, the two are not immediately connected. This is evident from the fact that a finite THG lifetime was observed even for low incident intensities, while SPM exhibited a threshold behavior, switching quickly from a near instantaneous response to a few-femtosecond decay time for $I_0 \geq 0.5\,\mathrm{TW\,cm^{-2}}$. Nevertheless, noninstantaneous self-refraction and THG seem to be equally well connected to the three-photon resonance, suggesting that the achievable minimum duration of pulses generated via KLM is limited by the finite dephasing time under such conditions. Although many materials may be employed for KLM [183–185], we are not aware of examples where the carrier frequency would correspond to a third of a resonance frequency. On the other hand, the loss of temporal resolution could be a much more relevant problem for characterization of few-cycle pulses in the visible or UV spectral range. Considering silica as the nonlinear medium for a given pulse characterization scheme, the three-photon resonance condition could arise for wavelengths shorter than 600 nm, as absorption typically starts at around $\approx 200\,\mathrm{nm}$ [186]. Even for LiF, the widest bandgap material available, problems could arise for $\lambda < 320\,\mathrm{nm}$ [187]. Note that moderate absorption can occur even below the bandgap energy due to defects and impurities in the material. Moreover, as the simulations yielded a finite lifetime for the nonlinear polarization in both solids and atomic potentials under resonant excitation, the above problems may not be limited to solids. Thus, attosecond pulse characterization techniques employing gaseous media [188] may also be affected. As a rule of thumb, caution is advised whenever an odd harmonic of the incident field is close to a material resonance.

VIII.3. Plasmon Dephasing in Au Nanoantennas

Encouraged by the success in measuring the $\approx 7\,\mathrm{fs}$ lifetime of the resonant third-order polarization in a dielectric medium, we now move on to study the dephasing of localized surface plasmon polaritons (SPPs) in metallic nanostructures, where even faster dy-

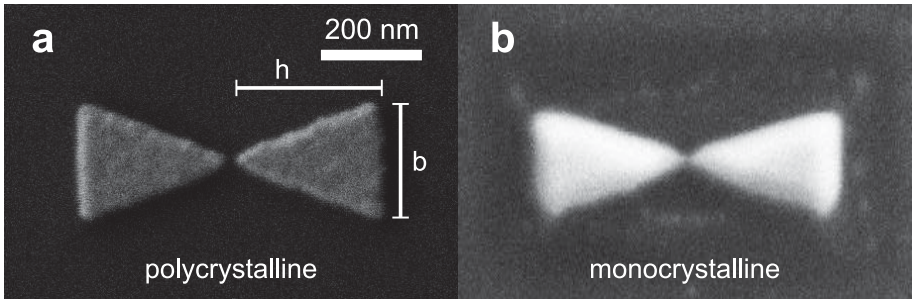

Figure VIII.6 – *Scanning electron microscope images of the employed single Au nanoantennas with a bowtie shape. Measurements by courtesy of V. Knittel.*

namics transpired. The experiments with Au bowtie nanoantennas presented here are courtesy of Vanessa Knittel and Daniel Brida from the University of Konstanz. The SHG-FROG and THG-iFROG reconstructions as well as the subsequent deconvolution analysis were performed by the author of this dissertation, aided by helpful discussions with V. Knittel and D. Brida. These results are, at the time of writing, previously unpublished. It should be noted that V. Knittel will also include some of these results in her upcoming dissertation [72] (also used as a reference here), where the Au nanoantennas are studied in greater depth. Here we will concentrate our efforts on the pulse retrieval, and the subsequent deconvolution analysis.

VIII.3.1. Experiments

As explained in Chapter II, metallic nanoantennas can greatly enhance the near field by essentially focusing the incident field into a tiny volume beyond the diffraction limit of light. In fact, the achieved near fields are so intense that a single Au bowtie nanoantenna produces a harmonic signal strong enough to be detected. While many antennas produce not only an even stronger harmonic emission, but also a higher field enhancement [189], having many emitters would lead to an inhomogeneous broadening of the emission spectrum. This presents an unnecessary complication for the interpretation of the measurement data, which we avoid by using single nanoantennas instead so that only homogeneous broadening is expected [7].

Two bowtie-shaped Au nanoantennas with differing crystallinity were employed for the experiments. The Au structures were grown on fused silica substrates. The first sample is polycrystalline, and was produced via electron beam lithography [15]. The second, a monocrystalline nanoantenna, was precision cut via focused gallium-ion beam milling [15] from a larger gold microplate grown via a wet-chemical method [190]. SEM images of the two samples are shown in Fig. VIII.6. The essential difference between the two samples is that the polycrystalline nanoantenna in Fig. VIII.6(a) has a relatively rough surface with many small defects, while the monocrystalline structure in Fig. VIII.6(b) is much smoother. The imperfections in the polycrystalline sample are expected to serve as scattering centers, leading to a faster dephasing time T_2 in comparison to the nearly ideally formed monocrystalline sample [15, 191]. The samples share the same geometry, with a height h to base b ratio of $h/b = 4:3$. The height is approximately 260 ± 20 nm, while the thicknesses of the structures are 30 and 60 nm for the polycrystalline and monocrystalline samples, respectively. The dimension of the nanoantennas were thus chosen so that the plasmon resonance $\lambda_r \approx 1200$ nm is found close to the carrier wavelength $\lambda_0 \approx 1150$ nm of the fundamental laser spectrum.

The THG-iFROG measurements yielding $E^{(\mathrm{NI})}(t)$ were conducted with a sophisticated Erbium-doped fiber laser system [192], providing ≈ 7.6-fs pulses with a spectrum that reaches all the way from 850 to 1550 nm, cf. Fig. VIII.7. The reference pulses $E(t)$ were measured with a standard SHG-FROG setup employing a BBO crystal. The SHG-FROG retrievals were performed by the author with the principal-components generalized projections algorithm [115].

The measured and reconstructed THG-iFROG traces are shown in Figs. VIII.8(a)–(d).

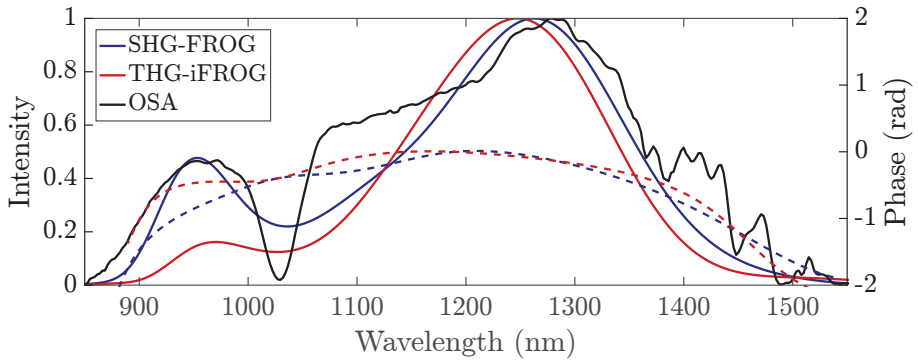

Figure VIII.7 – *Incident pulse spectrum (black) recorded with an optical spectrum analyser (OSA). The reconstructed spectral intensities (solid lines) and phases (dashed lines) for the subsequent experiments with SHG-FROG employing a BBO crystal (blue), and THG-iFROG and the polycrystalline nanoantenna (red) are shown as well.*

Note that the two samples produce visibly very similar traces, and telling the difference between the two by eye is difficult. Upon careful inspection, one can see that the measured monocrystalline trace in Fig. VIII.8(b) is confined to a slightly smaller spectral range than the polycrystalline trace above it in Fig. VIII.8(a). As discussed in Chapter II, the Lorentzian linewidth $\Delta\omega_r$ is inversely proportional to the dephasing time T_2. That is, the narrower spectrum of the monocrystalline trace indicates that a slower dephasing is at play, as expected. The reconstructed traces in Figs. VIII.8(c) and (d), obtained with our differential-evolution based algorithm, are an excellent match to the measurement data. Similar to the previous iFROG experiments, the representative pulse intensities and phases are obtained by averaging over 10 retrieval runs. The statistics are shown in Figs. VIII.8(e) and (f). The small standard deviations in both intensity and phase (at coordinates t where appreciable intensity is found) show that the iFROG retrievals give highly consistent results.

VIII.3.2. Deconvolution Analysis and Discussion

The representative pulse intensities from the noninstantaneous THG-iFROG measurements, employing the Au nanoantennas, and the reference pulses from the instantaneous SHG-FROG measurements are shown in Figs. VIII.9(a) and (b). The SHG-FROG intensities (blue solid lines) differ slightly between the two measurements likely because the measurements were not conducted immediately after one another, allowing the laser system to drift, not to mention the unavoidable uncertainty in the measurements and retrievals. Notice that the intensity envelopes for the nanoantenna pulses (red solid lines) are slightly broader in width (8.2 and 8.6 fs) than those obtained from the SHG-FROG measurements (7.5 and 7.7 fs). Time-domain deconvolution using the measured amplitudes yields dephasing constants T_2 of 2.5 fs for the polycrystalline antenna, and a considerably longer 4.1 fs for the monocrystalline sample. The convolution of the instantaneous SHG-FROG response with the single-sided exponential response function

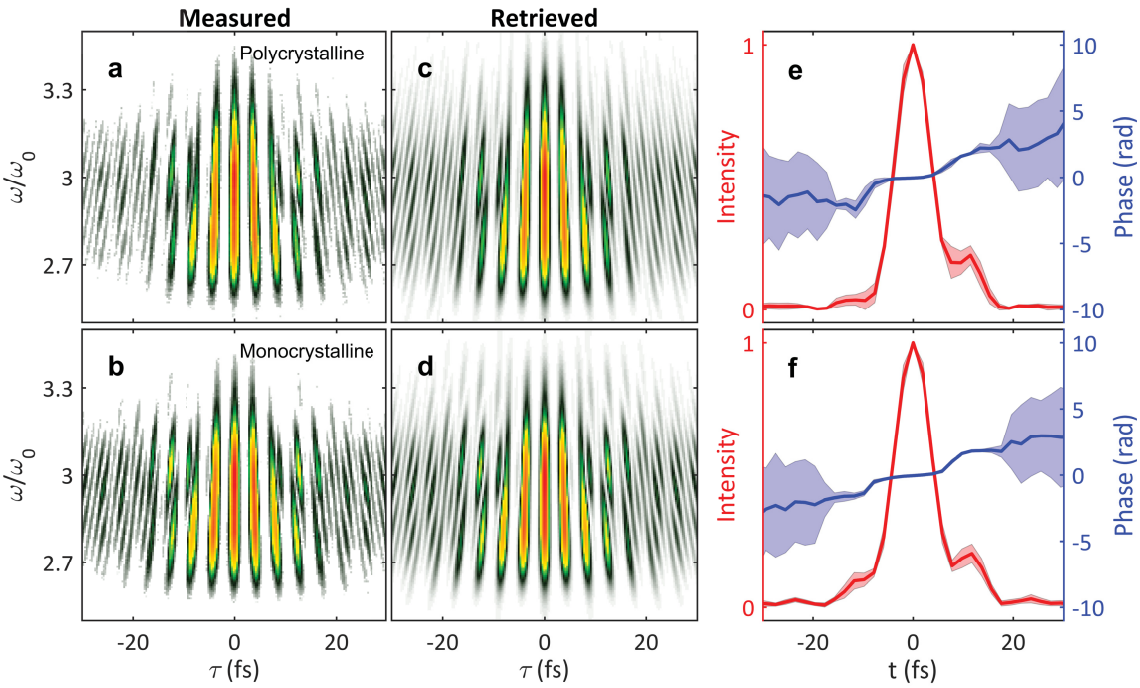

Figure VIII.8 – *THG-iFROG measurements for polycrystalline (top) and monocrystalline (bottom) gold bowtie nanoantennas. Measured (left) and retrieved (middle) traces. Statistics of ten runs (right) for retrieved pulse intensities (red) and phase (blue) in time-domain, shaded area indicates standard deviations.*

$R(t, T_2)$, as given by Eq. (VIII.9), yields the yellow dashed curves which fit the nanoantenna intensities well.

For comparison, we also perform the deconvolution in the spectral domain according to Eq. (VIII.10) by dividing the retrieved complex fundamental spectrum for THG-iFROG with the corresponding SHG-iFROG spectrum, cf. Fig. VIII.7. The results are shown in Figs. VIII.9(c) and (d). The complex Lorentzian line shapes, whose linewidths are given by $\Delta\omega_r = 2/T_2$ where T_2 are the dephasing times obtained from the time-domain deconvolution, are also shown. As discussed previously, the imaginary part of the Lorentzian corresponds to the imaginary part of the susceptibility χ, i.e., the absorption spectrum, while the real part describes the phase shift imposed onto the incident pulse by the plasmon resonance. The resonance frequency ω_r was tuned individually for both samples to obtain the best fit between the Lorentzian and $R(\omega)$. The corresponding resonance wavelengths are 1180 and 1205 nm for the polycrystalline and monocrystalline samples, respectively. These are a close match to the values obtained from boundary element method [71] simulations [72], 1180 and 1240 nm, respectively. Were the dephasing times T_2 unknown, they could have also been obtained from this spectral domain deconvolution simply by fitting a Lorentzian line shape to the measured response function $R(\omega)$.

The fact that the absorption line of either sample is roughly as wide as the fundamen-

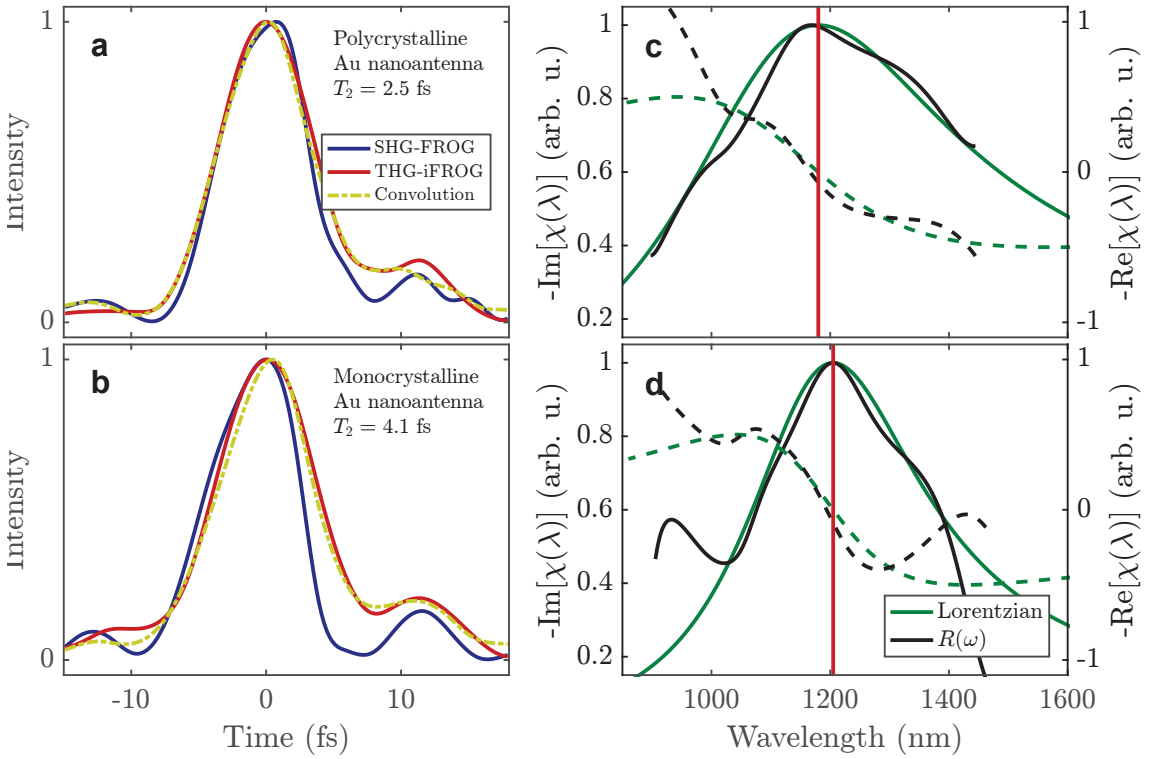

Figure VIII.9 – *Deconvolution analysis for polycrystalline (top) and monocrystalline (bottom) nanoantennas. Time-domain deconvolution (left) with an exponential dephasing function yields best agreement with $T_2 = 2.5$ fs and 4.1 fs (yellow dash-dotted line). In the frequency domain (right), the corresponding Lorentzian is shown (green). Spectral-domain deconvolution results, $R(\omega)$, are plotted in black. The imaginary (solid lines) and real parts (dashed lines) of the two functions agree reasonably well for both measurements. The empirical resonance wavelengths are indicated by the red lines.*

tal spectrum of the incident pulses means that the fundamental spectrum is not dramatically affected by the plasmon resonances, cf. Fig. VIII.7. This in turn leads to an uncertainty in the obtained $R(\omega)$, stemming from the division of the reconstructed spectra. The effect is especially large for the weak wings where the relative error in the reconstructed spectral amplitudes is high: dividing a very small spectral amplitude with an almost as small a value leads to an amplification of error. This is evident in Fig. VIII.9(d), where the imaginary part of $R(\omega)$ deviates significantly from the Lorentzian at $\lambda < 1000$ nm and $\lambda > 1400$ nm. Nevertheless, the central part of the absorption spectra for both samples agree well with the Lorentzian line shapes, and for the polycrystalline case even the weak wings are closely matched. The real parts corresponding to the phase shift show similar behavior, and are in good agreement for the majority of the reconstructed spectral range. Moreover, the characteristic *S*-shape of the phase is more or less reproduced. Aside from uncertainties in the measurements, another explanation for the reconstructed features in the response function $R(\omega)$ which differ from the Lorentzian is that they are, in fact, physically meaningful. This would show that the real-world nanoantenna is more

complicated than the ideal mathematical description of a damped harmonic oscillator. Definitive conclusions, however, would require a more systematic study.

To summarize these previously unpublished results, we employed THG-iFROG to successfully measure the dephasing times T_2 of localized surface plasmon polaritons in Au bowtie nanoantennas with differing crystal structures. As expected, a slower dephasing with $T_2 = 4.1\,\mathrm{fs}$ was observed for the monocrystalline sample, in comparison to $T_2 = 2.5\,\mathrm{fs}$ obtained for the polycrystalline sample with increased scattering from rough surface features. The measured ultrafast dephasing times are in good agreement with previous studies performed on similar structures [21, 23, 76]. In addition, we were able to reconstruct the complex-valued response function of the nanoantennas in the frequency domain, a capability that has been thus far out of reach for competing characterization techniques, such as simple interferometric autocorrelation employing THG. These proof-of-concept experiments show that THG-iFROG is well suited for the characterization of ultrafast but noninstantaneous optical nonlinearities in the femtosecond and nanometer scales.

CHAPTER IX

Conclusion

During the course of this work, characterization methods suitable for few-cycle NIR pulses were developed and subsequently applied to study nonlinear optical phenomena in solids at unprecedented time scales. The collinear beam geometry employed in all the presented techniques allowed the use of tight focusing and thus near-breakdown field intensities at the samples, which — together with the high repetition rate associated with unamplified pulses directly from an oscillator — lead to such a high sensitivity that single sub-wavelength nanostructures could be characterized.

A large portion of the research efforts were invested in iFROG which has two variants based on either SHG or THG. While previous solutions for SHG-iFROG exist, the THG modality was unravelled here for the first time. A mathematical formalism was developed, generalizing the inverse problem of pulse retrieval for both SHG and THG variants. The present solution is based on the extraction of various subtraces embedded in the measured iFROG traces via Fourier filtering techniques, and on the complementary analytic description of the subtraces. Minimizing the difference between the extracted subtraces and their simulated counterparts yields the sought-after complex electric field of the pulse. This is an optimization problem for which any general minimization procedure can in principle be applied. Given the complexity of the problem, a robust global minimization strategy appears the wisest choice. This role was filled by the evolutionary algorithm, differential evolution, which was shown to outperform previous solutions for SHG-iFROG in both numerical tests and real world measurements. It is especially noteworthy that introducing a considerable amount of noise into the measurements had little effect on the performance of the DE-based pulse retrieval, contrary to standard FROG algorithms such as generalized projections. The speed of convergence for the presented solution was found to be on par with GP, while the behavior of DE was more predictable and the results more consistent. Moreover, the performance of DE could still be im-

proved manyfold via parallelization, unlike for GP. For THG-iFROG, an experimental demonstration was given and verified to be accurate via a comparison to a reference measurement with a commercial SPIDER apparatus.

In addition to the advances made with iFROG, an entirely new ultrafast pulse characterization method based on a ptychographic algorithm was introduced. Sharing many aspects with iFROG, the novel technique named πFROG is based on SHG and also features a collinear beam geometry. Unlike iFROG, however, πFROG can unambiguously resolve the direction of time for the retrieved electric field, allowing the identification of leading and trailing satellites. As above, the proficiency of πFROG was proven via real-world characterizations of few-cycle pulses.

Utilizing the newly established THG-iFROG, nearly instantaneous optical effects were studied in resonantly excited nanostructures at unrivaled precision. The localized surface plasmon polaritons in Au nanoantennas were shown to dephase within only 2.5 and 4.1 fs, comparable to a single optical cycle of the driving field. Moreover, the complex response functions for the plasmonic resonances were obtained, a feat which previous examples based on interferometric autocorrelation cannot attain. Based on the presented evidence, THG-iFROG offers a decisive improvement over previous measurement techniques for probing the temporal dynamics in plasmonic nanostructures.

A slightly slower yet still an ultrafast lifetime of ≈ 7 fs for the resonantly induced third-order polarization in a TiO_2 thin film was measured, approximately equal to the pulse width of the driving field. A comparison with a numerically solved time-dependent Schrödinger equation not only corroborated the experimental findings, but also revealed a few-femtosecond persistence of the self-phase modulation effect. These findings highlight the fact that while resonant excitation can increase the nonlinear susceptibility of a given medium significantly, it comes at a cost of temporal resolution which can be crucial in ultrafast optics.

In addition to the characterization of ultrafast pulses and phenomena, the temporal resolution of iFROG facilitated the study of MPA induced photoluminescence in ZnO nanorods, where fractional power dependence exponents between 3 and 5 were measured. A model built on Keldysh-theory for photoionization indicated an interplay of multiple processes, with contributions from three- and four-photon absorption as well as avalanche ionization. While no evidence of two-photon absorption enhancing mechanisms suggested by previous studies was found, a varying degree of localization of the near field at the nanostructures was identified as a likely and sufficient cause for the observed differences in the employed nanorod samples, produced with differing growth techniques.

In summary, the newly developed collinear pulse characterization methods were shown to be a valuable addition to the growing number of means in the study of ultrafast nonlinear optical phenomena in solids. Offering unparalleled sensitivity, both the amplitude and phase response of nanometer-scale structures can be resolved with sub-femtosecond precision, nudging the frontiers of ultrafast nonlinear nano-optics one small step further.

APPENDIX A

Measurement of iFROG Traces

An iFROG measurement system consists of essentially three parts: an interferometer, a nonlinear-mixing step, and measurement of the nonlinear spectrum. With these constituents, an iFROG trace for a test pulse can be measured. A simplified schematic of an iFROG measurement system is illustrated in Fig. A.1. We will now discuss each of the three parts of the apparatus separately, in an order following the course of the test pulse.

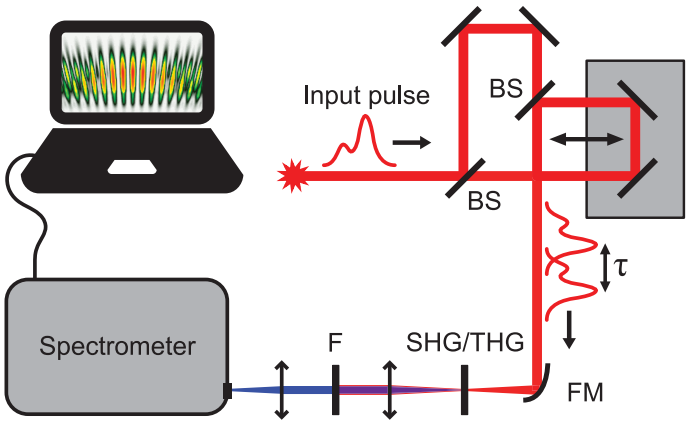

Figure A.1 – *Simplified schematic of an iFROG measurement system. The input pulse is split into two replicas by an interferometer. These are subsequently focused onto a nonlinear medium, where harmonic generation takes place. The harmonic radiation is first collimated, then separated from the residual fundamental field and possibly other, undesired spectral components, and finally recorded by a spectrometer as a function of the inter-pulse delay. List of abbreviations: beamsplitter (BS), focusing mirror (FM), filter (F).*

A.1. The Interferometer

As discussed in Chapter III, the interferometer produces two collinearly propagating replicas of the test pulse, and imposes a varying relative time-delay between the two. The amount of delay is controlled by expanding or contracting the optical path length in one of the interferometer arms by moving the mirrors with a translation stage. For an iFROG measurement, an interferometric precision for the delays is required, necessitating sub-carrier-wavelength step sizes from the translation stage. Such precision is mechanically challenging, but can be achieved with a piezoelectric translation stage. Another option is to use a translation stage employing an electric linear actuator, and, instead of step-wise movement, letting the stage move continuously through the desired range of positions in an open-loop configuration [12]. The position of the translation stage can then be measured with the aid of a chopper wheel, and trigger the spectral measurement based on the position. In our experiments, for simplicity, a piezoelectric stage (*PX 200*, piezosystem jena) was used in a closed-loop configuration.

Ideally, the two pulse replicas produced by the interferometer are identical in every aspect excluding the temporal separation. Aside from careful calibration to ensure collinear propagation of the emanating pulses, this condition demands that each replica experiences an equal amount of additional dispersion within the confines of the interferometer. The replicas are created with beamsplitters, e.g. a glass substrate with reflective thin film coating, transmitting 50% of the optical power of the incident field, and reflecting the remaining 50% at a right angle. Thin beamsplitters are preferred over other options, such as cube beamsplitters, so that the additional dispersion inflicted on the pulse replicas can be minimized. Avoidance of unnecessary dispersion is especially important for the measurement of few-cycle pulses, where the necessarily broad spectral bandwidth coupled with even a minor dispersion can have a significant effect on the temporal envelope of the investigated pulse. When such dispersion is not accounted for, the eventual pulse retrieval can give misleading results. The geometry of the interferometer is equally important when dispersion is considered. One might naively use a Michelson type interferometer [193]—comprised of a 50–50 beamsplitter and two mirrors, one of which is mounted on a delay stage—but such a device adds an unequal amount of dispersion for the two arms of the interferometer, cf. Fig. A.2(a). This is because one of the beams must travel *thrice* through the beamsplitter substrate while the other beam traverses the substrate only once.

This problem of unequal dispersion for the two interferometer arms can be circumvented in two ways. First is to add a dispersive element, e.g. an uncoated substrate window, in the arm in which the beamsplitter is traversed only once [194]. Such a dispersive element must produce exactly half of the dispersion caused by the beamsplitter—a condition which can be difficult to fulfill. One must also take possible reflection losses from the interfaces of the dispersive element into account, i.e. to make sure that the two pulse replicas created carry an equal amount of optical power. The reflection losses can be minimized by positioning the dispersive element in a Brewster's angle, provided that the input pulse is linearly polarized. Unfortunately there is a further complication for a

Michelson interferometer that cannot be easily avoided: when the optical path lengths for the two interferometer arms are equal, there is a phase difference of π between the two beams. The reason is that only one arm experiences a phase shift of π due to reflection at an air–solid interface of the beamsplitter, i.e., when arriving from a medium of low refractive index to an interface with a higher index medium, while the other arm is unaffected. There are, of course, additional phase shifts upon reflections from the mirrors, but as there are equally many mirror-bounces in either interferometer arm, this leads to no further complications. The difference of π, however, causes the interferometric pattern to have a minimum at zero delay instead of the expected maximum. The literature considering iFROG traces typically assumes no such phase shift, and the mathematics therein describe fields with a maximum at zero delay. The immediate outcome of this zero-instead-of-a-maximum ordeal is that an iFROG trace would contain two equal maxima instead of just one, thus the mathematics simply could not perfectly reproduce the measurement, leading to a systematic error in the pulse retrieval. This issue is easy to miss for long pulses, but becomes more significant in the few-cycle regime where the intensity falls rapidly after but a few interferometric fringes. Technically the single-maximum interference pattern in Fig. A.2(b) can be obtained from the two-maximum pattern in Fig. A.2(a) via a simple inversion ($I(\tau) \rightarrow I_{\max} - I(\tau)$), but in practice the zero point would unavoidably be contaminated with measurement noise, leading to a high relative error in the maximum of the inverted fringe pattern. This problem would also apply to the fringe pattern after eventual harmonic generation, thus negatively affecting subsequent pulse retrieval where high measured intensities have a large impact on the outcome of the reconstruction.

A more sophisticated approach is to replace the Michelson interferometer with a dispersion-balanced interferometer employing two identical beamsplitters instead of just one [12, 109], as illustrated in Fig. A.2(b). The two beamsplitters are arranged such that each beam is reflected once at an air–thin-film interface while traversing exactly the same amount of substrate material before the two beams are combined. In this way, both of the beams experience a total phase shift of π in the beamsplitters, and the above described problem with unequal number of phase shifts disappears. An easy way to assure that the two beamsplitters are as similar as possible is to start with a single beamsplitter, and cut it in two identical halves. In all cases of the measurements presented in Chapters IV and V a dispersion-balanced interferometer was employed.

A.2. The Nonlinear-Mixing Step

Once the collinearly propagating pulse replicas have been created, they can be used for harmonic generation. The pulses are guided into a nonlinear medium, typically in the focal point of a focusing element and followed by collimation. In order to avoid any unnecessary additional dispersion before the phase-sensitive harmonic generation process, reflective focusing optics are preferred. For our experiments, a parabolic off-axis mirror with a gold surface, and a rather short focal length of 25 mm was chosen to provide a wide, low-loss reflection bandwidth and a very small spot size. The smaller the spot

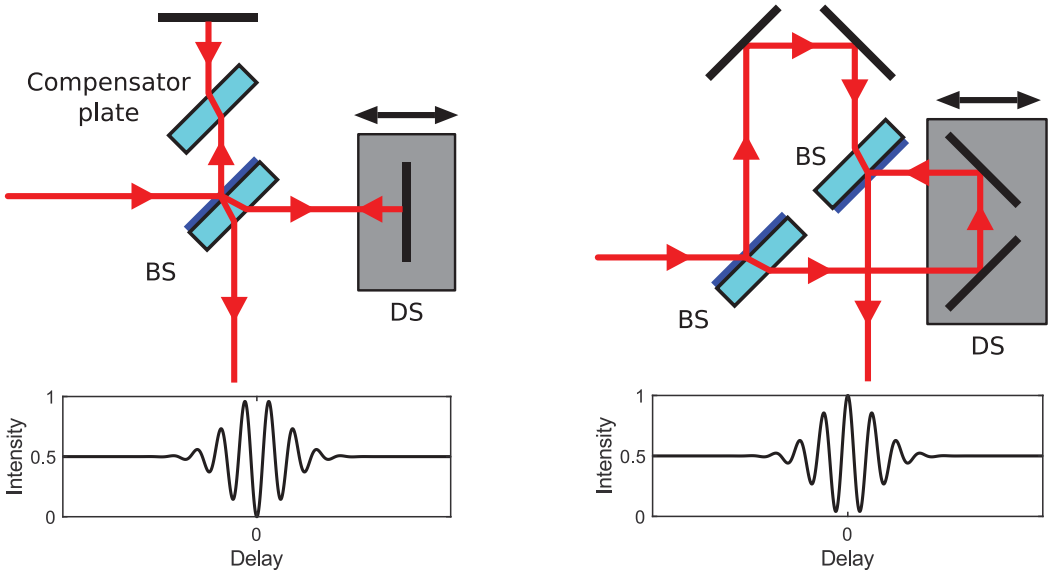

(a) *Michelson interferometer* **(b)** *Dual beamsplitter interferometer*

Figure A.2 – *Two possible interferometer geometries producing collinearly propagating pulse replicas, separated by a time delay which can be varied with a delay stage (DS).* ***a*** *A simple Michelson interferometer will always produce a linear interference pattern with two maxima (bottom).* ***b*** *On the contrary, a dual beamsplitter (BS) design gives the desired single-maximum interference pattern.*

size is, the higher the field intensity in the focus, and the more efficient the conversion of fundamental field to harmonics. The nonlinear medium must be chosen such that the appropriate harmonic-generation process — SHG or THG, depending on the desired iFROG variant — can occur and is efficient enough so that the generated harmonic field can be measured by a spectrometer with sufficiently high signal-to-noise ratio (SNR) to facilitate successful pulse retrieval. As discussed in Chapter II, various nonlinear media are employed in this dissertation, the properties of which are discussed in greater detail within their respective sections. The iFROG measurements presented in Chapters IV and V are based on either SHG or THG, with no other concomitant emission spectra. For SHG-iFROG, a β-barium borate (BBO) crystal was used in type I phase matching configuration. For THG-iFROG, the front interface of a 1 mm thick window of fused silica was employed. In Chapter VI, the above-mentioned BBO crystal is utilized for the novel πFROG method. In Chapter VIII, THG-iFROG is extended beyond simple pulse characterization to the study of noninstantaneous processes. For this purpose, THG from titanium dioxide thin film (Section VIII.2) and gold nanoantennas (Section VIII.3) are analyzed, and time constants in the order of few femtoseconds are measured. In Chapter VII, both SHG and THG, along with multiphoton absorption induced photoluminescence (PL), is generated from ZnO nanorods, and subsequently detected and analyzed with iFROG, providing an insight into the PL process.

Considering conventional pulse characterization with iFROG, choosing either SHG or THG as the nonlinearity leads to a few marked differences in obtainable sensitivity and

bandwidth, range of suitable archetypes for the nonlinear medium, and design of the measurement device. As a general rule of thumb for harmonic generation processes, the higher the order of the harmonic, the weaker the conversion efficiency from fundamental spectrum to harmonics. For the detection of the said harmonics generated for a given pulse with a certain pulse energy, this implies that THG as a $\chi^{(3)}$ process will most likely result in a much lower achievable SNR than SHG, a $\chi^{(2)}$ process. For our measurements, some of which are presented in Figs. IV.3 and IV.4, this is indeed the case: the SHG-iFROG measurements employing a BBO crystal were recorded with a considerably shorter exposure time than the THG-iFROG measurements using a fused silica window, and still the former has a significantly higher SNR than the latter. What THG loses in conversion efficiency it gains in simplicity. As discussed in Chapter II, THG as an odd-order process is allowed for both centrosymmetric and noncentrosymmetric media including gases and solids while SHG is allowed only for noncentrosymmetric solids [8]. Moreover, surface third-harmonic generation (STHG) can take place on any dielectric interface, e.g. air–glass, and has a very short interaction length [195]. Because the interaction length is short, phase matching is ensured for broad bandwidths, and for a large range of carrier wavelengths.

The opposite is true for bulk SHG, where the nonlinear medium must be carefully chosen to suit a particular laser. For the employed type I phase matching, the SHG crystal must be cut in a specific angle to ensure phase matching for the carrier wavelength and for a sufficiently broad wavelength range to encompass the entire fundamental spectrum of the pulse. If this design issue is neglected, efficient harmonic generation will not occur across the whole fundamental spectrum. Thus, information is lost, and the harmonic spectrum does not fully represent the original pulse, negatively affecting the subsequent pulse characterization. Polarization of the test pulse also plays a decisive role for bulk SHG, while STHG is largely independent of the input polarization, albeit some exceptions of THG pulse characterization schemes can be found where input beam polarization matters [110]. While collinear SHG-FROG has been demonstrated with type II phase matching [109, 111], employing two orthogonal linearly polarized beams, the measurements do not result in an iFROG trace with interferometric fringes, as mentioned in Chapter III. Moreover, because the two beams propagate on different optical axes of the crystal, the concomitant group velocity mismatch limits the achievable temporal resolution, which is a severe drawback for few-cycle pulse measurements. For the SHG-iFROG experiments presented in the current section, the employed type I phase matching scheme was found sufficient in bandwidth. Going back to harmonic generation from surfaces, one should note that because of inversion symmetry is necessarily broken at any given interface, *all* harmonic orders are electric dipole allowed. Nevertheless, for an interface between air and a medium with inversion symmetry (where bulk SHG is not allowed), the already weak surface THG is generally still stronger than surface SHG, which makes STHG more generally applicable for pulse characterization purposes [195]. For the same reasons, THG is often much more effective than SHG for metal surfaces and especially gold nanoantennas [23] such as our own.

A.3. The Detection of the Nonlinear Spectrum

Once the desired harmonic of the fundamental field has been generated, it can be collimated, spectrally isolated, and detected. While additional dispersion was avoided before the harmonic generation took place, any dispersion *after* the upconversion is not an issue because the harmonic power spectral density (PSD) measurement is insensitive to the phase of an electric field. Therefore, transmissive optics may be used, as long as the absorption of the harmonics within the optical elements is not severe enough to prevent adequate detection in any part of the upconverted spectrum. For all the measurements presented in this work (excluding the gold nanoantenna experiments in Section VIII.3), an aspherical lens made from UV-grade fused silica was used for collimation of the harmonics, and also of photoluminescence in the case of ZnO nanorods, the topic of Chapter VII. The collimated electric field contains a number of spectral components, only one of which is typically desired for an iFROG measurement. The fundamental field and possibly other spectral components emanating from the nonlinear medium must be rejected, and the chosen harmonic isolated before measurement of the PSD. This spectral filtering can be achieved in a number of ways. The various spectral components can be spatially dispersed with prisms or gratings, and a wavelength range can then be selected by simply blocking a part of the dispersed spectrum. Another solution is to use a number of spectral filters, chosen specifically for the desired wavelength range. The latter option was chosen for our experiments. Depending on the desired spectral range, two optical paths with differing filters could be chosen, see Fig. IV.1. The SHG and PL measurements employed color filters, absorbing the fundamental field at 800 nm while transmitting the SHG and PL around 400 nm. For SHG-iFROG, a linear polarizer was also used to further enhance the contrast between the s-polarized fundamental field and the p-polarized SHG light. For the THG-iFROG measurements, a pair of dielectric mirrors designed to reflect at 270 nm was used along with an interference filter for the same spectral range.

After the desired spectral components have been isolated, they can be guided to a spectrometer. For this purpose, we focused the upconverted light from either of the two filter paths with UV-grade fused-silica lenses into optical fibers, leading to a Czerny–Turner imaging spectrograph (*Shamrock SR-303i*, Andor). The spectrograph disperses the wavelengths of an input field with a system of gratings and mirrors, while an electron-magnifying charge-coupled device (EMCCD) (*Newton 970*, Andor) placed on the image plane of the spectrograph records the power spectral density. Although the camera allows electron-magnifying to be used with the purpose of increasing sensitivity, the feature was not ultimately employed, as no significant increase in signal-to-noise ratio was observed. The upconverted spectrum is measured for a range of delays deemed necessary for the pulse at hand, for our cases ranges of a few hundred femtoseconds were used with a step size of 200 attoseconds resulting in a few thousand measured spectra for each iFROG trace.

APPENDIX B

Derivation of the SHG-iFROG Subtraces

Setting $h = 2$ for second-harmonic generation, the SHG-iFROG trace is given by Eq. (IV.1):

$$I^{(2)}_{\mathrm{iFROG}}(\omega,\tau) \equiv \left| \int_{-\infty}^{+\infty} [\mathcal{E}(t) + \mathcal{E}(t-\tau)]^2 \, e^{-i\omega t} \, \mathrm{d}t \right|^2 . \tag{B.1}$$

Next, we aim to derive analytical forms for the modulation bands $M^{(2)}_m(\omega,\tau)$. To this end, let us introduce a few shorthand notations. We define the frequency $\Delta\omega$ to be the distance from the product of the carrier frequency and the harmonic order h

$$\Delta\omega \equiv \omega - h\omega_0 . \tag{B.2}$$

For SHG this yields $\Delta\omega = \omega - 2\omega_0$. The complex second-harmonic field is then given by

$$E^{(2)}(\Delta\omega) \equiv \int_{-\infty}^{+\infty} E^2(t) e^{-i\Delta\omega t} \, \mathrm{d}t . \tag{B.3}$$

The standard SHG-FROG field is defined as [60]

$$E^{(2)}_{\mathrm{FROG}}(\Delta\omega,\tau) \equiv \int_{-\infty}^{+\infty} E(t)E(t-\tau) e^{-i\Delta\omega t} \, \mathrm{d}t . \tag{B.4}$$

Using Eqs. (B.2) to (B.4), we can expand Eq. (B.1) into the following form [12] ,

$$I^{(2)}_{\mathrm{iFROG}}(\Delta\omega,\tau) = 2\left|E^{(2)}(\Delta\omega)\right|^2 + 4\left|E^{(2)}_{\mathrm{FROG}}(\Delta\omega,\tau)\right|^2 \tag{B.5a}$$

$$+ 8\cos\left[\left(\omega_0 + \tfrac{1}{2}\Delta\omega\right)\tau\right] \cdot \mathscr{R}\left\{E^{(2)}_{\mathrm{FROG}}(\Delta\omega,\tau)E^{(2)*}(\Delta\omega)e^{i\frac{1}{2}\Delta\omega\tau}\right\} \tag{B.5b}$$

$$+ 2\cos[(2\omega_0 + \Delta\omega)\tau] \cdot \left|E^{(2)}(\Delta\omega)\right|^2 . \tag{B.5c}$$

Note that each of the three rows in Eq. (B.5) is modulated by a cosine according to Eq. (IV.3), when setting $m = 0, 1, 2$ for the top, middle, and bottom rows, respectively. Therefore these rows correspond to the three modulation bands $M^{(2)}_m(\omega,\tau)$ which can now be separated,

$$M^{(2)}_0(\Delta\omega,\tau) \equiv 2\left|E^{(2)}(\Delta\omega)\right|^2 + 4\left|E^{(2)}_{\mathrm{FROG}}(\Delta\omega,\tau)\right|^2 \tag{B.6a}$$

$$M^{(2)}_1(\Delta\omega,\tau) \equiv 8\cos\left[\left(\omega_0 + \tfrac{1}{2}\Delta\omega\right)\tau\right] \cdot \mathscr{R}\left\{E^{(2)}_{\mathrm{FROG}}(\Delta\omega,\tau)E^{(2)*}(\Delta\omega)e^{i\frac{1}{2}\Delta\omega\tau}\right\} \tag{B.6b}$$

$$M^{(2)}_2(\Delta\omega,\tau) \equiv 2\cos[(2\omega_0 + \Delta\omega)\tau] \cdot \left|E^{(2)}(\Delta\omega)\right|^2 . \tag{B.6c}$$

Now that we have obtained the analytical forms for the modulation bands of the SHG-iFROG trace, we may proceed to use these to find and define the subtraces $S^{(2)}_n$. As stated above, there are $h = 2$ obtainable subtraces for SHG-iFROG. First of them is the DC subtrace $S^{(2)}_0$, which, in the absence of cosine factor, is trivially equal to the modulation band $M^{(2)}_0$,

$$S^{(2)}_0(\Delta\omega,\tau) \equiv M^{(2)}_0(\Delta\omega,\tau) = 2\left|E^{(2)}(\Delta\omega)\right|^2 + 4\left|E^{(2)}_{\mathrm{FROG}}(\Delta\omega,\tau)\right|^2 .$$

The FM subtrace $S^{(2)}_1$ is somewhat trickier to obtain. The goal is to remove the modulation due to the cosine in Eq. (B.6b). One way to accomplish this is to multiply the isolated modulation band $M^{(2)}_1$ with a cosine that has exactly the same argument as the cosine in Eq. (B.6b). Multiplication of two cosines gives a sum of two cosines, namely $\cos(\alpha)\cos(\beta) = \cos(\alpha-\beta)+\cos(\alpha+\beta)$, and since $\alpha = \beta$ in our case, one obtains $1+\cos(2\alpha)$. The new cosine term with can be ignored, leaving only the unity factor and thus removing the modulation. In the Fourier domain, this corresponds to a split of the original two bands (at delay-frequencies $\xi = \pm\omega_0\tau$) into three new bands, two of which reside at $\xi = \pm 2\omega_0$, and one at $\xi = 0$. The last one to be mentioned is selected, and defined as the FM subtrace. Obtaining the phase $\left(\omega_0 + \frac{1}{2}\Delta\omega\right)\tau$ for the cosine in Eq. (B.6b) is of course trivial for the analytical form, but bear in mind that the time delay τ is not exactly known for experimental data, and may be irregularly (or worse, erroneously) sampled. Furthermore, the latter factor of Eq. (B.6b) introduces additional modulation, effectively preventing the access to the argument of the cosine. For the highest modulation band, however, only the cosine is dependent on τ, and so its phase can be extracted. For these reasons, we introduce the phase $\phi_{\mathrm{mod}}(\omega,\tau)$ of the highest modulation band with the help of our operator $\mathscr{C}$ previously defined in Eq. (IV.5):

$$\phi_{\mathrm{mod}}(\Delta\omega,\tau) \equiv \mathrm{Unwrap}\left\{\mathrm{Arg}\left\{\mathscr{C}\left\{M^{(h)}_{m=h}(\Delta\omega,\tau)\right\}\right\}\right\} . \tag{B.7}$$

Eq. (B.7) corresponds to the above discussed Takeda algorithm. For SHG-iFROG this equation gives $\phi_{\text{mod}}(\Delta\omega,\tau) = (2\omega_0 + \Delta\omega)\,\tau$. Notice that this is exactly twice the argument of the cosine in Eq. (B.6b). We may now rewrite the FM band using the newly defined phase:

$$M_1^{(2)}(\Delta\omega,\tau) = 8\cos\left[\tfrac{1}{2}\phi_{\text{mod}}(\Delta\omega,\tau)\right]\cdot\mathscr{R}\left\{E_{\text{FROG}}^{(2)}(\Delta\omega,\tau)E^{(2)*}(\Delta\omega)e^{i\frac{1}{2}\Delta\omega\tau}\right\}. \tag{B.8}$$

Multiplying this with $\cos\left[\frac{1}{2}\phi_{\text{mod}}(\Delta\omega,\tau)\right]$ gives

$$\begin{aligned}\cos\left[\tfrac{1}{2}\phi_{\text{mod}}(\Delta\omega,\tau)\right]\cdot M_1^{(2)}(\Delta\omega,\tau) = {}& 4\left\{\cos[\phi_{\text{mod}}(\Delta\omega,\tau)]+1\right\}\\ &\cdot\mathscr{R}\left\{E_{\text{FROG}}^{(2)}(\Delta\omega,\tau)E^{(2)*}(\Delta\omega)e^{i\frac{1}{2}\Delta\omega\tau}\right\}.\end{aligned} \tag{B.9}$$

As explained above, ignoring the cosine term and the factor 4, we are left with only the second factor of Eq. (B.8), which we now define as the FM subtrace for SHG-iFROG

$$\begin{aligned}S_1^{(2)}(\Delta\omega,\tau) &\equiv \mathscr{R}\left\{E_{\text{FROG}}^{(2)}(\Delta\omega,\tau)E^{(2)*}(\Delta\omega)e^{i\frac{1}{2}\Delta\omega\tau}\right\}\\ &= \left|E_{\text{FROG}}^{(2)}(\Delta\omega,\tau)E^{(2)*}(\Delta\omega)\right|\cdot\cos\left[\phi_{\text{FROG}}^{(2)}(\Delta\omega,\tau)-\phi^{(2)}(\Delta\omega,\tau)+\tfrac{1}{2}\Delta\omega\tau\right].\end{aligned}$$

Notice that the equations given here allow the analytic computation of the subtrace $S_1^{(2)}$ (and $S_0^{(2)}$) for a given electric field $E(t)$. Another important fact concerning the eventual pulse retrieval is that the above described analytical extraction of the FM subtrace can be readily repeated numerically for experimental data. That is, the subtrace $S_1^{(2)}$ can be obtained from experimental data by (i) extracting the modulation band $M_1^{(2)}$ via Fourier filtering, (ii) multiplying this with $\cos\left[\frac{1}{2}\phi_{\text{mod}}\right]$, where ϕ_{mod} is extracted from $M_2^{(2)}$, (iii) and finally Fourier filtering the new band at zero delay-frequency. Another, equivalent method is to Fourier filter only the positive frequencies of $M_1^{(2)}$, producing a complex band, and then multiply this with $\exp\left(-i\frac{1}{2}\phi_{\text{mod}}\right)$. The analytic equivalent is to use the operator defined by Eq. (IV.5) on $M_1^{(2)}$, which yields otherwise the same result as Eq. (B.8), but the cosine is now an exponent,

$$\mathscr{C}\left\{M_1^{(2)}(\Delta\omega,\tau)\right\} = 4\,e^{i\frac{1}{2}\phi_{\text{mod}}(\Delta\omega,\tau)}\cdot\mathscr{R}\left\{E_{\text{FROG}}^{(2)}(\Delta\omega,\tau)E^{(2)*}(\Delta\omega)e^{i\frac{1}{2}\Delta\omega\tau}\right\}. \tag{B.10}$$

When Eq. (B.10) is multiplied with the complex conjugate of the exponent, only the subtrace $S_1^{(2)}$ (and the factor 4) is left.

APPENDIX C

Derivation of the THG-iFROG Subtraces

The derivation of the subtraces for THG-iFROG is analogous to what was shown in Appendix B for SHG-iFROG, albeit a bit more involved. These subtraces can likewise be obtained from numerical data, following a procedure analogous to what is described for SHG-iFROG in Appendix B. We start in exactly the same manner as with SHG-iFROG, by setting $h = 3$ for the appropriate nonlinear process (THG), and use Eq. (IV.1) again to obtain the THG-iFROG trace:

$$I^{(3)}_{\mathrm{iFROG}}(\omega,\tau) \equiv \left| \int_{-\infty}^{+\infty} [\mathcal{E}(t) + \mathcal{E}(t-\tau)]^3 \, e^{-i\omega t} \, \mathrm{d}t \right|^2 . \tag{C.1}$$

As before, we seek to define the modulation bands $M^{(3)}_m(\omega,\tau)$, and start by few helpful definitions. The frequency $\Delta\omega$ is given by Eq. (B.2) as $\Delta\omega = \omega - 3\omega_0$. The complex third-harmonic field is

$$E^{(3)}(\Delta\omega) \equiv \int_{-\infty}^{+\infty} E^3(t) e^{-i\Delta\omega t} \, \mathrm{d}t \,, \tag{C.2}$$

while the standard THG-FROG field is given by [60]

$$E^{(3)}_{\mathrm{FROG}}(\Delta\omega,\tau) \equiv \int_{-\infty}^{+\infty} E^2(t) E(t-\tau) e^{-i\Delta\omega t} \, \mathrm{d}t \,. \tag{C.3}$$

Note that we could just as well choose the above integrand to be $E(t)E^2(t-\tau)e^{-i\Delta\omega t}$. This would imply that the THG process involves two photons from the delayed test pulse replica and a single photon from the undelayed replica, while the opposite is true for

Eq. (C.3). In fact both forms are found to be present when Eq. (C.1) is expanded, see below. This is expected, as both processes are equally likely to occur. A shorthand notation $E^{(3)-}_{\mathrm{FROG}} \equiv E^{(3)}_{\mathrm{FROG}}(\Delta\omega, -\tau)$ for the time-reversed THG-FROG field will also be useful in our derivation.

We further introduce two new complex fields $K, L \in \mathbb{C}^2$,

$$K(\Delta\omega,\tau) \equiv E^{(3)}(\Delta\omega)E^{(3)*}_{\mathrm{FROG}}(\Delta\omega,\tau) + E^{(3)*}(\Delta\omega)E^{(3)}_{\mathrm{FROG}}(\Delta\omega,\tau) \tag{C.4}$$

$$L(\Delta\omega,\tau) \equiv E^{(3)*}_{\mathrm{FROG}}(\Delta\omega,\tau)E^{(3)}_{\mathrm{FROG}}(\Delta\omega,-\tau), \tag{C.5}$$

and their phases,

$$\phi_K(\Delta\omega,\tau) \equiv \mathrm{Arg}\{K(\Delta\omega,\tau)\} \tag{C.6}$$

$$\phi_L(\Delta\omega,\tau) \equiv \mathrm{Arg}\{L(\Delta\omega,\tau)\}\,. \tag{C.7}$$

With the definitions of Eqs. (C.2) to (C.6) at hand, Eq. (C.1) can now be expanded. We use Eq. (II.5) and start by expanding the factor $[\mathcal{E}(t)+\mathcal{E}(t-\tau)]^3$

$$\begin{aligned}
&[\mathcal{E}(t)+\mathcal{E}(t-\tau)]^3 \\
&= \left[E(t)e^{i\omega_0 t} + E(t-\tau)e^{i\omega_0(t-\tau)}\right]^3 \\
&= e^{i3\omega_0 t}\left[E(t) + E(t-\tau)e^{-i\omega_0\tau}\right]^3 \\
&= e^{i3\omega_0 t}\left[E^3(t) + 3E^2(t)E(t-\tau)e^{-i\omega_0\tau} + 3E(t)E^2(t-\tau)e^{-i2\omega_0\tau} + E^3(t-\tau)e^{-i3\omega_0\tau}\right]
\end{aligned} \tag{C.8}$$

Inserting this into Eq. (C.1) gives

$$\begin{aligned}
I^{(3)}_{\mathrm{iFROG}}(\omega,\tau) = \Bigg| \int_{-\infty}^{+\infty} e^{-i\Delta\omega t}\Big[&E^3(t) + 3E^2(t)E(t-\tau)e^{-i\omega_0\tau} \\
&+ 3E(t)E^2(t-\tau)e^{-i2\omega_0\tau} + E^3(t-\tau)e^{-i3\omega_0\tau}\Big]\mathrm{d}t\Bigg|^2,
\end{aligned} \tag{C.9}$$

where the substitution $\Delta\omega = \omega - 3\omega_0$ was made according to Eq. (B.2). Next, we write the integrals of the four terms in the integrand above separately

$$I^{(3)}_{\mathrm{iFROG}}(\omega,\tau) = \Bigg| \int_{-\infty}^{+\infty} e^{-i\Delta\omega t}\,E^3(t)\,\mathrm{d}t + \tag{C.10a}$$

$$\int_{-\infty}^{+\infty} e^{-i\Delta\omega t}\,E^2(t)E(t-\tau)\,\mathrm{d}t\cdot 3\,e^{-i\omega_0\tau} + \tag{C.10b}$$

$$\int_{-\infty}^{+\infty} e^{-i\Delta\omega t}\, E(t)E^2(t-\tau)\,\mathrm{d}t \cdot 3\, e^{-i2\omega_0\tau} + \tag{C.10c}$$

$$\int_{-\infty}^{+\infty} e^{-i\Delta\omega t}\, E^3(t-\tau)\,\mathrm{d}t \cdot e^{-i3\omega_0\tau}\Bigg|^2 . \tag{C.10d}$$

This equation may be expressed in a more compact way by identifying the four integrals it contains. Referring to Eq. (C.2), we find that the integral on the right hand side of Eq. (C.10a) is $E^{(3)}(\Delta\omega)$. Using Eq. (C.3), we find that the integral in Eq. (C.10b) is $E^{(3)}_{\mathrm{FROG}}(\Delta\omega,\tau)$. By using the translation property of the Fourier transform, the third integral, in Eq. (C.10c), becomes

$$\begin{aligned}\int_{-\infty}^{+\infty} e^{-i\Delta\omega t}\, E(t)E^2(t-\tau)\,\mathrm{d}t &= e^{-i\Delta\omega\tau}\cdot\int_{-\infty}^{+\infty} e^{-i\Delta\omega t}\, E(t+\tau)E^2(t)\,\mathrm{d}t \\ &= e^{-i\Delta\omega\tau}\cdot E^{(3)}_{\mathrm{FROG}}(\Delta\omega,-\tau),\end{aligned} \tag{C.11}$$

where Eq. (C.3) was used again. The fourth integral, in Eq. (C.10d), can also be simplified using the translation property and Eq. (C.2),

$$\begin{aligned}\int_{-\infty}^{+\infty} e^{-i\Delta\omega t}\, E^3(t-\tau)\,\mathrm{d}t &= e^{-i\Delta\omega\tau}\cdot\int_{-\infty}^{+\infty} e^{-i\Delta\omega t}\, E^3(t)\,\mathrm{d}t \\ &= e^{-i\Delta\omega\tau}\cdot E^{(3)}(\Delta\omega).\end{aligned} \tag{C.12}$$

With the four integrals identified, we rewrite Eq. (C.10) as

$$\begin{aligned}I^{(3)}_{\mathrm{iFROG}}(\Delta\omega,\tau) = \Big| & E^{(3)}(\Delta\omega) + E^{(3)}_{\mathrm{FROG}}(\Delta\omega,\tau)\cdot e^{-i\omega_0\tau} \\ & + E^{(3)}_{\mathrm{FROG}}(\Delta\omega,-\tau)\cdot e^{-i(2\omega_0+\Delta\omega)\tau} + E^{(3)}(\Delta\omega)\cdot e^{-i(3\omega_0+\Delta\omega)\tau}\Big|^2 .\end{aligned} \tag{C.13}$$

The next step is to rid ourselves of the squared modulus in Eq. (C.13). As $|z|^2 = z^*\cdot z, z\in\mathbb{C}$, we can expand Eq. (C.13) by multiplying the above sum with its complex conjugate. This yields 15 new terms, which form 6 pairs of complex conjugates along with the squared moduli of each term. These terms can then be reordered and factored into four rows based on which factor $\exp[im\omega_0\tau], m = 0\ldots3$ they contain. In addition, we make use of the identity $z + z^* = 2\mathscr{R}\{z\}$, and omit the arguments of the fields, yielding

$$\begin{aligned}&I^{(3)}_{\mathrm{iFROG}}(\Delta\omega,\tau) = \\ &\quad 2\left|E^{(3)}\right|^2 + 9\left|E^{(3)}_{\mathrm{FROG}}\right|^2 + 9\left|E^{(3)-}_{\mathrm{FROG}}\right|^2\end{aligned} \tag{C.14a}$$

$$+ 6\mathscr{R}\left\{e^{i\omega_0\tau}\cdot\left[E^{(3)}E^{(3)*}_{\mathrm{FROG}} + E^{(3)*}E^{(3)-}_{\mathrm{FROG}}\right]\right\} + 18\mathscr{R}\left\{e^{-i(\omega_0+\Delta\omega)\tau}\cdot E^{(3)*}_{\mathrm{FROG}}E^{(3)-}_{\mathrm{FROG}}\right\} \tag{C.14b}$$

$$+ 6\mathscr{R}\left\{e^{-i(2\omega_0+\Delta\omega)\tau}\cdot\left[E^{(3)}E^{(3)*}_{\mathrm{FROG}} + E^{(3)*}E^{(3)-}_{\mathrm{FROG}}\right]\right\} \tag{C.14c}$$

$$+ 2\mathscr{R}\left\{e^{-i(3\omega_0+\Delta\omega)\tau}\right\}\cdot\left|E^{(3)}\right|^2. \tag{C.14d}$$

Finally, by using the definitions Eqs. (C.4) and (C.5) for K and L, respectively, and the identity $\mathscr{R}\{z\} = |z|\cos[\phi_z], \phi_z \equiv \mathrm{Arg}\{z\}$, we obtain

$$I^{(3)}_{\mathrm{iFROG}}(\Delta\omega,\tau) = 2\left|E^{(3)}\right|^2 + 9\left|E^{(3)}_{\mathrm{FROG}}\right|^2 + 9\left|E^{(3)-}_{\mathrm{FROG}}\right|^2 \tag{C.15a}$$

$$+ 6\cos[\phi_K + \omega_0\tau]\cdot|K| + 18\cos[\phi_L - (\omega_0+\Delta\omega)\tau]\cdot|L| \tag{C.15b}$$

$$+ 6\cos[\phi_L - (2\omega_0+\Delta\omega)\tau]\cdot|K| \tag{C.15c}$$

$$+ 2\cos[(3\omega_0+\Delta\omega)\tau]\cdot\left|E^{(3)}\right|^2. \tag{C.15d}$$

Here we have omitted the arguments for the various fields for the sake of brevity. Again, the different modulation bands are identified with the help of Eq. (IV.3), finding $h+1 = 4$ modulation bands as expected,

$$M^{(3)}_0 \equiv 2\left|E^{(3)}\right|^2 + 9\left|E^{(3)}_{\mathrm{FROG}}\right|^2 + 9\left|E^{(3)-}_{\mathrm{FROG}}\right|^2 \tag{C.16a}$$

$$M^{(3)}_1 \equiv 6\cos[\phi_K + \omega_0\tau]\cdot|K| + 18\cos[\phi_L - (\omega_0+\Delta\omega)\tau]\cdot|L| \tag{C.16b}$$

$$M^{(3)}_2 \equiv 6\cos[\phi_K - (2\omega_0+\Delta\omega)\tau]\cdot|K| \tag{C.16c}$$

$$M^{(3)}_3 \equiv 2\cos[(3\omega_0+\Delta\omega)\tau]\cdot\left|E^{(3)}\right|^2. \tag{C.16d}$$

Now we can proceed to define the subtraces $S^{(3)}_n$ for THG-iFROG. This time there are $h = 3$ obtainable subtraces. First one is the DC subtrace $S^{(3)}_0$, which is again trivially defined as being equal to the DC modulation band $M^{(3)}_0$,

$$S^{(3)}_0(\Delta\omega,\tau) \equiv M^{(3)}_0(\Delta\omega,\tau) = 2\left|E^{(3)}(\Delta\omega)\right|^2 + 9\left|E^{(3)}_{\mathrm{FROG}}(\Delta\omega,\tau)\right|^2 + 9\left|E^{(3)}_{\mathrm{FROG}}(\Delta\omega,-\tau)\right|^2.$$

For THG-iFROG there is also an FM subtrace, but there is also a second-harmonic modulation (SHM) subtrace. The strategy to obtain both of these is exactly the same as what was done for $S^{(2)}_1$, that is to (i) obtain phase ϕ_{mod} of the highest modulation band, (ii) multiply a lower modulation band with a cosine whose argument is derived from ϕ_{mod}, and (iii) designate the DC component of the newly formed bands as the sought after subtrace. Let us start with the phase ϕ_{mod} for THG-iFROG, or $h = 3$. Using Eq. (B.7) we have $\phi_{\mathrm{mod}}(\omega,\tau) = (3\omega_0+\Delta\omega)\tau$. This time the FM modulation band $M^{(3)}_1$ consists of two terms instead of one, each of which has their own cosine factor with different arguments. We will see below that this does not pose a problem for the derivation of the FM subtrace $S^{(3)}_1$ which we begin now.

First we multiply the FM modulation band $M_1^{(3)}$ with cosine whose argument is $\frac{1}{3}\phi_{\mathrm{mod}}$,

$$\begin{aligned}
\cos\left[\tfrac{1}{3}\phi_{\mathrm{mod}}\right]\cdot M_1^{(3)} &= \cos\left[\left(\omega_0+\tfrac{1}{3}\Delta\omega\right)\tau\right] \\
&\quad\cdot\left\{6\cos[\phi_K+\omega_0\tau]\,|K|+18\cos[\phi_L-(\omega_0+\Delta\omega)\,\tau]\,|L|\right\} \\
&= \tfrac{6}{2}\,|K|\left\{\cos\left[\phi_K+\omega_0\tau+\left(\omega_0+\tfrac{1}{3}\Delta\omega\right)\tau\right]\right. \\
&\qquad\left.+\cos\left[\phi_K+\omega_0\tau-\left(\omega_0+\tfrac{1}{3}\Delta\omega\right)\tau\right]\right\}+ \\
&\quad\tfrac{18}{2}\,|L|\left\{\cos\left[\phi_L-(\omega_0+\Delta\omega)\,\tau+\left(\omega_0+\tfrac{1}{3}\Delta\omega\right)\tau\right]\right. \\
&\qquad\left.+\cos\left[\phi_L-(\omega_0+\Delta\omega)\,\tau-\left(\omega_0+\tfrac{1}{3}\Delta\omega\right)\tau\right]\right\} \\
&= 3\,|K|\left\{\cos\left[\phi_K+2\omega_0\tau+\tfrac{1}{3}\Delta\omega\tau\right]+\cos\left[\phi_K-\tfrac{1}{3}\Delta\omega\tau\right]\right\}+ \\
&\quad 9\,|L|\left\{\cos\left[\phi_L-\tfrac{2}{3}\Delta\omega\tau\right]+\cos\left[\phi_L-\left(2\omega_0+\tfrac{4}{3}\Delta\omega\right)\tau\right]\right\}. \qquad \text{(C.17)}
\end{aligned}$$

This leaves us in a similar situation encountered with the FM subtrace of SHG-iFROG in Eq. (B.9) in the sense that within the last two rows of Eq. (C.17) there are terms with a fast modulation due to a cosine with $\omega_0\tau$ in the argument, and terms that do not have such modulation. As before, we select the latter terms, of which there are two, an define these as the FM subtrace for THG-iFROG,

$$\begin{aligned}
S_1^{(3)}(\Delta\omega,\tau) \equiv\; & 3\,|K(\Delta\omega,\tau)|\cdot\cos\left[\phi_K(\Delta\omega,\tau)-\tfrac{1}{3}\Delta\omega\tau\right]+ \\
& 9\,|L(\Delta\omega,\tau)|\cdot\cos\left[\phi_L(\Delta\omega,\tau)-\tfrac{2}{3}\Delta\omega\tau\right].
\end{aligned}$$

The derivation is more simple for the second-harmonic modulation subtrace $S_2^{(3)}$, because the corresponding modulation band $M_2^{(3)}$ only has a single term, cf. Eq. (C.16c). Omitting the field arguments again, we multiply the modulation band with $\cos\left[\frac{2}{3}\phi_{\mathrm{mod}}\right]$,

$$\begin{aligned}
\cos\left[\tfrac{2}{3}\phi_{\mathrm{mod}}\right]\cdot M_2^{(3)} &= \cos\left[\left(2\omega_0+\tfrac{2}{3}\Delta\omega\right)\tau\right]\cdot\left\{6\cos\left[\phi_K-(2\omega_0+\Delta\omega)\,\tau\right]\cdot|K|\right\} \\
&= \tfrac{6}{2}\,|K|\cdot\left\{\cos\left[\phi_K-(2\omega_0+\Delta\omega)\,\tau+\left(2\omega_0+\tfrac{2}{3}\Delta\omega\right)\tau\right]\right. \\
&\qquad\left.+\cos\left[\phi_K-(2\omega_0+\Delta\omega)\,\tau-\left(2\omega_0+\tfrac{2}{3}\Delta\omega\right)\tau\right]\right\} \\
&= 3\,|K|\cdot\left\{\cos\left[\phi_K-\tfrac{1}{3}\Delta\omega\tau\right]+\cos\left[\phi_K-\left(4\omega_0+\tfrac{5}{3}\Delta\omega\right)\tau\right]\right\}. \qquad \text{(C.18)}
\end{aligned}$$

Once more, we select the term without a fast modulation due to $\omega_0\tau$, ignore the coefficient, and so obtain the SHM subtrace for THG-iFROG,

$$S_2^{(3)}(\Delta\omega,\tau) \equiv |K(\Delta\omega,\tau)| \cdot \cos\left[\phi_K(\Delta\omega,\tau) - \tfrac{1}{3}\Delta\omega\tau\right]$$

As with SHG-iFROG, both of these subtraces can also be derived with the help of the operator $\mathscr{C}$. Applying the operator on the FM band, $\mathscr{C}\{M_1^{(3)}\}$, and multiplying the result with an exponential function instead of a cosine of $\frac{1}{3}\phi_{\text{mod}}$ yields $S_1^{(3)}$. Likewise, $\exp\left(-i\frac{2}{3}\phi_{\text{mod}}\right)\cdot\mathscr{C}\{M_2^{(3)}\} = S_2^{(3)}$.

Acronyms

πFROG ptychographic-interferometric FROG 27, 82, 134

ADC analog-to-digital conversion 65
AI avalanche ionization 16, 102

BBO β-barium borate 12, 39, 134
BGR bandgap renormalization 102
BPF bandpass filter 82

CB conduction band 15
CCD charge-coupled device 65
CEP carrier-envelope phase 23

d-scan dispersion scan 27
DC direct current 47, 50
DCM double-chirped mirror 40
DE differential evolution 4, 33, 57
DoS density of states 102

EA evolutionary algorithm 57
EMCCD electron-magnifying charge-coupled device 136
ePIE extended ptychographic iterative engine 35, 36

FM fundamental modulation 50, 87
FROG frequency-resolved optical gating 2, 24, 28, 39
FROG-CRAB FROG for complete reconstruction of attosecond bursts 24
FTL Fourier-transform limited 11, 50, 82, 83
FWHM full width at half maximum 7, 82

GD group delay 11
GDD group-delay dispersion 11, 40, 82
GP generalized projections 30, 68

GVD group-velocity dispersion 11

iAC interferometric autocorrelation 2, 53, 58, 97
iFROG interferometric FROG 2, 25, 28, 39

MIIPS multiphoton intrapulse interference phase scan 27
MPA multiphoton absorption 1, 16, 94, 134

NIR near-infrared 1

PCGP principal component generalized projections 32
PIE ptychographic iterative engine 35
PL photoluminescence 2, 16, 93, 134, 136
PSD power spectral density 136

RMS root-mean-square 56, 59, 65, 114

SEM scanning electron microscope 95, 121
SHG second-harmonic generation 12, 39, 134
SHG-iFROG second-harmonic generation interferometric FROG 134
SHM second-harmonic modulation 50, 86, 146
SNR signal-to-noise ratio 3, 63, 66, 73, 75, 134
SPIDER spectral-interferometry for direct electric-field reconstruction 2, 24, 25, 40
SPM self-phase modulation 14, 118
SPP surface plasmon polariton 2, 17, 120
STHG surface third-harmonic generation 76, 135
SVEA slowly-varying envelope approximation 12, 59

TDP time-domain ptychography 35, 81
TDSE time-dependent Schrödinger equation 116
THG third-harmonic generation 2, 14, 39, 134
THG-iFROG THG interferometric FROG 134
TOD third-order dispersion 11
TRPL time-resolved photoluminescence 95

VB valence band 15
VLS vapor-liquid-solid 95
VPT vapor phase transport 95

XFROG cross-correlation FROG 30

Bibliography

[1] T. Brabec and F. Krausz, *Intense few-cycle laser fields: Frontiers of nonlinear optics*. Rev. Mod. Phys. **72**, 545–591 (2000).

[2] G. A. Mourou, T. Tajima, and S. V. Bulanov, *Optics in the relativistic regime*. Rev. Mod. Phys. **78** (2006).

[3] F. Krausz and M. Ivanov, *Attosecond physics*. Rev. Mod. Phys. **81**, 163–234 (2009).

[4] K. Zhao, Q. Zhang, M. Chini, Y. Wu, X. Wang, and Z. Chang, *Tailoring a 67 attosecond pulse through advantageous phase-mismatch*. Opt. Lett. **37**, 3891 (2012).

[5] M. Mero, J. Liu, W. Rudolph, D. Ristau, and K. Starke, *Scaling laws of femtosecond laser pulse induced breakdown in oxide films*. Phys. Rev. B **71**, 115109 (2005).

[6] R. Kienberger, E. Goulielmakis, M. Uiberacker, A. Baltuska, V. Yakovlev, F. Bammer, A. Scrinzi, T. Westerwalbesloh, U. Kleineberg, U. Heinzmann, M. Drescher, and F. Krausz, *Atomic transient recorder*. Nature **427**, 817–821 (2004).

[7] J.-C. Diels and W. Rudolph, *Ultrashort Laser Pulse Phenomena* (Academic Press, 2006).

[8] R. W. Boyd, *Nonlinear optics* (Academic Press, 2008).

[9] I. A. Walmsley and C. Dorrer, *Characterization of ultrashort electromagnetic pulses*. Adv. Opt. Photonics **1**, 308–437 (2009).

[10] K. W. Delong, C. L. Ladera, R. Trebino, B. Kohler, and K. R. Wilson, *Ultrashort-pulse measurement using noninstantaneous nonlinearities: Raman effects in frequency-resolved optical gating*. Opt. Lett. **20**, 486–488 (1995).

[11] I. Amat-Roldán, I. Cormack, P. Loza-Alvarez, E. Gualda, and D. Artigas, *Ultrashort pulse characterisation with SHG collinear-FROG*. Opt. Express **12**, 1169–1178 (2004).

[12] G. Stibenz and G. Steinmeyer, *Interferometric frequency-resolved optical gating*. Opt. Express **13**, 2617–2626 (2005).

[13] D. Kane and R. Trebino, *Characterization of arbitrary femtosecond pulses using frequency-resolved optical gating*. IEEE J. Quantum Electron. **29**, 571–579 (1993).

[14] C. Iaconis and I. a. Walmsley, *Spectral phase interferometry for direct electric-field reconstruction of ultrashort optical pulses.* Opt. Lett. **23**, 792–794 (1998).

[15] P. Biagioni, J.-S. Huang, and B. Hecht, *Nanoantennas for visible and infrared radiation*. Rep. Prog. Phys. **75**, 024402 (2012).

[16] A. Truegler, *Springer Series in Materials Science 232: Optical Properties of Metallic Nanoparticles*, Springer Series in Materials Science (Springer International Publishing, Cham, 2016).

[17] S. K. Das, C. Schwanke, A. Pfuch, W. Seeber, M. Bock, G. Steinmeyer, T. Elsaesser, and R. Grunwald, *Highly efficient THG in TiO_2 nanolayers for third-order pulse characterization*. Opt. Express **19**, 16985–16995 (2011).

[18] M. Mascheck, S. Schmidt, M. Silies, T. Yatsui, K. Kitamura, M. Ohtsu, D. Leipold, E. Runge, and C. Lienau, *Observing the localization of light in space and time by ultrafast second-harmonic microscopy*. Nat. Photonics **6**, 293–298 (2012).

[19] M. Silies, M. Mascheck, D. Leipold, H. Kollmann, S. Schmidt, J. Sartor, T. Yatsui, K. Kitamura, M. Ohtsu, H. Kalt, E. Runge, and C. Lienau, *Near-field-assisted localization: effect of size and filling factor of randomly distributed zinc oxide nanoneedles on multiple scattering and localization of light*. Appl. Phys. B Lasers Opt. **122**, 1–11 (2016).

[20] M. Simon, F. Traeger, A. Assion, B. Lang, S. Voll, and G. Gerber, *Femtosecond time-resolved second-harmonic generation at the surface of alkali metal clusters*. Chem. Phys. Lett. **296**, 579–584 (1998).

[21] B. Lamprecht, J. R. Krenn, A. Leitner, and E. R. Aussenegg, *Resonant and off-resonant light-driven plasmons in metal nanoparticles studied by femtosecond-resolution third-harmonic generation*. Phys. Rev. Lett. **83**, 4421–4424 (1999).

[22] M. W. Klein, T. Tritschler, M. Wegener, and S. Linden, *Lineshape of harmonic generation by metallic nanoparticles and metallic photonic crystal slabs*. Phys. Rev. B - Condens. Matter Mater. Phys. **72**, 1–12 (2005).

[23] T. Hanke, G. Krauss, D. Traeutlein, B. Wild, R. Bratschitsch, and A. Leitenstorfer, *Efficient nonlinear light emission of single gold optical antennas driven by few-cycle near-infrared pulses*. Phys. Rev. Lett. **103**, 1–4 (2009).

[24] T. Hanke, J. Cesar, V. Knittel, A. Truegler, U. Hohenester, A. Leitenstorfer, and R. Bratschitsch, *Tailoring spatiotemporal light confinement in single plasmonic nanoantennas*. Nano Lett. **12**, 992–996 (2012).

[25] J. M. Yi, V. Smirnov, X. Piao, J. Hong, H. Kollmann, M. Silies, W. Wang, P. Grob, R. Vogelgesang, N. Park, and C. Lienau, *Suppression of radiative damping and enhancement of second harmonic generation in bull's eye nanoresonators*. ACS Nano **10**, 475–483 (2016).

[26] M. Mueller, V. Kravtsov, A. Paarmann, M. B. Raschke, and R. Ernstorfer, *Nanofocused Plasmon-Driven Sub-10 fs Electron Point Source*. ACS Photonics **3**, 611–619 (2016).

[27] A. Anderson, K. S. Deryckx, X. G. Xu, G. Steinmeyer, and M. B. Raschke, *Few-femtosecond plasmon dephasing of a single metallic nanostructure from optical response function reconstruction by interferometric frequency resolved optical gating*. Nano Lett. **10**, 2519–2524 (2010).

[28] S. Schmidt, B. Piglosiewicz, D. Sadiq, J. Shirdel, J. S. Lee, P. Vasa, N. Park, D.-S. Kim, and C. Lienau, *Adiabatic Nanofocusing on Ultrasmooth Single-Crystalline Gold Tapers Creates a 10-nm-Sized Light Source with Few-Cycle Time Resolution*. ACS Nano **6**, 6040–6048 (2012).

[29] B. K. Canfield, H. Husu, J. Laukkanen, B. Bai, M. Kuittinen, J. Turunen, and M. Kauranen, *Local field asymmetry drives second-harmonic generation in noncentrosymmetric nanodimers*. Nano Lett. **7**, 1251–1255 (2007).

[30] G. Taft, A. Rundquist, M. M. Murnane, I. P. Christov, H. C. Kapteyn, K. W. DeLong, D. N. Fittinghoff, M. A. Krumbuegel, J. N. Sweetser, and R. Trebino, *Measurement of 10-fs laser pulses*. IEEE J. Sel. Top. Quantum Electron. **2**, 575–584 (1996).

[31] A. Baltuška, M. S. Pshenichnikov, and D. a. Wiersma, *Amplitude and phase characterization of 4.5-fs pulses by frequency-resolved optical gating*. Opt. Lett. **23**, 1474–1476 (1998).

[32] Y. Nishiyama, K. Imura, and H. Okamoto, *Observation of Plasmon Wave Packet Motions via Femtosecond Time-Resolved Near-Field Imaging Techniques*. Nano Lett. **15**, 7657–7665 (2015).

[33] J. M. Yi, D. Hou, H. Kollmann, V. Smirnov, Z. Pápa, P. Dombi, M. Silies, and C. Lienau, *Probing Coherent Surface Plasmon Polariton Propagation Using Ultrabroadband Spectral Interferometry*. ACS Photonics **4**, 347–354 (2017).

[34] Q. Liu, L. Seiffert, A. Trabattoni, M. C. Castrovilli, M. Galli, P. Rupp, F. Frassetto, L. Poletto, M. Nisoli, E. Ruehl, F. Krausz, T. Fennel, S. Zherebtsov, F. Calegari, and M. F. Kling, *Attosecond streaking metrology with isolated nanotargets*. J. Opt. (United Kingdom) **20** (2018).

[35] M. F. Ciappina, J. A. Pérez-Hernández, A. S. Landsman, W. A. Okell, S. Zherebtsov, B. Foerg, J. Schoetz, L. Seiffert, T. Fennel, T. Shaaran, T. Zimmermann, A. Chacón, R. Guichard, A. Zaïr, J. W. G. Tisch, J. P. Marangos, T. Witting, A. Braun, S. A. Maier, L. Roso, M. Krueger, P. Hommelhoff, M. F. Kling, F. Krausz, and M. Lewenstein, *Attosecond physics at the nanoscale*. Reports Prog. Phys. **80**, 054401 (2017).

[36] W. A. Okell, T. Witting, D. Fabris, C. A. Arrell, J. Hengster, S. Ibrahimkutty, A. Seiler, M. Barthelmess, S. Stankov, D. Y. Lei, Y. Sonnefraud, M. Rahmani, T. Uphues, S. A. Maier, J. P. Marangos, and J. W. G. Tisch, *Temporal broadening of attosecond photoelectron wavepackets from solid surfaces*. Optica **2**, 383 (2015).

[37] B. Foerg, J. Schoetz, F. Sueßmann, M. Foerster, M. Krueger, B. Ahn, W. A. Okell, K. Wintersperger, S. Zherebtsov, A. Guggenmos, V. Pervak, A. Kessel, S. A. Trushin, A. M. Azzeer, M. I. Stockman, D. Kim, F. Krausz, P. Hommelhoff, and M. F. Kling, *Attosecond nanoscale near-field sampling*. Nat. Commun. **7**, 1–7 (2016).

[38] G. Stibenz and G. Steinmeyer, *Structures of interferometric frequency-resolved optical gating*. IEEE J. Sel. Top. Quantum Electron. **12**, 286–296 (2006).

[39] R. Storn and K. Price, *Differential Evolution – A Simple and Efficient Heuristic for global Optimization over Continuous Spaces*. J. Glob. Optim. **11**, 341–359 (1997).

[40] P. Rocca, G. Oliveri, and A. Massa, *Differential Evolution as Applied to Electromagnetics*. IEEE Antennas Propag. Mag. **53**, 38–49 (2011).

[41] P. Sidorenko, O. Lahav, Z. Avnat, and O. Cohen, *Ptychographic reconstruction algorithm for frequency-resolved optical gating: super-resolution and supreme robustness*. Optica **3**, 1320–1330 (2016).

[42] A. M. Heidt, D.-M. Spangenberg, M. Bruegmann, E. G. Rohwer, and T. Feurer, *Improved retrieval of complex supercontinuum pulses from XFROG traces using a ptychographic algorithm*. Opt. Lett. **41**, 4903–4906 (2016).

[43] M. Lucchini, M. Bruegmann, A. Ludwig, L. Gallmann, U. Keller, and T. Feurer, *Ptychographic reconstruction of attosecond pulses*. Opt. Express **23**, 29502–29513 (2015).

[44] D. Spangenberg, E. Rohwer, M. H. Bruegmann, and T. Feurer, *Ptychographic ultrafast pulse reconstruction*. Opt. Lett. **40**, 1002–1005 (2015).

[45] J. M. Rodenburg and H. M. L. Faulkner, *A phase retrieval algorithm for shifting illumination*. Appl. Phys. Lett. **85**, 4795–4797 (2004).

[46] A. M. Maiden and J. M. Rodenburg, *An improved ptychographical phase retrieval algorithm for diffractive imaging*. Ultramicroscopy **109**, 1256–1262 (2009).

[47] W. Hoppe, *Beugung im inhomogenen Primaerstrahlwellenfeld. I. Prinzip einer Phasenmessung von Elektronenbeungungsinterferenzen*. Acta Crystallogr. Sect. A **25**, 495–501 (1969).

[48] T. Witting, D. Greening, D. Walke, P. Matia-Hernando, T. Barillot, J. P. Marangos, and J. W. G. Tisch, *Time-domain ptychography of over-octave-spanning laser pulses in the single-cycle regime*. Opt. Lett. **41**, 4218–4221 (2016).

[49] S. Schmidt, M. Mascheck, M. Silies, T. Yatsui, K. Kitamura, M. Ohtsu, and C. Lienau, *Distinguishing between ultrafast optical harmonic generation and multi-photon-induced luminescence from ZnO thin films by frequency-resolved interferometric autocorrelation microscopy*. Opt. Express **18**, 25016 (2010).

[50] C. F. Zhang, Z. W. Dong, G. J. You, R. Y. Zhu, S. X. Qian, H. Deng, H. Cheng, and J. C. Wang, *Femtosecond pulse excited two-photon photoluminescence and second harmonic generation in ZnO nanowires*. Appl. Phys. Lett. **89**, 042117 (2006).

[51] T. Voss, I. Kudyk, L. Wischmeier, and J. Gutowski, *Nonlinear optics with ZnO nanowires*. Phys. status solidi **246**, 311–314 (2009).

[52] J. Dai, Q.-F. Dai, J.-H. Zeng, S. Lan, X. Wan, and S.-L. Tie, *Negative Slope for Second Harmonic Generation Observed at High Excitation Intensities in ZnO Nanorods*. IEEE J. Quantum Electron. **49**, 903–909 (2013).

[53] J. Dai, J.-H. Zeng, S. Lan, X. Wan, and S.-L. Tie, *Competition between second harmonic generation and two-photon-induced luminescence in single, double and multiple ZnO nanorods*. Opt. Express **21**, 10025 (2013).

[54] S. K. Das, M. Biswas, D. Byrne, M. Bock, E. McGlynn, M. Breusing, and R. Grunwald, *Multiphoton-absorption induced ultraviolet luminescence of ZnO nanorods using low-energy femtosecond pulses*. J. Appl. Phys. **108**, 043107 (2010).

[55] R. Prasanth, L. K. van Vugt, D. A. M. Vanmaekelbergh, and H. C. Gerritsen, *Resonance enhancement of optical second harmonic generation in a ZnO nanowire*. Appl. Phys. Lett. **88**, 181501 (2006).

[56] J. Dai, M.-H. Yuan, J.-H. Zeng, Q.-F. Dai, S. Lan, C. Xiao, and S.-L. Tie, *Three-photon-induced blue emission with narrow bandwidth from hot flower-like ZnO nanorods*. Opt. Express **23**, 29231 (2015).

[57] K. Pedersen, C. Fisker, and T. G. Pedersen, *Second-harmonic generation from ZnO nanowires*. Phys. status solidi **5**, 2671–2674 (2008).

[58] D. Dai, S. Xu, S. Shi, M. Xie, and C. Che, *Observation of both second-harmonic and multiphoton-absorption-induced luminescence in ZnO*. IEEE Photonics Technol. Lett. **18**, 1533–1535 (2006).

[59] L. V. Keldysh, *Ionization in the Field of a Strong Electromagnetic Wave*. Sov. physics, JETP **20**, 1307–1314 (1965).

[60] R. Trebino, *Frequency-resolved optical gating: the measurement of ultrashort laser pulses*, 1st ed. (Springer Science+Business Media, New York, 2000).

[61] P. E. Powers, *Fundamentals of Nonlinear Optics*, 1st ed. (CRC Press, Boca Raton, 2011), p. 329.

[62] G. New, *Introduction to Nonlinear Optics* (Cambridge University Press, 2011).

[63] O. Svelto, *Principles of lasers* (2010), pp. 1–620.

[64] C. Kittel, *Introduction to Solid State Physics* (John Wiley & Sons, Inc., 2005).

[65] A. E. Siegman, *Lasers* (University Science Books, 1986).

[66] J. C. Maxwell, *VIII. A dynamical theory of the electromagnetic field*. Philos. Trans. R. Soc. London **155**, 459–512 (1865).

[67] M. Beversluis, A. Bouhelier, and L. Novotny, *Continuum generation from single gold nanostructures through near-field mediated intraband transitions*. Phys. Rev. B - Condens. Matter Mater. Phys. **68**, 1–10 (2003).

[68] T. Weber, T. Kiel, S. Irsen, K. Busch, and S. Linden, *Near-field study on the transition from localized to propagating plasmons on 2D nano-triangles*. Opt. Express **25**, 16947 (2017).

[69] N. Liu, M. L. Tang, M. Hentschel, H. Giessen, and A. P. Alivisatos, *Nanoantenna-enhanced gas sensing in a single tailored nanofocus*. Nat. Mater. **10**, 631–636 (2011).

[70] T. Rybka, M. Ludwig, M. F. Schmalz, V. Knittel, D. Brida, and A. Leitenstorfer, *Sub-cycle optical phase control of nanotunnelling in the single-electron regime*. Nat. Photonics **10**, 667–670 (2016).

[71] U. Hohenester and A. Truegler, *MNPBEM - A Matlab toolbox for the simulation of plasmonic nanoparticles*. Comput. Phys. Commun. **183**, 370–381 (2012).

[72] V. Knittel, "Ultrafast nonlinear response of plasmonic nanoantennas", PhD thesis (University of Konstanz, 2018).

[73] K. B. Crozier, A. Sundaramurthy, G. S. Kino, and C. F. Quate, *Optical antennas: Resonators for local field enhancement*. J. Appl. Phys. **94**, 4632–4642 (2003).

[74] A. C. Lesina, P. Berini, and L. Ramunno, *Origin of third harmonic generation in plasmonic nanoantennas*. Opt. Mater. Express **7**, 1575 (2017).

[75] J. McLaughlin, *Connection between dissipative and resonant conservative nonlinear oscillators*. J. Stat. Phys. **19**, 587–591 (1978).

[76] C. Soennichsen, T. Franzl, T. Wilk, G. von Plessen, J. Feldmann, O. Wilson, and P. Mulvaney, *Drastic reduction of plasmon damping in gold nanorods*. Phys. Rev. Lett. **88**, 774021–774024 (2002).

[77] L. Gallmann, G. Steinmeyer, D. H. Sutter, T. Rupp, C. Iaconis, I. a. Walmsley, and U. Keller, *Spatially resolved amplitude and phase characterization of femtosecond optical pulses*. Opt. Lett. **26**, 96 (2001).

[78] T. Witting, F. Frank, C. A. Arrell, W. A. Okell, J. P. Marangos, and J. W. G. Tisch, *Characterization of high-intensity sub-4-fs laser pulses using spatially encoded spectral shearing interferometry*. Opt. Lett. **36**, 1680–1682 (2011).

[79] G. Pariente, V. Gallet, A. Borot, O. Gobert, and F. Quéré, *Space-time characterization of ultra-intense femtosecond laser beams*. Nat. Photonics **10**, 547–553 (2016).

[80] P. Bowlan, U. Fuchs, R. Trebino, and U. D. Zeitner, *Measuring the spatiotemporal electric field of tightly focused ultrashort pulses with sub-micron spatial resolution*. Opt. Express **16**, 13663–13675 (2008).

[81] S. Akturk, X. Gu, P. Bowlan, and R. Trebino, *Spatio-temporal couplings in ultrashort laser pulses*. J. Opt. **12** (2010).

[82] R. Trebino and D. J. Kane, *Using phase retrieval to measure the intensity and phase of ultrashort pulses: frequency-resolved optical gating*. J. Opt. Soc. Am. A **10**, 1101–1111 (1993).

[83] K. W. DeLong, R. Trebino, J. Hunter, and W. E. White, *Frequency-resolved optical gating with the use of second-harmonic generation*. J. Opt. Soc. Am. B **11**, 2206 (1994).

[84] W. Kornelis, J. Biegert, J. W. G. Tisch, M. Nisoli, G. Sansone, C. Vozzi, S. De Silvestri, and U. Keller, *Single-shot kilohertz characterization of ultrashort pulses by spectral phase interferometry for direct electric-field reconstruction*. Opt. Lett. **28**, 281–283 (2003).

[85] M. Rhodes, G. Steinmeyer, J. Ratner, and R. Trebino, *Pulse-shape instabilities and their measurement*. Laser Photonics Rev. **7**, 557–565 (2013).

[86] B. Borchers, S. Koke, A. Husakou, J. Herrmann, and G. Steinmeyer, *Carrier-envelope phase stabilization with sub-10 as residual timing jitter*. Opt. Lett. **36**, 4146 (2011).

[87] E. Goulielmakis, M. Schultze, M. Hofstetter, V. S. Yakovlev, J. Gagnon, M. Uiberacker, A. L. Aquila, E. M. Gullikson, D. T. Attwood, R. Kienberger, F. Krausz, and U. Kleineberg, *Single-Cycle Nonlinear Optics*. Science (80-.). **320**, 1614–1617 (2008).

[88] Y. Mairesse and F. Quéré, *Frequency-resolved optical gating for complete reconstruction of attosecond bursts*. Phys. Rev. A **71**, 011401 (2005).

[89] T. Witting, S. J. Weber, J. W. G. Tisch, and J. P. Marangos, *Spatio-temporal characterization of mid-infrared laser pulses with spatially encoded spectral shearing interferometry*. Opt. Express **20**, 27974–27980 (2012).

[90] J. R. Birge and F. X. Kaertner, *Analysis and mitigation of systematic errors in spectral shearing interferometry of pulses approaching the single-cycle limit [Invited]*. J. Opt. Soc. Am. B **25**, A111 (2008).

[91] C. Dorrer and I. Kang, *Complete temporal characterization of short optical pulses by simplified chronocyclic tomography*. Opt. Lett. **28**, 1481–3 (2003).

[92] B. H. Kolner and M. Nazarathy, *Temporal imaging with a time lens*. Opt. Lett. **14**, 630 (1989).

[93] P. Ryczkowski, M. Naerhi, C. Billet, J.-M. Merolla, G. Genty, and J. M. Dudley, *Real-time full-field characterization of transient dissipative soliton dynamics in a mode-locked laser*. Nat. Photonics (2018).

[94] P. Londero, O. Kuzucu, and A. L. Gaeta, *Spectral amplitude and phase measurement of ultrafast pulses using all-optical differential tomography*. Opt. Lett. **36**, 1686 (2011).

[95] R. Salem, M. A. Foster, and A. L. Gaeta, *Application of space-time duality to ultrahigh-speed optical signal processing*. Adv. Opt. Photonics **5**, 274 (2013).

[96] S. Akturk, C. D'Amico, and A. Mysyrowicz, *Measuring ultrashort pulses in the single-cycle regime using frequency-resolved optical gating*. J. Opt. Soc. Am. B **25**, A63–A69 (2008).

[97] G. Stibenz and G. Steinmeyer, *Optimizing spectral phase interferometry for direct electric-field reconstruction*. Rev. Sci. Instrum. **77**, 073105 (2006).

[98] H. Timmers, Y. Kobayashi, K. F. Chang, M. Reduzzi, D. M. Neumark, and S. R. Leone, *Generating high-contrast, near single-cycle waveforms with third-order dispersion compensation*. Opt. Lett. **42**, 811–814 (2017).

[99] V. V. Lozovoy, I. Pastirk, and M. Dantus, *Multiphoton intrapulse interference. IV. Ultrashort laser pulse spectral phase characterization and compensation.* Opt. Lett. **29**, 775–777 (2004).

[100] M. Miranda, T. Fordell, C. Arnold, A. L'Huillier, and H. Crespo, *Simultaneous compression and characterization of ultrashort laser pulses using chirped mirrors and glass wedges*. Opt. Express **20**, 688–697 (2012).

[101] F. Silva, M. Miranda, B. Alonso, J. Rauschenberger, V. Pervak, and H. Crespo, *Simultaneous compression, characterization and phase stabilization of GW-level 1.4 cycle VIS-NIR femtosecond pulses using a single dispersion-scan setup*. Opt. Express **22**, 10181–10190 (2014).

[102] J. A. Armstrong, *Measurement of picosecond laser pulse widths*. Appl. Phys. Lett. **10**, 16–18 (1967).

[103] K. Sala, G. Kenney-Wallace, and G. Hall, *CW autocorrelation measurements of picosecond laser pulses*. IEEE J. Quantum Electron. **16**, 990–996 (1980).

[104] J. A. Giordmaine, P. M. Rentzepis, S. L. Shapiro, and K. W. Wecht, *Two-photon excitation of flourescence by picosecond light pulses*. Appl. Phys. Lett. **11**, 216–218 (1967).

[105] J.-C. M. Diels, J. J. Fontaine, I. C. McMichael, and F. Simoni, *Control and measurement of ultrashort pulse shapes (in amplitude and phase) with femtosecond accuracy*. Appl. Opt. **24**, 1270–1282 (1985).

[106] J. W. Nicholson and W. Rudolph, *Noise sensitivity and accuracy of femtosecond pulse retrieval by phase and intensity from correlation and spectrum only (PICASO)*. J. Opt. Soc. Am. B **19**, 330–339 (2002).

[107] S. Berweger, J. M. Atkin, X. G. Xu, R. L. Olmon, and M. B. Raschke, *Femtosecond Nanofocusing with Full Optical Waveform Control*. Nano Lett. **11**, 4309–4313 (2011).

[108] T. Balciunas, C. Fourcade-Dutin, G. Fan, T. Witting, A. A. Voronin, A. M. Zheltikov, F. Gerome, G. G. Paulus, A. Baltuška, and F. Benabid, *A strong-field driver in the single-cycle regime based on self-compression in a kagome fibre*. Nat. Commun. **6**, 6117 (2015).

[109] D. N. Fittinghoff, J. a. Squier, C. P. Barty, J. N. Sweetser, R. Trebino, and M. Mueller, *Collinear type II second-harmonic-generation frequency-resolved optical gating for use with high-numerical-aperture objectives.* Opt. Lett. **23**, 1046–1048 (1998).

[110] R. Chadwick, E. Spahr, J. A. Squier, C. G. Durfee, B. C. Walker, and D. N. Fittinghoff, *Fringe-free, background-free, collinear third-harmonic generation frequency-resolved optical gating measurements for multiphoton microscopy*. **31**, 3366–3368 (2006).

[111] L. Gallmann, G. Steinmeyer, D. H. Sutter, N. Matuschek, and U. Keller, *Collinear type II second-harmonic-generation frequency-resolved optical gating for the characterization of sub-10-fs optical pulses.* Opt. Lett. **25**, 269–271 (2000).

[112] S. Linden, H. Giessen, and J. Kuhl, *XFROG – A New Method for Amplitude and Phase Characterization of Weak Ultrashort Pulses*. Phys. Stat. Sol **206**, 119–124 (1998).

[113] L. Xu, E. Zeek, and R. Trebino, *Simulations of frequency-resolved optical gating for measuring very complex pulses*. J. Opt. Soc. Am. B **25**, A70 (2008).

[114] K. W. DeLong, B. Kohler, K. Wilson, D. N. Fittinghoff, and R. Trebino, *Pulse retrieval in frequency-resolved optical gating based on the method of generalized projections*. Opt. Lett. **19**, 2152–2154 (1994).

[115] D. J. Kane, *Real-time measurement of ultrashort laser pulses using principal component generalized projections*. IEEE J. Sel. Top. Quantum Electron. **4**, 278–284 (1998).

[116] D. N. Fittinghoff, K. W. DeLong, R. Trebino, and C. L. Ladera, *Noise sensitivity in frequency-resolved optical-gating measurements of ultrashort pulses*. J. Opt. Soc. Am. B **12**, 1955–1967 (1995).

[117] J. A. Nelder and R. Mead, *A Simplex Method for Function Minimization*. Comput. J. **7**, 308–313 (1965).

[118] C. Lin, A. Qing, and Q. Feng, *Synthesis of unequally spaced antenna arrays by a new differential evolutionary algorithm*. Int. J. Commun. Networks Inf. Secur. **1**, 20–25 (2009).

[119] R. Hegerl and W. Hoppe, *Dynamische Theorie der Kristallstrukturanalyse durch Elektronenbeugung im inhomogenen Primaerstrahlwellenfeld*. Ber. Bunsenges. Phys. Chem. **74**, 1148–1154 (1970).

[120] D. Spangenberg, P. Neethling, E. Rohwer, M. H. Bruegmann, and T. Feurer, *Time-domain ptychography*. Phys. Rev. A **91**, 021803 (2015).

[121] J. Hyyti, "Frequency-Resolved Optical Gating for Investigating Ultrafast Optical Phenomena on the Few-Cycle Scale", Master's Thesis (Tampere University of Technology, 2013).

[122] V. Saptari, *Fourier-Transform Spectroscopy Instrumentation Engineering* (SPIE Press, Bellingham, WA, 2003).

[123] M. Takeda, H. Ina, and S. Kobayashi, *Fourier-transform method of fringe-pattern analysis for computer-based topography and interferometry*. J. Opt. Soc. Am. **72**, 156–160 (1982).

[124] K. W. DeLong, R. Trebino, and D. J. Kane, *Comparison of ultrashort-pulse frequency-resolved-optical-gating traces for three common beam geometries*. J. Opt. Soc. Am. B **11**, 1595–1608 (1994).

[125] K. W. DeLong, D. N. Fittinghoff, and R. Trebino, *Practical issues in ultrashort-laser-pulse measurement using frequency-resolved optical gating*. IEEE J. Quantum Electron. **32**, 1253–1264 (1996).

[126] Y. Chen, S. Yang, and Z. Nie, *Synthesis of Uniform Amplitude Thinned Linear Phased Arrays Using the Differential Evolution Algorithm*. Electromagnetics **27**, 287–297 (2007).

[127] K. A. Michalski, *Electromagnetic imaging of elliptical-cylindrical conductors and tunnels using a differential evolution algorithm*. Microw. Opt. Technol. Lett. **28**, 164–169 (2001).

[128] D. Kurup, M. Himdi, and A. Rydberg, *Design of an unequally spaced reflectarray*. IEEE Antennas Wirel. Propag. Lett. **2**, 33–35 (2003).

[129] K. Irie, A. E. McKinnon, K. Unsworth, and I. M. Woodhead, *A model for measurement of noise in CCD digital-video cameras*. Meas. Sci. Technol. **19**, 045207 (2008).

[130] H. P. Yuen and V. W. Chan, *Noise in homodyne and heterodyne detection.* Opt. Lett. **8**, 177–179 (1983).

[131] M. Kitagawa, N. Imoto, and Y. Yamamoto, *Realization of number-phase minimum-uncertainty states and number states by quantum nondemolition measurement*. Phys. Rev. A **35**, 5270–5273 (1987).

[132] R. Paschotta, A. Schlatter, S. C. Zeller, H. R. Telle, and U. Keller, *Optical phase noise and carrier-envelope offset noise of mode-locked lasers*. Appl. Phys. B Lasers Opt. **82**, 265–273 (2006).

[133] R. Trebino, *Code for retrieving a pulse intensity and phase from its FROG trace, version 1.2, Georgia Institute of Technology*, `http://frog.gatech.edu/code.html`, (2012).

[134] D. J. Kane, G. Rodriguez, A. J. Taylor, and T. S. Clement, *Simultaneous measurement of two ultrashort laser pulses from a single spectrogram in a single shot*. J. Opt. Soc. Am. B **14**, 935–943 (1997).

[135] G. I. Haham, P. Sidorenko, O. Lahav, and O. Cohen, *Multiplexed FROG*. Opt. Express **25**, 33007–33017 (2017).

[136] D.-M. Spangenberg, M. Bruegmann, E. Rohwer, and T. Feurer, *All-optical implementation of a time-domain ptychographic pulse reconstruction setup*. Appl. Opt. **55**, 5008–5013 (2016).

[137] C. Klingshirn, *ZnO: From basics towards applications*. Phys. status solidi **244**, 3027–3073 (2007).

[138] Y. R. Ryu, T. S. Lee, J. A. Lubguban, H. W. White, Y. S. Park, and C. J. Youn, *ZnO devices: Photodiodes and p-type field-effect transistors*. Appl. Phys. Lett. **87**, 153504 (2005).

[139] A. Tsukazaki, A. Ohtomo, T. Onuma, M. Ohtani, T. Makino, M. Sumiya, K. Ohtani, S. F. Chichibu, S. Fuke, Y. Segawa, H. Ohno, H. Koinuma, and M. Kawasaki, *Repeated temperature modulation epitaxy for p-type doping and light-emitting diode based on ZnO*. Nat. Mater. **4**, 42–46 (2004).

[140] M. H. Huang, S. Mao, H. Feick, H. Yan, Y. Wu, H. Kind, E. Weber, R. Russo, and P. Yang, *Room-Temperature Ultraviolet Nanowire Nanolasers*. Science (80-.). **292**, 1897–1899 (2001).

[141] C. Couteau, A. Larrue, C. Wilhelm, and C. Soci, *Nanowire lasers*. Nanophotonics **4**, 90–107 (2015).

[142] M. Godlewski, E. Guziewicz, K. Kopalko, G. Łuka, M. I. Łukasiewicz, T. Krajewski, B. S. Witkowski, and S. Gierałtowska, *Zinc oxide for electronic, photovoltaic and optoelectronic applications*. Low Temp. Phys. **37**, 235–240 (2011).

[143] C. Zhang, F. Zhang, S. Qian, N. Kumar, J.-i. Hahm, and J. Xu, *Multiphoton absorption induced amplified spontaneous emission from biocatalyst-synthesized ZnO nanorods*. Appl. Phys. Lett. **92**, 233116 (2008).

[144] D. Sridhar, J. Xie, J. K. Abraham, and V. K. Varadan, "Synthesis and photonic property study of ZnO nanowires for a real time photodynamic therapy monitoring probe", in Proc. spie 6528, nanosensors, microsens. biosens. syst. 2007, edited by V. K. Varadan (Apr. 2007), p. 65281L.

[145] A. B. Djurišić and Y. H. Leung, *Optical Properties of ZnO Nanostructures*. Small **2**, 944–961 (2006).

[146] D. C. Reynolds, D. C. Look, and B. Jogai, *Fine structure on the green band in ZnO*. J. Appl. Phys. **89**, 6189–6191 (2001).

[147] R. Raji and K. Gopchandran, *ZnO nanostructures with tunable visible luminescence: Effects of kinetics of chemical reduction and annealing*. J. Sci. Adv. Mater. Devices **2**, 51–58 (2017).

[148] C. Klingshirn and H. Haug, *Optical properties of highly excited direct gap semiconductors*. Phys. Rep. **70**, 315–398 (1981).

[149] K. B. Nordstrom, K. Johnsen, S. J. Allen, A.-P. Jauho, B. Birnir, J. Kono, T. Noda, H. Akiyama, and H. Sakaki, *Excitonic Dynamical Franz-Keldysh Effect*. Phys. Rev. Lett. **81**, 457–460 (1998).

[150] S. I. Park, Y. Tchoe, H. Baek, J. Heo, J. K. Hyun, J. Jo, M. Kim, N.-J. Kim, and G.-C. Yi, *Growth and optical characteristics of high-quality ZnO thin films on graphene layers*. APL Mater. **3**, 016103 (2015).

[151] E. McGlynn, M. O. Henry, and J.-P. Mosnier, "Chapter 14", in *Handb. nanosci. technol. vol. ii*, edited by A. Narlikar and Y. Y. Fu (Oxford University Press, 2009).

[152] H. J. Fan, P. Werner, and M. Zacharias, *Semiconductor Nanowires: From Self-Organization to Patterned Growth*. Small **2**, 700–717 (2006).

[153] F. Gueell, J. O. Ossó, A. R. Goñi, A. Cornet, and J. R. Morante, *Direct imaging of the visible emission bands from individual ZnO nanowires by near-field optical spectroscopy*. Nanotechnology **20**, 315701 (2009).

[154] D. Byrne, E. McGlynn, K. Kumar, M. Biswas, M. O. Henry, and G. Hughes, *A Study of Drop-Coated and Chemical Bath-Deposited Buffer Layers for Vapor Phase Deposition of Large Area, Aligned, Zinc Oxide Nanorod Arrays*. Cryst. Growth Des. **10**, 2400–2408 (2010).

[155] C. Gray, J. Cullen, C. Byrne, G. Hughes, I. Buyanova, W. Chen, M. O. Henry, and E. McGlynn, *Growth of isotopically enriched ZnO nanorods of excellent optical quality*. J. Cryst. Growth **429**, 6–12 (2015).

[156] C. W. Cheng, E. J. Sie, B. Liu, C. H. A. Huan, T. C. Sum, H. D. Sun, and H. J. Fan, *Surface plasmon enhanced band edge luminescence of ZnO nanorods by capping Au nanoparticles*. Appl. Phys. Lett. **96**, 071107 (2010).

[157] M. A. Versteegh, T. Kuis, H. T. Stoof, and J. I. Dijkhuis, *Ultrafast screening and carrier dynamics in ZnO: Theory and experiment*. Phys. Rev. B - Condens. Matter Mater. Phys. **84**, 1–19 (2011).

[158] K. J. Button, D. R. Cohn, M. von Ortenbert, B. Lax, E. Mollwo, and R. Helbig, *Zeeman Splitting of Anomalous Shallow Bound States in ZnO*. Phys. Rev. Lett. **28**, 1637–1639 (1972).

[159] W. L. Bond, *Measurement of the refractive indices of several crystals*. J. Appl. Phys. **36**, 1674–1677 (1965).

[160] L. Bányai and S. W. Koch, *A simple theory for the effects of plasma screening on the optical spectra of highly excited semiconductors*. Zeitschrift fuer Phys. B Condens. Matter **63**, 283–291 (1986).

[161] J. M. Zhang and Y. Liu, *Fermi's golden rule: Its derivation and breakdown by an ideal model*. Eur. J. Phys. **37** (2016).

[162] B. C. Stuart, M. D. Feit, S. Herman, A. M. Rubenchik, B. W. Shore, and M. D. Perry, *Nanosecond-to-femtosecond laser-induced breakdown in dielectrics*. Phys. Rev. B **53**, 1749–1761 (1996).

[163] J. Jasapara, A. Nampoothiri, W. Rudolph, D. Ristau, and K. Starke, *Femtosecond laser pulse induced breakdown in dielectric thin films*. Phys. Rev. B **63**, 045117 (2001).

[164] R. Hollinger, Z. Samsonova, D. Gupta, C. Spielmann, R. Roeder, L. Trefflich, C. Ronning, and D. Kartashov, *Enhanced absorption and cavity effects of three-photon pumped ZnO nanowires*. Appl. Phys. Lett. **111**, 213106 (2017).

[165] C. F. Zhang, Z. W. Dong, G. J. You, S. X. Qian, and H. Deng, *Multiphoton route to ZnO nanowire lasers*. Opt. Lett. **31**, 3345–3347 (2006).

[166] M. A. M. Versteegh, D. Vanmaekelbergh, and J. I. Dijkhuis, *Room-Temperature Laser Emission of ZnO Nanowires Explained by Many-Body Theory*. Phys. Rev. Lett. **108**, 157402 (2012).

[167] X. Han, G. Wang, Q. Wang, L. Cao, R. Liu, B. Zou, and J. G. Hou, *Ultraviolet lasing and time-resolved photoluminescence of well-aligned ZnO nanorod arrays*. Appl. Phys. Lett. **86**, 1–3 (2005).

[168] N. Nedyalkov, T. Sakai, T. Miyanishi, and M. Obara, *Near field properties in the vicinity of gold nanoparticles placed on various substrates for precise nanostructuring*. J. Phys. D. Appl. Phys. **39**, 5037–5042 (2006).

[169] A. L. Cavalieri, E. Goulielmakis, B. Horvath, W. Helml, M. Schultze, M. Fieß, V. Pervak, L. Veisz, V. S. Yakovlev, M. Uiberacker, A. Apolonski, F. Krausz, and R. Kienberger, *Intense 1.5-cycle near infrared laser waveforms and their use for the generation of ultra-broadband soft-x-ray harmonic continua*. New J. Phys. **9**, 242 (2007).

[170] W. A. Okell, T. Witting, D. Fabris, D. Austin, M. Bocoum, F. Frank, A. Ricci, A. Jullien, D. Walke, J. P. Marangos, R. Lopez-Martens, and J. W. G. Tisch, *Carrier-envelope phase stability of hollow fibers used for high-energy few-cycle pulse generation*. Opt. Lett. **38**, 3918 (2013).

[171] C. Manzoni, O. D. Muecke, G. Cirmi, S. Fang, J. Moses, S. W. Huang, K. H. Hong, G. Cerullo, and F. X. Kaertner, *Coherent pulse synthesis: Towards sub-cycle optical waveforms*. Laser Photonics Rev. **9**, 129–171 (2015).

[172] E. Matsubara, K. Yamane, T. Sekikawa, and M. Yamashita, *Generation of 26 fs optical pulses using induced-phase modulation in a gas-filled hollow fiber*. J. Opt. Soc. Am. B **24**, 985 (2007).

[173] S. Smolorz and F. Wise, *Femtosecond two-beam coupling energy transfer from Raman and electronic nonlinearities*. J. Opt. Soc. Am. B **17**, 1636 (2000).

[174] M. T. Hassan, T. T. Luu, A. Moulet, O. Raskazovskaya, P. Zhokhov, M. Garg, N. Karpowicz, A. M. Zheltikov, V. Pervak, F. Krausz, and E. Goulielmakis, *Optical attosecond pulses and tracking the nonlinear response of bound electrons*. Nature **530**, 66–70 (2016).

[175] B. Luk'Yanchuk, N. I. Zheludev, S. A. Maier, N. J. Halas, P. Nordlander, H. Giessen, and C. T. Chong, *The Fano resonance in plasmonic nanostructures and metamaterials*. Nat. Mater. **9**, 707–715 (2010).

[176] J. Reisloehner and A. N. Pfeiffer, *The role of delay times in subcycle-resolved probe retardation measurements*. Phys. E Low-Dimensional Syst. Nanostructures **76**, 223–230 (2016).

[177] Y. Barad, H. Eisenberg, M. Horowitz, and Y. Silberberg, *Nonlinear scanning laser microscopy by third harmonic generation*. Appl. Phys. Lett. **70**, 922 (1997).

[178] M. Hofmann, "Einfluss dynamischer Resonanzen auf die Wechselwirkung optischer Femtosekunden-Pulse mit transparenten Dielektrika", PhD thesis (TU Berlin, 2016).

[179] M. Korbman, S. Yu Kruchinin, and V. S. Yakovlev, *Quantum beats in the polarization response of a dielectric to intense few-cycle laser pulses*. New J. Phys. **15** (2013).

[180] T. Paasch-Colberg, A. Schiffrin, N. Karpowicz, S. Kruchinin, o. Sağlam, S. Keiber, O. Razskazovskaya, S. Muehlbrandt, A. Alnaser, M. Kuebel, V. Apalkov, D. Gerster, J. Reichert, T. Wittmann, J. V. Barth, M. I. Stockman, R. Ernstorfer, V. S. Yakovlev, R. Kienberger, and F. Krausz, *Solid-state light-phase detector*. Nat. Photonics **8**, 214–218 (2014).

[181] M. Sheik-Bahae, D. Hutchings, D. Hagan, and E. V. Stryland, *Dispersion of bound electron nonlinear refraction in solids*. IEEE J. Quantum Electron. **27** (1991).

[182] H. G. Muller, *An efficient propagation scheme for the time-dependent Schrodinger equation in the velocity gauge*. Laser Phys. **9**, 138–148 (1999).

[183] S. Uemura and K. Torizuka, *Generation of 10 fs pulses from a diode-pumped Kerr-lens mode-locked Cr:LiSAF laser*. Japanese J. Appl. Phys. Part 1-Regular Pap. Short Notes Rev. Pap. **39**, 3472–3473 (2000).

[184] H. Zhao and A. Major, *Powerful 67 fs Kerr-lens mode-locked prismless Yb:KGW oscillator*. Opt. Express **21**, 31846 (2013).

[185] E. Sorokin, N. Tolstik, and I. T. Sorokina, *Kerr-Lens Mode-locked Cr:ZnS Laser*. **38**, 8–10 (2012).

[186] R. Kitamura, L. Pilon, and M. Jonasz, *Optical constants of silica glass from extreme ultraviolet to far infrared at near room temperature*. Appl. Opt. **46**, 8118 (2007).

[187] A. Milgram and M. P. Givens, *Extreme ultraviolet absorption by lithium fluoride*. Phys. Rev. **125**, 1506–1509 (1962).

[188] M. Chini, K. Zhao, and Z. Chang, *The generation, characterization and applications of broadband isolated attosecond pulses*. Nat. Photonics **8**, 178–186 (2014).

[189] K. D. Ko, A. Kumar, K. H. Fung, R. Ambekar, G. L. Liu, N. X. Fang, and K. C. Toussaint, *Nonlinear optical response from arrays of Au bowtie nanoantennas*. Nano Lett. **11**, 61–65 (2011).

[190] B. Radha and G. U. Kulkarni, *A real time microscopy study of the growth of giant Au microplates*. Cryst. Growth Des. **11**, 320–327 (2011).

[191] M. Kuttge, E. J. Vesseur, J. Verhoeven, H. J. Lezec, H. A. Atwater, and A. Polman, *Loss mechanisms of surface plasmon polaritons on gold probed by cathodoluminescence imaging spectroscopy.* Appl. Phys. Lett. **93** (2008).

[192] D. Brida, G. Krauss, A. Sell, and A. Leitenstorfer, *Ultrabroadband Er: Fiber lasers*. Laser Photonics Rev. **8**, 409–428 (2014).

[193] A. Michelson and E. Morley, *On the Relative Motion of the Earth and the Luminiferous Ether*. Am. J. Sci. **34**, 333–345 (1887).

[194] P. Hariharan, *Basics of Interferometry*, 2nd ed. (2007).

[195] T. Y. F. Tsang, *Optical third-harmonic generation at interfaces*. Phys. Rev. A - At. Mol. Opt. Phys. **52**, 4116–4125 (1995).

Selbständigkeitserklärung

Ich erkläre, dass ich die Dissertation selbständig und nur unter Verwendung der von mir gemäß § 7 Abs. 3 der Promotionsordnung der Mathematisch-Naturwissenschaftlichen Fakultät, veröffentlicht im Amtlichen Mitteilungsblatt der Humboldt-Universität zu Berlin Nr. 126/2014 am 18.11.2014 angegebenen Hilfsmittel angefertigt habe.

Berlin, den 10. September 2018 Janne Juhani Hyyti